

Doctoral Thesis

**Ionomer-Stabilised Pt and Pt-Ti Bimetallic Electrocatalysts for  
the Proton Exchange Membrane Fuel Cell**

in Partial Fulfillment of the Requirements for the Degree  
Doctor of Philosophy

Presented to the School of Chemical Engineering  
of the University of Birmingham (United Kingdom) by

**Oliver Curnick**

in July 2012

Supervisor: Dr. Paula M. Mendes

Co-Supervisor: Dr. Bruno G. Pollet

UNIVERSITY OF  
BIRMINGHAM

**University of Birmingham Research Archive**

**e-theses repository**

This unpublished thesis/dissertation is copyright of the author and/or third parties. The intellectual property rights of the author or third parties in respect of this work are as defined by The Copyright Designs and Patents Act 1988 or as modified by any successor legislation.

Any use made of information contained in this thesis/dissertation must be in accordance with that legislation and must be properly acknowledged. Further distribution or reproduction in any format is prohibited without the permission of the copyright holder.

## **Declaration**

Hereby I declare that I wrote this document myself with the help of no more than the mentioned literature and auxiliary means.

Up to now, this document was not published or presented to another examinations office in the same or similar shape.

Birmingham, July 2012

---

place and date

---

signature (Oliver Curnick)

## Acknowledgments

# Acknowledgments

This thesis represents the culmination of my research carried out between October 2009 and July 2012 in the School of Chemical Engineering at the University of Birmingham. I would like to thank several individuals for their contributions, support and assistance throughout this period .

Firstly, I am grateful to my supervisors, Dr. Paula Mendes and Dr. Bruno Pollet, for providing the opportunity to work in their research groups, and for their support and guidance throughout this process. Thanks, also to the other members of the Mendes and Hydrogen & Fuel Cell research groups for their assistance with various practical aspects of this work. Special thanks to Dr. Parvez Iqbal and Professor Jon Preece for allowing an inept physicist to work in their chemistry lab; to Professor Frank Marken at the University of Bath, for an illuminating introduction to electrochemistry; and to Steve Fryatt of Alvatek for kindly lending essential equipment.

This work would not have been possible without the assistance of technical staff at the University of Birmingham; namely Paul Stanley, Ming Chu and Theresa Morris of the Centre for Electron Microscopy; Jackie Deans in the School of Chemistry, Artur Majewski in Chemical Engineering and Bob & Bill in the Mechanical Engineering workshop .

Finally, thank you to my family and to Ellen, my third supervisor, for their support and encouragement throughout my second (and I promise, last) stint as a full-time student.

## Abstract

### Abstract

At present, the commercial viability of proton exchange membrane fuel cells (PEMFCs) for widespread, clean domestic and automotive power generation is hindered by issues of cost and durability. These issues relate significantly to the precious metal-based electrocatalysts required at the electrodes. This work aims to address the need for more durable catalysts with lower precious metal content, through the development of novel materials and preparation routes for electrocatalysts and catalyst layers.

In typical state-of-the-art Pt/C catalyst layers, the inefficient percolation of the Nafion® ionomer binder within mesoporous and microporous regions of the electrode limits the extent of the triple-phase reaction zone, such that a significant fraction of the Pt catalyst is under-utilised or entirely inactive. In this work, 'Nafion®-Pt/C' catalysts have been derived from ionomer-stabilised Pt nanoparticles synthesised via a novel, wet-chemical route that offers unprecedented control over the formation of the Pt-ionomer interface. The initial aim of this study is to investigate whether, by providing a means to optimise the ionomer percolation within the catalyst layer, the Nafion®-Pt/C preparation route could offer enhanced catalyst utilisation and facilitate reduction of Pt loading.

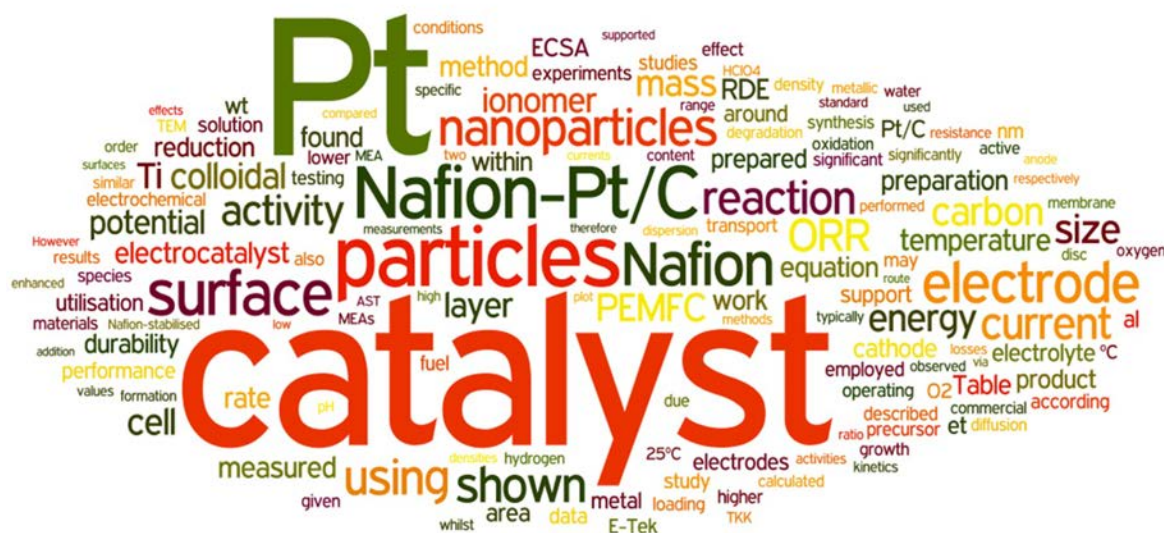
Nafion®-Pt/C catalysts have been characterised electrochemically using half-cell, rotating disc electrode techniques to determine their active surface area, catalytic activity and selectivity towards the oxygen reduction reaction. Membrane electrode assemblies have been fabricated using Nafion®-Pt/C catalysts, and *in-situ* single-cell testing has been carried out to determine polarisation characteristics, catalyst utilisation and catalyst layer effectiveness.

The durability of Nafion®-Pt/C catalysts has been investigated by ex-situ accelerated stress testing, with post-mortem characterisation of aged catalysts to identify degradation modes. Nafion®-Pt/C catalysts with agglomerated Pt particles exhibited a twofold improvement in durability vs. commercial catalysts, whilst offering similar mass activities towards oxygen reduction. The enhanced durability was attributed to inhibition of Pt dissolution and particle growth mechanisms by a passivating layer of Nafion® introduced during the synthesis of Nafion®-stabilised colloidal Pt.

The second part of this work investigated, for the first time, methods for the wet-chemical synthesis of bimetallic nanoparticles consisting of an early transition-metal core (Ti) enclosed in a

## Abstract

Pt shell. Previous studies on extended (bulk) surfaces have shown that Pt-Ti alloys exhibit higher intrinsic activity towards oxygen reduction than Pt alone, whilst being less prone to degradation than other alloys of Pt such as Pt-Ni, Pt-Co and Pt-Fe. Core@shell bimetallic particles offer dramatically superior Pt utilisation compared with mixed alloys by confining the precious metal component to a few atomic layers at the surface of each particle. Oxidation of Ti nanoparticles during purification prevented successful synthesis of metallic Ti@Pt particles, but led instead to the formation of Pt nanoparticles on a TiO<sub>2</sub> support.



## List of publications

# List of publications

1. O. J. Curnick, B. G. Pollet, P. M. Mendes, “Nafion®-stabilised Pt/C electrocatalysts with efficient catalyst layer ionomer distribution for proton exchange membrane fuel cells”, *RSC Advances*, In press, doi: 10.1039/c2ra21071a **2012**
2. O. J. Curnick, P. M. Mendes, B. G. Pollet, “Morphological Origins of the Enhanced Durability of a Pt/C Catalyst Derived from Nafion®-stabilised Colloidal Pt Nanoparticles”, *ECS Transactions*, 33 (1) **2010** p. 557-561
3. O. J. Curnick, P. M. Mendes, B. G. Pollet, “Enhanced Durability of a Pt/C Catalyst Derived from Nafion®-stabilised Colloidal Pt Nanoparticles”, *Electrochem Comm*, 12 **2010** p. 1017-1020

## Glossary of terms and abbreviations

***$\alpha$***

Transfer coefficient for an electrochemical reaction

***$A_{EC}$***  [ **$\text{cm}^2$** ]

Total electrochemically-active surface area of an electrode

***$A_{geo}$***  [ **$\text{cm}^2$** ]

Geometric surface area of an electrode

***$A_{phys}$***  [ **$\text{m}^2 \cdot \text{g}^{-1}$**  <sub>pt</sub>]

The mass-specific physical surface area of a catalyst or electrode

**AST**

Accelerated Stress Test

***$b$***  [ **$\text{mV} \cdot \text{decade}^{-1}$** ]

Tafel slope

**BEV**

Battery Electric Vehicle

**BOP/BOS (Balance of Plant/Balance of Stack)**

Components (valves, pumps, flow controllers, humidifiers, pressure regulators etc.) which maintain correct operating conditions for a PEMFC stack.

***$C$***  [ **$\text{mol} \cdot \text{dm}^{-3}$** ]

Reactant concentration per unit volume of solvent

**CV**

Cyclic voltammogram

***$D$***  [ **$\text{cm}^2 \cdot \text{s}^{-1}$** ]

Diffusion coefficient

***$D_{eff}$***  [ **$\text{cm}^2 \cdot \text{s}^{-1}$** ]

Effective diffusion coefficient observed in an RDE experiment

***$E$***  [**V**]



## Glossary of terms and abbreviations

Electrode potential

### **ECSA (Specific Electrochemical Surface Area) [m<sup>2</sup>.g<sup>-1</sup>]**

The surface area available for electron transfer, per unit mass of active catalyst material within an electrode.

$$\text{ECSA} = \frac{A_{\text{EC}}}{L_{\text{Pt}} \cdot A_{\text{geo}}}$$

### **EDX**

Energy-dispersive X-ray Spectroscopy

### **$E_f(p_0)$ (Effectiveness factor) [%]**

The ratio of mass activity of an electrocatalyst observed in PEMFC testing to the mass activity observed for the same catalyst in ex-situ (RDE) testing.

### **EIS**

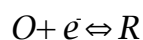
Electrochemical Impedance Spectroscopy

### **$\eta$ [V]**

Overpotential – the deviation of electrode potential from the equilibrium potential

### **Exchange current density, $J_0$ [A.cm<sup>-2</sup>]**

For an electrocatalytic reaction occurring at an electrode:



The exchange current density is the rate of this reaction at equilibrium, normalised by electrochemical surface area. This is a measure of the electrocatalytic activity of a catalyst species.

### **$E_w$**

Equivalent weight of PFSI ionomer

### **$F$ [C.mol<sup>-1</sup>]**

The Faraday constant (= 96485 C.mol<sup>-1</sup>)

### **GC**

Glassy Carbon

### **GDE**

Gas Diffusion Electrode

## Glossary of terms and abbreviations

### **GDL**

Gas Diffusion Layer

### **HOR**

Hydrogen Oxidation Reaction – occurs at the anode of the direct-hydrogen fuel cell.



### **$I$ [A]**

Electrical current

### **$\hat{i}$**

Complex number  $\hat{i} = \sqrt{-1}$

### **ICE**

Internal Combustion Engine

### **$I_D$ [A]**

Disc current in an RRDE experiment

### **$I_k$ [A]**

Kinetic current

### **$I_R$ [A]**

Ring current in an RRDE experiment

### **$J_k$ [A.cm<sup>-2</sup>]**

Kinetic current density

### **$J$ [A.m<sup>-2</sup>]**

Current density - current per unit geometric surface area of an electrode

### **$J_{lim}$ [A.m<sup>-2</sup>]**

Diffusion-limited current density

### **$k$ [mol.s<sup>-1</sup>]**

Reaction rate constant

### **$L_{Pt}$ [mg.cm<sup>-2</sup>]**

Platinum loading per unit geometric electrode area

## Glossary of terms and abbreviations

### LSV

Linear sweep voltammogram

### MA (Mass activity / Mass-specific activity) [ $\text{A}\cdot\text{g}_{\text{Pt}}^{-1}$ ]

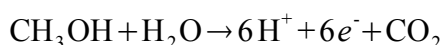
Kinetic current per unit mass of the active electrocatalyst (Pt) within an electrode.

### MEA

Membrane Electrode Assembly

### MOR

Methanol Oxidation Reaction occurs at the anode of the direct methanol fuel cell



### N

RRDE collection efficiency

### Nafion®

An ionomer derived from polytetrafluoroethylene, containing sulfonic acid groups which facilitate the transport of cations through its internal structure. Nafion® membrane is commonly employed as the electrolyte material in the PEMFC.

*Nafion® is a registered trademark of E. I. Du Pont de Nemours and Company.*

### NFP (Nafion® Fractional Percentage) [wt %]

Mass fraction of Nafion® within a catalyst layer consisting of Pt, carbon and Nafion®.

### $p$ [kPa]

Partial pressure

### PEMFC

Proton Exchange Membrane Fuel Cell

Polymer Electrolyte Membrane Fuel Cell

### ORR

Oxygen Reduction Reaction – occurs at PEM fuel cell cathode:



## Glossary of terms and abbreviations

### **PFSI**

Perfluorinated Sulfonated Ionomer (e.g. Nafion)

### **Power density [kW.m<sup>-3</sup>]**

Power output per unit volume of a power generation system, including BOP components.

See also **specific power**.

### **ppm**

Parts per million

### **R [J.K<sup>-1</sup>.mol<sup>-1</sup>]**

The gas constant (= 8.314 J.K<sup>-1</sup>.mol<sup>-1</sup>)

### **r [nm]**

Particle radius

### **r\* [nm]**

Critical nucleation radius

### **R<sub>ct</sub> [Ω]**

Charge transfer resistance

### **RDE**

Rotating Disc Electrode

### **RHE**

Reversible Hydrogen Electrode. Potentials throughout this paper are quoted against this reference electrode, unless otherwise stated.

### **RPM**

Revolutions per minute

### **RRDE**

Rotating Ring-Disc Electrode

### **S**

Degree of supersaturation

### **σ<sub>sl</sub> [J.m<sup>-2</sup>]**

Solid-liquid interfacial energy

## Glossary of terms and abbreviations

### **Specific power [kW.kg<sup>-1</sup>]**

Power output per unit mass of a power generation system, including BOP components.

See also **power density**.

### **SA (Specific activity) [A.m<sup>-2</sup>]**

At a given potential, the current density per unit electrochemically-active surface area of the electrode.

### **SHE**

Standard Hydrogen Electrode

### **TEM**

Transmission Electron Microscopy

### **TGA**

Thermogravimetric Analysis

### **THF**

Tetrahydrofuran

### **UHQ**

Ultra-high quality (referring to the purity of deionised water with a conductivity of 18.2 MΩ.cm)

### **UPD**

Underpotentially deposited (as in H<sub>upd</sub> – underpotentially-deposited hydrogen)

### **U<sub>Pt</sub> (Catalyst utilisation) [%]**

The ratio of ECSA to  $A_{phys}$  for a catalyst preparation or electrode.

### **$\nu$ [cm<sup>2</sup>.s<sup>-1</sup>]**

Kinematic viscosity

### **$\hat{Z}$ Complex impedance**

## Table of contents

# Table of contents

|       |   |      |
|-------|---|------|
| ▶     | <b>Acknowledgments</b> .....  | iii  |
| ▶     | <b>Abstract</b> .....   | v    |
| ▶     | <b>List of publications</b> .....   | vii  |
| ▶     | <b>Glossary of terms and abbreviations</b> .....                            | viii |
| ▶     | <b>Table of contents</b> .....  | xv   |
| ▶ 1   | <b>Background</b> .....   | 1    |
| ▶ 1.1 | Motivation.....   | 1    |
| ▶ 1.2 | Hydrogen as a clean energy vector.....                                      | 2    |
| ▶ 1.3 | Fuel Cells.....   | 3    |
| ▶ 1.4 | Competing and complimentary technologies.....                               | 7    |
| ▶ 1.5 | Commercialisation of PEM fuel cells.....                                    | 10   |
| ▶ 2   | <b>Introduction to the PEMFC</b> .....                                      | 15   |
| ▶ 2.1 | Polymer electrolytes.....   | 15   |
| ▶ 2.2 | Stack construction and operation.....                                       | 16   |
| ▶ 2.3 | Thermodynamics.....   | 18   |
| ▶ 2.4 | Fuel cell polarisation curves.....  | 20   |
| ▶ 3   | <b>Review on PEMFC electrocatalysts</b> .....                               | 27   |
| ▶ 3.1 | A Brief History of PEMFC electrocatalysts.....                              | 27   |
| ▶ 3.2 | Quantitative measures of electrocatalyst performance.....                   | 30   |
| ▶ 3.3 | Experimental methods for the evaluation of electrocatalyst performance..... | 31   |
| ▶ 3.4 | Previous studies on state-of-the-art Pt/C electrocatalysts.....             | 41   |
| ▶ 3.5 | Previous studies on ionomer-stabilised electrocatalysts.....                | 44   |
| ▶ 4   | <b>Preparation of Nafion®-Pt/C electrocatalysts</b> .....                   | 59   |
| ▶ 4.1 | Aims and Objectives.....  | 59   |
| ▶ 4.2 | Methods & Materials.....  | 59   |
| ▶ 4.3 | Results and Discussion.....   | 69   |
| ▶ 4.4 | Conclusions.....  | 83   |
| ▶ 5   | <b>Electrochemical characterisation of Nafion®-Pt/C catalysts</b> .....     | 85   |
| ▶ 5.1 | Aims and objectives.....  | 85   |
| ▶ 5.2 | Methods and Materials.....  | 86   |
| ▶ 5.3 | Results and Discussion.....   | 88   |
| ▶ 5.4 | Conclusions.....  | 109  |
| ▶ 6   | <b>Catalyst Durability</b> .....  | 111  |
| ▶ 6.1 | Background.....   | 111  |
| ▶ 6.2 | Aims and Objectives.....  | 117  |
| ▶ 6.3 | Methods and Materials.....  | 117  |
| ▶ 6.4 | Results and discussion.....   | 120  |
| ▶ 6.5 | Conclusions.....  | 125  |
| ▶ 7   | <b>In-situ testing</b> .....  | 127  |
| ▶ 7.1 | Background.....   | 127  |
| ▶ 7.2 | Methods and materials.....  | 128  |
| ▶ 7.3 | Results and discussion.....   | 135  |
| ▶ 7.4 | Conclusions.....  | 143  |

## Table of contents

|       |   |     |
|-------|---|-----|
| ▶ 8   | <b>Pt-Ti bimetallic catalysts</b> ..... | 145 |
| ▶ 8.1 | Background.....                         | 145 |
| ▶ 8.2 | Aims and objectives.....                | 157 |
| ▶ 8.3 | Methods and materials.....              | 158 |
| ▶ 8.4 | Results and discussion.....             | 165 |
| ▶ 8.5 | Conclusions and recommendations.....    | 172 |
| ▶ 9   | <b>Summary</b> .....                    | 175 |
| ▶ 9.1 | Nafion-Pt/C.....                        | 175 |
| ▶ 9.2 | Ti@Pt core@shell electrocatalysts.....  | 176 |
| ▶     | <b>Index of figures</b> .....           | 181 |
| ▶     | <b>Bibliography</b> .....               | 191 |

# 1 Background

“A significant time generally elapses before any new technological development is fully exploited. The fuel cell, first demonstrated by Sir William Grove in 1839, has taken longer than most, despite the promise of clean and efficient power generation”

Dr. Gary Acres OBE, Former Director of Research, Johnson Matthey Plc, February 2000

## 1.1 Motivation

The continued exploitation of rapidly-depleting fossil fuels to meet growing global demand for energy is economically and environmentally unsustainable. Anthropogenic greenhouse gas emissions (e.g. CO<sub>2</sub>, CH<sub>4</sub>) related to the extraction, processing and utilisation of fossil fuels have raised atmospheric concentrations of CO<sub>2</sub> significantly beyond the natural historical maximum of around 300 ppm (Figure 1.1 a). The current concentration of ~ 390 ppm is considered to present a significant risk of irreversible climate change [1], and continues to rise (Figure 1.1 b).

Simultaneously, reserves of easily-accessible fossil fuels are dwindling, resulting in continually rising financial and environmental costs in exploration, extraction and processing activities, as the exploitation of non-ideal deposits in sensitive areas becomes necessary to meet global demand. The rate of global oil production now exceeds the rate at which new reserves are being discovered.

Meanwhile, demand for energy continues to grow – particularly in developing nations but also in developed countries. The UK, for instance, became a net importer of energy in 2005, and still depends on fossil fuels for 90% of its energy requirements. Overall energy demand in the UK is increasing, with transportation seeing the fastest growth in demand, as shown in Figure 1.1 (c). Thus the continuing reliance on fossil fuels also threatens the energy security of many nations, including the UK, whose viable reserves of fossil fuels are very limited or depleted.



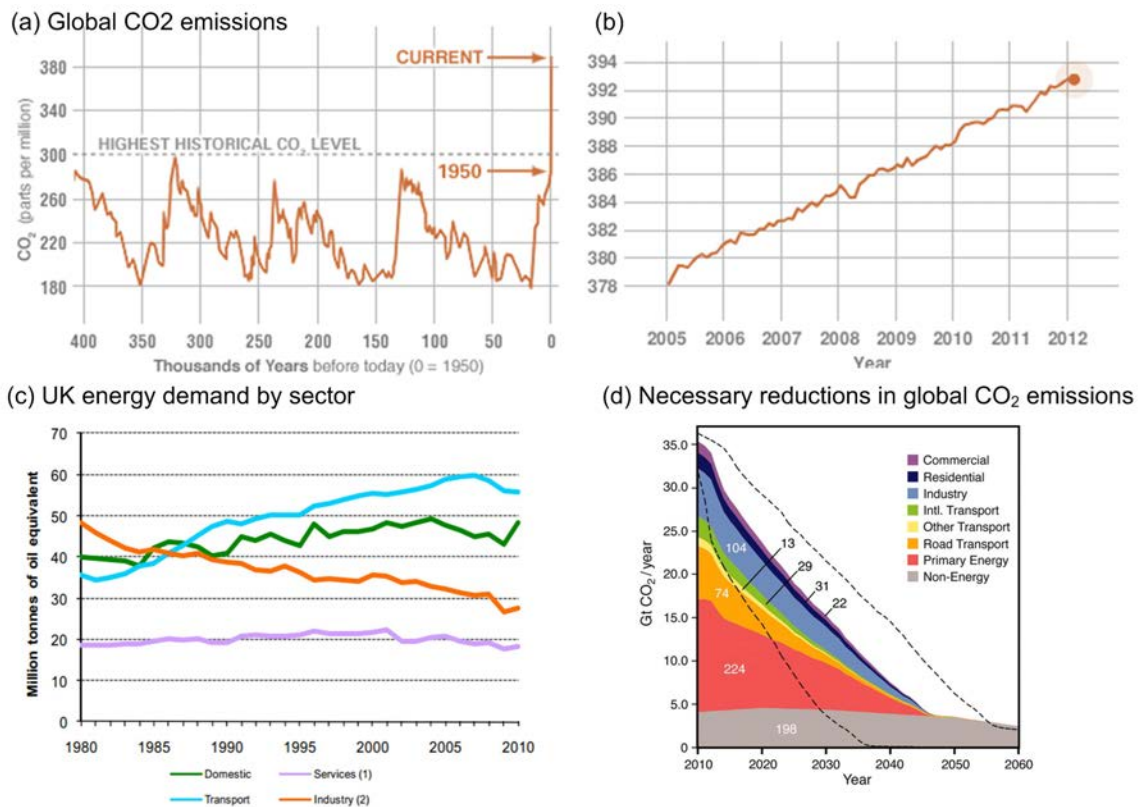


Figure 1.1: (a) Historical global average atmospheric CO<sub>2</sub> concentrations over the last 400,000 years (ice core data); (b) rising global atmospheric CO<sub>2</sub> levels since 2005; (c) UK energy demand by sector since 1980; (d) CO<sub>2</sub> emissions reductions by sector 2010-2060 thought to be necessary in order to limit global surface temperature rise to < 1.5°C [1].

To minimise the risk of global temperature increases exceeding 1.5°C, greenhouse gas emissions must be curtailed dramatically over the next half-decade – beginning now, and reaching pre-industrial levels by 2060 [1] as shown in Figure 1.1 (d).

To achieve such dramatic emissions reductions, whilst addressing simultaneously the issue of increasing energy demand and improving energy security requires a transition to renewable primary energy sources (e.g. wind, solar, hydro) and the adoption of clean and efficient energy distribution and conversion technologies to replace hydrocarbon fuels and thermomechanical engines.

## 1.2 Hydrogen as a clean energy vector

Hydrogen represents a promising clean energy vector – that is, a means by which energy can be stored, distributed and converted into useful work at point of use - whose only by-product when combusted, or reacted electrochemically with oxygen, is water.

Other than the absence of emissions at point of use, one of the other advantages of an energy system based around hydrogen as an energy vector is that it can be derived from a diverse range of primary energy sources [2], including solar energy via a variety of possible routes as shown in

## 1 Background

Figure 1.2. At present, the majority of industrially-produced hydrogen is derived from methane via steam reformation, which of course produces CO<sub>2</sub> and also results in a certain level of undesirable impurities (e.g. CO, SO<sub>2</sub>) in the product. Hydrogen produced from water via thermolysis, electrolysis or photolysis is generally free from impurities and generates no CO<sub>2</sub> emissions or, in the case of electrolysis, the carbon footprint of the electricity used in the process – i.e. potentially zero, if the electricity is derived from primary renewables or biomass.

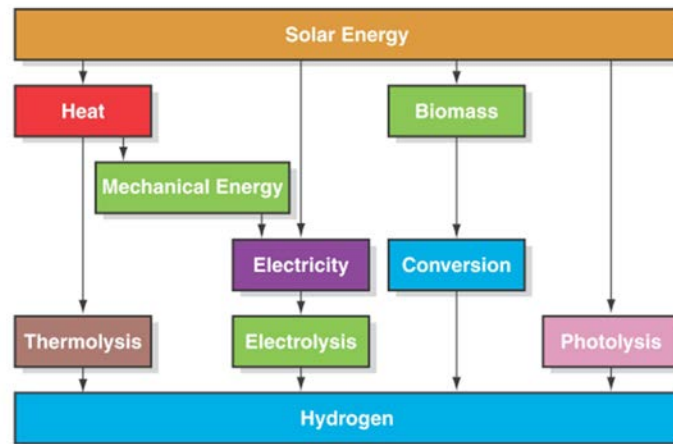


Figure 1.2: Several possible routes for the production of hydrogen from solar energy. Reproduced from [2]

Distribution and storage of hydrogen in large volumes for commercial, domestic and automotive purposes represents a significant challenge – compounded by its low volumetric energy density – but is arguably no more a challenge than was the establishment of the existing infrastructure for the transportation, distribution and storage of hydrocarbon fuels.

Perhaps the most significant benefit of a hydrogen-based energy system is the opportunity to employ more efficient energy conversion technologies to produce useful work from hydrogen fuel at the point of use. The ubiquity of combustion engines and turbines in the current energy system is a product of the chemical complexity of prevailing hydrocarbon fuels, which are unsuitable for use in more efficient, electrochemical energy conversion technologies. By contrast, the chemical simplicity of hydrogen makes it an ideal fuel for electrochemical conversion technologies, such as fuel cells.

### 1.3 Fuel Cells

A fuel cell is an electrochemical device for the conversion of chemical energy into electrical energy, much the same as a battery. Indeed, both batteries and fuel cells belong to a class of devices known as Galvanic cells, which represent the oldest and most direct method for the

---

production of an electrical current via a reaction between chemical substances. Whereas a battery contains a finite supply of chemical reactants, and therefore has a limited life before it must be discarded or recharged, a fuel cell is supplied by reactants stored externally and will go on producing electrical power for as long as reactants are supplied to it.

The fuel cell principle was first demonstrated by Sir William Grove in 1839. Using the apparatus depicted in Figure 1.3, Grove was able to demonstrate that the hydrogen and oxygen evolved by electrolysis at platinum electrodes immersed in dilute sulphuric acid solution could then be consumed at the same electrodes, with the production of an electrical current: a process which Grove dubbed 'reverse electrolysis'.

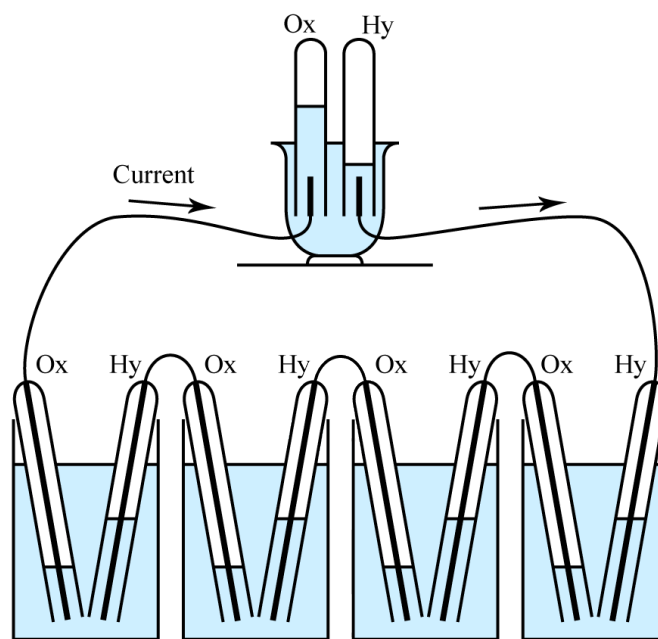


*Figure 1.3: William Grove's gaseous voltaic battery, demonstrated in 1839, consisted of platinum electrodes contained within sealed glass test tubes, in contact with a sulphuric acid solution.*

Generally, a fuel cell consists of two electrodes (anode and cathode) separated by an electrolyte. In all cases, a fuel (usually hydrogen, but hydrocarbon fuels can be used in some variants) is oxidised at the anode, whilst oxygen (usually supplied from ambient air) is reduced at the cathode. The electrolyte charge carrier varies between different types of system, and can be  $\text{OH}^-$ ,  $\text{H}^+$ ,  $\text{CO}_3^{2-}$  or  $\text{O}^{2-}$ . Electrons liberated from fuel molecules at the anode flow through an external electrical circuit to the cathode. There are several different types of fuel cell, each having different operating characteristics as illustrated in Figure 1.4 and described briefly below.

## 1 Background

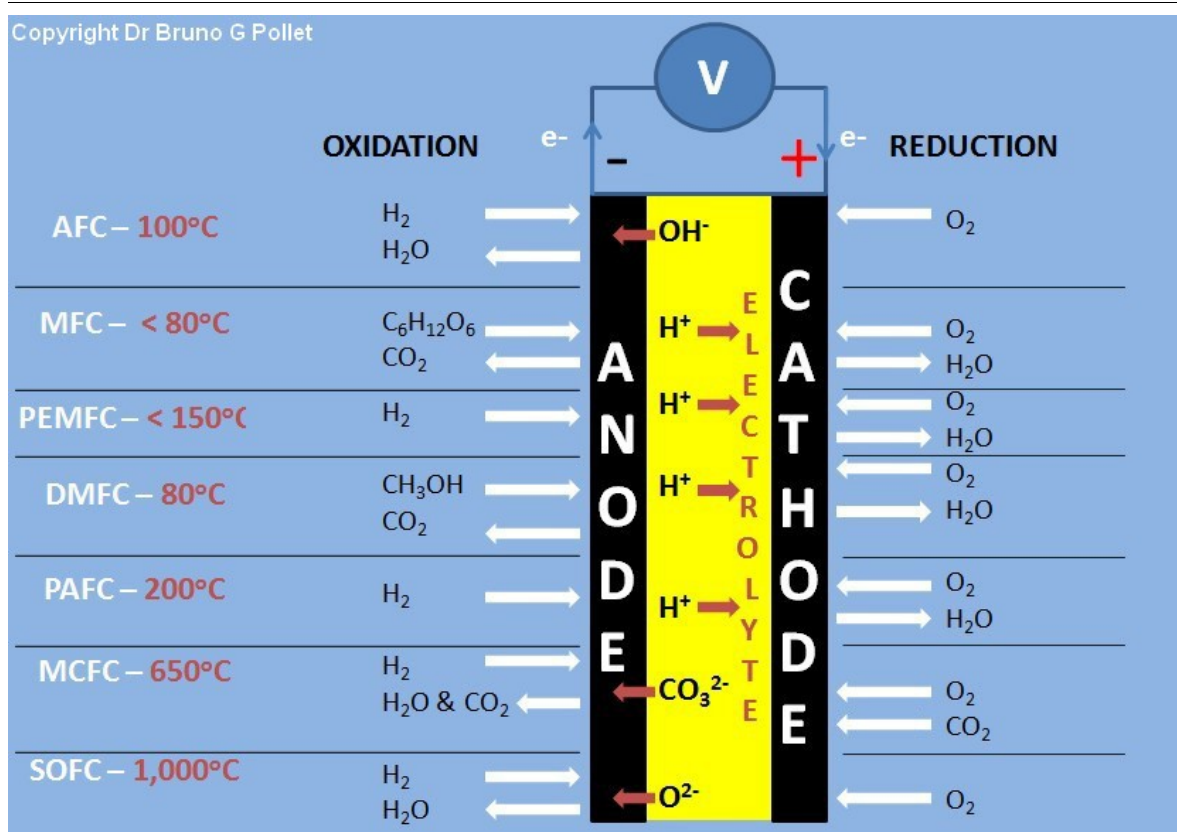


Figure 1.4: Schematic showing the operating temperatures, anode and cathode reactants and electrolyte charge carriers for several types of fuel cell: Alkaline fuel cell (AFC), microbial fuel cell (MFC), proton exchange membrane fuel cell (PEMFC), direct methanol fuel cell (DMFC), phosphoric acid fuel cell (PAFC), molten carbonate fuel cell (MCFC) and solid oxide fuel cell (SOFC). Reproduced from [3]

### 1.3.1 Alkaline Fuel Cell (AFC)

The AFC employs an aqueous alkaline electrolyte – usually a KOH solution, and is therefore restricted to operating temperatures below 100°C. The electrolyte is also subject to poisoning by CO<sub>2</sub>, which means that pure oxygen must be used at the cathode, as opposed to air. Despite this practical limitation, and the fact that the gravimetric power density [kW.kg<sup>-1</sup>] of the AFC is rather low owing to its aqueous electrolyte; AFCs have been employed successfully in specialist applications such as spacecraft[29].

### 1.3.2 Microbial Fuel Cell (MFC)

The MFC differs significantly from other types of fuel cell in that it employs live bacteria to facilitate the oxidation reaction at the anode, as opposed to an inorganic catalyst. The fuel, or substrate, is typically a carbohydrate or fatty acid but substrates with mixed compositions such as wastewater streams can also be employed. Bacteria live in the anode compartment and oxidise the substrate via normal anaerobic metabolic pathways, producing CO<sub>2</sub>, protons and electrons. The MFC cathode is much the same as in an ordinary PEMFC, containing a Pt catalyst to facilitate the

---

reduction of O<sub>2</sub>. The MFC has a very low volumetric and gravimetric power density, making them suitable only for stationary applications.

### 1.3.3 Proton Exchange Membrane Fuel Cell (PEMFC)

The PEMFC employs a polymeric membrane as its electrolyte material, which transports protons produced by oxidation of hydrogen at the anode to the cathode, where they participate in the reduction of oxygen, with pure water being the only by-product. The cation-conducting polymer (or *ionomer*) membrane is typically very thin (~ 20 μm) and light, so that PEM fuel cells have very high power densities. The operating temperature of the PEMFC is governed largely by the membrane material. At present, membranes are typically made from perfluorinated sulfonic acid (PFSA) polymers such as Nafion® or Aquivion, which are limited to less than 100°C in operation as they rely on liquid water to provide their proton conductivity. Operation at low temperatures demands the use of precious-metal catalysts to facilitate electrode reactions. The development of membrane materials that can operate at higher temperatures (up to 200°C) is an active area of research. Although precious metal catalysts are still required at these temperatures, they are less prone to poisoning by contaminants, and water management is greatly simplified.

The scalability of PEMFCs makes them extremely versatile, with successful demonstrations having been made in stationary power, portable and automotive applications ranging from < 10 W up to 1 MW[30]. This work is concerned with the development of cathode (oxygen reduction) catalysts for the PEMFC.

### 1.3.4 Direct Methanol Fuel Cell (DMFC)

Methanol can be oxidised by precious metal catalysts and is far easier to store and handle than hydrogen, making it convenient for use as an anode reactant in fuel cells. DMFCs employ polymeric membranes akin to hydrogen-fuelled PEMFCs, although they are usually thicker to limit the crossover of methanol to the cathode, which lowers the efficiency of the cell. Despite the advantages of methanol as a fuel, DMFCs are limited to low-power applications because their power output (and therefore their power density) is limited by the relatively slow reaction kinetics of the methanol oxidation reaction (MOR) compared to hydrogen oxidation. Additionally, the oxidation of methanol produces CO<sub>2</sub> as a by-product, meaning that DMFCs do not share the zero-emission credentials of hydrogen-fuelled PEMFCs, and Pt catalysts are effectively poisoned by CO produced as an intermediate in the anode reaction, so CO-tolerant catalysts are necessary.

Variants of the DMFC include the DEFC (Direct Ethanol Fuel Cell), and DBFC (Direct Borohydride Fuel Cell), which employ ethanol and sodium borohydride solution as the anode reactant respectively.

## 1 Background

---

### 1.3.5 Phosphoric Acid Fuel Cell (PAFC)

Molten phosphoric acid ( $\text{H}_3\text{PO}_4$ ) at between 150-200°C serves as the electrolyte in the PAFC. Whilst Pt-based electrocatalysts are still required on both electrodes, the high operating temperature makes them particularly tolerant to CO poisoning, meaning that reformat hydrogen can be utilised as the anode reactant with minimal purification. However, the high operating temperature and chemically-aggressive electrolyte present a significant challenge from a materials durability perspective, and together with slow start-up and low power density this makes the PAFC unsuitable for applications other than large-scale stationary power generation: a field in which PAFCs have been successfully deployed, albeit in small volumes, with units reported to have achieved 30,000 hours operation[31].

### 1.3.6 Molten Carbonate Fuel Cell (MCFC)

Similar to the PAFC, the MCFC uses a molten sodium- or lithium carbonate electrolyte, which requires an operating temperature of around 650°C. At such high temperatures, precious metal catalysts can be substituted for inexpensive alternatives such as Raney nickel, and hydrocarbon fuels such as methane or propane become viable for use as anode reactants. However the same durability and start-up issues suffered by the PAFC also apply to the MCFC, meaning that they are suitable only for large-scale stationary applications.

### 1.3.7 Solid Oxide Fuel Cell (SOFC)

The SOFC has the highest operating temperature of any fuel cell variant, requiring temperatures up to 1000°C for its ceramic electrolyte to conduct  $\text{O}^{2-}$  ions from cathode to anode. Inexpensive catalysts (typically nickel) can be utilised, as well as hydrocarbon fuels. The extreme operating temperature allows easy recovery of waste heat, so that SOFCs are particularly suitable for combined heat and power (CHP) systems. Early designs employing planar electrodes suffered from issues of slow start-up and poor durability toward thermal cycling, but these problems have been diminished by the advent of tubular and micro-tubular cell geometries. Whilst materials durability remains a significant challenge in the development of SOFCs, commercial products are already beginning to emerge for industrial and residential CHP applications.

## 1.4 Competing and complimentary technologies

For automotive applications, fuel cells are in direct competition with the ubiquitous internal combustion engine, as well as recently-emerging alternative platforms such as battery-electric and hybrid drivetrains. At the same time, hydrogen-fuelled systems rely on the development and

---

adoption of certain other technologies, such as primary renewable energy sources (solar, wind). There follows a brief comparison of PEMFCs to various alternative technologies, assessing the relative merits and interplay between each:

### 1.4.1 Internal Combustion Engines

The main argument in favour of fuel cells over internal combustion engines (ICEs) is one of improved efficiency. The ICE, both in its petrol and diesel-fuelled incarnations is ostensibly a heat engine, producing useful work by exploiting the thermal gradient that exists between fuel burning in the cylinder(s), and the ambient air. The maximum efficiency  $\epsilon_{max}$  of any closed-cycle heat engine operating between two temperatures  $T_H$  and  $T_C$  is given by Carnot's theorem according to

$$\epsilon_{max} = 1 - \left( \frac{T_C}{T_H} \right) \quad (1.1)$$

which for a petrol engine operating between  $T_H = 1090$  K and  $T_C = 293$ K, yields  $\epsilon_{max} = 73\%$ . Practically, though, the efficiency of even a modern ICE is far lower than this (typically 20-25 %), as a result of irreversible losses from friction, heat transfer, inefficient combustion and various other factors. By comparison, fuel cells are electrochemical devices so the Carnot limit does not apply to them. There are still several irreversible losses (detailed later) that reduce the efficiency of practical PEMFCs, but it is possible to achieve overall efficiencies of around 40%.

Although ICEs can be made to have net zero emissions by fuelling with hydrogen or biofuels, their inferior efficiency makes them increasingly unattractive in a world of ever-increasing energy demand. However, the ICE has benefited from over 100 years of research and development, such that modern units have excellent performance and durability characteristics. To be accepted by consumers, any replacement technology must have at least equal performance and durability characteristics, whilst being available at a similar cost.

### 1.4.2 Batteries and supercapacitors

Pure battery-electric vehicles (BEVs) are now available from several automakers. Current vehicles typically employ lithium ion battery technology, which adds significantly to the cost (and weight) of the vehicle. The main limitation of BEVs compared to both ICE and fuel cell vehicles is their limited range. Depending on the size of the battery, driving style and parasitic loads from vehicle equipment (headlights, air conditioning, windscreen wipers etc.), a range of between 50-100 miles can be expected from current vehicles from full charge. With current battery technology, recharging then takes from twenty minutes using a fast-charge device, to several hours using mains electricity. Their limited range and inconvenient refuelling requirements restrict the practicality of

## 1 Background

---

BEVs; at least in the minds of consumers familiar with the convenience of the 300+ mile range and fast refuelling of ICE vehicles. Unless there are significant advances in battery technology, providing a five to ten-fold increase in energy density and similar reductions in cost, whilst enabling fast recharging without affecting long-term durability, it seems that BEVs will only ever gain niche appeal.

Figure 1.5 below shows a Ragone plot for several energy storage and generation technologies relevant to automotive applications. The plot shows the peak gravimetric power density on the vertical axis, and gravimetric energy density on the horizontal axis, allowing different devices and systems to be compared in terms of their suitability for a given application. For automotive applications, high energy densities of around  $1000 \text{ Wh.kg}^{-1}$  or greater are necessary to provide adequate range, whilst peak power densities upwards of  $100 \text{ W.kg}^{-1}$  are required for acceleration and hill-climbing.

Whilst they are often seen as a competing technology to PEMFCs, in fact batteries naturally compliment PEMFCs in hybrid systems for automotive applications, where they are well-suited to supply the peak power demands of the vehicle during acceleration and hill climbing, and can serve in a load-smoothing capacity to avoid rapid changes in load on the fuel cell, which are undesirable from a durability perspective. Another attractive technology for hybrid fuel cell systems is the *supercapacitor*: a device akin to a battery but with far higher peak power density (Figure 1.5). Hybrid systems combining PEM fuel cells with batteries and/or supercapacitors have been shown to offer good performance in terms of overall system power and energy densities, as well as potentially lower overall costs than a pure fuel cell or pure battery-electric power plant [32].



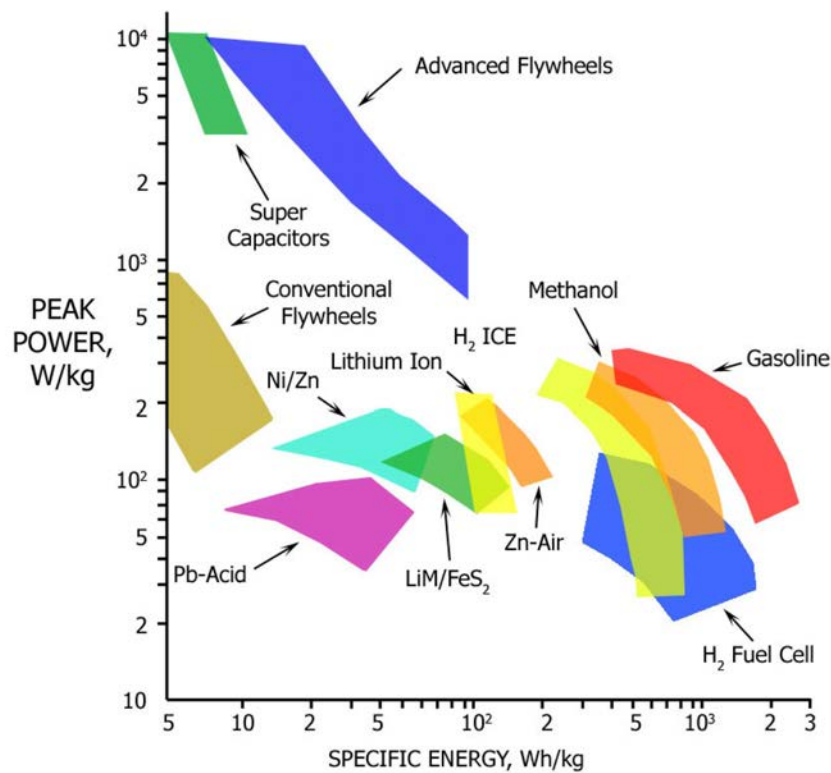


Figure 1.5: Ragone plot comparing energy storage and generation technologies in terms of their peak power density and mass-specific energy density. Adapted from [4]

### 1.4.3 Primary renewables

To achieve a truly sustainable energy solution, hydrogen for fuel cells must be produced without the emission of greenhouse gases, including CO<sub>2</sub>. At present in the UK, even hydrogen produced by electrolysis has a carbon footprint associated with the grid electricity used in the process, which produces around 560 g.kWh<sup>-1</sup> of CO<sub>2</sub> [33]. Therefore the emergence of a truly zero-carbon hydrogen economy relies on the development and proliferation of primary renewable energy sources, such as wind power and solar photovoltaics. In fact, fuel cells and electrolyzers naturally compliment intermittent wind and solar energy sources, as they allow efficient conversion of electrical energy to hydrogen (by electrolysis) for storage during times of excess production, and similarly efficient back-conversion to electricity when demand exceeds supply.

## 1.5 Commercialisation of PEM fuel cells

PEMFCs have already been commercialised successfully in certain specialised markets such as materials handling, portable electronics and remote power generation. However, to realise their full energy- and emissions-saving potential they must be deployed widely in mass-market applications in the automotive and domestic sectors. This requires wholesale changes throughout

## 1 Background

the current energy system in order to establish the necessary infrastructure for the generation and distribution of hydrogen, not to mention changes in energy policy and consumer behaviour that extend far beyond the scope of this study.

With regard to the PEMFC technology itself; at present issues of cost and durability are considered to present the most significant barriers to mass-market penetration of PEMFC systems, and it is toward the alleviation of these issues to which the vast majority of PEMFC research is currently directed.

### 1.5.1 Cost and durability targets

To guarantee commercial viability in automotive applications, PEMFC systems must achieve parity with conventional ICEs in terms of their cost and durability. As of August 2011, automotive ICEs cost between \$25-35 kW<sup>-1</sup> (£16-23 kW<sup>-1</sup>) with operational lifetimes in excess of 5000 hours[34].

The US Department of Energy has specified targets for the cost and durability of PEMFCs at the system and stack level as shown in Table 1.1.

|                                      | 2011 status |                                | 2020 targets |                                |
|--------------------------------------|-------------|--------------------------------|--------------|--------------------------------|
|                                      | Stack       | System (inc. balance of plant) | Stack        | System (inc. balance of plant) |
| Power density (W.L <sup>-1</sup> )   | 2200        | 400                            | 2500         | 850                            |
| Specific power (W.kg <sup>-1</sup> ) | 1200        | 400                            | 2000         | 650                            |
| Cost (\$/kW)                         | 22          | 49                             | 15           | 30                             |
| Durability (hours)*                  | 2500        | 2500                           | 5000         | 5000                           |

Table 1.1: Status and targets for PEMFC performance reported and specified by the US Department of Energy. Figures are for an 80kW (net) integrated PEMFC system suitable for automotive applications[34]. \*durability based on time to 10% drop in rated power in an automotive drive cycle.

As an indication of the speed of progress being made in reducing the cost of PEMFC systems, the figures given for 2011 in Table 1.1 represent an 80% reduction in cost compared to 2002 levels, as illustrated in Figure 1.6 (a)[5].

Durability aspects are discussed in detail in chapter 6.

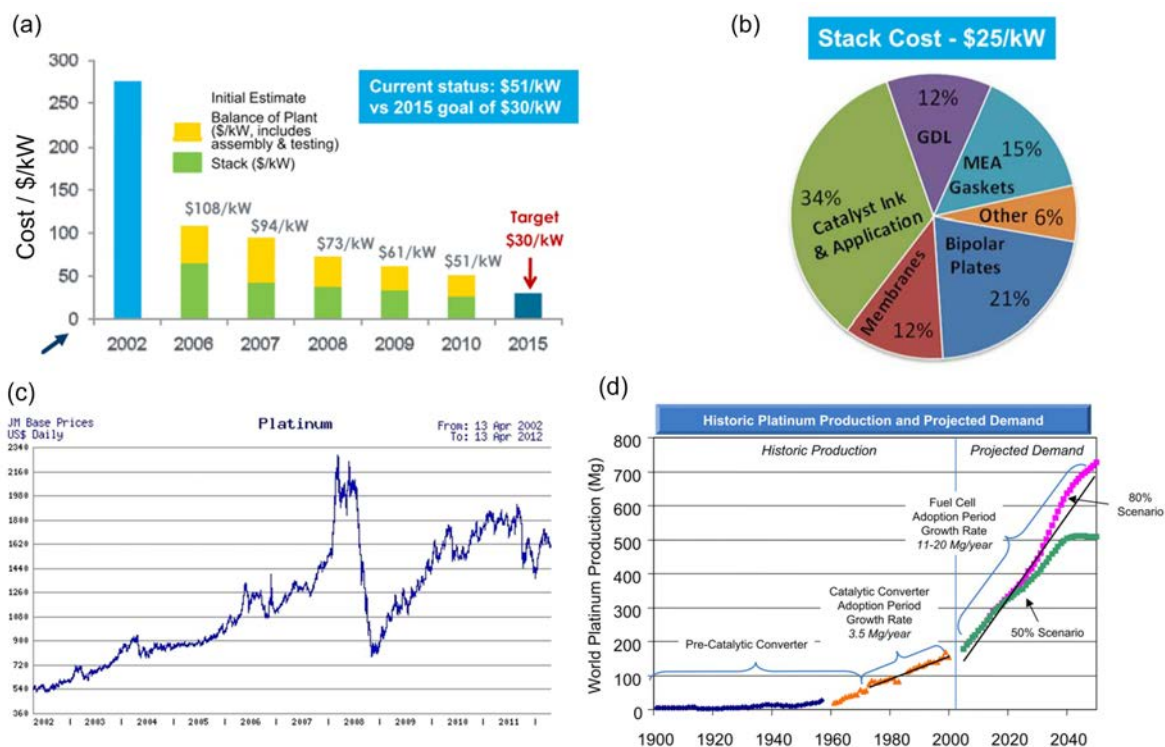


Figure 1.6: (a) Historical and projected costs for automotive fuel cell systems (state of the art technology projected to high volume production 500k units/year); (b) breakdown of stack costs based on current leading technologies scaled to high volume (500k units/year) production rates; (c) commodity price of refined platinum over the last 10 years (US\$/troy oz); (d) historical and projected global demand for platinum, with future demand based on two scenarios for adoption of FCVs (50% takeup, 80% takeup). Reproduced from [5](a) & (b), [6](c) and [7] (d)

## 1.5.2 Routes to reduced cost

Modern ICE vehicles contain between 5-25 g of platinum group metals (PGMs) as emission-reduction catalysts in the catalytic converters which form part of their exhaust systems. Therefore there is a strong precedent for the incorporation of these materials into mass-market products, and there is no reason why the need for PGMs should preclude the realisation of commercially viable PEMFCs. However, according to US DOE projections shown in Figure 1.6 (b) the precious metal electrocatalyst makes the single largest contribution to the cost of PEMFC stacks in a high-volume production scenario. Figure 1.6 (c) shows the commodity value of platinum over the last decade, and reveals a generally-increasing trend. Indeed, the only significant drop in the value of Pt was seen in the second half of 2008, when demand for Pt fell during the global economic crisis – a dramatic demonstration of the correlation between price and demand in the PGM market. It follows that there would be a significant increase in the commodity price of Pt if new uses (e.g. uptake of FCVs) emerged to create additional demand for these scarce resources, as predicted by a forecast published by the US Department of Energy shown in Figure 1.6 (d).

## 1 Background

---

Reductions in precious metal loading, or rather improvements in overall precious metal utilisation ( $\text{kW}\cdot\text{g}^{-1}_{\text{PGM}}$ ) are therefore essential in order to safeguard the viability of fuel cell technology in automotive applications – especially in the long term.

There are, broadly speaking, three strategies for the reduction of precious metal loading in PEMFC stacks under investigation at this time:

### **Non-precious metal catalysts**

Electrocatalysts for the anode and cathode reactions in the hydrogen-fuelled PEMFC containing no PGMs have been under development for some time[35-48]. Recent demonstrations of iron-based catalysts have shown volumetric activity ( $\text{A}\cdot\text{cm}^{-3}$ ) comparable to that of Pt[49], but the durability of these materials remains far inferior to that of Pt-based catalysts – especially at the PEMFC cathode. Whilst viable non-PGM electrocatalysts may well emerge in the long term, Pt-based catalysts remain the most promising option for the short and medium-term rollout of commercial PEMFC systems.

### **PGM-based catalysts with reduced precious metal loading**

The precious metal requirements of PGM-based electrocatalysts can be compared in terms of their *mass activity* (MA) towards a given reaction, which can be seen as the product of their surface-specific activity (SA) [ $\text{A}\cdot\text{m}^{-2}$ ] and active electrochemical surface area (ECSA) [ $\text{m}^2\cdot\text{g}^{-1}$ ] according to equation (1.2).

$$MA[\text{A}\cdot\text{g}_{\text{Pt}}^{-1}] = SA[\text{A}\cdot\text{m}^{-2}] \cdot ECSA[\text{m}^2 \cdot \text{g}_{\text{Pt}}^{-1}] \quad (1.2)$$

It follows that increases in MA can be realised via increases in SA and/or ECSA – indicating two distinct routes for the reduction of Pt loading:

- Increasing electrochemical surface area [ $\text{m}^2\cdot\text{g}^{-1}$ ] e.g. by reducing catalyst particle size, or by increasing the proportion of the catalyst that is electrochemically active within the catalyst layer.
- Increasing specific activity [ $\text{A}\cdot\text{m}^{-2}$ ] e.g. by alloying Pt with other metals to modify the intrinsic activity of the catalyst surface – discussed further in chapter 8.

This study aims to apply both of these approaches in order to realise improvements in mass activity. Chapters 3-7 are concerned with attempts to increase active surface area by modifying the morphology of a Pt electrocatalyst, whilst chapter 8 is aimed at the development of Pt alloy catalysts with enhanced intrinsic specific activity towards the PEMFC cathode reaction.

## 2 Introduction to the PEMFC

The PEMFC was first developed in the 1960s by General Electric as an alternative to the alkaline fuel cell technology that was being developed at that time. Its defining feature is the polymeric membrane that divides the electrodes and serves as the proton-conducting electrolyte, which affords dramatically improved volumetric and gravimetric power density compared to systems requiring bulky aqueous or molten electrolytes.

### 2.1 Polymer electrolytes

The initial development of the PEMFC was enabled by the advent of proton-conducting polymer materials or *ionomers* in the 1960s. Early ionomers were based on sulfonated polystyrene, but the majority of modern PEMFC electrolyte membranes are made from more chemically-resistant perfluorinated sulfonated ionomer (PFSI) materials such as Nafion® and Aquivion®, manufactured by Dupont and Solvay Solexis, respectively.

PFSIs generally consist of a fluorinated hydrocarbon backbone, similar to Teflon, which is functionalised by side chains containing sulfonic acid ( $R-SO_3H^+$ ) groups, which furnish proton conductivity on these otherwise relatively inert materials[50].

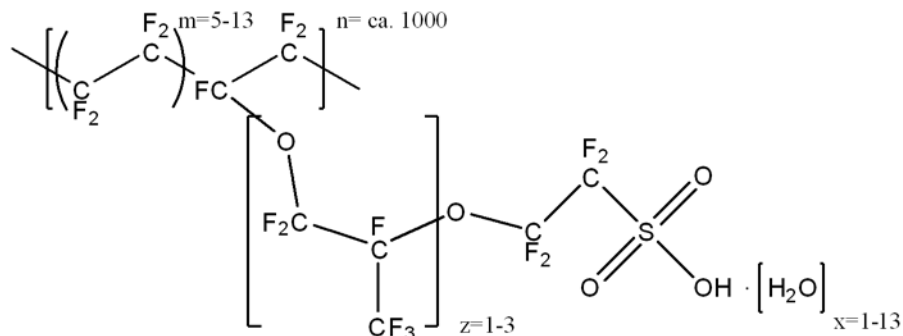


Figure 2.1: A generalised chemical structure for perfluorinated sulfonated ionomers.

In a solid PFSI membrane the hydrophilic, sulfonated side chains tend to cluster together, forming internal pores which, when adequately hydrated, facilitate transport of protons in the form of hydronium ions  $H_3O^+$  whilst remaining relatively impermeable to anions and electrically neutral species. The sulfonic acid groups have an extremely high dissociation constant ( $pK_a \sim -6$ ), providing efficient proton transport and affording high conductivities of  $0.01 - 0.1 \text{ S.cm}^{-1}$  at  $80-90^\circ\text{C}$ . Operation at higher temperatures is precluded by the need for liquid water to hydrate the membrane, and a Nafion glass transition temperature of around  $105^\circ\text{C}$ . There is currently growing

---

interest in the elevation of PEMFC operating temperature to 120-200°C in order to achieve enhanced tolerance to impurities, lower catalyst loading, superior water management and improved efficiency; which has spurred the development of alternative PEM materials including phosphoric-acid containing polymer matrices[51-53] and sulfonated graphene oxide[54].

In addition to forming the electrolyte membrane, PFSI materials are also present in PEMFC catalyst layers, and are central to the strategy employed in this study for improving catalyst utilisation – discussed further in chapter 3.

## 2.2 Stack construction and operation

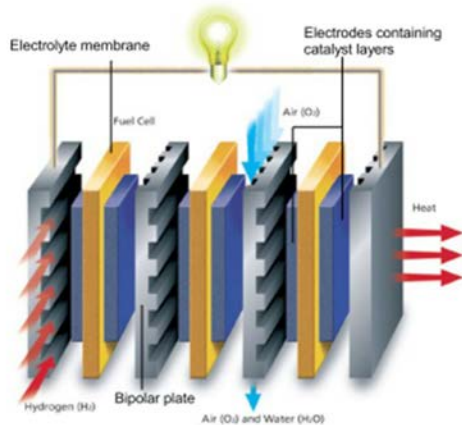
A PEMFC stack consists of a series of cells separated by bipolar plates or flow field plates (FFPs) as shown in Figure 2.2 (a). Typically fabricated from graphite or stainless steel to provide electrical connectivity between adjacent cells, the FFPs also feature channels through which reactant gases are supplied and waste water is removed. Insulating gaskets (not shown in the figure) provide sealing and separation between adjacent plates to prevent leakage of reactants and electrical short-circuits.

The cells themselves each consist of two electrodes separated by an ionomeric proton exchange membrane (PEM) as shown in Figure 2.2 (b). As shown in Figure 2.2, hydrogen is supplied to the anode, where the catalytic hydrogen oxidation reaction (HOR) occurs, liberating two protons and two electrons. The electrons travel around an external electrical circuit driven by the potential difference between anode (-ve) and cathode (+ve), whilst the protons diffuse through the ionomer membrane to the cathode. Air (or oxygen) supplied to the cathode reacts with these protons and electrons in the Pt-catalysed oxygen reduction reaction (ORR) to form water, which is then removed from the cell.

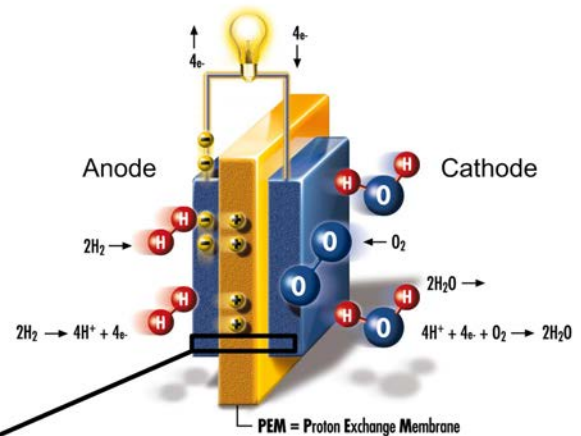
The electrodes on either side of the membrane are arguably the most complex components in the system, consisting of an active catalyst layer (CL) within which reactions take place, in addition to a gas diffusion layer (GDL) which serves to distribute and deliver reactant gases uniformly across the CL, whilst facilitating removal of waste water to prevent flooding of the cell and providing electrical connection between the catalyst layer and bipolar plate.

## 2 Introduction to the PEMFC

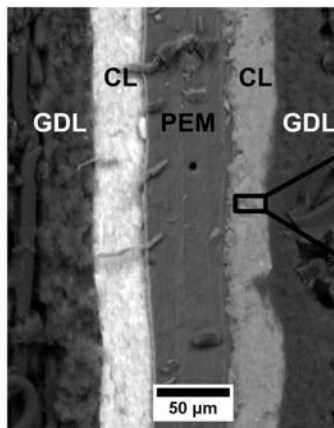
(a) PEMFC stack (3 cells)



(b) PEMFC single cell



(c) Membrane Electrode Assembly cross section



(d) Pt/C electrocatalyst

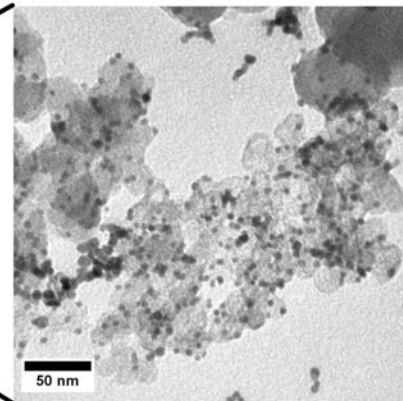


Figure 2.2: (a) Schematic diagram of a PEMFC stack consisting of 3 individual cells (reproduced from [8]), (b) PEMFC single cell showing reactions taking place at anode and cathode (reproduced from [8]), (c) SEM cross section of a PEMFC MEA with the proton exchange membrane (PEM), catalyst layers (CL) and gas diffusion layers (GDL) labelled, (d) TEM image of a typical Pt/C electrocatalyst.

The scanning electron microscope image in Figure 2.2 (c) shows a cross-section of a typical PEMFC membrane electrode assembly. The typical thicknesses of the membrane, catalyst layers and GDLs are 10-50 $\mu\text{m}$ , 5-30 $\mu\text{m}$  and 200-400  $\mu\text{m}$  respectively, so that an entire cell (excluding gaskets and FFPs) can be as little as 450  $\mu\text{m}$  in thickness.

Figure 2.2 (d) shows a transmission electron microscope image of a typical PEMFC catalyst, which consists of Pt nanoparticles (the small, dark particles in the image) 2-10 nm in diameter dispersed on a carbon black (larger, grey agglomerates). The Pt nanoparticles form the electrochemically-active component of the catalyst, and their size affords them a large specific surface area of 80-120  $\text{m}^2 \cdot \text{g}^{-1}$  to support electrode reactions. The carbon support serves to improve the dispersion of Pt particles and inhibit their agglomeration, whilst providing electrical connectivity throughout the catalyst layer and back to the GDL.

---

To summarise from a different perspective, Figure 2.2 illustrates the various length scales and processes that must be addressed in the engineering of a PEMFC stack – from the nanoscale morphology of the catalyst layers to the millimeter-scale geometry of the flow channels within the flow field plates. This work is concerned with engineering on some of the smallest of these length scales – that is, with the optimisation of the microstructure of the catalyst layer, and the nanoscale composition and morphology of the electrocatalyst itself.

## 2.3 Thermodynamics

Fuel cells are energy conversion devices by definition. As such, their conversion efficiency is an important practical attribute, and one which can be both calculated theoretically and measured experimentally.

For a fuel cell, the maximum energy available for conversion to useful (electrical) work is given by the Gibbs free energy change for the overall cell reaction, determined by the difference in the energy of formation between reactants and products. For the reaction of H<sub>2</sub> and O<sub>2</sub> to form liquid water, the standard Gibbs free energy change (at 298K and 100kPa) is given by

$$\Delta G^\phi = G_{f, products}^\phi - G_{f, reactants}^\phi$$

$$\Delta G^\phi = G_{f, H_2O}^\phi - G_{f, H_2}^\phi - G_{f, O_2}^\phi = -237.2 - 0 - 0 = -237.2 \text{ kJ.mol}^{-1} \quad (2.1)$$

This value represents the maximum useful work that it is possible to liberate from one mole of H<sub>2</sub> and O<sub>2</sub> reacting under these conditions.

The Gibbs free energy change is a function of temperature and reactant concentration (or partial pressure for gaseous reactants) according to

$$\Delta G = \Delta G^\phi + RT \ln \left( \frac{P_{H_2O}}{P_{H_2} P_{O_2}^{1/2}} \right) \quad (2.2)$$

where  $\Delta G^\phi$  is the standard Gibbs free energy change;  $P_{H_2}$ ,  $P_{O_2}$  and  $P_{H_2O}$  are the partial pressures of H<sub>2</sub>, O<sub>2</sub> and H<sub>2</sub>O respectively; R is the gas constant and T is the absolute temperature.

In an electrochemical system operated reversibly such that all available Gibbs free energy is converted to electrical energy, then the emf between the anode and cathode is given by equation (2.3).

$$\Delta G = -nFE_{rev} \quad (2.3)$$

where n is the number of electrons involved in the reaction and F is Faraday's constant, equal to 96485 C.mol<sup>-1</sup>.

Substituting equation (2.3) into (2.2) gives

---



## 2 Introduction to the PEMFC

$$E_{rev} = E^\phi + \frac{RT}{nF} \ln \left( \frac{P_{H_2} P_{O_2}^{1/2}}{P_{H_2O}} \right) \quad (2.4)$$

where  $E^\phi$  is the reversible potential under standard conditions, which for a  $H_2/O_2$  system is 1.23 V. Equation (2.4) is known as the Nernst equation, and relates the open circuit voltage  $E_{rev}$  of a fuel cell (or indeed any Galvanic cell) to the temperature and partial pressures (or concentrations) of reactants and products. The variation of  $E_{rev}$  with temperature is shown in Figure 2.3 (a).

Thus at a typical operating temperature of around  $80^\circ\text{C}$ , the open circuit potential of an  $H_2/O_2$  fuel cell is around 1.17 V.

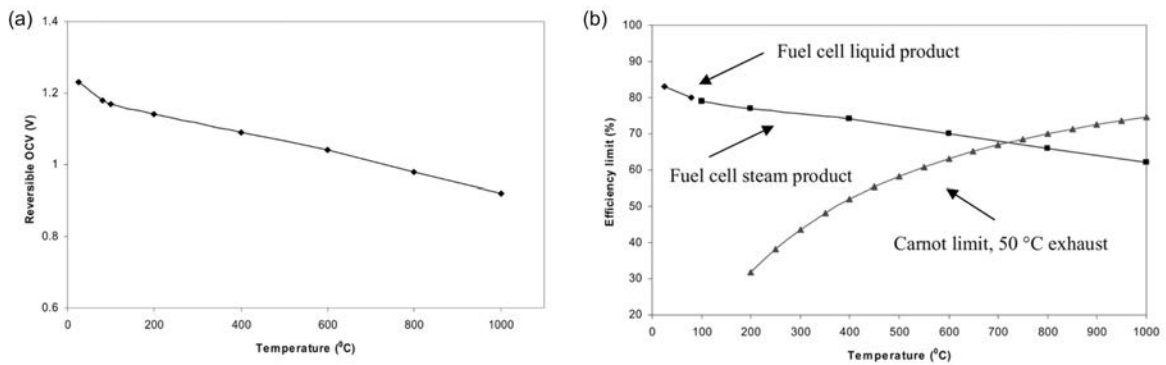


Figure 2.3: (a) Variation in reversible (open circuit) cell potential as given by the Nernst equation for a fuel cell operating on  $H_2$  and  $O_2$ ; (b) comparison of maximum theoretical efficiencies of an  $H_2/O_2$  fuel cell and a Carnot heat engine operating at various temperatures, and 100 kPa pressure. Reproduced from [9]

The maximum theoretical efficiency  $\epsilon_{max}$  of a fuel cell is given by the ratio of the Gibbs free energy change to the higher heating value (HHV) of the fuel. In the case of the  $H_2/O_2$  fuel cell operating under standard conditions (298K, 100 kPa):

$$\epsilon_{max} = \frac{\Delta G}{\Delta H^\phi} = \frac{237.1 \text{ kJ.mol}^{-1}}{286 \text{ kJ.mol}^{-1}} = 83\% \quad (2.5)$$

The temperature dependence of  $\Delta G$  means that the maximum efficiency decreases with increasing temperature, as illustrated in Figure 2.3 (b). However, only at operating temperatures above  $700^\circ\text{C}$  does the theoretical efficiency of an ideal (Carnot) heat engine exceed that of an  $H_2/O_2$  fuel cell and, in practice, the efficiency losses pertaining to the ICE mentioned above in section 1.4.1 exceed those of a high-temperature fuel cell system, such that the fuel cell remains the more efficient device.

## 2.4 Fuel cell polarisation curves

The thermodynamic treatment above describes the maximum theoretically-attainable performance of a fuel cell operating on hydrogen and oxygen (or air). In the absence of any of the limitations described in the following, at 80°C such a cell would produce a constant voltage of 1.17 V, regardless of the current being drawn. In practice, there are various sources of voltage loss determining the current-voltage (I-V) response of the cell, which typically resembles that shown in Figure 2.4 and is known as a *polarisation curve*.

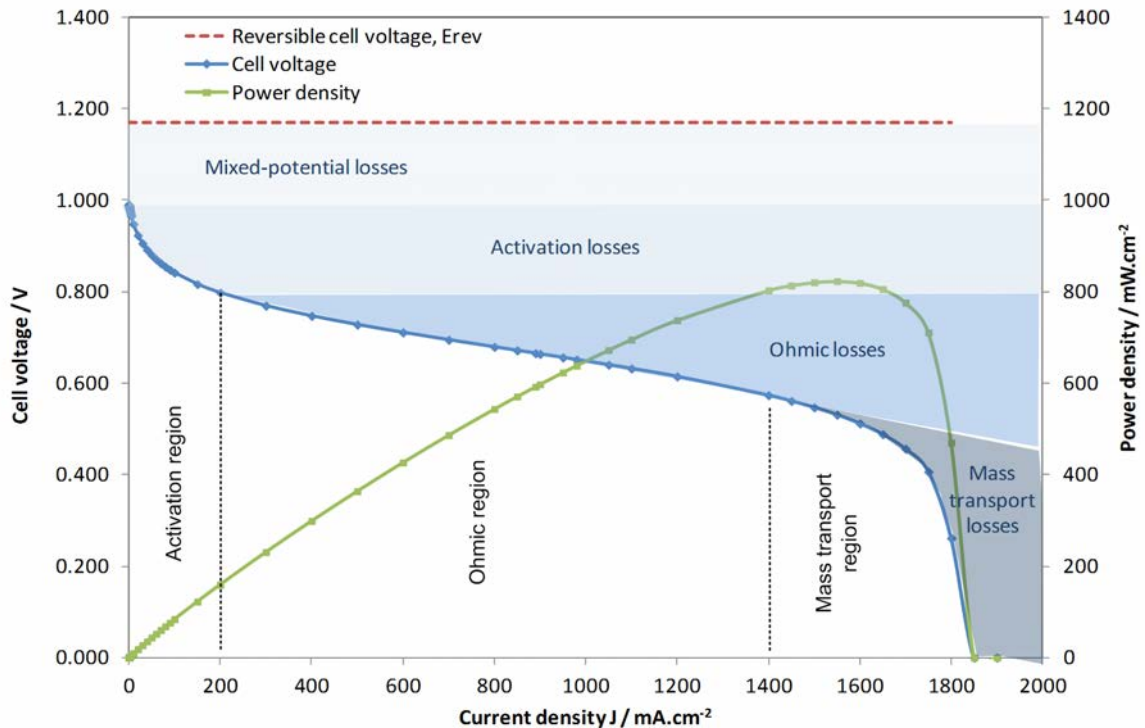
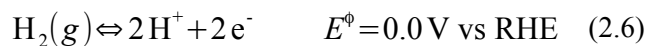


Figure 2.4: A typical PEMFC polarisation curve, showing contributions of mixed potential, activation, Ohmic and mass transport losses to the overall polarisation response.

### 2.4.1 Mixed potential losses

From Figure 2.4 the open-circuit voltage (OCV) of the PEMFC, at around 1.0 V at 80°C, is considerably lower than the theoretical cell voltage determined above. This is because, as well as the oxygen reduction equilibrium, there are also secondary reactions taking place at the cathode:

1. The PEM electrolyte membrane is very slightly permeable to hydrogen gas, and any that reaches the cathode is oxidised according to equation (2.6).



## 2 Introduction to the PEMFC

---

The decrease in OCV due to hydrogen crossover depends on the thickness and permeability of the membrane, and also on temperature, but is typically in the range of 25-90 mV[55].

2. Oxygen-containing species undergo reversible adsorption at the surface of the Pt catalyst at the cathode according to equation (2.7).



Typical losses in OCV due to the Pt/PtO reaction amount to between 90-190 mV[55].

The polarisation curve itself can be divided into three regions as shown in Figure 2.4, which in order of increasing current density are dominated sequentially by losses related to (i) cathode reaction kinetics (activation losses), (ii) Ohmic resistances and (iii) mass-transport limitations.

### 2.4.2 Ohmic losses

There are several sources of Ohmic resistance within the cell or stack: the bulk electrical resistance of cell materials, contact resistances at interfaces between components (bipolar plates, catalyst layers, current collector cables etc.), and the ionic resistance of the electrolyte membrane and catalyst layers all contribute to the overall resistance of the cell. These Ohmic resistances generally produce a simple linear decrease in cell voltage with increasing current according to Ohm's Law<sup>1</sup>:

$$-\Delta E = \Delta I R_\Omega \quad (2.8)$$

where  $R_\Omega$  is the total internal Ohmic resistance of the cell, with contributions as described above. Practically, values for  $R_\Omega$  can be estimated from the slope of the linear portion of the polarisation curve, or can be measured accurately using *current interrupt* or *electrochemical impedance spectroscopy* techniques.

### 2.4.3 Mass transport losses

As current density is increased, there comes a point at which reactants cannot be supplied quickly enough to the active catalytic layers of the electrode to satisfy the current demand. The concentration(s) of reactants at the electrode surface then decrease, causing the electrode potential also to decrease. The onset of mass transport limitation typically occurs above 1 A.cm<sup>-2</sup> in modern PEMFCs operating at atmospheric pressure.

---

<sup>1</sup> In practice,  $R_\Omega$  is a function of operating temperature and ionomer hydration, and so can vary with current density and operating conditions.

---

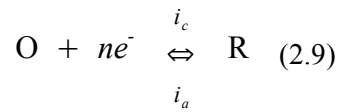
---

## 2.4.4 Activation losses and electrode kinetics

The so-called activation losses observed in the low current region of the PEMFC polarisation curve occur as a result of limitations on the rate or *kinetics* of electrochemical reactions taking place at either electrode.

All electrochemical reactions involve the transfer of electrons to or from the electrode material (Pt in the case of the PEMFC) to one or more reactants. The electrical current flowing to or from the electrode is therefore a direct measure of the rate of the reaction occurring at the electrode surface.

Considering the general case of a redox reaction taking place at an electrode:



In the forward direction ( $\text{O} \rightarrow \text{R}$ ), electrons are transferred from the electrode to the reactant(s), producing the *cathodic* current  $i_c$ . In the reverse direction ( $\text{R} \rightarrow \text{O}$ ), electrons are transferred from reactant to electrode, producing the *anodic* current  $i_a$ . In the absence of any Ohmic or mass transport-related losses, the current  $i_k$  flowing at an electrode due to reaction (2.9) is determined purely by the kinetics of the reaction, and is the sum of the cathodic and anodic currents:

$$i_k = i_a - i_c \quad (2.10)$$

or, normalised by the electrochemical surface area  $A_{EC}$  [ $\text{m}^2$ ] of the electrode, equation (2.10) becomes

$$J_k = J_a - J_c \quad (2.11)$$

where  $J [\text{A.cm}^{-2}] = i [\text{A}] / A_{EC} [\text{cm}^2]$ .

When no net current is flowing to or from the electrode ( $J_k=0$ ), the reaction (2.9) is in equilibrium and the cell voltage is determined by the Nernst equation as described above. Under such conditions, the currents due to the reaction proceeding in the forward and reverse reactions are equal in magnitude.

$$J_k=0 \quad : \quad J_a = -J_c = J_0 \quad (2.12)$$

The exchange current density  $J_0$  [ $\text{A.cm}^{-2}$ ] is an intrinsic property of the electrode material, and is a direct measure of its catalytic activity towards a given reaction.

The equilibrium can be perturbed by adjusting the potential on the electrode so that it becomes polarised either more positive or more negative than the reversible (Nernst) potential. A net current will then flow as the reaction proceeds to re-establish equilibrium concentrations of O and

## 2 Introduction to the PEMFC

---

R. The magnitude of the net current  $i_k$  depends on the applied *overpotential*,  $\eta$  : the amount by which the applied potential  $E$  deviates from the reversible (equilibrium) potential  $\eta = E - E_{rev}$

$$J_k = J_0 \left( \exp \left[ \frac{\alpha_A n F}{RT} \eta \right] - \exp \left[ \frac{-\alpha_C n F}{RT} \eta \right] \right) \quad (2.13)$$

Equation (2.13) is known as the Butler-Volmer equation, and is a fundamental equation of electrode kinetics, relating the observed current to the applied overpotential, and *vice versa*. The terms  $\alpha_A$  and  $\alpha_C$  are the transfer coefficients for the anodic and cathodic reactions, representing physical aspects of the interaction of reactant molecules and intermediates with the electrode surface[56]. Typically  $\alpha_A + \alpha_C = 1$ , so equation (2.13) becomes

$$J_k = J_0 \left( \exp \left[ \frac{\alpha n F}{RT} \eta \right] - \exp \left[ \frac{-(1-\alpha) n F}{RT} \eta \right] \right) \quad (2.14)$$

with  $0 < \alpha < 1$ . The two exponential terms in equation (2.14) represent the rates of the forward and reverse reactions in (2.9).

$$J_a = J_0 \exp \left[ \frac{\alpha n F}{RT} \eta \right] \quad (2.15)$$

$$J_c = -J_0 \exp \left[ \frac{-(1-\alpha) n F}{RT} \eta \right] \quad (2.16)$$

The forward and reverse components of the net overall current are shown graphically as a function of overpotential in Figure 2.5 (a). The net overall current response given by equation (2.14) is shown in Figure 2.5 (b) for three different values of the exchange current density  $J_0$ . From this figure it is evident that, for a given overpotential, a higher  $J_0$  leads to a higher current. This is the basis for reducing the activation losses in the PEMFC: by increasing the activity of the electrocatalysts towards the electrode reactions, higher currents can be achieved at a lower voltage loss.

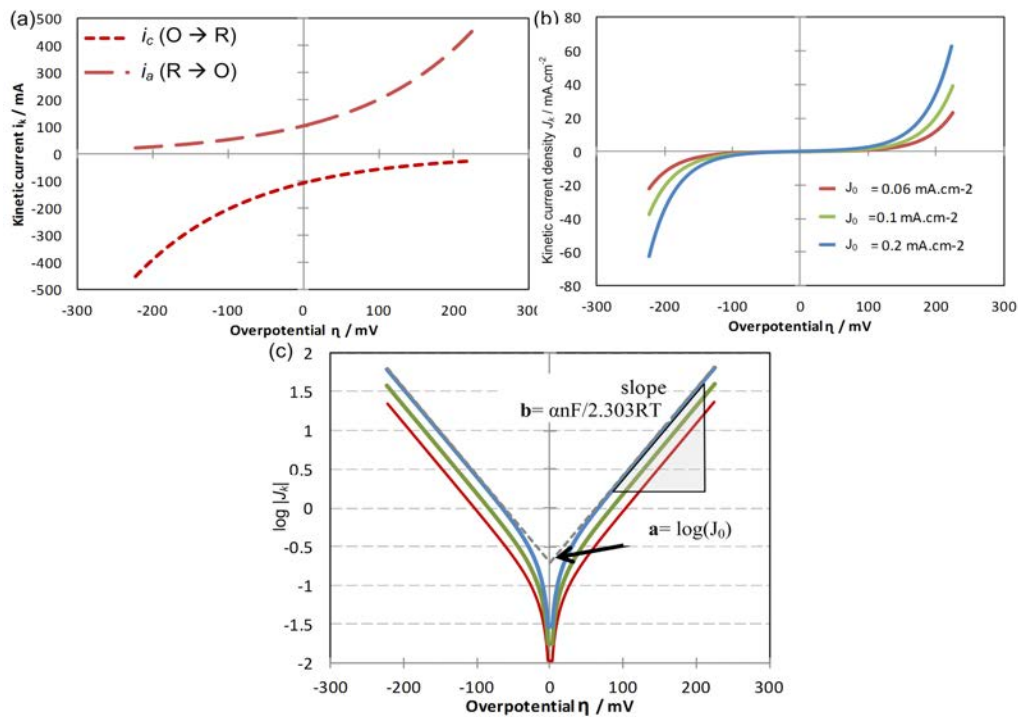


Figure 2.5: (a) Forward and reverse components of the measured current due to the reaction in equation (2.9) as a function of applied overpotential; (b) plots of current vs. overpotential showing the effect of exchange current density  $J_0$  on the shape of the curve; (c) Tafel plots of  $\log|J_k|$  vs. overpotential, illustrating the determination of  $J_0$  and the Tafel slope,  $b$ .

At high overpotentials, the rate of the opposing reaction becomes negligible so that one term in the Butler-Volmer equation can be eliminated e.g. for a cathodic reaction at high (negative) overpotentials ( $\eta < -80$  mV)

$$J_k = J_0 e^{\frac{-\alpha n F \eta}{R T}} \quad (2.17)$$

Rearrangement of equation (2.17), and conversion to base 10 logarithm gives

$$\log(J_k) = \log(J_0) - \frac{\alpha n F}{2.303 R T} \eta \quad (2.18)$$

Equation (2.18) is known as a Tafel equation; a linear equation of the form  $y = a + bx$ , with

$a = \log(J_0)$  corresponding to the intercept at  $\eta = 0$  and  $b = \frac{\alpha n F}{2.303 R T}$  (the Tafel slope) to the slope of the linear portion of a plot of  $\log|J_k|$  vs.  $\eta$  shown in Figure 2.5 (c). This is known as a Tafel plot, from which the parameters  $J_0$  and  $\alpha$  (or  $n$ ) can be determined.

For a reaction with a rate-limiting step involving the transfer of a single electron,  $n=1$ , and assuming a typical value for  $\alpha=0.5$  then the Tafel slope,  $b$  is equal to  $-120$  mV.decade<sup>-1</sup>.

## 2 Introduction to the PEMFC

---

### **Anode vs. cathode kinetics**

The kinetics of the anode and cathode reactions in the PEMFC differ considerably. At the anode, hydrogen oxidation is relatively facile, involving the transfer of a single electron with a relatively high exchange current density of around 3-10 mA.cm<sup>-2</sup>. As a result, the anode makes only a very minor contribution to cell activation losses (typically < 10 mV when operating on pure hydrogen). By comparison, the ORR is a relatively complex reaction, involving the transfer of 4 electrons and proceeds in the presence of strongly-bound adsorbates which reduce the availability of active sites. As a result, the exchange current density of the ORR is up to an order of magnitude lower than that of the HOR, at around 0.5-1 mA.cm<sup>-2</sup>, with the implication that cathode kinetics make by far the largest contribution to activation losses. According to the Tafel equation (2.18) and assuming a Tafel slope of 120 mV.decade<sup>-1</sup>, the cathode overpotential at 100 mA.cm<sup>-2</sup> is around -240 mV.

Because of the slow kinetics of the ORR, the catalyst loading at the PEMFC cathode is typically much larger than that at the anode, by a factor of 4 or more. The optimisation of the cathode catalyst layer therefore offers the greatest potential for reductions in Pt loading, and ORR catalysis will be the focus of this research.

## 3 Review on PEMFC electrocatalysts

This chapter catalogues the development of Pt-based electrocatalysts for PEMFC applications and introduces commonly-used experimental methods for the quantitative measurement and comparison of catalyst performance. The stabilisation of Pt electrocatalysts using conductive ionomers is proposed as a means to improve the performance of PEMFC catalyst layers, and previous work on the subject is reviewed.

### 3.1 A Brief History of PEMFC electrocatalysts

Since the 1960s, continuous efforts to improve fuel cell catalysis – and PEMFC catalysis in particular – have brought dramatic increases in performance and reductions in precious metal loading. The most important developments to date are summarised in the following.

#### 3.1.1 Pt black

The first PEMFCs utilised finely-divided platinum black as the anode and cathode electrocatalyst. With a typical particle size of around 50-100 nm, the physical surface area of Pt black catalysts is around  $10 \text{ m}^2 \cdot \text{g}^{-1}_{\text{Pt}}$ . With such low specific surface areas, Pt loadings of  $> 4 \text{ mg}_{\text{Pt}} \cdot \text{cm}^{-2}$  were necessary in order to achieve practically useful power densities.

#### 3.1.2 Carbon-supported Pt electrocatalysts

Perhaps the single most important development in fuel cell catalysis to date was the advent of carbon-supported electrocatalysts in the 1970s [57]. Supported catalysts typically consist of precious metal nanoparticles of diameter  $< 10 \text{ nm}$  dispersed on a high surface-area carbon black. The surface area of the carbon support is typically  $300\text{-}1500 \text{ m}^2 \cdot \text{g}^{-1}$ , allowing excellent dispersion of Pt nanoparticles up to metal loadings of around 60 wt %. The ability to disperse such small active catalyst particles homogeneously whilst avoiding agglomeration means that physical Pt surface areas can reach  $120 \text{ m}^2 \cdot \text{g}^{-1}_{\text{Pt}}$ .

#### 3.1.3 Ionomer dispersed within catalyst layer

Although the advent of supported electrocatalysts brought dramatic improvements in physical surface area, the proportion of this surface area that was electrochemically active remained relatively low. This is because reactions only occur at regions within the catalyst layer where catalytic surfaces are in simultaneous contact with reactant gases and proton-conducting media,



whilst also having electrical connection to the rest of the electrode. Such regions are known as *triple-phase boundaries*, and for early catalyst layers based on Pt/C were restricted to a thin layer at the PEM/CL interface, with the implication that the remainder of the expensive Pt catalyst displayed relatively low activity – relying on product water alone to provide proton conductivity throughout the majority of the CL.

A major milestone in the development of PEMFC electrocatalysts was achieved with the incorporation of proton-conducting ionomer within the pore structure of the catalyst layer as shown in Figure 3.1 (a), which was first demonstrated in the late 1980s [58]. By forming catalyst layers from inks containing dispersions of Pt/C catalyst along with Nafion® ionomer, the triple-phase boundary could be extended throughout the thickness of the catalyst layer, resulting in far more of the physical Pt surface area becoming electrochemically active. The proportion of the physical catalyst surface area that is electrochemically active is known as the *catalyst utilisation* ( $U_{Pt}$ ), and is given by equation (3.1), where  $ECSA$  and  $A_{phys}$  are the specific electrochemically active and physical surface areas of the catalyst respectively:

$$U_{Pt} = \frac{ECSA}{A_{phys}} \times 100\% \quad (3.1)$$

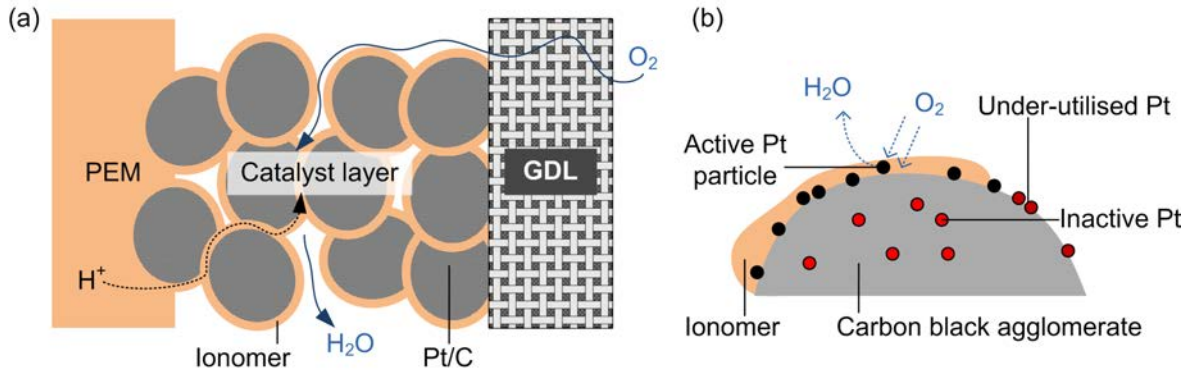


Figure 3.1: Schematic representations of (a) a cross-section of the (cathode) catalyst layer, illustrating the porous structure formed by ionomer-coated Pt/C agglomerates and showing pathways for reactant and proton transport; (b) a single Pt/C agglomerate, showing partial ionomer coverage resulting in under-utilisation of Pt particles (•), and inactive Pt particles (•) within microporous regions of the carbon support.

Despite the success of this method, which has become standard procedure for the preparation of PEMFC catalyst layers, it has certain limitations which restrict catalyst utilisation to around 80%. Several studies have shown that the ionomer forms a proton-conducting network throughout the macroporous and mesoporous regions of the catalyst layer [59], but that it does not penetrate into the micropores (<2 nm diameter) within the carbon support [60]. This implies that the Pt nanoparticles residing within the carbon micropores are isolated from the proton-conducting network and do not contribute to the catalytic reactions, leading to significant losses in active Pt surface area within the catalyst layer as illustrated in Figure 3.1 (b). Furthermore, experimental and

### 3 Review on PEMFC electrocatalysts

---

theoretical investigations have shown that it is difficult even to approach complete ionomer coverage of Pt particles within mesopores when using the standard chemical preparation route. Attempting to increase coverage by addition of ionomer beyond about 33 wt % Nafion® results in reduced performance as a result of electrical isolation of catalyst agglomerates and blockage of gas diffusion pathways by excessive ionomer [61-64].

#### 3.1.4 Towards improved catalyst utilisation

Several strategies for improving catalyst utilisation have been explored to date; for example:

- Song *et al* demonstrated improvements in ionomer distribution, including introduction of Nafion® within primary pores of the carbon support, by treatment of catalyst inks at 200°C in an autoclave prior to application[65].
- Electrodeposition of Pt particles [66-69] is attractive from the point of view of improving catalyst utilisation, as particles are formed only where triple-phase junctions exist. However, the size of the deposited particles is usually rather large, and cannot easily be controlled.
- Alternative carbon support materials, including nanotubes [70-75], mesoporous carbons [76-77] and graphene-based materials [78] have been shown to provide enhanced electronic conductivity and favourable pore structures for mass transport and ionomer distribution in some cases.
- Catalyst layers based on novel nanostructured substrates dispense with the need for ionomer in the catalyst layer. For instance, the nanostructured thin film (NSTF) CLs developed by 3M consist of electrically-conductive perylene red whiskers which are sputter-coated with Pt or Pt alloy and form a sub-micron thick active layer on application to the PEM as shown in Figure 3.2 [10]. Proton transport within the thin catalyst layer in close proximity to the PEM can be facilitated efficiently by liquid water alone.
- Given that the main limitation on the extent of the triple-phase reaction zone within standard Pt/C catalyst layers is poor connectivity between the ionomer and Pt[79], the engineering of an effective Pt-ionomer interface is a promising route for the improvement of catalyst utilisation. Previous studies into the engineering of Pt/membrane interfaces are documented in the literature. For instance, Foster *et al* demonstrated the preparation of Pt-functionalised composite membranes by evaporative deposition of Pt salts onto Nafion®, followed by electrodeposition of conductive polymers [80]. Lee *et al* formed Pt nanoparticles inside a recast Nafion® film by ion-exchange followed by chemical reduction [81].

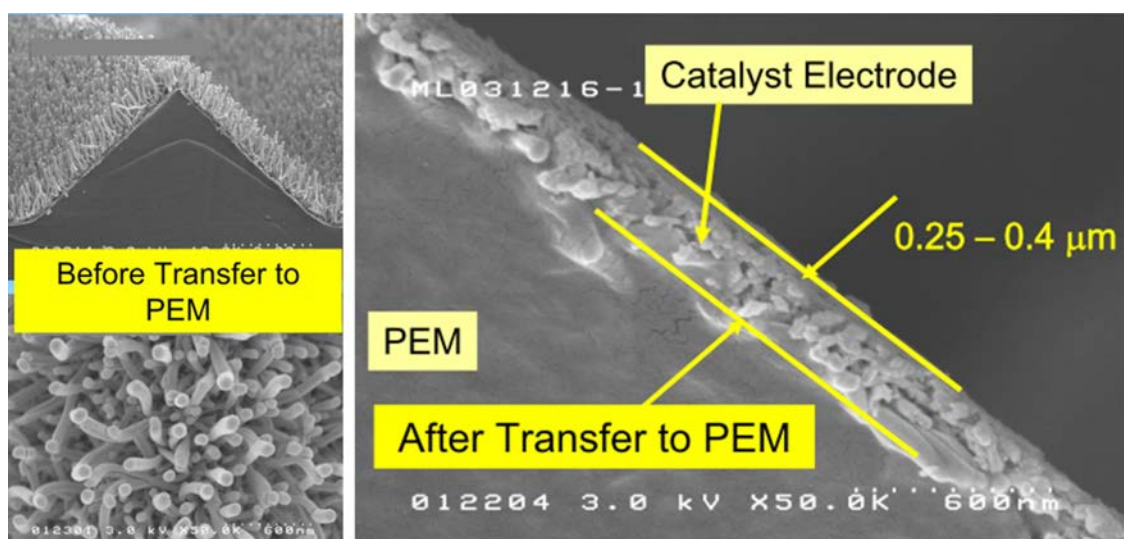


Figure 3.2: SEM images of 3M's NSTF catalyst for the PEMFC, which is fabricated by physical deposition of Pt onto a microstructured corrugated substrate coated with conductive organic whiskers. Reproduced from [10].

Extension of this strategy beyond the two-dimensional interface of the membrane to the three-dimensional, porous structure of the Pt/C catalyst layer has received limited attention to date. There are a few studies in the literature reporting functionalisation of Pt nanoparticles with PFSI ionomers [13-16] for use as PEMFC electrocatalysts. These previous studies will be reviewed in detail in section 3.5 below. This work aims to develop the ionomer-functionalised Pt strategy to improve catalyst utilisation.

## 3.2 Quantitative measures of electrocatalyst performance

In assessing the utility of an oxygen reduction electrocatalyst, it is important to take into account the following aspects of its performance:

- Catalytic activity or reaction kinetics
  - The exchange current density  $J_0$  [ $\text{A}\cdot\text{cm}^{-2}$ ] provides a quantitative measure of the activity of a catalyst towards a given reaction, under the specific conditions (temperature, concentration/pressure, active site availability) employed in the measurement.
- Selectivity
  - The ORR has two possible pathways. One results in the direct conversion of  $\text{O}_2$  to  $\text{H}_2\text{O}$ , with the transfer of 4 electrons according to



### 3 Review on PEMFC electrocatalysts

---

- The other proceeds via a peroxide intermediate, via a series 2e- pathway according to



- The four-electron pathway in reaction 3.2 is favoured both from the point of view of thermodynamics (it generates a larger cell voltage) and durability (peroxide accelerates degradation of the ionomer membrane).
- Durability
  - Ideally, catalysts should not be modified, consumed or degraded in their operating environment, but at the highly positive potential and low pH of the PEMFC cathode, Pt-based catalysts can undergo various degradation processes which result in a decline in their activity (and selectivity) over time. Quantification of electrocatalyst durability can be challenging, and is discussed in detail in chapter 6.
- Utilisation  $U_{Pt}$ 
  - As introduced above, *catalyst utilisation* represents the proportion of the catalyst's physical surface area that is electrochemically active.

## 3.3 Experimental methods for the evaluation of electrocatalyst performance

### 3.3.1 *In-situ* vs. *ex-situ* (half-cell) characterisation

The screening of novel electrocatalyst materials is often carried out in *ex-situ* half-cell experiments. Compared to *in-situ* testing involving the fabrication of single-cell or short-stack PEMFCs, half-cell testing typically requires comparatively small quantities of catalyst material (a few mg); involves far fewer variables in the preparation of electrodes; offers considerably higher throughput and, if carried out with care, affords data which are less prone to uncertainties and errors.

Apart from a few studies employing solid-state electrolytes (Nafion® membranes) [82-83], most *ex-situ* methods for the evaluation of electrocatalytic activity toward PEMFC reactions make use of liquid electrolytes. Whilst this means that the test environment is significantly different to that in a practical PEMFC, it is nevertheless possible to obtain good quantitative agreement between *ex-situ* half-cell and *in-situ* measurements [12].

Generally in half-cell experiments on PEMFC electrocatalysts, a small catalysed working electrode (typically a glassy carbon disc 3-6mm diameter, with a catalyst loading of 10-100  $\mu\text{g}\cdot\text{cm}^{-2}$ ), is immersed in an aqueous acidic electrolyte (0.1-0.5 M  $\text{H}_2\text{SO}_4$  or  $\text{HClO}_4$ ), along with reference and

---

counter electrodes as depicted in Figure 3.3, and whose purposes are described in the following. Potentiodynamic experiments are carried out under purge with inert gas (typically N<sub>2</sub> or Ar) or O<sub>2</sub>.

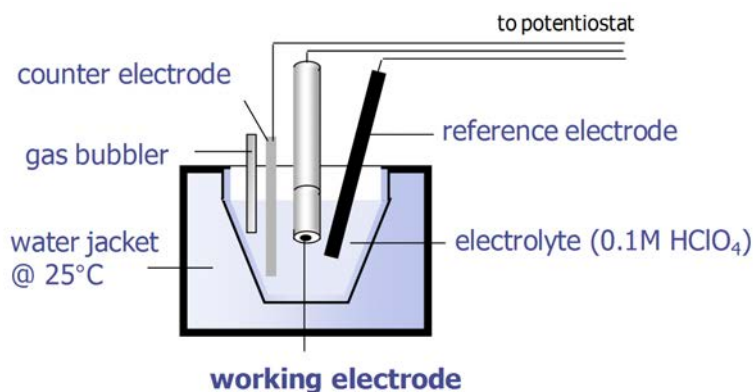


Figure 3.3: A typical 3-electrode half-cell

### 3.3.2 Hardware requirements for *ex-situ* half-cell testing

#### Potentiostat

A basic necessity in any electrochemical experiment is the ability to accurately measure and control the polarisation on the electrode of interest, termed the *working electrode*. After all, it is the electrode polarisation that determines the 'driving force' for any electrochemical reaction taking place at the electrode/electrolyte interface. The polarisation can be measured in terms of the potential difference between the working electrode and some other electrode (*reference electrode*) placed in the same electrolyte, on which proceeds a second electrochemical reaction with a well-defined electrode potential. For accurate measurement of the working electrode potential, it is imperative that the reference electrode remains minimally polarised i.e. no net current should flow from/to it. This condition can be achieved through the use of a *potentiostat*, which controls the potential on a third electrode (*counter electrode*) such that the current balances that on the working electrode, allowing the reference electrode to remain at equilibrium.

#### Cleaning of glassware

Successful and reproducible electrochemical experiments require all components of the system to be rigorously cleaned of impurities that could affect the catalyst. In particular, halide anions (F<sup>-</sup>, Cl<sup>-</sup>, Br<sup>-</sup>), organics and sulphurous compounds have a detrimental effect on the rate of ORR on Pt catalysts.

### 3 Review on PEMFC electrocatalysts

---

#### **Electrolyte selection**

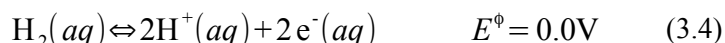
For absolute determination of catalytic activity towards ORR, it is important that the electrolyte is non-adsorbing; there should be no component or impurity in the electrolyte that can undergo specific adsorption to Pt surfaces, and in doing so block active sites and reduce the observed kinetic current density. Many common electrolytes are therefore unsuitable for measurement of ORR kinetics. Notably, the bisulfate ( $\text{SO}_4^-$ ) anion can block Pt surface sites by undergoing specific adsorption, particularly to Pt(111)-type fcc surfaces [84-86]. The same is true of halide anions [87], including chloride ( $\text{Cl}^-$ ) [85, 88]. Perchloric acid ( $\text{HClO}_4$ ) is non-adsorbing and is therefore commonly employed in the characterisation of PEMFC electrocatalysts [22].

Reagent grade perchloric acid contains around 10 ppm chloride as an impurity, and even at this level the ORR kinetics will be affected. A chloride concentration of  $< 3\text{ppm}$  is required for accurate measurement of absolute ORR activity.

#### **Reference electrodes**

The effects of adsorbing anions on the rate of ORR places restrictions on the choice of reference electrode, which being in direct contact with the electrolyte should not contain any adsorbing species. In particular, electrodes containing  $\text{Cl}^-$  and  $\text{SO}_4^{2-}$  should be avoided, which rules out the common saturated calomel (SCE), silver/silver chloride (Ag/AgCl) and mercury sulphate (MSE) electrodes. Although the reference electrode can be separated from the bulk electrolyte by a salt bridge, the rate of diffusion of ions through the bridge is still finite, and therefore an alternative reference electrode is desirable, especially for long experiments.

The Reversible Hydrogen Electrode (RHE) is a convenient non-contaminating reference electrode for studies on ORR catalysts. It consists of a Pt wire, gauze or foil in direct contact with both an acidic electrolyte and gaseous  $\text{H}_2$ , establishing a triple-phase boundary at which the equilibrium in (3.4) is established, providing a reference potential against which the working electrode polarisation can be measured. It so happens that, by convention, the equilibrium in (3.4) is designated a standard electrode potential of 0.0 V.

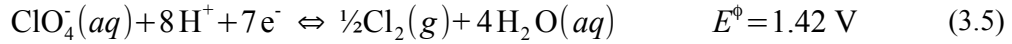


The RHE contains no adsorbing anions, so poses no contamination risk to the experiment.

#### **Counter electrode**

The function of the counter electrode is simply to generate an equal and opposite current to that flowing to/from the working electrode, so that the reference electrode can remain at equilibrium.

Pt is often chosen as a counter electrode material, as it is inert and will not decompose electrolytically to contaminate the electrolyte. The counter electrode potential is controlled by the potentiostat, and can vary by up to  $\pm 50$  V vs. the working electrode (the maximum potential difference is known as the *compliance voltage*), although for typical experiments where working electrode currents are of the order of  $< 1$  mA, such extreme potential differences are rarely required. Nevertheless, for ORR experiments in  $\text{HClO}_4$  it is important to minimise the counter electrode polarisation to avoid contamination of the electrolyte via unwanted reactions such as:



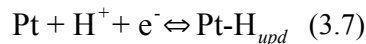
Indeed, it is desirable to limit the magnitude of any Faradaic currents on the counter electrode, and ensure that any reactions occurring at its surface are not mass-transport limited, by ensuring that its active surface area is an order of magnitude larger than that of the working electrode.

### 3.3.3 Electrochemical Surface Area (ECSA) measurements

The electrochemical surface area of an electrode is an important property which must be determined in order to calculate and compare current densities measured for different catalysts and catalyst loadings. The electrochemical surface area is a quantitative measure of the surface area available for electron transfer. For a thin-film catalyst layer on a GC electrode (Pt loading 20-100  $\mu\text{g}\cdot\text{cm}^{-2}$ ), the total electrochemically-active surface area ( $A_{EC}$ ) is typically 10-20 times higher than the geometric area of the electrode ( $A_{geo}$ ). The ratio of the total electrochemically active surface area to the geometric surface area is termed the roughness factor,  $r_f = A_{EC}/A_{geo}$ . The *ECSA* is the electrochemically-active surface area per unit mass of active catalyst material in the electrode, calculated for Pt/C electrodes according to equation (3.6).

$$\text{ECSA} [\text{m}^2 \cdot \text{g}_{\text{Pt}}^{-1}] = \frac{A_{EC} [\text{cm}^2]}{10L_{\text{Pt}} [\text{mg}_{\text{Pt}} \cdot \text{cm}^{-2}] \cdot A_{geo} [\text{cm}^2]} \quad (3.6)$$

For Pt electrodes,  $A_{EC}$  can be conveniently measured using the hydrogen underpotential deposition ( $\text{H}_{\text{upd}}$ ) technique. In an acidic electrolyte,  $\text{H}^+$  is reversibly adsorbed to a coverage of precisely one full monolayer at potentials between +0.05 and +0.4 V vs RHE via the reaction[89]



where  $\text{H}_{\text{upd}}$  represents surface-adsorbed hydrogen, said to be *underpotentially-deposited* because the deposition occurs at an overpotential lower than that for bulk  $\text{H}_2$  evolution [7]. Cyclic voltammograms recorded at 25 mV/s between 0.05 – 1.1 V display distinctive peaks due to  $\text{H}_{\text{upd}}$  processes, as shown in Figure 3.4. The process is reversible, with adsorption taking place on the negative-going (cathodic) sweep, and desorption following when the sweep is reversed at 0.05 V. On polycrystalline Pt surfaces, hydrogen adsorption/desorption occurs at different potentials on the

### 3 Review on PEMFC electrocatalysts

(100), (110) and (111) vertices, leading to this characteristic voltammogram in which the definition of the individual peaks is indicative of surface cleanliness [90].

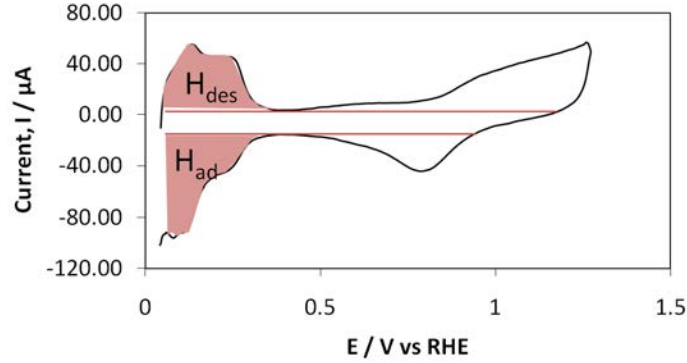


Figure 3.4: Typical cyclic voltammogram for a Pt electrode, showing regions of  $H_{\text{upd}}$  adsorption ( $H_{\text{ad}}$ ) and desorption ( $H_{\text{des}}$ ). The linear baselines indicated in red are set so as to eliminate contributions to current from charge/discharge of the electrochemical double layer (Coulombic current).

Setting baselines to correct for Coulombic current as shown in Figure 3.4 and taking the average of the integrated areas of  $H_{\text{upd}}$  adsorption & desorption peaks gives total charge passed during  $H^+$  adsorption,  $Q_{H_{\text{upd}}} = (Q_{\text{ad}} + Q_{\text{des}})/2$  in units of [ $\mu\text{C}$ ]. The electrochemically active surface area per unit mass Pt (ECSA) [ $\text{m}^2 \cdot \text{g}^{-1} \text{Pt}$ ] can then be calculated using equation (3.8) [90]

$$\text{ECSA} = Q_{H_{\text{upd}}} / 10 \cdot \sigma_{\text{H}} \cdot L_{\text{Pt}} \cdot A_{\text{geo}} \quad (3.8)$$

Where  $L_{\text{Pt}}$  is the catalyst loading [ $\text{mg Pt} \cdot \text{cm}^{-2}$ ] per unit geometric area of the electrode,  $A_{\text{geo}}$  [ $\text{cm}^2$ ], and  $\sigma_{\text{H}} = 210 \mu\text{C} \cdot \text{cm}^{-2}$ , which is the charge required for the formation of a monolayer of  $H_{\text{upd}}$  on a clean, smooth polycrystalline Pt surface. This value for  $\sigma_{\text{H}}$  is only approximately correct for highly-faceted Pt nanoparticle surface, but is widely used in the literature. Values for ECSA are typically expressed in units of  $\text{m}^2 \cdot \text{g}^{-1} \text{Pt}$ .

The ECSA can also be measured by alternative methods such as CO-stripping. In this method, the catalyst is deliberately poisoned with a layer of reversibly-adsorbed CO, either by purging the electrolyte with CO gas under potential control, or by adding methanol to the electrolyte and performing methanol oxidation. The adsorption of CO on surface Pt atoms occurs with a well-defined 1:1 stoichiometry, and the ECSA can be calculated from the charge required to remove the adsorbed CO during a positive-going potential sweep (voltammetric stripping). However, facilities for the extraction of toxic CO gas were not available for this study, and residual MeOH can be difficult to remove entirely from the catalyst film. Therefore the  $H_{\text{upd}}$  technique was used throughout this work.



---

### Ex-situ catalyst utilisation measurements

The ratio of ECSA to the physical (Pt) surface area of the catalyst is known as the catalyst utilisation, and can be calculated according to equation (3.1) (page 28).

A utilisation of 100% indicates that the entire Pt surface area is available for electron transfer, with the implication that all Pt particles are sited at triple-phase boundaries. In acidic liquid electrolyte testing, the entire catalyst is saturated in a proton-conducting medium, so one would expect very high catalyst utilisations. This is quite a different scenario to that of a gas diffusion electrode, which relies on percolations of the proton-conducting ionomer to extend the three-phase reaction zone throughout the catalyst layer. One aim of this study will be to investigate how the thickness of the catalyst film on the RDE affects the measured utilisation. If the film is sufficiently thick, then it may approximate the GDE and can be used to screen different catalyst ink compositions to optimise catalyst utilisation before preparation of GDEs. Given that the amount of catalyst required for RDE thin films is two orders of magnitude less than is required to prepare a GDE, the ability to perform such a screening process without resorting to the preparation of several MEAs is highly desirable; especially when limited quantities of a catalyst are available.

### **3.3.4 Hydrodynamic voltammetry using the RDE**

Currents measured in electrochemical experiments are usually limited in some way by transport of reactants to the electrode surface. Experimentally, we can control mass transport, and hence isolate the kinetic currents  $i_K$  using *forced-convection* or *hydrodynamic* techniques, in which the mass transport characteristics determining the limiting current  $i_D$  at the electrode interface are well-understood and can be precisely controlled. The most common hydrodynamic technique for the evaluation of electrocatalysts is the *rotating-disc electrode* (RDE) technique. For studies on supported catalysts, the RDE typically consists of a glassy carbon disc electrode embedded in a PTFE sheath as shown in Figure 3.5 (a). The disc is typically 2-6 mm in diameter, and is coated in a thin film of the catalyst to be tested. In a typical RDE experiment, linear sweep voltammetry - that is, a potentiodynamic sweep through a potential range of interest - is carried out at several different rotation rates  $\omega$ , producing a series of linear sweep voltammograms as shown in Figure 3.6 (a).

### 3 Review on PEMFC electrocatalysts

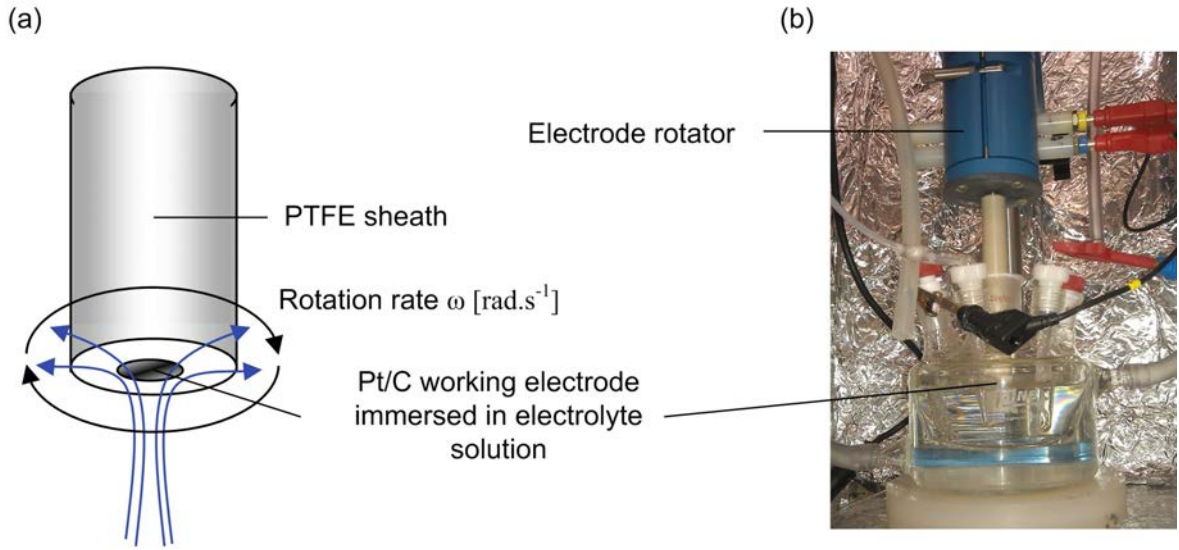


Figure 3.5: (a) Schematic of the RDE assembly and its mass transport characteristics (b) a practical RDE setup as part of an electrochemical half-cell

The current density  $J$  measured in an electrochemical environment contains kinetic ( $J_k$ ) and diffusion-limited ( $J_{lim}$ ) components which combine in a reciprocal sum according to the Koutecky-Levich equation:

$$\frac{1}{J} = \frac{1}{J_k} + \frac{1}{J_{lim}} \quad (3.9)$$

For an RDE, the diffusion-limited component,  $J_{lim}$  of measured current is related to the rotation rate,  $\omega$  according to the Levich equation:

$$J_{lim} = 0.620n F A_{geo} D_0^{2/3} \omega^{1/2} \nu^{-1/6} C_0^* \quad (3.10)$$

Where  $A_{geo}$  [cm<sup>2</sup>] is the geometric surface area of the disc electrode,  $D_0$  [cm<sup>2</sup>.s<sup>-1</sup>] is the diffusion coefficient of the reactive species,  $\omega$  [rad.s<sup>-1</sup>] is rotation rate ( $= 2\pi f = 2\pi[\text{RPM}]/60$  - where  $f$  [s<sup>-1</sup>] is the frequency of rotation,  $\nu$  [cm<sup>2</sup>.s<sup>-1</sup>] is the kinematic viscosity of the electrolyte and  $C_0^*$  [mol.cm<sup>-3</sup>] is the bulk concentration of the reactive species[56].

There are then two methods for extracting purely kinetically-controlled currents  $J_k$  from measured current data:

- **K-L plot method**

Substituting (3.10) into (3.9) gives a useful form of the Koutecky-Levich equation for RDE experiments:

$$\frac{1}{J} = \frac{1}{J_k} + \frac{1}{0.620n F A_{geo} D_0^{2/3} \omega^{1/2} \nu^{-1/6} C_0^*} \quad (3.11)$$

Koutecky-Levich (K-L) plots of  $J^{-1}$  vs.  $\omega^{-1/2}$  at any potential within the mixed kinetic-diffusion region(s) of the polarisation curve should yield a straight lines with intercepts equal to  $1/J_k$  as shown in Figure 3.6 (b) and (c). The potentials for the K-L plot should be chosen such that the currents are within 10% and 80% of the limiting current, and ideally below the half-wave potential to minimise errors in the calculation of kinetic currents[91]. The number of electrons transferred in the reaction,  $n$  can be calculated from the slope provided that the other parameters in the Levich equation are known.

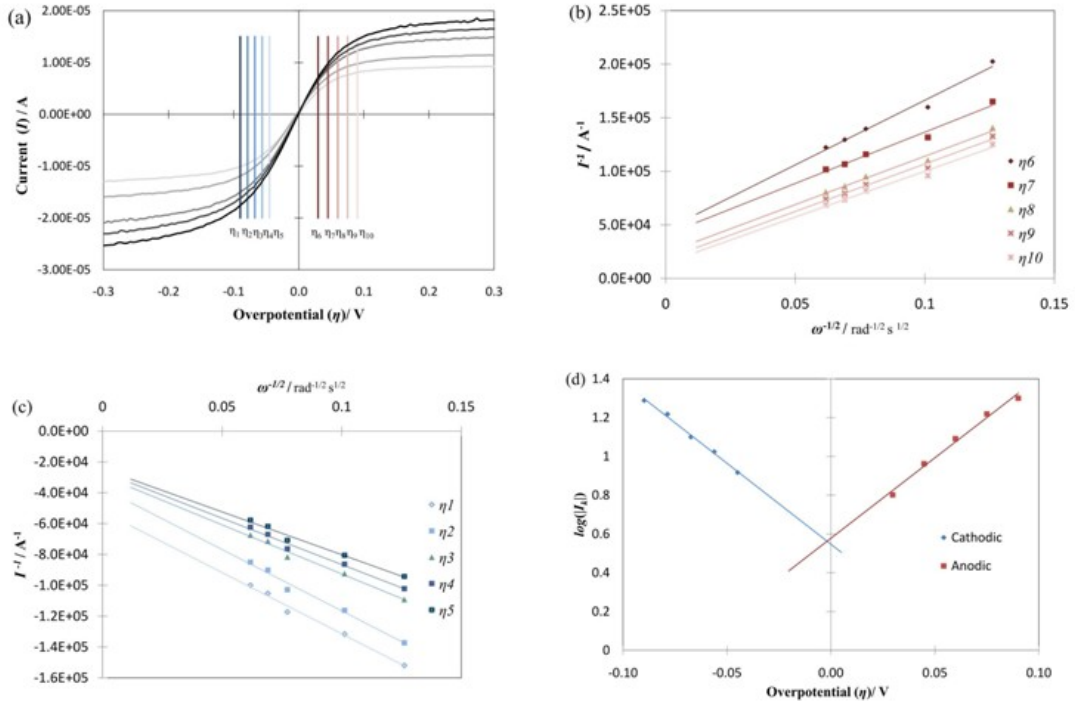


Figure 3.6: (a) Rotating disc voltammograms recorded at  $25 \text{ mV s}^{-1}$  in a  $10 \text{ mM}$  solution of potassium ferricyanide and potassium ferrocyanide in a background electrolyte of  $0.5 \text{ M KCl}$ , using a  $5 \text{ mm Pt}$  disc working electrode. Rotation rates  $\omega = 600, 933, 1600, 2000, 2500 \text{ rpm}$ . The vertical lines at  $\eta_1$ - $\eta_{10}$  indicate the overpotentials within the mixed kinetic/diffusion-controlled regions chosen for the plots in (b) and (c); (b) Koutecky–Levich plots for the anodic branches and (c) cathodic branches of the voltammograms. Extrapolation of the linear plots to  $\omega^{-1/2}=0$  yields the kinetic current  $J_k$  for each overpotential  $\eta$ . (d) Tafel plot using  $i_k$  values determined from the intercepts of Koutecky–Levich plots. Reproduced from [11]

Kinetic current densities,  $J_K$  can be found from the intercepts of the K-L plot at  $\omega^{-1/2} = 0$ , which effectively correspond to an infinite rotation rate, and therefore an infinite mass transport rate.

- **Direct calculation**

Rearranging the Koutecky-Levich equation (3.9) for  $J_k$  gives:

$$J_k = \frac{J \cdot J_{\text{lim}}}{J_{\text{lim}} - J} \quad (3.12)$$

### 3 Review on PEMFC electrocatalysts

---

For any linear sweep voltammogram displaying a well-defined diffusion-limiting current plateau, kinetic current densities  $J_k$  can be calculated from the measured current density  $J$  and the diffusion-limited current density  $J_{lim}$  according to (3.12). It is important to note that this analysis is only valid for the region of the voltammogram which is under mixed kinetic/diffusion control (the region between -0.1 and +0.1 V in Figure 3.6 a).

Once values for  $J_k$  are known for a suitable range of potentials, a Tafel plot of  $\log(J_k)$  vs  $\eta$  can be drawn as shown in Figure 3.6 (d) and earlier in Figure 2.5 (c) (page 24):

For an irreversible cathodic process such as the ORR, only the negative overpotential region of the plot in Figure 3.6 (d) is seen.

The exchange current density and Tafel slope can be determined from the Tafel plot as described earlier in section 2.4.4 on page 24.

#### 3.3.5 RDE experiments on supported catalysts

Strictly, the Levich equation is only valid for a smooth, flat electrode and therefore its application to thin-film RDE experiments involving a porous catalyst layer with a high roughness factor involves a degree of approximation. To avoid difficulties in the analysis of RDE data, the preparation of the thin-film electrode is important: the film should be uniform and homogeneous across the entire surface of the glassy carbon disc [92], and should be sufficiently thin as to present minimal internal diffusion resistance. Previous work indicates that reactant transport is impaired in catalyst films thicker than about 1  $\mu\text{m}$  [93-94], such that the Levich equation can no longer be applied and extraction of kinetic parameters requires complex analysis involving mathematical modelling to account for the agglomerate structure of the thick film [94]. The ionomer content of the catalyst layer is also important: it has been shown that Nafion® films thicker than 0.5  $\mu\text{m}$  impart a significant barrier to the diffusion of  $\text{O}_2$  to catalyst sites, which complicates calculation of kinetic current densities [95-97] and should therefore be avoided by keeping the ionomer content within a suitable range.

In a typical ORR experiment the current is recorded during an anodic potential sweep (+0.05 to +1.2V vs RHE) at a range of rotation rates. The direction of the sweep is important: in an anodic sweep (0.05  $\rightarrow$  1.2 V), the Pt surface is initially in its pristine, reduced state, whereas for the corresponding cathodic sweep (1.2  $\rightarrow$  0.05 V), the Pt surface is initially covered in adsorbed oxide species, which lower the rate of ORR [25, 98].

**In practice**, for ORR measurements on Pt catalysts, extrapolating the linear region of the Tafel plot from the useful potential range for kinetics measurements (typically +0.8 to +1.0 V) to the reversible potential (+1.23 V at 25°C) involves performing linear regression over several orders of

magnitude in  $J_k$ , with the result that the values obtained are subject to significant error [99]. For more reliable comparison of catalytic activities, it has become something of a convention in the literature to report *specific activities* (SAs) (kinetic current density normalised by active surface area  $A_{EC}$ , [ $\text{A}\cdot\text{m}^{-2}_{\text{real}}$ ]) at +0.85 or +0.9 V vs. RHE instead of  $J_0$  [12].

### 3.3.6 Rotating Ring-Disc Electrode studies

The reduction of  $\text{O}_2$  on Pt may proceed via two routes: either directly to  $\text{H}_2\text{O}$  via a  $4e^-$  pathway, or via a  $2e^-$  series pathway to  $\text{H}_2\text{O}_2$ . Peroxide production at the PEMFC cathode is undesirable for reasons of efficiency and membrane degradation, so novel electrocatalysts must be tested for their selectivity towards the  $4e^-$  reaction pathway. Any modification of the Pt/electrolyte interface may produce changes in selectivity; for instance, at potentials below 0.4 V, the presence of underpotentially-deposited hydrogen on the Pt surface can modify the ORR reaction pathway such that the  $2e^-$  reduction of  $\text{O}_2$  to  $\text{H}_2\text{O}_2$  can proceed at a noticeable rate [100]. The RRDE is a variation on the RDE technique which allows quantification of peroxide production during ORR. The catalysed disc electrode is surrounded by a concentric Pt ring electrode as shown in Figure 3.7.

Under rotation, peroxide generated on the disc flows outwards towards the ring, where it is oxidised according to

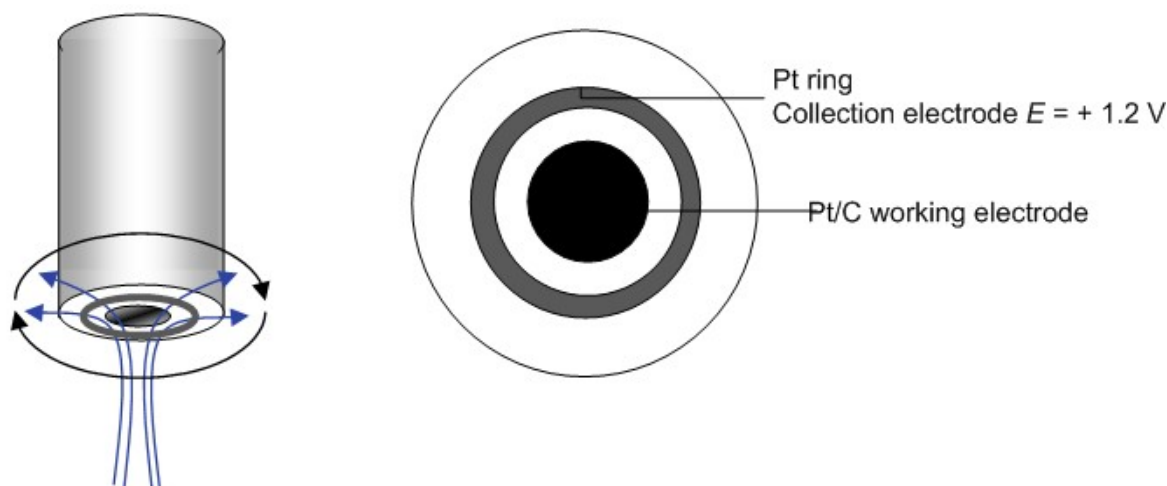


Figure 3.7: Schematic of the RRDE assembly and its mass transport characteristics

The potential on the ring is set to around +1.2 V so that the oxidation proceeds under pure diffusion limitation, to ensure that as much peroxide is 'collected' as possible. However, the natural diffusion of peroxide away from the surface of the disc in the direction perpendicular to the disc means that only a fraction of the peroxide is detected. The *collection efficiency*,  $N$  of the RRDE is dependent on its geometry, and can be measured experimentally.

### 3 Review on PEMFC electrocatalysts

Once the collection efficiency is known, the rate of peroxide formation can be calculated at any potential using

$$\chi_{\text{H}_2\text{O}_2} = \frac{2I_R/N}{I_D + I_R/N} \quad (3.14)$$

where  $\chi_{\text{H}_2\text{O}_2}$  is the number of moles of  $\text{H}_2\text{O}_2$  formed per mole of  $\text{O}_2$ ,  $I_R$  is the ring (collection electrode) current and  $I_D$  is the disc (working electrode) current. The rate of peroxide formation is potential-dependent, with Pt/C catalyst typically yielding 5-10 %  $\text{H}_2\text{O}_2$  at  $E=0.1$  V[100-104].

### 3.4 Previous studies on state-of-the-art Pt/C electrocatalysts

To the author's knowledge, there are presently three principle manufacturers of Pt/C electrocatalysts whose products appear regularly in the literature: Tanaka Kikinzoku Kogyo (TKK, Japan), Johnson Matthey Plc (JM, United Kingdom) and E-Tek (now part of BASF Fuel Cell Inc., Germany). Their Pt/C products (excluding alloys such as Pt-Ru, Pt-Co) are summarised in Table 3.1.

| Manufacturer / Brand | Product      | Nominal composition   |
|----------------------|--------------|---|
| TKK                  | TEC10E40E    | 40 wt % Pt on HSA C   |
|                      | TEC10E50E    | 50 wt % Pt on HSA carbon  |
|                      | TEC10E60TPM  | 60 wt % Pt on HSA C   |
|                      | TEC10E70TPM  | 70 wt % Pt on HSA C   |
|                      | TEC10V30E    | 30 wt % Pt on Vulcan XC-72  |
|                      | TEC10V40E    | 40 wt % Pt on Vulcan XC-72  |
|                      | TEC10V50E    | 50 wt % Pt on Vulcan XC-72  |
| JM                   | HISPEC 2000  | 10 wt % Pt on C   |
|                      | HISPEC 3000  | 20 wt % Pt on C   |
|                      | HISPEC 4000  | 40 wt % Pt on C   |
|                      | HISPEC 8000  | 50 wt % Pt on C   |
|                      | HISPEC 9000  | 60 wt % Pt on C   |
|                      | HISPEC 9100  | 60 wt % on HSA C  |
|                      | HISPEC 13100 | 70 wt % on HSA C  |
| E-Tek*               | HP           | Available as 20, 30, 40, 50, 60 and 80 wt % Pt on a Vulcan XC-72 carbon support |

Table 3.1: Current commercially-available Pt/C electrocatalysts. HSA = high-surface area.

The literature provides numerous reports on the catalytic activity of commercially-available electrocatalysts; many of which are in good mutual agreement. However, even in half-cell

experiments, results are affected by variations in electrode preparation and experimental procedures [12, 22, 105-108]. A summary of results reported for two of the most common electrocatalysts found in the literature is given in Table 3.2. It is clear that there are significant variations in specific electrochemical surface area (ECSA), specific activity (SA) and mass activity (MA) towards the ORR. Measurements are dependent on electrode preparation [109], temperature [110], reagent purity [105] and experimental parameters such as scan rate and upper/lower vertex potentials [12].

| Ref   | T / °C | Electrolyte                         | Scan rate<br>/ mV.s <sup>-1</sup> | ECSA /<br>m <sup>2</sup> .g <sup>-1</sup> <sub>Pt</sub> | SA @ +0.9 V<br>/ A.m <sup>-2</sup> | MA @ +0.9V<br>/ A.g <sup>-1</sup> <sub>Pt</sub> | <i>J<sub>lim</sub></i> close to theoretical? | Full catalyst utilisation? | Background subtraction? |
|---|--------|-------------------------------------|-----------------------------------|---|------------------------------------|---|--|----------------------------|-------------------------|
| <b>TKK TEC10E50E 46 wt % Pt on HSA carbon, Pt particle size 2-3 nm</b>  |        |                                     |                                   |   |                                    |   |  |                            |                         |
| [12]  | 60     | 0.1M HClO <sub>4</sub>              | 20                                | 80  | 2.65 ± 0.25                        | 210   | ☺  | ☺                          | ☒                       |
| [105]   | 30     | 0.1M HClO <sub>4</sub>              | 20                                | 61  | 3.47                               | 210   | ☺  | ☒                          | ☺                       |
| [106]   | 60     | 0.1M HClO <sub>4</sub>              | 20                                | -   | 1.62*                              | -   | ☺  | ?                          | ☒                       |
| [107]   | 60     | 0.1M HClO <sub>4</sub>              | 25                                | -   | 3.0 ± 0.4                          | -   | ☺  | ?                          | ☒                       |
| [107]   | 25     | 0.1M HClO <sub>4</sub>              | 25                                | -   | 2.0 ± 0.4                          | -   | ☺  | ☺                          | ☒                       |
| [108]   | 25     | 0.1M HClO <sub>4</sub>              | 50                                | 76  | 4.9                                | 374   | ☺  | ☺                          | ☺                       |
| [22]  | 25     | 0.1M HClO <sub>4</sub>              | 10                                | 80  | 2.92                               | 266   | ☒  | ☺                          | ☺                       |
| [111]   | 65     | 0.1M HClO <sub>4</sub>              | 5                                 | 117   | 2.26                               | 264   | ?  | ☺                          | ?                       |
| <b>E-Tek HP 20 wt % Pt on Vulcan XC-72, Pt particle size 3.7 ± 1 nm</b> |        |                                     |                                   |   |                                    |   |  |                            |                         |
| [100]   | 60     | 0.5M HClO <sub>4</sub>              | 5                                 | 65  | 0.65                               | 43  | ☺  | ☺                          | ?                       |
| 10  | 60     | 0.5M H <sub>2</sub> SO <sub>4</sub> | 5                                 | 65  | 0.35                               | 23  | ☺  | ☺                          | ?                       |
| [109]   | 30     | 0.1M HClO <sub>4</sub>              | 20                                | 61 ± 2  | 5.11 ± 0.25                        | 310 ± 20  | ☺  | ☺                          | ☺                       |
| [12]  | 60     | 0.1M HClO <sub>4</sub>              | 20                                | 69 ± 4  | 2.8 ± 0.2                          | 195 ± 5   | ☺  | ☺                          | ☒                       |
| [12]  | 60     | 0.1M HClO <sub>4</sub>              | 5                                 | 69 ± 4  | 2.15 ± 0.15                        | 145 ± 15  | ☺  | ☺                          | ☒                       |

Table 3.2: Summary of electrocatalyst properties reported in previous half-cell studies using hydrodynamic voltammetric techniques for the characterisation of Pt/C catalysts. Specific activities (SA) [A.m<sup>-2</sup>] and mass activities (MA) [A.g<sup>-1</sup>] are reported for the ORR at 0.9 V vs SHE. \* denotes value calculated from data given in the publication, assuming a Tafel slope of -60 mV.dec<sup>-1</sup>. The columns on the right indicate whether certain requirements were met in terms of data quality and data analysis.

By far the most widely cited of these publications is ref [12] (869 citations at time of writing) by Gasteiger *et al*, which reports the characterisation of several commercial Pt/C catalysts using both

### 3 Review on PEMFC electrocatalysts

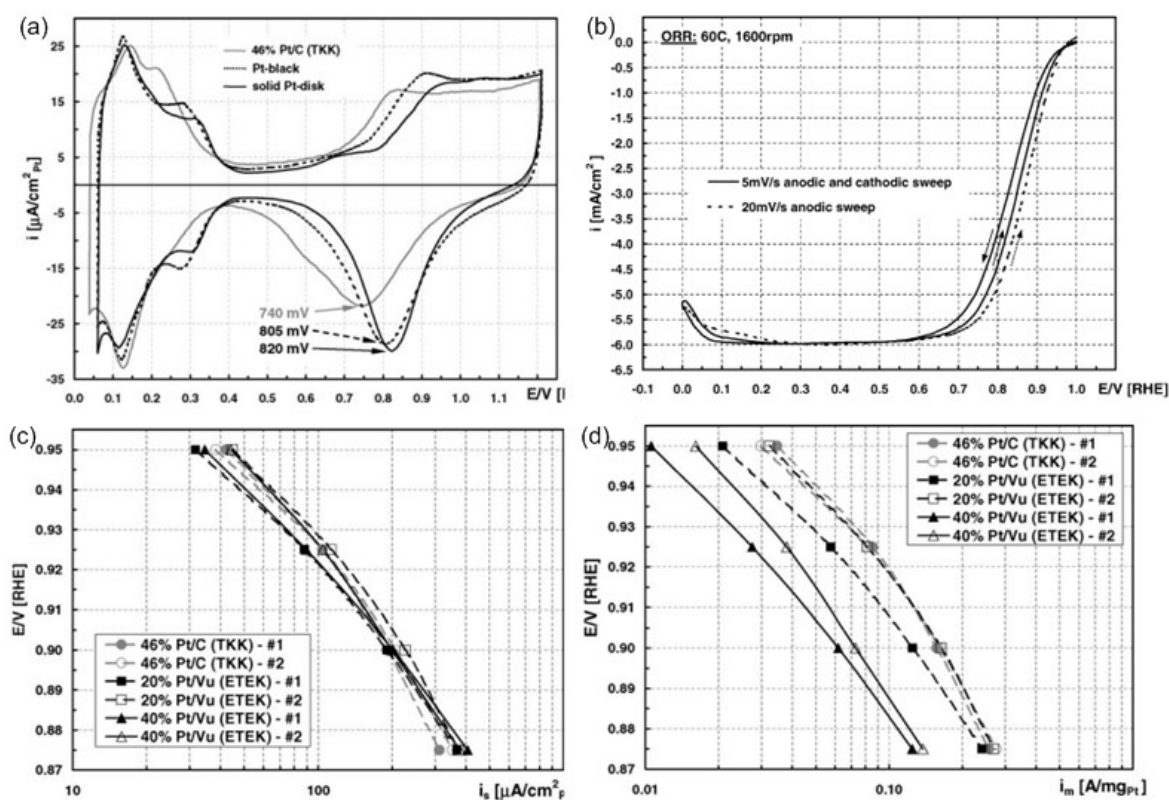


Figure 3.8: (a) Cyclic voltammograms of carbon-supported Pt, Pt-black, and polycrystalline Pt in terms of Pt-surface area normalized current densities ( $\text{mA} \cdot \text{cm}^{-2}_{\text{Pt}}$ ), recorded in 0.1 M HClO<sub>4</sub> at 25°C and 20 mV/s. (b) ORR current densities on 20% Pt/Vulcan ( $14.3 \text{ mg Pt cm}^{-2}$ ) at 1600 rpm in 0.1 M HClO<sub>4</sub> at 60°C: sweeps at 5 mV/s (solid line) and 20 mV/s (dashed line; positive-going sweep only). (c) Specific activities,  $i_s$  and (d) mass activities,  $i_m$ , for the ORR at 60°C on Pt/C catalysts (two repeats each) (Pt-loadings ranging from 12.7 to  $14.3 \text{ mg Pt cm}^{-2}$ ). Data are shown for the positive-going sweep at 5 mV/s going from 0 to 1.0 V (RHE) in O<sub>2</sub>-saturated 0.1 M HClO<sub>4</sub> at 1600 rpm. All potentials are referred to the reversible hydrogen electrode under the same conditions. Reproduced from [12]

the RDE and *in-situ* methods. In their RDE studies, they measure ECSA from cyclic voltammograms such as those shown in Figure 3.8 (a) using the  $H_{\text{upd}}$  technique (see page 34). Values for ECSAs are within 10% of the specific physical surface area for all catalysts, indicating attainment of full utilisation. RDE voltammograms in Figure 3.8 (b) show rapid onset of ORR activity from around +1.0 V, reaching mass-transport limitation by around +0.6 V, with well-defined limiting current plateaus from +0.6 to +0.2 V. The limiting current densities of  $-6.0 \text{ mA} \cdot \text{cm}^{-2}_{\text{geo}}$  are close to the theoretical value predicted by the Levich equation ( $-5.6 \text{ mA} \cdot \text{cm}^{-2}_{\text{geo}}$  at 1600 RPM, 60°C), indicating proper distribution of the active catalyst over the surface of the disc electrode. Tafel plots in Figure 3.8 (c) are correctly normalised by electrochemical surface area to account for differences in particle size, and Tafel slopes in the range +0.95 to +0.90 V are close to the theoretical value of  $-65 \text{ mV} \cdot \text{dec}^{-1}$  at 60°C. Mass activities shown in Figure 3.8 (d) follow the expected trend in that they increase with decreasing Pt particle size, and the repeat measurements shown in (c) and (d) provide evidence of a reasonably reproducible method, with variations in SA



---

and MA of <10 % at +0.9 V. Values for SA and MA at +0.9 V for the TKK 46 wt% catalyst were reported as 2.65 A.m<sup>2</sup><sub>Pt</sub> and 210 A.g<sup>-1</sup><sub>Pt</sub>, respectively.

The self-consistency of these results, their agreement with theoretical predictions, and the provision of detailed descriptions of the experimental procedures has led to this work becoming something of a benchmark for ORR electrocatalysts in the PEMFC research community. There is, however, one significant criticism to be levelled at this study in that it fails to account for capacitive and background Faradaic currents when analysing data. The authors offer assurance that the effect of such currents are small (<4% at 5mV/s and 15% at 20mV/s), but more recently Nesselberger *et al* have found background correction to be essential for rigorous analysis of ORR kinetics data; especially when comparing Pt/C catalysts with different carbon supports [108]. By correcting for these small but significant anodic currents, the SA and MA of the TKK 46 wt% Pt/C were found to be somewhat higher than reported by Gasteiger *et al* (4.9 A.m<sup>2</sup><sub>Pt</sub> and 374 A.g<sup>-1</sup><sub>Pt</sub>).

## 3.5 Previous studies on ionomer-stabilised electrocatalysts

There have been relatively few attempts to synthesise ionomer-stabilised Pt-based electrocatalysts for fuel cell applications. In fact, only four publications on the subject are known to the author. They are reviewed here in chronological order of publication.

### 3.5.1 Sarma et al (2005)

The earliest work known to the author is that of Sarma *et al*, who employed Nafion® ionomer dispersions in the preparation of supported Pt-Ru catalysts for methanol oxidation [13]. In their work, a Vulcan XC-72 carbon support was dispersed in a solution of H<sub>2</sub>PtCl<sub>6</sub> and RuCl<sub>3</sub> which were then reduced using MeOH under reflux at pH 11. The addition of Nafion® ionomer dispersion to the precursor mixture prior to the reduction step was found to produce a decrease in average particle size from 5-7 nm (without Nafion®) to 3-4 nm (with Nafion®), as measured from TEM micrographs in Figure 3.9.

The authors specify a 'Nafion®:catalyst' mass ratio of 3:1, which assuming this includes the carbon support gives a Nafion®:metal(Pt+Ru) ratio of 10:1. The authors then prepared working electrodes from their Nafion®-stabilised Pt-Ru/C catalyst by coating small amounts onto carbon cloth. Measurement of catalytic activity towards the methanol oxidation reaction (MOR) was performed in 0.5 M H<sub>2</sub>SO<sub>4</sub> containing various concentrations of MeOH. They found that, at low MeOH concentrations (5%), the Nafion®-stabilised catalyst displayed significantly higher mass activity toward MOR than an E-Tek 40 wt % commercial catalyst (MAs @ +0.4 V vs SHE were

### 3 Review on PEMFC electrocatalysts

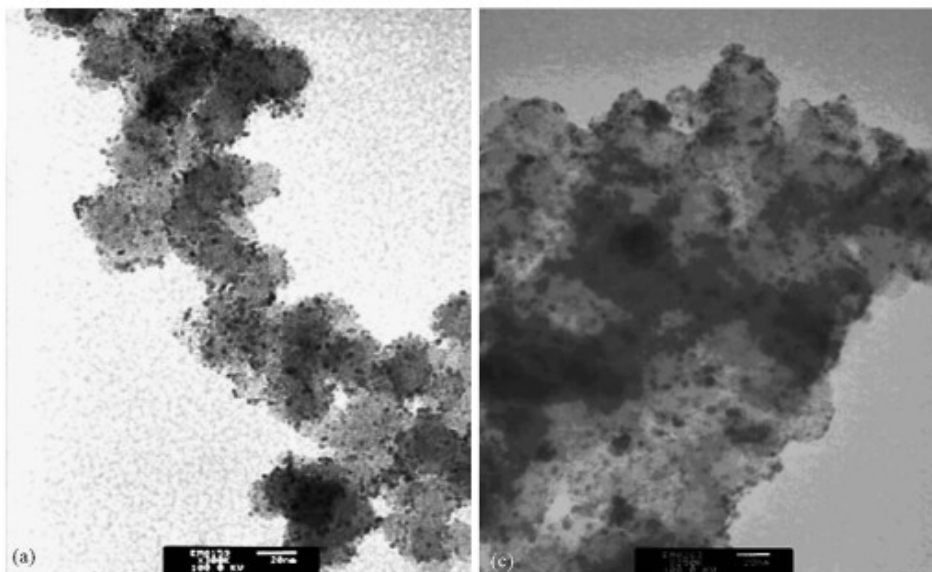


Figure 3.9: Pt-Ru/C electrocatalysts prepared by MeOH reduction a) in the presence of Nafion® dispersion and b) without Nafion®. Reproduced from [13]

1.82 and 0.55 A.g<sup>-1</sup> respectively). However, it is not clear whether the data was corrected for mass transport effects or the Ohmic resistance of the electrolyte. In any case, activity toward MOR is of limited relevance to this work, which is concerned only with the oxygen reduction reaction.

#### 3.5.2 Liu et al (2006)

The following year, Liu *et al* described for the first time the preparation of colloidal Pt nanoparticles stabilised by Nafion® ionomer [14]. Initially, they employed UV-visible

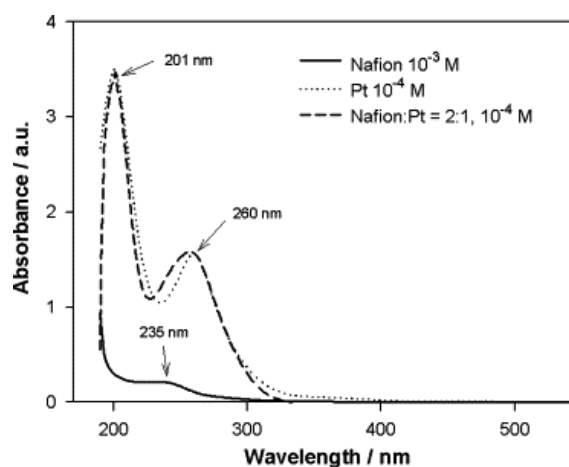


Figure 3.10: UV-vis absorption spectra of Nafion® ( $10^{-3}$  M),  $H_2PtCl_6$  ( $10^{-4}$  M) and Nafion: $H_2PtCl_6$  = 2:1 mixture ( $10^{-4}$  M) solutions. Reproduced from [14].

---

spectroscopy to study the interaction between the  $\text{PtCl}_6^{2-}$  anion and Nafion® dispersion, revealing a small shift in the absorbance peaks at 201 and 260 nm (Figure 3.10) which they ascribed to coordination of S or O from Nafion® sidechains to  $\text{Pt}^{2+}$  and  $\text{Pt}^{4+}$ . This interaction between Pt precursor and ionomer provides a basis for the stabilisation of colloidal nanoparticles produced in the subsequent reduction reaction, and will be discussed in more detail in the following chapter.

Having demonstrated this interaction, the authors then employed an alcohol reduction method to produce colloidal Pt, and explored the effect of reaction temperature and Pt:Nafion® ratio on the morphology of the product. By refluxing  $\text{H}_2\text{PtCl}_6$  in a 40/60 v/v mixture of EtOH/water at pH 8.5 in the presence of Nafion® dispersion, they obtained dispersions of colloidal Pt with agglomerated morphologies as shown in Figure 3.11 and Figure 3.12.

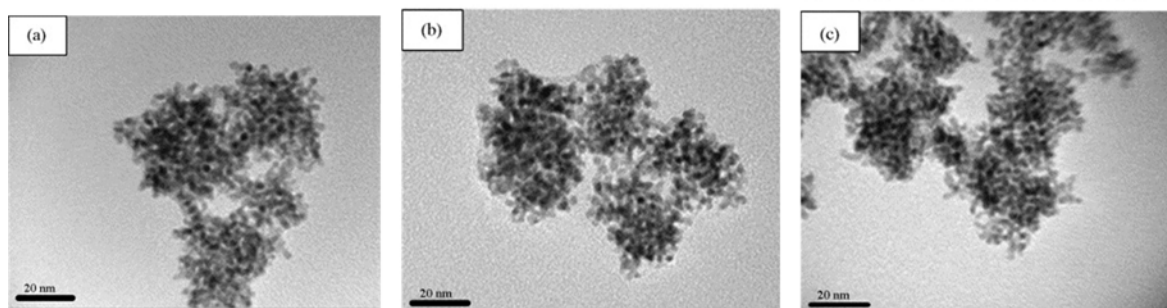


Figure 3.11: TEM images of Nafion®-Pt nanoparticle colloids synthesized at different reflux temperatures with Nafion®/Pt = 2:1: (a) 65 °C, (b) 75 °C and (c) 82 °C. Reproduced from [14].

The authors report the use of Nafion®:Pt *molar* ratios from 1:2 to 8:1, but it is unclear on what basis these ratios are calculated, given that the average molecular weight of Nafion® cannot be determined. They also investigated the effect of reflux temperature (65, 75, 82 °C) on the morphology of the product, obtaining the series of products shown in Figure 3.11.

### 3 Review on PEMFC electrocatalysts

---

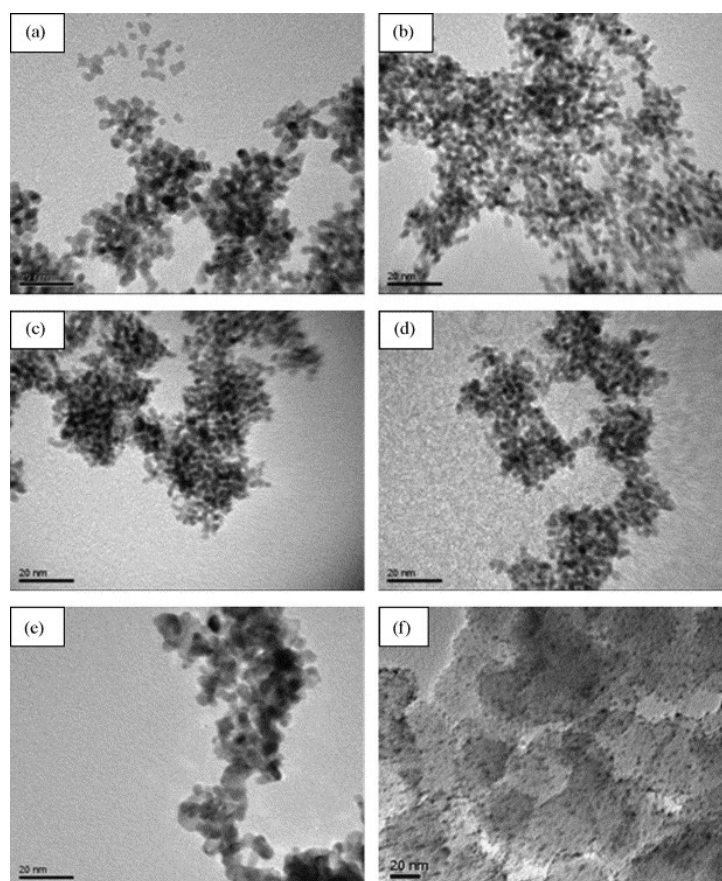


Figure 3.12: TEM micrographs of Nafion®-stabilised colloidal Pt synthesised at 82 °C in the presence of different Nafion®/Pt 'molar' ratios: (a) 1:2, (b) 2:1, (c) 4:1 and (d) 8:1. TEM images of Pt black (E-TEK) and 20 wt% Pt/C (E-TEK) electrocatalysts are shown in (e) and (f). Reproduced from [14].

From XRD measurements, the authors were able to discern small but significant variations in particle size as a function of both Nafion®:Pt ratio and reaction temperature as summarised in Table 3.3, with size decreasing with increasing temperature, and the smallest particles being produced at an apparently optimal Nafion®:Pt ratio of 2:1.

| Synthesis conditions | Particle size / nm | Physical surface area / m <sup>2</sup> .g <sup>-1</sup> |
|----------------------|--------------------|---|
| Nafion®:Pt           |                    |   |
| 1:2                  | 4.3                | 65  |
| 1:1                  | 2.8                | 100   |
| 2:1                  | 2.7                | 104   |
| 4:1                  | 3                  | 93  |
| 8:1                  | 3.2                | 87  |
| Temperature °C       |                    |   |
| 65                   | 4.4                | 60  |
| 75                   | 3.2                | 87  |
| 82                   | 2.7                | 104   |

Table 3.3: Particle sizes and surface areas obtained from XRD measurements on reaction products as reported by Liu et al in [14]

In their subsequent electrochemical characterisation, the authors used the as-prepared colloidal products, seemingly without any purification, and applied them to a GCE pre-coated with a carbon black/Nafion® film. In the absence of any TEM micrographs of this carbon-supported catalyst, the distribution of the Nafion®-stabilised Pt particles on the support is unknown. The activities of the various Nafion®-stabilised catalysts towards oxygen reduction and methanol oxidation were measured and compared against commercial Pt-black and 20 wt % Pt/C (on Vulcan-XC72) catalysts from E-Tek. This study was the first to attempt to measure ORR activity of Nafion®-stabilised Pt electrocatalysts. The authors performed experiments in 1 M H<sub>2</sub>SO<sub>4</sub>, and also measured ORR activity in the presence of 0.5 M MeOH to assess the suitability of the catalyst for use on the DMFC cathode, where catalysts with a low activity towards methanol oxidation are desirable in order to reduce efficiency losses from methanol crossover. Their findings were reported as follows:

- In the absence of MeOH, there exists an inverse correlation between Nafion® content in the as-synthesised colloidal Pt and specific activity toward the ORR.
- The best ORR activity was found for the catalyst with the lowest Nafion® content (3.2 A.m<sup>-2</sup> at +0.7 V), and was similar to that found for a 20wt % E-Tek catalyst (3.1 A.m<sup>-2</sup> at +0.7 V).
- Nafion®-stabilised catalysts have a significantly lower activity toward MOR than the commercial Pt/C and Pt black catalysts.

However, examination of the RDE data shown in Figure 3.13, along with details of their experimental procedure, casts doubt on the accuracy of their results and the validity of their conclusions.

### 3 Review on PEMFC electrocatalysts

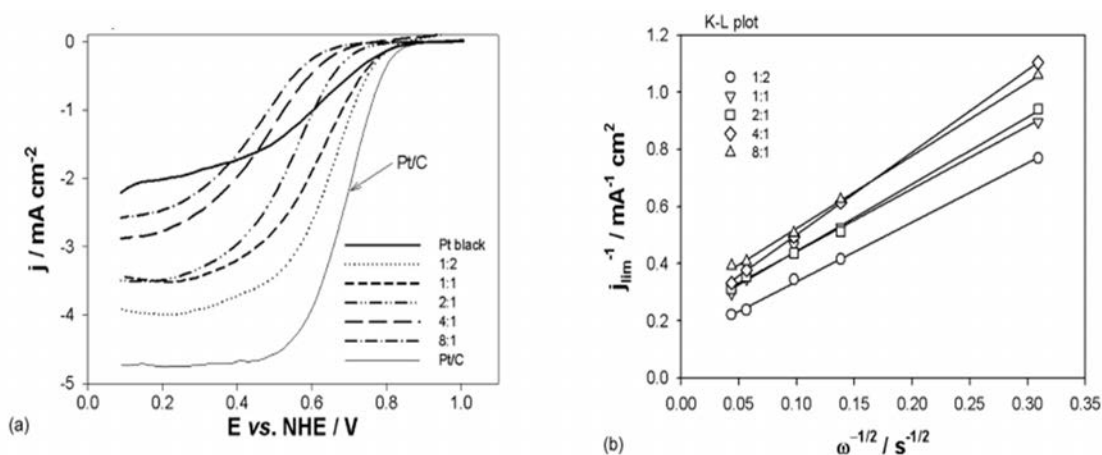


Figure 3.13: (a) RDE data recorded at  $5 \text{ mV}\cdot\text{s}^{-1}$  3000 RPM in  $\text{O}_2$ -purged  $1 \text{ M H}_2\text{SO}_4$  for Nafion®-stabilised colloidal Pt synthesised at different Nafion®:Pt ratios, compared against E-Tek 40 wt% Pt/C and Pt black; (b) Inverse Levich plots for the various catalysts, from limiting currents ( $J_{lim}$ ) recorded at  $E=+0.4 \text{ V}$ . Reproduced from [14].

- In Figure 3.13 (a), onset potentials and half-wave potentials for the ORR are much lower than should be expected, including those of the commercial catalyst. This is probably a result of poisoning of the catalyst by  $\text{Cl}^-$  from the Ag/AgCl reference electrode. Significant quantities of chloride will also remain in the as-prepared product following synthesis, which may explain the lower onset potentials observed for the Nafion®-stabilised catalysts.
- At 3000 RPM, the limiting current density according to the Levich equation should be  $-6.7 \text{ mA}\cdot\text{cm}^{-2}$ . The highest limiting current presented in Figure 3.13 (a) (for the E-Tek Pt/C catalyst) is  $\sim 4.8 \text{ mA}\cdot\text{cm}^{-2}$ , which is some 28% lower than expected, indicating that the quality of the catalyst film on the RDE is very poor, and in the case of the Nafion®-stabilised catalysts that the active Pt nanoparticles are not distributed evenly across the disc. This is probably due to the method used to prepare the working electrodes, whereby Nafion®-stabilised colloidal Pt was deposited onto a GC disc electrode pre-coated with carbon black.

The combination of these two problems means that quantification of kinetic currents from the RDE data is subject to significant error. Generally, the electrochemical characterisation in this work appears to have been carried out rather poorly, and therefore the results and conclusions are questionable.

#### 3.5.3 Cheng *et al* (2009)

A group from Wuhan University of Technology, China in collaboration with Oxford University improved upon the work described above by producing well-dispersed colloidal Pt nanoparticles stabilised by Nafion® [15]. In their work,  $\text{H}_2\text{PtCl}_6$  solution in 33/67 v/v ethanol/water was

refluxed at 90 °C and pH 8-10 in the presence of Nafion® dispersion, with a Nafion®:Pt mass ratio of 1:2.4, producing stable dispersions of well-dispersed colloidal Pt nanoparticles as shown in Figure 3.14 (A) and (C). A Vulcan XC-72 carbon black was then added to the as-prepared colloidal Pt to produce the supported catalyst shown in Figure 3.14 (D), which was then purified by filtration and washing. The authors refer to the supported catalyst as *Nafion®-Pt/C*, and this nomenclature will be adopted throughout this work.

The average particle size of the Nafion®-Pt colloid was calculated at 3.3 nm, and the authors claimed that the size could be controlled by varying the Nafion®:Pt ratio, although the results of this study are not presented in the paper.

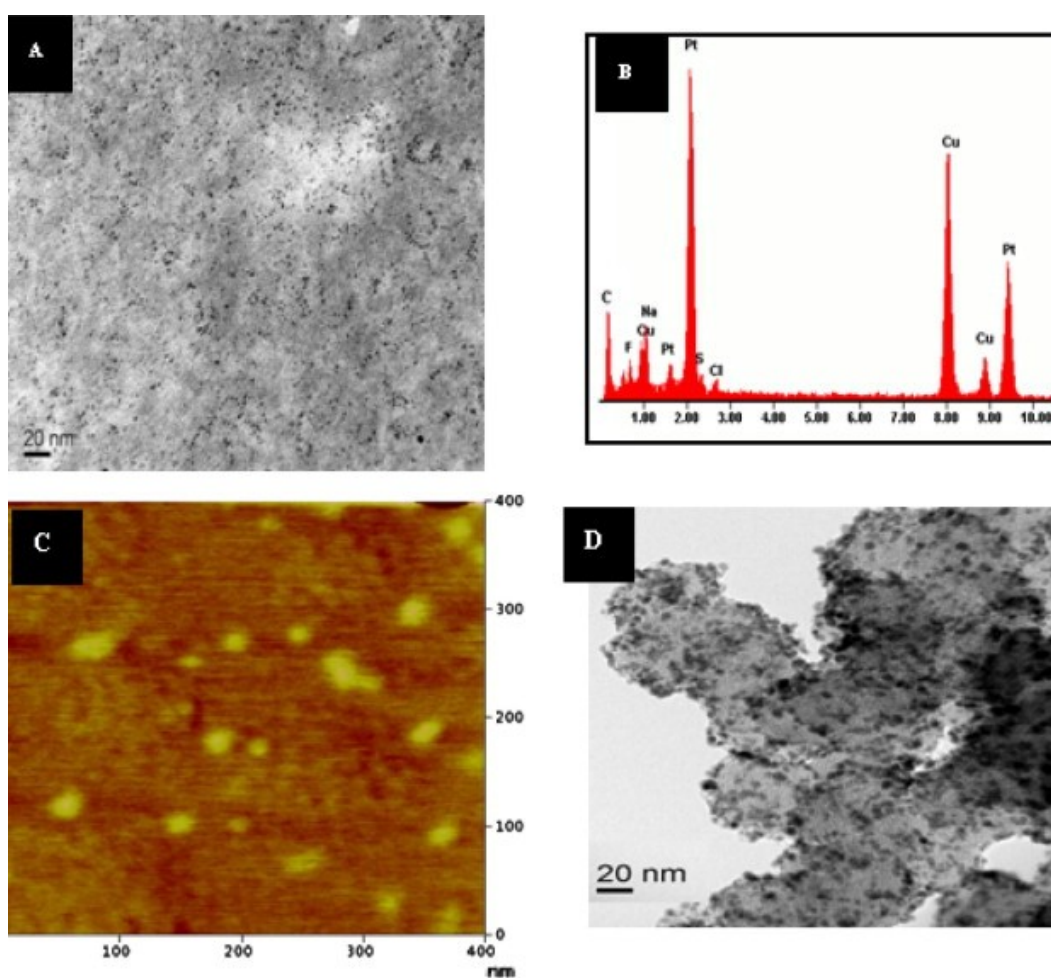


Figure 3.14: (A) TEM image, (B) energy dispersive X-ray spectrum and (C) atomic force microscope image of the Nafion®-stabilised Pt colloids deposited on mica surfaces, (D) TEM image of 40 wt % Nafion®-Pt/C catalyst. Reproduced from [15]

The authors measured ECSA using cyclic voltammetry (Figure 3.15 A), Whilst the ECSA of the Nafion®-Pt/C catalyst is not reported directly, it can be inferred from the results of their degradation study to be around  $67 \text{ m}^2 \cdot \text{g}^{-1}_{\text{Pt}}$  compared with around  $62 \text{ m}^2 \cdot \text{g}^{-1}_{\text{Pt}}$  for the commercial Pt/C. The fact that these are significantly lower than the physical surface areas of the catalysts

### 3 Review on PEMFC electrocatalysts

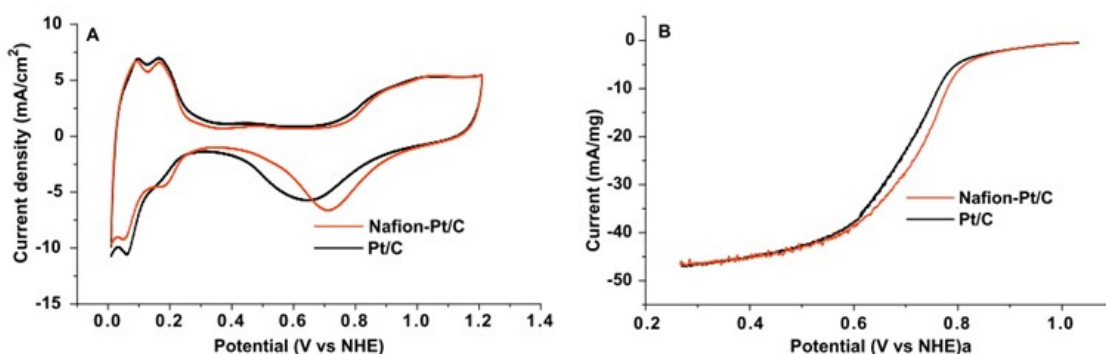


Figure 3.15: (A) Cyclic voltammograms for 40 wt % Nafion®-Pt/C and 40 wt % commercial Pt/C in 0.5 M H<sub>2</sub>SO<sub>4</sub> recorded at 50 mV.s<sup>-1</sup>; (B) RDE voltammograms for Nafion®-Pt/C and commercial Pt/C in O<sub>2</sub>-purged 0.5 M H<sub>2</sub>SO<sub>4</sub> at 25°C, 1600 RPM, sweep rate of 5 mV.s<sup>-1</sup>. Reproduced from [15].

(assumed to be 80-90 m<sup>2</sup>.g<sup>-1</sup><sub>Pt</sub> from the particle size information given in the paper) suggests problems with the working electrode preparation.

The authors proceeded to measure the ORR activity of their Nafion®-Pt/C catalyst using the thin-film RDE technique at 25°C in 0.5 M H<sub>2</sub>SO<sub>4</sub>. RDE voltammograms recorded at 5 mV/s and 1600 RPM are shown in Figure 3.15 (b), in which the Nafion®-Pt/C catalyst displays a significant increase in onset potential for ORR. The mass activity of the Nafion®-Pt/C catalyst at 0.8 V was reported as 6.35 A.g<sup>-1</sup>, which was significantly higher than that found for a commercial Pt/C catalyst (4.77 A.g<sup>-1</sup>). The authors do not specify which commercial catalyst they used, but this value seems rather low: even at +0.9 V, commercial Pt/C catalysts with particle size 2-3 nm have mass activities of the order of 50 A.g<sup>-1</sup> in 0.5 M H<sub>2</sub>SO<sub>4</sub>[22]. The authors do not state whether these activities are corrected for mass transport and ohmic resistance, and in fact it seems that they are raw data read from the LSV curves in Figure 3.15 (B). However, because the currents measured at 0.8 V are so low relative to the limiting current, the effect of such corrections would be minimal. It is possible that the electrolyte was contaminated with Cl<sup>-</sup> from the SCE reference electrode and/or that the catalyst loading on the working electrode was too high, such that the catalyst was not fully utilised.

Given that the mass activity of the baseline commercial Pt/C is so low, and in light of evidence of poor experimental procedures, the conclusion that Nafion®-Pt/C is inherently more active towards ORR is questionable. However, the authors do present some convincing results and conclusions regarding the enhanced durability of the Nafion®-Pt/C catalyst., which they measure relative to a commercial 40 wt % catalyst using an *ex-situ* AST technique in 0.5 M H<sub>2</sub>SO<sub>4</sub> at 25°C. Potential was cycled between +0.6 and + 1.2 V at 20 mV.s<sup>-1</sup>, and ECSA was measured at regular intervals. As shown in Figure 3.16, the Nafion®-Pt/C catalyst was significantly more durable than the commercial Pt/C. Losses of around 60% of initial ECSA were observed after 12300 cycles for the



Nafion®-Pt/C catalyst, compared to just 4500 cycles for the standard Pt/C catalyst. These losses were attributed to Pt particle growth, observed in post-mortem TEM analyses of the catalysts. The authors attributed the enhanced durability of the Nafion®-Pt/C catalyst to the stabilising effect of Nafion® surrounding Pt particles, which they suggested may inhibit migration and sintering. The pre- and post-AST Pt particle size distributions in Figure 3.16 (c) & (d) show that particle growth is certainly a major degradation pathway under this cycling regime, although the rather cathodic upper potential limit employed in this AST test means that carbon corrosion is also likely to have made a significant contribution to degradation. However, both catalysts use identical support materials (Vulcan XC-72), so differences in durability cannot be attributed to the carbon support and must originate instead with the precious metal component.

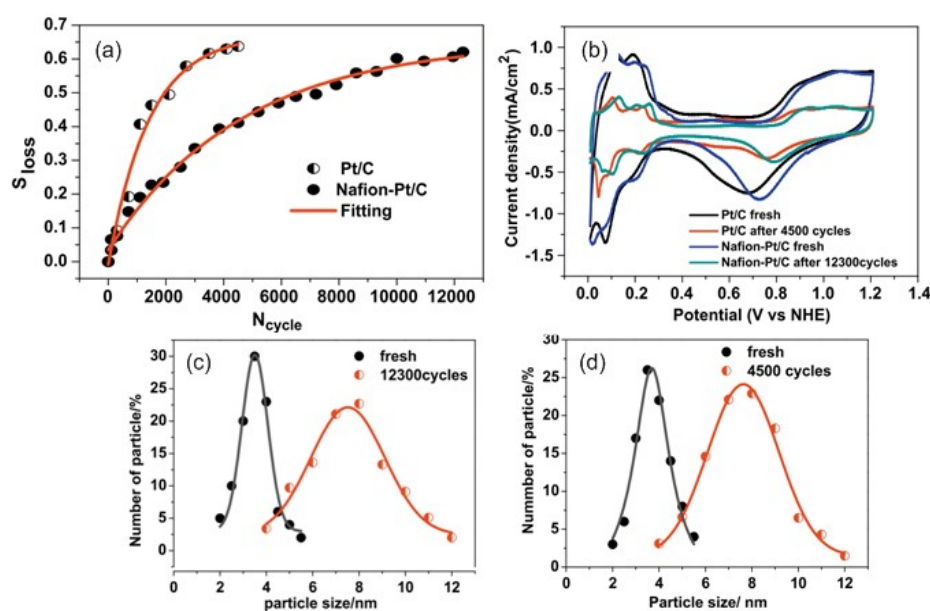


Figure 3.16: (a) ECSA losses for Nafion®-Pt/C and standard Pt/C as a function of the number of AST cycles ( $0.5 \text{ M H}_2\text{SO}_4$ ,  $25^\circ\text{C}$ ,  $+0.6$  to  $+1.2 \text{ V}$ ,  $20 \text{ mV}\cdot\text{s}^{-1}$ ); (b) pre- and post-AST cyclic voltammograms for Nafion®-Pt/C and standard Pt/C; and Pt particle size distributions for (c) Nafion®-Pt/C and (d) standard Pt/C catalysts, showing increases in particle size after 12300 cycles (Nafion®-Pt/C) and 4500 cycles (standard Pt/C).

### 3.5.4 Yin et al (2010)

Finally, and most recently, the same group that produced the 2009 work [15] applied the Nafion®-stabilised preparation route to the production of a Pt-based electrocatalyst supported on the conductive ceramic material titanium diboride ( $\text{TiB}_2$ ) [16], which offers improved corrosion resistance compared with carbon black [16]. The Nafion®-stabilised colloidal Pt was synthesised in a similar manner to the 2009 work. A solution of  $\text{H}_2\text{PtCl}_6$  in 50/50 v/v ethanol/water was refluxed at  $80^\circ\text{C}$  and pH 9 in the presence of Nafion® dispersion at a Nafion®:Pt ratio of 1.7:1. The schematic in Figure 3.17 (A) illustrates the proposed action of Nafion® in stabilising the

### 3 Review on PEMFC electrocatalysts

colloidal Pt, and the persistence of a capping layer of Nafion® around the Pt particles following addition of the TiB<sub>2</sub> support.

From the TEM image in Figure 3.17 (B), the colloidal Pt particles were found to have an average particle size of ~1.5 nm, but in subsequent Scherrer analysis of XRD data from the Nafion®-Pt/TiB<sub>2</sub> supported catalyst, the average Pt particle size was found to be 3.4 nm. The authors do not comment on this discrepancy, but it seems that some Pt particle growth takes place during preparation of the supported catalyst.

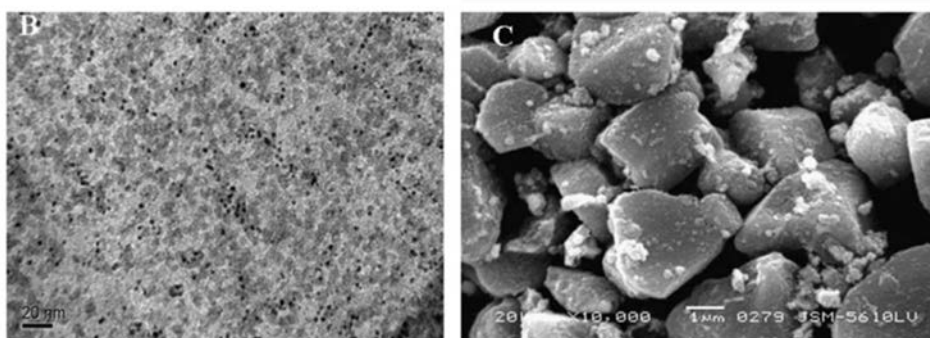
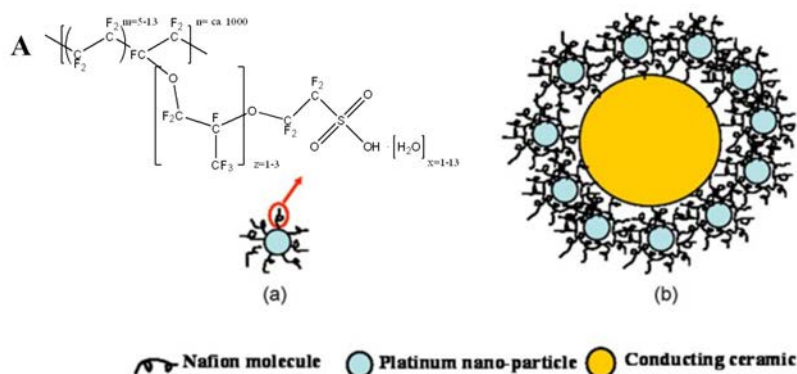


Figure 3.17: (A) Schematic of the Pt colloid particles and the Pt/TiB<sub>2</sub> catalysts with Nafion® acting as a stabiliser ; (B) TEM image of the Pt colloid particles and (C) SEM micrograph of TiB<sub>2</sub> powders .  
Reproduced from [16] .

The ORR activity and durability of the catalyst were measured using RDE experiments to determine the ORR activity of their Nafion®-Pt/TiB<sub>2</sub> electrocatalyst. The limiting current densities in Figure 3.18 give an indication of working electrode film quality, and that of the Nafion®-Pt/TiB<sub>2</sub> catalyst (~ -4.6 mA.cm<sup>-2</sup>) is significantly lower than the theoretical value of -6.2 mA.cm<sup>-2</sup> predicted by the Levich equation, suggesting that the electrode was poorly prepared. The authors present the upwards shift in onset potential for the Nafion®-Pt/TiB<sub>2</sub> catalyst as evidence of enhanced ORR activity, and report specific activities at +0.9 V of 2.9 and 1.1 A.m<sup>-2</sup> for the Nafion®-Pt/TiB<sub>2</sub> and Pt/C catalysts respectively. In common with their previous work, it is unclear whether these values are mass-transport and ohmic-drop corrected, and it appears that they are incorrectly normalised by *geometric* surface area instead of ECSA so that they fail to account for differences in particle size and utilisation between the two catalysts. The Nafion®-Pt/TiB<sub>2</sub>

catalyst has an ECSA of just  $34.7 \text{ m}^2 \cdot \text{g}^{-1}_{\text{Pt}}$  compared to  $61.4 \text{ m}^2 \cdot \text{g}^{-1}_{\text{Pt}}$  for the commercial Pt/C, so proper normalisation of this data would suggest that the specific activity of Nafion®-Pt/TiB<sub>2</sub> is increased by some 4.7 x relative to Pt/C (assuming the same Pt loading on both electrodes). Mass activities are not reported and cannot be calculated or inferred from data given in the paper. The authors attribute the apparent increase in specific activity to a favourable interaction between Pt and the TiB<sub>2</sub> substrate, which is supported by previous work on similar materials in which metal-support interactions were found to facilitate electron transfer for the ORR[112-113]. Thus it is not possible to isolate any effect of surface-adsorbed Nafion® on ORR kinetics.

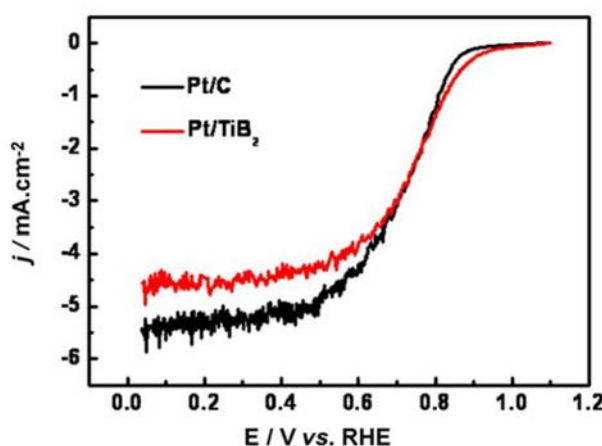


Figure 3.18: RDE voltammograms for Nafion®-Pt/TiB<sub>2</sub> and commercial Pt/C catalysts recorded in O<sub>2</sub>-saturated 0.5M H<sub>2</sub>SO<sub>4</sub> at 25°C, 1600 rpm. Reproduced from [17]

The main focus of the Yin *et al* study was to investigate the durability of their TiB<sub>2</sub>-supported electrocatalysts, with the ORR activity being of secondary importance. The authors employed the same AST protocol reported in [15] to evaluate the durability of their Pt/TiB<sub>2</sub> electrocatalyst derived from Nafion®-stabilised colloidal Pt. ECSA was measured at several intervals up to 6000 potential cycles to produce the degradation curves shown in Figure 3.19 (a). The Nafion®-stabilised Pt/TiB<sub>2</sub> catalyst was found to have significantly better durability under this AST regime than a commercial Pt/C catalyst (20 wt % on Vulcan XC-72, HiSpec, JM). The authors attributed the enhanced durability of the Nafion®-Pt/TiB<sub>2</sub> catalyst to the superior corrosion resistance of the TiB<sub>2</sub> support, as well as inhibition of particle migration and sintering by a mediating layer of Nafion®. The wide potential window employed in this AST test means that it activates both carbon corrosion and Pt migration/dissolution processes, meaning that contributions to degradation from each of these mechanisms cannot be individually resolved. Furthermore, differences in the strength of the Pt-support interaction between the two catalysts may also account for some of the variation in durability. However, comparison of Figure 3.16 (a) and Figure 3.19 (a) reveals that the Nafion®-Pt/C and Nafion®-Pt/TiB<sub>2</sub> catalysts display rather similar degradation behaviour,

### 3 Review on PEMFC electrocatalysts

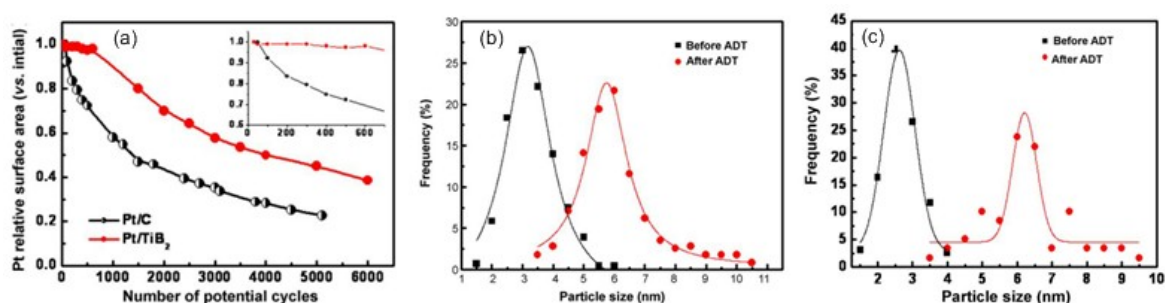


Figure 3.19: (a) Comparison of catalyst durability Pt/TiB<sub>2</sub> vs Pt/C during AST testing (cyclic voltammetry +0.6 to +1.2 V, 20mV.s<sup>-1</sup>, 0.5 M H<sub>2</sub>SO<sub>4</sub> 25°C); pre- and post-AST particle size distributions for (b) Pt/TiB<sub>2</sub> catalyst and (c) Pt/C catalyst

suggesting that their enhanced durability properties are related to the Nafion®-stabilised Pt component, rather than any aspect of the support material.

Generally, then, where catalysts have been derived from Nafion®-stabilised colloidal nanoparticles in the past, they have exhibited enhanced durability with respect to commercial catalysts prepared *via* standard routes.

| Ref  | Nafion®:Pt mass | Particle size / nm | SA [A.m <sup>-2</sup> ] | MA [A.g <sup>-1</sup> ] | Conditions   |
|------|-----------------|--------------------|-------------------------|-------------------------|--|
| [14] | 1 : 2           | 4.3                | 3.2 @ 0.7 V             | 57                      | 1M H <sub>2</sub> SO <sub>4</sub><br>25°C<br>5mV/s     |
|      | 1 : 1           | 2.8                | 1.5                     | 27                      |  |
|      | 2 : 1           | 2.7                | 0.4                     | 7                       |  |
|      | 4 : 1           | 3                  | 0.2                     | 3.6                     |  |
|      | 8 : 1           | 3.2                | 0.1                     | 1.8                     |  |
| [15] | 1 : 2.4         | 3.3                | 0.1*                    | 6.35 @ 0.8 V            | 0.5M H <sub>2</sub> SO <sub>4</sub><br>25°C<br>5mV/s   |
| [16] | 1.7 : 1         | 1.5                | 2.9 @ 0.9 V             | Not available           | 0.5M H <sub>2</sub> SO <sub>4</sub><br>25°C<br>20 mV/s |

Table 3.4: Summary of ORR activities reported in previous works for Nafion®-stabilised Pt electrocatalysts. \* indicates estimated values based on ECSA.

---

### 3.5.5 Summary and implications for this work

#### Synthesis of Nafion®-stabilised Pt/C catalysts

The synthetic methods and resulting product morphologies from all four of the studies reviewed above are summarised in Table 3.5.

| Ref  | Solvent<br>(% alcohol/H <sub>2</sub> O) | Reaction<br>conditions | Nafion®:Pt<br>mass | Particle size /<br>nm | Morphology                |
|------|---|------------------------|--------------------|-----------------------|---------------------------|
| [13] | MeOH (15/85)                            | 70 °C, pH 11           | 10 : 1 (Pt+Ru)     | 3-4                   | Well-dispersed<br>Pt-Ru/C |
|      | MeOH (25/75)                            | 70 °C, pH 11           | 10 : 1 (Pt+Ru)     | 3-15                  | Well-dispersed<br>Pt-Ru/C |
| [14] | EtOH (40/60)                            | 82 °C, pH 8.5          | 1 : 2*             | 4.3                   | Agglomerated              |
|      | EtOH (40/60)                            | 82 °C, pH 8.5          | 1 : 1*             | 2.8                   | Agglomerated              |
|      | EtOH (40/60)                            | 82 °C, pH 8.5          | 2 : 1*             | 2.7                   | Agglomerated              |
|      | EtOH (40/60)                            | 82 °C, pH 8.5          | 4 : 1*             | 3                     | Agglomerated              |
|      | EtOH (40/60)                            | 82 °C, pH 8.5          | 8 : 1*             | 3.2                   | Agglomerated              |
|      | EtOH (40/60)                            | 75 °C, pH 8.5          | 2 : 1*             | 3.2                   | Agglomerated              |
|      | EtOH (40/60)                            | 65 °C, pH 8.5          | 2 : 1*             | 4.4                   | Agglomerated              |
| [15] | EtOH (33/67)                            | 90 [114]C, pH 8-10     | 1 : 2.4            | 3.3                   | Well-dispersed            |
| [16] | EtOH (50/50)                            | 80 °C, pH 9            | 1.7 : 1            | 1.5                   | Well-dispersed            |

Table 3.5: Summary of reaction conditions and Nafion®-Pt product morphologies for the studies reviewed above. \* 'molar' ratios as reported in [14].

The original approach employed by Sarma *et al* [13] is of limited relevance to this work, as the presence of the carbon support during the reduction step raises the possibility that Pt particles may be deposited within carbon micropores, isolated from the ionomer network. Nevertheless it is encouraging that the presence of Nafion® led to a decrease in particle size.

Of all the studies, only the final two by Cheng *et al* [15] and Yin *et al* [16] can be regarded as successful in the synthesis of well-dispersed Nafion®-stabilised colloidal Pt nanoparticles. Interestingly, the reaction conditions employed by Cheng [15] and Yin [16] are very similar to those used by Liu *et al* [14], but there are dramatic differences in morphology between the former and the latter. It is possible that the agglomerated morphologies observed by Liu *et al* [14] are simply an artefact of poor TEM specimen preparation.

The use of the alcohol reduction method in all of these studies is somewhat controversial, given that the method must be performed at high pH by addition of NaOH, and at ~80°C. It is well known that treatment of Nafion® with aqueous NaOH at high temperatures leads to conversion of

### 3 Review on PEMFC electrocatalysts

---

Nafion® to the Na<sup>+</sup> form [115], which has significantly lower proton conductivity than the protonated H<sup>+</sup> form[116]. In order to maintain proton conductivity in catalysts and catalyst layers derived from Nafion®-stabilised Pt, a low temperature synthetic procedure that can be performed at low pH would be preferable, and the development of such a method will be a primary objective of this research.

#### Electrochemical characteristic of Nafion®-stabilised catalysts

None of the previous studies on Nafion®-stabilised electrocatalysts present convincing, conclusive results for ORR activity. The variability in reported SA and MA values for commercial Pt/C catalysts shown in Table 3.2 (page 42) is testament to the difficulty of achieving accurate, reproducible measurements of absolute ORR activity with the RDE technique, and reinforces the need to validate all experimental procedures on well-characterised materials prior to testing novel electrocatalysts. Of the results presented in Table 3.2, only those from refs [109] and [108] can be considered to be reliable benchmarks for ORR activity, as the others fail to meet one or more of the following criteria, which define successful RDE experiments and analyses:

- For determination of absolute ORR activity, a non-adsorbing electrolyte (HClO<sub>4</sub>) should be used.
- ECSA should be within ~ 10% of the physical surface area of the catalyst as determined by TEM measurements i.e. catalyst utilisation of > 90% [12].
- Limiting current densities  $J_{lim}$  in ORR voltammograms on the RDE should be within 10% of the theoretical value predicted by the Levich equation for a given rotation rate and temperature[107].
- Background currents should be eliminated from the ORR data by subtracting voltammograms recorded under N<sub>2</sub> purge[108].
- Corrections to raw I-E data should be made for the ohmic resistance of the electrolyte[117].

# 4 Preparation of Nafion®-Pt/C electrocatalysts

This chapter describes the preparation of electrocatalysts derived from Nafion®-stabilised colloidal Pt nanoparticles. The aim of this work is to direct the formation of the Nafion®-Pt interface to create a more efficient percolation of ionomer within the PEMFC catalyst layer, thereby improving catalyst utilisation as described in the previous chapter.

## 4.1 Aims and Objectives

Considering the previous work described in section 3.5, the aims and objectives of this part of the study are as follows:

- To synthesise **stable, colloidal dispersions of Pt nanoparticles stabilised by Nafion® ionomer**. Reaction conditions such as solvent, reducing agent, temperature, pH and Nafion®:Pt ratio will be optimised such that as-synthesised colloidal Pt particles are:
  - **well-dispersed** (not agglomerated),
  - of **controllable size** in the range 1-20 nm,
  - and have a **narrow size distribution**  $\pm 5$  nm.
- To produce **Nafion®-Pt/C supported electrocatalysts** and catalyst inks from the colloidal Pt, ensuring that:
  - the **Nafion® content** in the ink is suitable for the preparation of GDEs and thin-film catalysed RDEs, i.e. **10 wt % < NFP < 40 wt %**;
  - the Pt particles are **well-dispersed on the carbon support**;
  - the **Pt and Nafion® content** in the catalyst ink can be precisely determined to an accuracy of 5%.

## 4.2 Methods & Materials

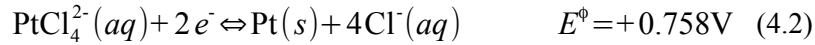
### 4.2.1 Synthesis of platinum nanoparticles

A **colloidal route** was chosen for the preparation of Pt nanoparticles on the basis that the method allows the Pt-Nafion® interface to be established prior to addition of the carbon support via stabilisation of colloidal Pt nanoparticles using Nafion® ionomer. Additionally, the colloidal route allows good control over the composition and morphology of the resulting particles; can be

---

easily adapted for different metals at a later date and is supported by a wealth of previous studies in the literature.

The general reaction scheme involves the chemical reduction in aqueous solution of a precursor containing platinum in its +2 or +4 oxidation state.



As mentioned previously, the aim is to produce a stable colloid consisting of well dispersed particles with a narrow size distribution.

### **Theory of precipitation reactions**

During the forward reaction in (4.2) the solvated  $\text{Pt}^{2+}$  cation is reduced, producing a sparingly soluble product ( $\text{Pt}^0$ ). If the rate of the forward reaction is significant then the solution will quickly become supersaturated, and precipitation of  $\text{Pt}(\text{s})$  will occur.

The formation of colloidal nanoparticles via precipitation reactions involves nucleation, growth and agglomeration processes, which in combination determine the morphology of the product.

#### **Nucleation**

For the equilibrium in (4.2), the degree of supersaturation,  $S$ , is given by  $S = \frac{C}{C_0}$  where  $C$  and  $C_0$  are the concentration and solubility of monatomic  $\text{Pt}^0$ , respectively.

Nucleation occurs as a result of random, localised fluctuations in  $\text{Pt}(\text{s})$  concentration. In a supersaturated solution, there exists an equilibrium critical radius,  $r^*$

$$r^* = \left( \frac{2\sigma_{SL}vC_\infty}{k_B T \ln(S)} \right) \left( \frac{1}{C - C_0} \right) \quad (4.3)$$

where  $\sigma_{SL}$  is the solid-liquid interfacial tension [ $\text{J}\cdot\text{m}^{-2}$ ],  $v$  is the atomic volume of  $\text{Pt}(\text{s})$  present [ $\text{m}^3\cdot\text{mol}^{-1}$ ],  $C_\infty$  is the bulk solute concentration,  $k_B$  is the Boltzmann constant and  $T$  is the temperature [118]. Nuclei formed in solution with radius  $r > r^*$  will continue to grow, whilst those with  $r < r^*$  will re-dissolve. As shown in Figure 4.1 (a), the critical nucleation radius is highly dependent on the level of supersaturation,  $S$  [18]. Hence the minimum size of particles formed in a precipitation reaction, is governed by solubility and concentration, but also by temperature and interfacial tension.



## 4 Preparation of Nafion®-Pt/C electrocatalysts

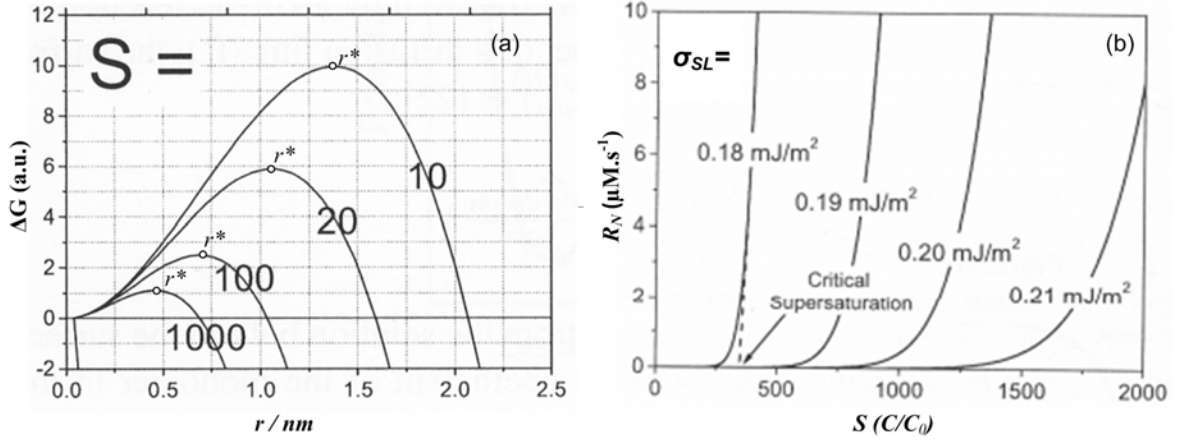


Figure 4.1: (a) Theoretical plot based on equation (4.4) illustrating the variation of overall Gibbs free energy with nucleus radius at a fixed interfacial tension  $\sigma_{SL}=0.2$  J.m<sup>-2</sup> and  $T=500$  K, showing critical nucleation radii  $r^*$  at  $S=10,20,100$  and  $1000$ ; (b) the rate of nucleation vs. supersaturation  $S$  as given by equation (4.6), for various values of the interfacial tension  $\sigma_{SL}$ . Reproduced from [18].

The rate at which nucleation events occur is dependent on the activation energy for cluster formation,  $\Delta G^*$ , given by:

$$\Delta G^* = \frac{4}{3} \pi \sigma_{SL} r^{*2} = \frac{16 \pi \sigma_{SL}^3 v^2}{3 k_B^2 T^2 \ln^2(S)} \quad (4.4)$$

Application of the Arrhenius law gives the rate of homogeneous nucleation,  $R_N$  as

$$R_N = A \exp \left[ \frac{-(\Delta G^*)}{k_B T} \right] \quad (4.5)$$

where  $N$  is the number of nuclei formed per unit time per unit volume,  $V$ ;  $A$  is a pre-exponential factor usually of the order  $\sim 10^{25} - 10^{56}$  s<sup>-1</sup>.m<sup>-3</sup> [119].

Combining (4.4) and (4.1) gives

$$R_N = A \exp \left[ \frac{-16 \pi \sigma_{SL}^3 v^2}{3 k_B^3 T^3 \ln^2(S)} \right] \quad (4.6)$$

From (4.6) we can infer that the rate of nucleation remains negligible until a certain degree of supersaturation,  $S=S^*$  is reached, at which point  $R_N$  increases dramatically as shown in Figure 4.1 (b). For the equilibrium in (4.2), the degree of supersaturation by Pt(s) is determined by the concentration and rate of addition of the precursor and/or reducing agent, and the kinetics of the reduction reaction. Practically, therefore these parameters can offer a degree of control over the nucleation process.

---

## **Growth**

Once stable nuclei ( $r > r^*$ ) are present in solution, they will usually undergo diffusion-controlled growth as monatomic Pt(s) arrives or is formed at the nuclei surfaces. Concentration gradients and temperature preside over the growth process. In the case of a typical diffusion-controlled growth process, and assuming an infinitely-thick diffusion layer around each particle, the rate of growth is given by

$$\frac{dr}{dt} = \frac{2\sigma_{SL} D v^2 C_\infty}{r R T} \left( \frac{1}{r^*} - \frac{1}{r} \right) \quad (4.7)$$

where  $r$  is the particle radius,  $C_\infty$  is the bulk concentration of the solute (assumed constant) and  $R$  is the gas constant. Thus the growth rate is directly proportional to the diffusion coefficient of the solute,  $D$  and inversely proportional to temperature  $T$  [120].

## **Ostwald Ripening**

In addition to diffusion-limited growth, the average particle size also increases via Ostwald ripening; a complex phenomenon during which smaller particles are essentially consumed by larger ones. A mathematical model for this process is given by LSW theory[121], whose main principles are as follows:

1. For a diffusion-limited process, the average particle radius,  $\bar{r}$  is dependent on the cube root of time, as[122]

$$\bar{r}(t) = \sqrt[3]{Kt} \quad (4.8)$$

where  $K = \frac{4}{9} \alpha D$  and  $\alpha$  is a constant.

2. During ripening, the number density of particles,  $N$ , decays as[122]

$$N(t) = \frac{0.22 Q_0}{\bar{r}(t)^2} = \frac{0.22}{2D\alpha t} \quad (4.9)$$

where  $Q_0$  is the total initial supersaturation. During ripening, the number of particles is therefore inversely proportional to ripening time.

3. The size distribution of particles undergoing ripening evolves as

$$f(r, t) = \left[ \frac{N(t)}{\bar{r}(t)} \right] p_0(\rho(t)) \quad (4.10)$$

where  $\rho(t) \equiv r/\bar{r}(t)$  and  $p_0(\rho)$  is a time-independent function of particle size.

## 4 Preparation of Nafion®-Pt/C electrocatalysts

### Conditions for monodispersity

From equations (4.3) to (4.8) we can infer that, for the synthesis of a colloidal dispersion of monodisperse nanocrystals:

The processes of nucleation and growth must be separated in time – that is, the two should not be allowed to occur simultaneously.

The nucleation process must be relatively fast, whilst growth & ripening occur relatively slowly.

All nuclei should form simultaneously, without any subsequent nucleation once growth begins, in order to maintain a narrow size distribution.

### Colloidal stabilisers

Following kinetically- and diffusion-controlled nucleation and growth of colloidal nanoparticles, there is a tendency towards agglomeration due to interparticle attraction and thermodynamically-driven minimisation of surface interfacial energy. The agglomeration process can be inhibited by introduction of a stabiliser, which attaches to particle surfaces and prevents contact between them. Stabilisers generally operate either by *steric* or *electrostatic* repulsion, or in some cases a combination of the two.

#### Steric stabilisation

Steric stabilisation is achieved through attachment of bulky ligands to the particle surface to prevent particle-particle contact. Polymers are commonly employed, e.g. poly(vinylpyrrolidone) (PVP), which forms dative covalent bonds with the surface of metal particles via carbonyl groups [19] as shown in Figure 4.2.

There is some concern that surface-adsorbed species may impair catalytic performance by blocking active sites. In previous studies, hydrogenations catalysts derived from PVP-stabilised colloidal Pt have demonstrated good performance[123], but for thorough evaluation of catalytic activity it is often necessary to remove the capping polymer from the surface of the particles[124].

#### Electrostatic stabilisation

The attachment of charged ligands to colloidal particles allows stabilisation via electrostatic repulsion. Citrates have been used in numerous previous works to prepare very stable colloidal Au

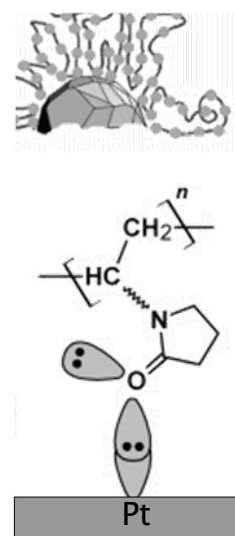


Figure 4.2: Schematic showing the proposed stabilisation mechanism for PVP. Reproduced from [19]

---

[125] and Pt nanoparticles [126-128]. The stability and morphology of electrostatically stabilised colloids are influenced by pH and the presence of other ionic species [125, 129].

### **Mechanism of colloidal stabilisation by Nafion® ionomer dispersion**

Nafion® has been found to adsorb onto metallic Pt surfaces by coordination of  $\text{SO}_3^-$  groups with Pt [85]. Therefore it is proposed that it may offer similar steric stabilising properties as PVP toward colloidal Pt. Additionally the presence of charged sulfonate moieties may provide a degree of electrostatic stabilisation, akin to that offered by citrate ions.

It is further proposed that stabilisation using Nafion® may result in catalysts with improved 3-phase contact (carbon-Nafion®-Pt) and therefore improved Pt utilisation, as well as a potentially simpler route for the preparation of colloiddally-derived PEMFC catalysts. Because it forms an active component of the catalyst layer, the removal of capping Nafion® from the Pt surface is unnecessary – even undesirable.

This study employs 10 wt % Nafion® dispersion ( $\text{H}^+$  form, equivalent weight  $E_w \sim 1,100$ ) in a mixture of water and lower aliphatic alcohols from Ion Power.

### **Borohydride reduction**

Sodium borohydride in aqueous solution was chosen as the reducing agent for this work. The use of this reagent for the synthesis of metallic nanoparticles has been previously documented [130-132] and provides a straightforward, low-cost method for the reduction of the Pt precursor at room temperature in aqueous solution. Additionally, based on the strategy developed in 4.2.1, the fast reduction kinetics offered by borohydride are expected to increase the nucleation rate and lower the average particle size of the colloidal product compared with previous work, which employed weakly-reducing ethanol for this purpose.

The overall reaction scheme is as follows:

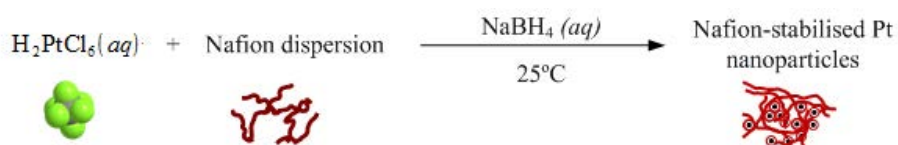


Figure 4.3: Reaction scheme for the synthesis of Nafion®-stabilised colloidal Pt using  $\text{NaBH}_4$

**Experimental procedure** All glassware was cleaned with aqua regia before use, and rinsed using UHQ water (Millipore). In a typical experiment, the chloroplatinic acid precursor (99.995% trace metals basis, Sigma) was prepared as a solution ( $\sim 20$  mM) in UHQ water. Nafion® dispersion (10 wt % in water/ethanol, Ion Power) was added in the required ratio to a 10 ml aliquot of the precursor and stirred at around 600 rpm for at least 30min. Meanwhile, an aqueous solution

## 4 Preparation of Nafion®-Pt/C electrocatalysts

---

of 0.05 M NaBH<sub>4</sub> (AR, Sigma) was prepared and an aliquot of this containing a four-fold molar excess of BH<sub>4</sub><sup>-</sup> was infused into the Pt precursor mixture through a PTFE tube at a rate of 48.5 ml.min<sup>-1</sup> using a syringe pump.

Once the reaction was complete, a few drops of 1 M HCl were added to quench any excess borohydride. Reaction products are stored in foil-wrapped vials to eliminate the effects of any UV sensitivity.

### 4.2.2 Preparation of supported catalysts

Prior to electrochemical characterisation, the Pt nanoparticles must be deposited on a carbon support, the purpose of which is: i) to provide a substrate for the even dispersion of active catalyst particles, ii) to impart electrical conductivity to the catalyst layer and iii) to provide a 'scaffold' for the porous structure of the catalyst layer. Vulcan XC-72 R carbon black (Fuel Cell Store) was dispersed in an 80/20 v/v mixture of water and isopropanol at a concentration of 2 mg.ml<sup>-1</sup>, then sonicated in an ultrasonic bath for 1 hour to produce a uniform, stable dispersion free from coarse agglomerates.

**Two preparation routes: 'A' and 'B'** The carbon support could be added either before purification (route 'B') or after purification (route 'A') of colloidal Pt described in section 4.2.3 . The effect of each of these preparation routes on Pt particle morphology was investigated, and is discussed later in section 4.3.2 . In either case, an aliquot of the Vulcan dispersion was added to the colloidal Pt under sonication to achieve the desired Pt/C ratio. Catalysts containing both 20 wt % and 50 wt % Pt were prepared by adjusting the quantity of carbon dispersion added.

TEM imaging was used to confirm adherence of Pt nanoparticles to the carbon support, and check for the presence of free particles remaining in solution.

### 4.2.3 Purification

The *as-synthesised* product of the reduction reaction contains soluble by-products including chloride and borate salts as well as a large excess of Nafion® ionomer dispersion. Chloride ions especially can have a detrimental effect on the electrocatalytic performance of a PEMFC catalyst, so it is desirable to remove them from the product prior to use in an electrochemical context. Furthermore, a supported catalyst prepared from the as-synthesised colloidal Pt would contain over 90 wt % Nafion®, which would produce a catalyst layer with very little pore space for reactant transport, so it is necessary to reduce the ionomer content to between 10 – 40 wt % typically employed in practical catalyst layers.

---

**Purification of colloidal Pt and Pt/C** Application of conventional filtration and washing is impossible due to the size of the particles present. Therefore a repeated centrifugation/redispersion procedure is the most viable route for purification. Acetone was added to the as-synthesised colloidal Pt or supported Pt/C in the ratio 1:1 v/v. The addition of acetone was found to be necessary in order to initiate precipitation. These dispersions were then centrifuged for 1 hour at 20,000 RPM ( $33,987 \times g$ ) and 4°C in a Sigma 3K30 refrigerated centrifuge. The supernatant containing soluble impurities and excess ionomer was discarded, and the precipitate re-dispersed in 50/50 (v/v) UHQ water and acetone. The process was repeated four times.

**Preparation of catalyst inks** Following the final centrifugation step, instead of 50/50 v/v water/acetone, the precipitate was re-dispersed under sonication in 80/20 v/v water/isopropanol. A minimal volume of dispersant was used (typically 1-2 ml), in order to maximise the concentration of solids (Pt, Nafion®, carbon)

#### **4.2.4 Determination of Pt and Nafion® content**

Preparation of the working electrodes and gas diffusion electrodes with well-defined Pt and Nafion® loadings requires knowledge of the Pt and Nafion® concentrations in the ink (mg/ml). Known volumes of catalyst ink were added to aluminium oxide crucibles, then dried in a vacuum oven overnight at 60°C, -900 mbar.g prior to thermogravimetric analysis (TGA) to determine Pt and Nafion® contents in [mg.ml<sup>-1</sup>] – see section 4.2.5 (page 68).

#### **4.2.5 Physical characterisation of platinum nanoparticles**

A range of techniques are required to build a detailed description of the physical nature of the catalyst, summarised in a non-exhaustive list in Table 4.1.

## 4 Preparation of Nafion®-Pt/C electrocatalysts

| Instrument/Technique                             |  | Quantities measured  |
|--|--|--|
| Transmission Electron Microscopy (TEM)           | Low magnification imaging                        | Particle size distribution, dispersion                       |
|  | High-resolution imaging (HRTEM)                  | Particle shape, crystalline structure                        |
|  | Energy-Dispersive X-ray Spectroscopy (EDS)/(EDX) | Composition, segregation                                     |
|  | Selected-Area Electron Diffraction (SAED)        | Crystalline structure  |
| Dynamic Light Scattering (DLS)                   |  | Particle size distribution                                   |
| X-Ray Diffraction (XRD)                          |  | Crystal structure, lattice parameters                        |
| Thermogravimetric Analysis (TGA)                 |  | Composition and ink concentrations of Pt, Nafion® and carbon |
| X-Ray Fluorescence Spectroscopy (XRF)            |  | Elemental composition  |
| X-Ray Photoelectron Spectroscopy (XPS)           |  | Composition, oxidation state                                 |
| Mass Spectrometry                                |  | Composition  |
| Atomic Emission Spectroscopy (AES)               |  | Composition  |
| Nuclear Magnetic Resonance Spectroscopy (NMR)    |  | Structure and composition of organic ligands                 |
| UV-Visible / Infrared Spectroscopy (UV-Vis/FTIR) |  | Composition  |

Table 4.1 : Physical characterisation techniques for nanoparticles and supported catalysts.

In this study, characterisation was performed using low-mag TEM, HRTEM, EDX, DLS and TGA.

### **Transmission Electron Microscopy (TEM)**

**Specimen preparation** A drop of the sample (as-synthesised colloidal Pt or Pt/C dispersed in water/ethanol) was placed onto a formvar-coated carbon-on-copper TEM specimen grid (300 mesh, Agar Scientific). The specimen was dried at 40°C in a vacuum oven, then cooled to room temperature in a dessicator and stored in a sealed container.

**Low-magnification** bright-field imaging was performed using a JEOL 1200ex LaB<sub>6</sub> TEM at an accelerating voltage of 80kV.

From the resulting micrographs, particle size distributions were calculated using the graphical analysis software *ImageJ* [133]. Using the method outlined in the appendix, the software

---

computes the area of each identifiable particle in the image. These areas were converted to diameters by assuming that particles are spherical and in 2D projection.

**High-resolution** images were recorded using a FEI Tecnai F20 Field-Emission TEM operating at 200kV.

**EDX** was performed using the FEI Tecnai F20 TEM at 200kV and an Oxford ISIS X-ray detector.

### **Dynamic Light Scattering (DLS)**

As its name suggests DLS is a light-scattering technique in which the intensity of laser light scattered by particles undergoing Brownian motion is used to determine their size distribution. The equipment employs a correlator to determine the autocorrelation function of the recorded intensity of scattered light, from which the diffusion constant(s) of the particles can be determined provided that the refractive index,  $n$  of the dispersant is known. The hydrodynamic radii of the light-scattering particles can then be calculated using the Stokes-Einstein equation:

$$D = \frac{k_B T}{6\pi\eta\bar{r}} \quad (4.11)$$

where  $D$  is the diffusion constant,  $\eta$  is the viscosity of the dispersant and  $\bar{r}$  is the particle hydrodynamic radius.

The success and accuracy of the technique therefore depends on a prior knowledge of the viscosity and refractive index of the dispersant, which may not be straightforward in the case of binary solvents or when stabilisers are present in solution.

Further, the radius reported is that of a sphere with equivalent hydrodynamic radius to that determined by equation (4.11), and therefore may not represent the true dimensions of a rough or faceted particle, one that is highly anisotropic, or one that is surrounded by bulky surfactant molecules. Despite these complexities, the technique involves far less preparation than the TEM technique and is useful for quickly comparing size distributions for samples prepared under similar conditions and with similar compositions.

### **Thermogravimetric Analysis (TGA)**

In its most basic application, TGA involves the measurement of mass change of a sample due to thermal oxidation or decomposition as it is heated according to a predetermined temperature programme. The gaseous atmosphere around the sample can be controlled to create an oxidative, inert or reductive chemical environment as required. In this work, TGA will be employed to



## 4 Preparation of Nafion®-Pt/C electrocatalysts

measure the composition of catalysts and catalyst layers at various stages of purification. Baturina *et al* investigated the thermal stability of PEMFC catalysts and catalyst layer materials using TGA[20]. As shown in Figure 4.4 (a), they found that the Vulcan XC72 support underwent thermal oxidation at approximately 600 °C, and that the onset temperature was lowered to around 350 °C in the presence of Pt, which catalyses the combustion reaction. The shoulder observed between 150 – 350 °C was attributed to Pt-catalysed oxidation of carbonyl (C=O) groups on the Vulcan support. The amount of Pt in the catalyst could be quantified from the residual mass at 800 °C. They also demonstrated the viability of determining Nafion® content by TGA. Figure 4.4 (b) shows TG data for a catalyst layer consisting of Pt/C and Nafion® ionomer. The mass losses up to 300°C are attributed to carbonyl decomposition. The second mass loss between 300 – 350 °C is due to decomposition of Nafion®, which is catalysed by Pt so occurs at a lower temperature than for a pure Nafion® film. The losses from 350 °C are from the carbon support. Again, Pt could be quantified from the residual mass at 800 °C. The method will be validated independently in this work.

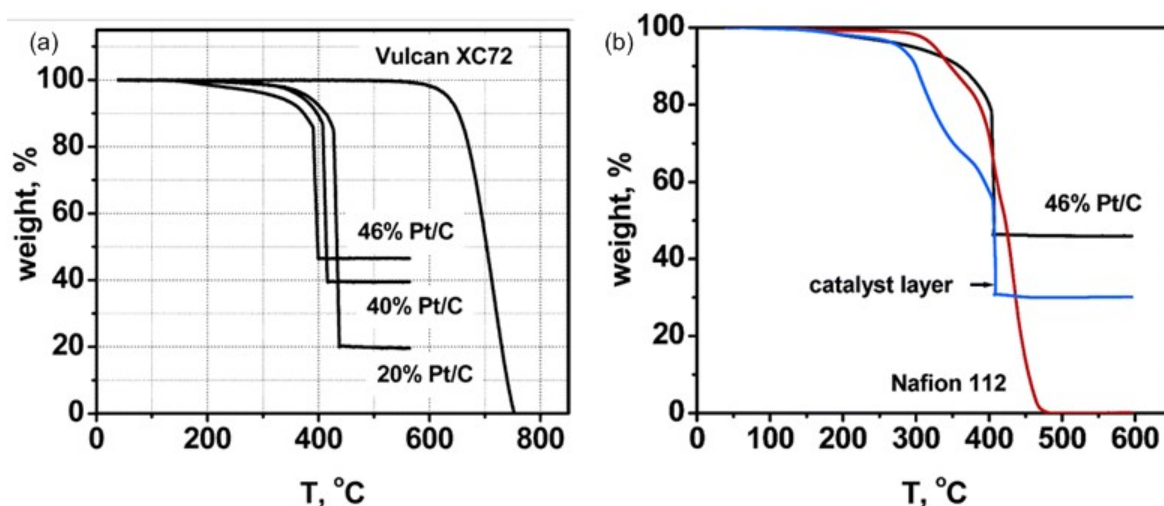


Figure 4.4: TG data recorded in air for (a) Vulcan XC-72 carbon black, and supported catalysts containing 20, 40 and 46 wt% Pt on C; (b) a Nafion® 112 membrane, a 46wt% Pt/C catalyst and a catalyst layer containing both Pt/C and Nafion®. Reproduced from [20]. Copyright 2006 American Chemical Society.

## 4.3 Results and Discussion

### 4.3.1 Synthesis of Nafion®-stabilised colloidal Pt

In a typical synthesis, the clear, yellow chloroplatinic acid / Nafion® mixture turned dark brown immediately upon addition of sodium borohydride, with concomitant evolution of hydrogen gas. The colour darkened over the course of a few minutes, after which no further changes were

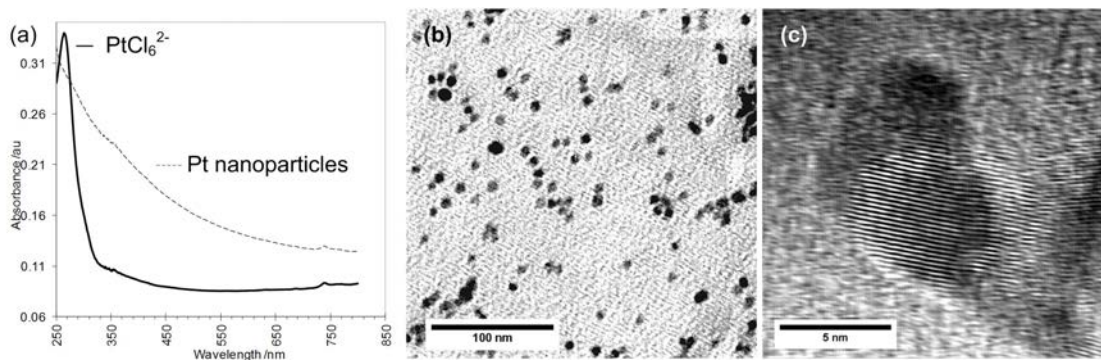


Figure 4.5: (a) UV-visible spectra for  $\text{H}_2\text{PtCl}_6$  solution and Nafion®-stabilised colloidal Pt nanoparticles; (b) Low-magnification TEM micrograph of as-synthesised Nafion®-stabilised colloidal Pt; (c) HR-TEM micrograph of colloidal Pt nanoparticles showing lattice fringes

observed. The formation of metallic nanoparticles is confirmed by the UV spectra in Figure 4.5 (a), which show the disappearance of the peak at 264 nm due to the  $\text{PtCl}_6^{2-}$  anion, and the evolution of a characteristically featureless spectrum in the range 250-750 nm. The product consisted of discrete particles as shown in Figure 4.5 (b), with average sizes in the range 5-25 nm, depending on reaction conditions. The crystallinity of the colloidal Pt nanoparticles was confirmed by the presence of Pt lattice fringes in bright-field HR-TEM micrographs as shown in Figure 4.5 (c).

### **Effect of Nafion® concentration**

The Pt:Nafion® mass ratio was found to have a significant effect on the morphology and stability of the colloidal Pt. The characteristic TEM micrographs shown in Figure 4.6 demonstrate a significant improvement in Pt particle dispersion and a reduction in the degree of agglomeration upon increasing the Nafion® content from Nafion®:Pt = 1:1 < 5:1 < 30:1. Despite its obvious effect on particle dispersion, the size distributions in Figure 4.6 (a-c) reveal that the Nafion®:Pt ratio has relatively little influence on the primary Pt particle size.

Dynamic light scattering (DLS) was found to be inherently unreliable for the characterisation of particle size distributions for Nafion®-stabilised colloidal Pt with differing Nafion® contents. DLS measurements performed on the colloidal Pt synthesised at the various Nafion®:Pt ratios produced the size distributions shown in Figure 4.7. At first sight the Nafion®:Pt ratio appears to have a small but significant effect on the average particle size, which decreases from 10 nm to 8 nm. However, the kinematic viscosities and refractive indices of the three colloidal dispersions vary significantly owing to their different Nafion® contents, and these are important parameters in the analysis of light scattering data based on the Stokes-Einstein equation (4.11). In light of this finding, all particle size distributions were measured from TEM images in the remainder of this study.

## 4 Preparation of Nafion®-Pt/C electrocatalysts

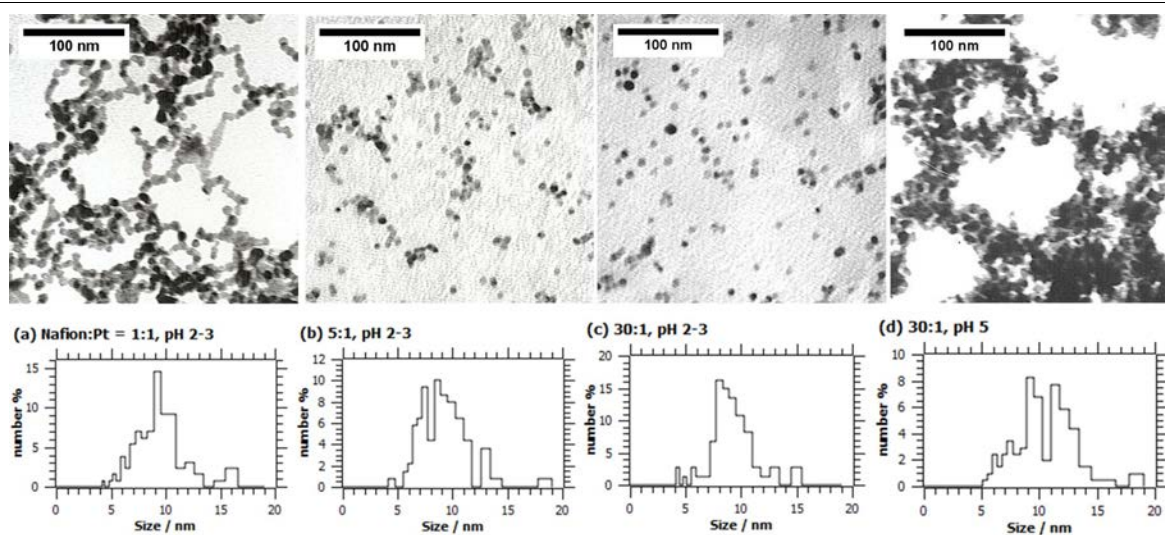


Figure 4.6: (a-c) TEM images and particle size distributions of Nafion®-stabilised colloidal Pt prepared at various Pt:Nafion® m/m ratios, and (d) at elevated pH.

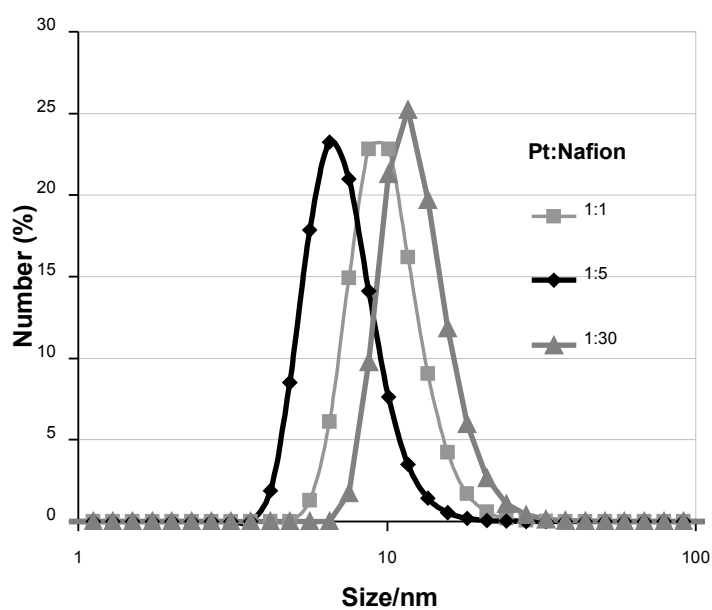


Figure 4.7: DLS size distributions for as-synthesised colloidal Pt prepared at Pt:Nafion® ratios of 1:1, 1:5 and 1:30

| Pt:Nafion® ratio | Synthesis pH | Observations  | Precipitated?    |
|------------------|--------------|---|------------------|
| No Nafion®       | 2-3          | Coarse, black precipitate   | Immediately      |
| 1:1              | 2-3          | Clear, dark brown colloidal dispersion formed without precipitate | After 24hours    |
| 1:2              | 2-3          |   | After 24-48hours |
| 1:5              | 2-3          |   | After 72 hours   |
| 1:30             | 2-3          |   | After 1 week     |
| 1:30             | 5            | Dark brown colloid with coarse precipitate                        | Immediately      |
| 1:30             | 8-9          | Coarse precipitate in gel-like suspension                         | Immediately      |

Table 4.2: Table 3: Summary of observations on varying Pt:Nafion® ratio and synthesis pH

### **Effect of pH**

In a different set of experiments, the pH of the precursor was adjusted from an initial value of pH 2-3 using NaOH or NaHCO<sub>3</sub>, prior to addition of borohydride, and at a Pt:Nafion® ratio of 1:30. Interestingly, the samples synthesised at elevated pH showed poor morphology compared with those whose pH was unmodified. At pH 5, a small quantity of coarse precipitate was formed immediately during synthesis in addition to the usual dark brown colloidal dispersion. The TEM micrograph in Figure 4.6 (d) reveals that the colloidal particles are highly agglomerated.

At pH 8-9 no nanosized particles were produced. Instead a coarse, black precipitate was observed, whilst the dispersant developed a gel-like character.

The deterioration of morphology & colloid stability on increasing pH can be attributed to a perturbation of the electrostatic stabilisation mechanism of Nafion®. It has been shown previously that the adsorption of Nafion® from colloidal dispersion onto solid substrates is affected by the pH of the continuous phase; with adsorption inhibited at pH > 4 due to electrostatic repulsion between anionic Nafion® sidechains and the negatively-charged substrate [134]. Similar effects are observed for other electrostatic stabilisers [124-125]. On the basis of these experiments, all subsequent reactions were performed without any upward adjustment of pH.

### **Effect of reaction temperature**

According to (4.6) and (4.5) an increase in reaction temperature should result in an increase in nucleation rate and a decrease in particle growth rate, yielding a product with a smaller average particle size. However, syntheses performed at elevated temperature (60 °C) were found to produce coarse precipitates. It appears that the Nafion®-Pt interaction is weakened at elevated

## 4 Preparation of Nafion®-Pt/C electrocatalysts

temperature, thus lowering the stability of the colloidal dispersion. In light of these findings, all subsequent experiments were performed at room temperature  $22 \pm 3$  °C.

### Scale effects

Initial experiments yielding ~ 5 mg of colloidal Pt were scaled-up to 50 mg and 100 mg in order to produce sufficient material for the preparation of membrane electrode assemblies (see chapter 7), The concentrations of the reagents, rates of addition and stirring were maintained the same as in 5 mg scale syntheses. The larger-scale syntheses produced products with significantly larger average particle sizes.

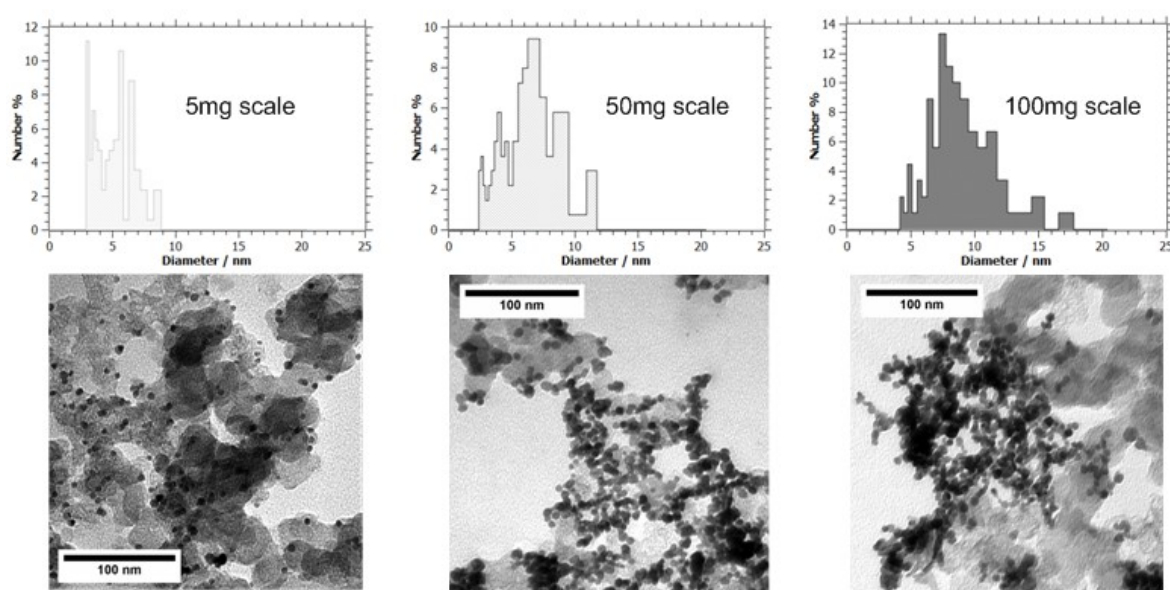


Figure 4.8: Pt particle size distributions and TEM micrographs for colloidal Pt synthesised at three batch scales 5mg, 50mg and 100mg

The supported catalysts shown in the TEM images in Figure 4.8 were all derived from colloidal Pt synthesised using a Pt:Nafion® ratio of 1:30, with a  $\text{PtCl}_6^{2-}$  concentration of  $2.3 \mu\text{M}$  and using a 180 mM solution of  $\text{NaBH}_4$  infused at  $48.5 \text{ ml} \cdot \text{min}^{-1}$  whilst stirring at 600 rpm. Experiments on scales of 5mg, 50mg and 100mg produced average Pt particle sizes of 5.8, 7.8 and 9.2 nm, respectively. This scale effect is likely to be due to inefficient stirring of the reaction mixture, and could probably be eliminated by careful design of the reaction vessel.

### Control of particle size using polyol additives

As discussed above, the Nafion®:Pt ratio was found to have very little influence on the size of the colloidal Pt particles produced by the synthesis. Therefore an alternative method was developed for the control of Pt nanoparticle size. Experiments were carried out in which the composition of

---

the continuous phase was adjusted to 50 % vol. of either ethylene glycol, propane-1,2-diol or glycerol, with water making up the balance in each case. The Pt:Nafion® mass ratio was 1:30 and the concentrations of all solutes were maintained identical to a control experiment using water alone.

Polyols are commonly employed in the synthesis of colloidal metal nanoparticles, where they can serve as both a solvent and reducing agent [8-14]. At ambient temperature the reduction kinetics are slow, so in a typical polyol synthesis the reaction is performed at high temperature (80 – 150 °C) and pH (8 - 10) in order to initiate and sustain nucleation. These conditions have been found to be unsuitable for the production of Nafion®-stabilised colloidal Pt, so in these experiments the  $\text{Pt}^{4+} \rightarrow \text{Pt}^0$  reduction reaction is facilitated by sodium borohydride. Under the conditions employed in the Nafion®-Pt synthesis (22 °C, pH < 3), the polyol additives make a negligible additional contribution to the rate of  $\text{Pt}^0$  formation. Instead, the polyol additives are intended to reduce the particle size of the colloidal product via two alternative modes of action:

1. Increased solution viscosity lowers particle growth rate. As shown in Table 4.3, the mixtures of water and polyol additives have significantly higher viscosities than pure water alone. A higher solution viscosity will lead to a decrease in the diffusion coefficient  $D$  of monatomic  $\text{Pt}^0$ , which from the growth rate equation (4.5) will effect a proportional decrease in growth rate.
2. By coordination with the surface of metal nuclei during formation, the polyol additives can reduce the solid-liquid interfacial tension  $\sigma_{SL}$  [135-136], thereby lowering both the critical nucleation radius and the activation energy for cluster formation in accordance with equations (4.4) and (4.1).

Importantly, from Table 4.3 it should be noted that the dielectric constants of the water-polyol mixtures are well within the range over which Nafion® is soluble ( $\epsilon > 10$ ) [137].

#### 4 Preparation of Nafion®-Pt/C electrocatalysts

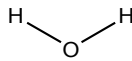
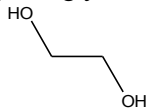
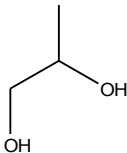
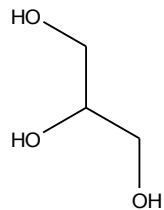
|  | Pure form                               |  | Mixture 50/50 vol with water       |   |
|--|---|--|------------------------------------|---|
|  | Kinematic viscosity<br>20 °C (cSt)[138] | Dielectric<br>constant $\epsilon$ 20 °C<br>[138] | Kinematic viscosity<br>20 °C (cSt) | Dielectric<br>constant $\epsilon$ 20 °C |
| Water<br>   | 1                                       | 80   | 1                                  | 80                                      |
| Ethylene glycol<br>                                   | 17.8                                    | 37   | 3.66 [139]                         | 58.5 [139]                              |
| Propane-1,2-diol<br>( $\alpha$ -propylene glycol)<br> | 52                                      | 32   | Not available                      | 56 [140]                                |
| Glycerol<br>   | 648                                     | 46   | 5.29 [141]                         | 63 [142]                                |

Table 4.3: Comparison of physical properties of polyol additives for size control of Nafion®-stabilised colloidal Pt

The TEM micrographs and particle size distributions in Figure 4.9 show the effect of each of the polyol additives on the morphology of the as-prepared colloidal Pt product. The polyol additives led to a decrease in average particle size as summarised in Table 4.4. From Figure 4.9, the morphologies of the polyol-assisted products appear rather agglomerated compared to the control sample in Figure 4.9 (a), but this is probably an artefact of slower drying of the TEM specimens for samples containing high-boiling additives. As-prepared colloidal dispersions were stable against precipitation for several days. The addition of ethylene glycol yielded the smallest average particle size (4.6 nm). On this basis, and in light of concerns over the difficulty of removal of significantly less volatile propane-1,2-diol and glycerol additives from the reaction product, the product of the ethylene glycol-assisted synthesis was selected for further investigation.

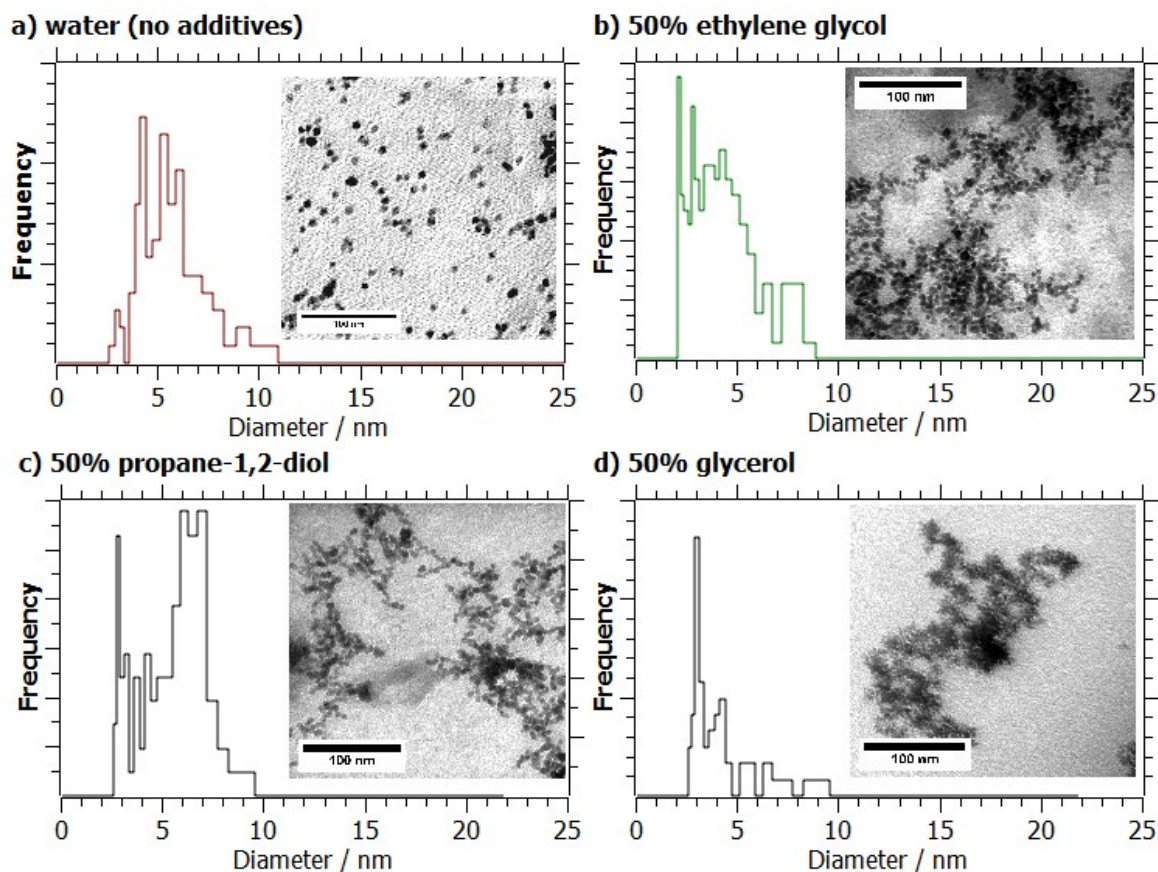


Figure 4.9: Particle size distributions and (inset) TEM micrographs for as-prepared synthetic products using a) water alone (no additives), b) 50/50 water/ethylene glycol, c) 50/50 water/propane-1,2-diol and d) 50/50 water/glycerol. All products synthesised on the 50 mg scale.

| Solvent composition       | Phys. surface area $A_{\text{phys}}$ / $\text{m}^2/\text{g}_{\text{Pt}}$ | Sauter diameter / nm |
|---------------------------|--|----------------------|
| Water only (no additives) | 37   | 7.8                  |
| 50% ethylene glycol       | 62   | 4.6                  |
| 50% propylene glycol      | 41   | 6.9                  |
| 50% glycerol              | 57   | 5.0                  |

Table 4.4: Comparison of physical surface areas ( $A_{\text{phys}}$ ) and average particle diameters for colloidal Pt nanoparticles synthesised in the presence of various polyol additives (50 mg scale)

### 4.3.2 Preparation of supported catalysts

The extent of Pt nanoparticle agglomeration on the final supported catalyst could be varied by addition of the carbon support either *prior to* or *following* purification of colloidal Pt. The products of these two preparation routes are designated as *Nafion®-Pt/C B* and *Nafion®-Pt/C A*, respectively, and the routes are illustrated in Figure 4.10.



## 4 Preparation of Nafion®-Pt/C electrocatalysts

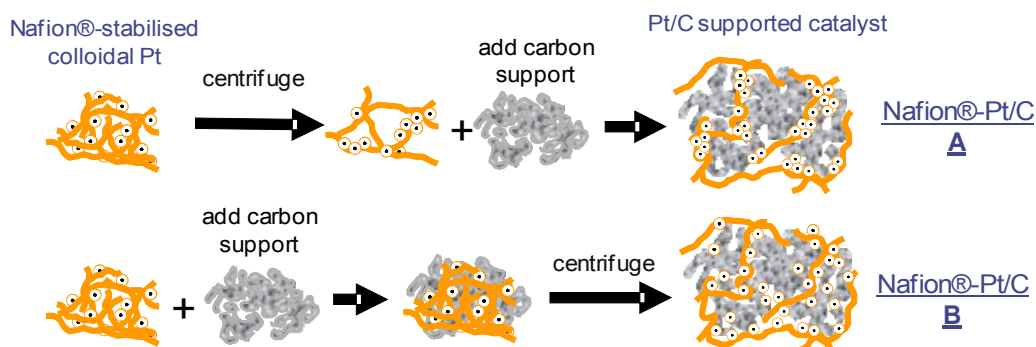


Figure 4.10: Comparison of preparation routes for Nafion®-Pt/C A and B. Pt particles can be made to agglomerate (A) or disperse evenly (B) on the carbon support depending on whether the support is added after (A) or before (B) removal of excess Nafion® by centrifugation.

The TEM micrographs in Figure 4.12 illustrate the dramatic variation in morphology that can be produced simply by adding the carbon support at different stages during the purification.

### Nafion®-Pt/C A

In this route, the as-synthesised colloidal Pt was purified by centrifugation to remove reaction by-products and excess Nafion® *prior* to addition of the carbon support. Centrifugation resulted in complete precipitation of the colloidal Pt. The clear, colourless supernatant liquid containing soluble impurities and excess Nafion® was removed and discarded. The precipitate was easily re-dispersed under sonication in 50/50 v/v water/acetone, and the centrifugation process was repeated. The concentrations of Pt and Nafion® in Nafion®-stabilised colloidal Pt catalysts was determined by thermogravimetric analysis. In an initial experiment, a recast Nafion® film was found to undergo thermal decomposition between 320 – 550 °C in air (see Figure 4.15 on page 80). In experiments on dried films of colloidal Nafion®-Pt, mass losses within this temperature region were attributed to the removal of Nafion®, whilst the residual mass at 800 °C was attributed to Pt. The Nafion® content, determined thermogravimetrically, was found to decrease with successive centrifugation steps as shown in Figure 4.11.

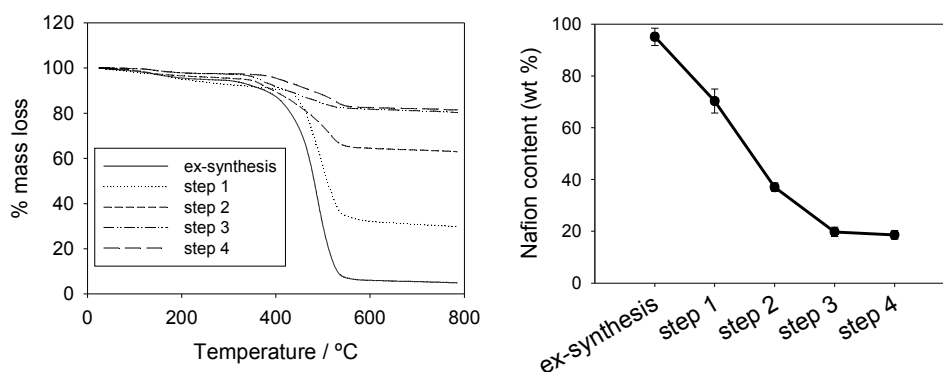


Figure 4.11: a) Thermogravimetric mass loss profiles obtained in air with a  $50 \text{ K}\cdot\text{min}^{-1}$  thermal ramp and b) Nafion® content of the colloidal Pt as a function of the number of centrifugation steps.

During purification, the removal of stabilising Nafion® led to the formation of loosely-agglomerated networks of Pt particles as shown in Figure 4.12 b. It is thought that these networks are directed along and around residual ionomer chains in the purified product. From Figure 4.11(b) it is clear that a residual 20 wt % Nafion® remains after the 3<sup>rd</sup> centrifugation cycle, and this could not be removed by subsequent centrifugation steps, implying that residual Nafion® is strongly bound within these Pt agglomerates.

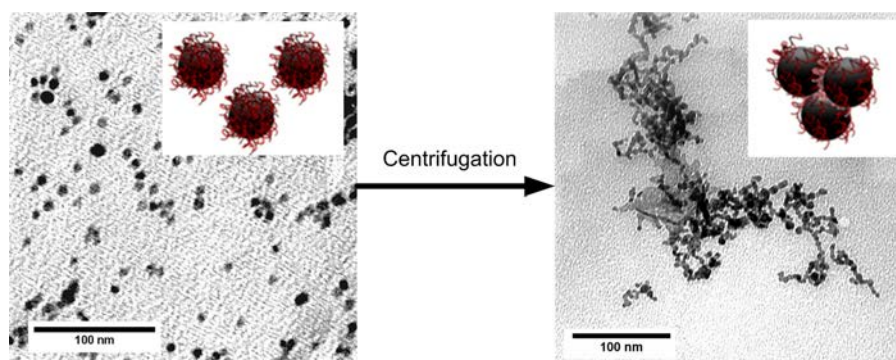


Figure 4.12: TEM images and (inset) schematic illustrations of the morphology of Nafion®-stabilised colloidal Pt before and after purification

An attempt was made to resolve the spatial distribution of the Nafion® in order to confirm the proposed co-location with Pt particles. Elemental mapping of sulphur was performed using EDX by scanning transmission electron microscopy. As shown in Figure 4.15, the spatial distribution of sulphur (and therefore Nafion®) corresponded roughly with that of Pt particles, although limited spatial resolution and sample drift prevented an entirely conclusive analysis.

## 4 Preparation of Nafion®-Pt/C electrocatalysts

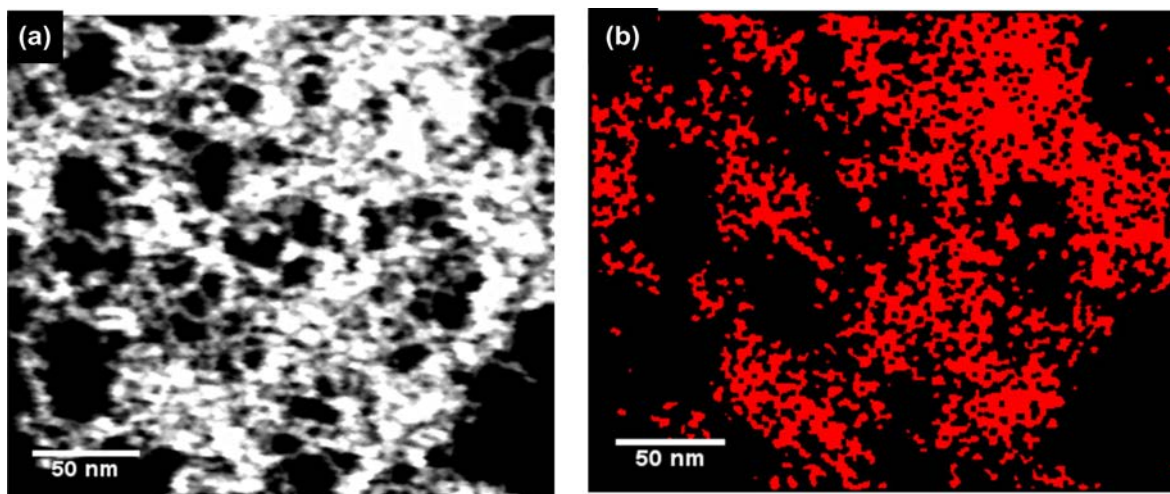


Figure 4.13: a) STEM micrograph of purified Nafion®-stabilised Pt nanoparticles (grey/white), b) EDX map of elemental sulphur distribution (red) indicating the presence of Nafion® within Pt agglomerates

Based on the Pt concentration calculated from TGA results for the purified colloidal Pt, an aliquot of Vulcan XC-72R dispersion was added to the colloidal Pt under sonication to give a Pt:carbon ratio of 1:1 (equivalent to a 50 wt % Pt/C catalyst). Pt agglomerates were found to adhere spontaneously to the carbon support, as shown in the TEM micrograph in Figure 4.14 (a).

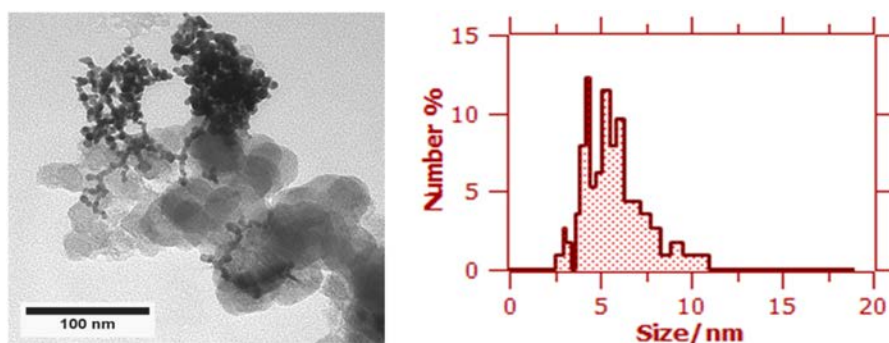


Figure 4.14: a) TEM micrograph and b) Pt particle size distribution for Nafion®-Pt/C A catalyst following purification of colloidal Pt and addition of the carbon support

### **Nafion®-Pt/C B**

In contrast to the method described for Nafion®-Pt/C A, in this route the carbon support was added to the as-synthesised colloidal Pt *prior* to purification. The same centrifugation process was then applied to the supported catalyst to remove reaction by-products.

TGA analysis of the purified product was complicated by a contribution to the TG mass loss due to thermal oxidation and decomposition of the carbon support. To assess the suitability of the TGA method for the determination of Nafion®, Pt and carbon contents in Nafion®-Pt/C, analyses were performed on uncatylsed carbon black, Nafion® and a mixture of Nafion® and carbon black (30/70 by mass) to verify that the mass ratios of these components could be determined from mass losses over distinct temperature ranges. As shown in Figure 4.15, a recast Nafion® film was found to undergo thermal decomposition between 320 – 550 °C. Meanwhile, the onset of thermal oxidation of the Vulcan XC-72R material began at around 560 °C, and continued until around 720 °C.

The fact that carbon and Nafion® components are oxidised over distinct and separate temperature ranges should allow their relative concentrations to be quantified, as demonstrated by the results for the 30/70 mixture of Nafion® and carbon black shown in Figure 4.15 (a), in which mass losses of 30% and 70% can be ascribed to Nafion® and Vulcan XC-72R, respectively. However, the onset temperature for carbon oxidation is lowered considerably in the presence of Pt, which catalyses the oxidation reaction such that it begins as low as 350 °C [20]. Consequently, for Nafion®-Pt/C supported catalysts, the TG losses from Nafion® and carbon overlap slightly, as shown in Figure 4.15 (b). Despite this, the overlap is sufficiently small that a reasonable determination of Nafion® and carbon content can be made.

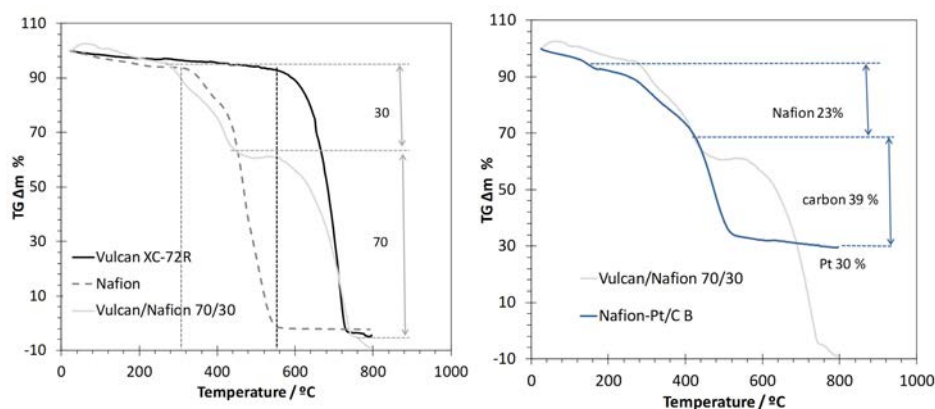


Figure 4.15: TGA curves for a) Vulcan XC-72R, Nafion® and a mixture of both and b) purified Nafion®-Pt/C B catalyst after 4 centrifugation cycles; obtained by heating from 25 - 800 °C at 10 °C.min<sup>-1</sup> in air.

After four centrifugation cycles, the Nafion®-Pt/C B type catalyst was found to contain around 23 wt % Nafion®, which could not be removed by further centrifugation. The carbon support offers a large surface area for the adsorption of Nafion®, and it is therefore unsurprising that more residual Nafion® remains in purified Nafion®-Pt/C B-type catalysts than in those where the purification is performed in the absence of the carbon support.

## 4 Preparation of Nafion®-Pt/C electrocatalysts

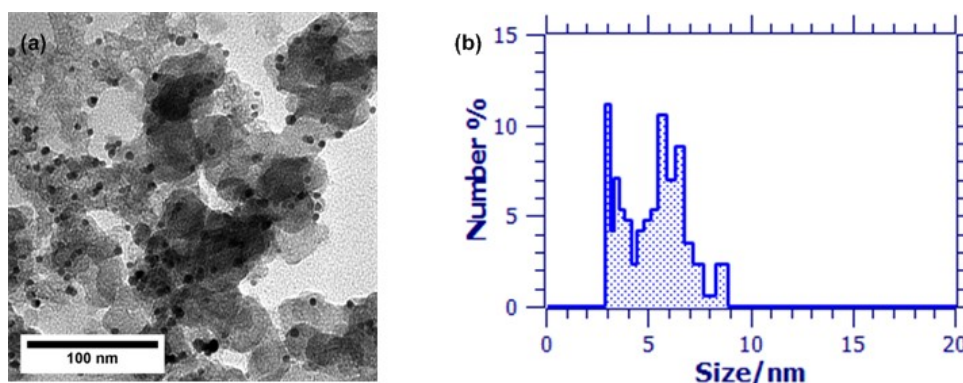


Figure 4.16: a) TEM micrograph and b) Pt particle size distribution for purified Nafion®-Pt/C B catalyst

The excellent dispersion of Pt nanoparticles in the Nafion®-Pt/C B catalyst seen in Figure 4.16 is in stark contrast to the agglomerated networks of Pt particles observed for Nafion®-Pt/C A. During purification, removal of excess ionomer reduces the stability of the colloidal dispersion, such that Pt particles begin to precipitate. In the 'B' preparation route, the presence of the carbon support during purification provides a substrate onto which particles can adsorb as they precipitate from colloidal dispersion, thus avoiding the agglomeration observed in Figure 4.12 (b).

The final compositions of the Nafion®-Pt/C A and B catalysts following purification are shown in Table 4.5. The final ratio of Pt:C in the Nafion®-Pt/C B catalyst was slightly lower than the desired 50:50, due to the loss of a small amount of Pt in the supernatant during the purification process. The Nafion® content of the catalyst ink is expressed as the *Nafion® Fraction Percentage* (NFP) after Antolini et al [143], calculated according to:

$$\text{NFP} = \frac{M_{\text{Nafion}}}{M_{\text{Pt}} + M_{\text{Carbon}} + M_{\text{Nafion}}} \times 100 \quad (4.12)$$

where  $M_{\text{Nafion}}$ ,  $M_{\text{Pt}}$  and  $M_{\text{Carbon}}$  are the concentrations [ $\text{mg}\cdot\text{ml}^{-1}$ ] of Nafion®, Pt and carbon black in the ink respectively.

|                | Pt wt % on C | Pt (wt %)    | Vulcan XC-72R (wt %) | Nafion®(wt %)<br>(NFP) |
|----------------|--------------|--------------|----------------------|------------------------|
| Nafion®-Pt/C A | 50           | $47.6 \pm 2$ | $47.6 \pm 2$         | $4.8 \pm 0.9$          |
| Nafion®-Pt/C B | 44           | $33 \pm 1$   | $42 \pm 2$           | $25 \pm 2$             |

Table 4.5: Final compositions of the Nafion®-Pt/C A and B catalysts following purification

---

## Nafion®-EG-Pt/C

A third supported catalyst was prepared from the Nafion®-stabilised colloidal Pt synthesised using ethylene glycol. Due to the difficulties encountered in quantifying Nafion® and carbon contents for 'B'-type catalysts, and because the Nafion®-Pt/C A catalyst showed good performance in interim electrochemical testing (see chapter 5), the Nafion®-EG-Pt/C catalyst was prepared according to route 'A'; that is, the purification was performed prior to addition of the carbon support.

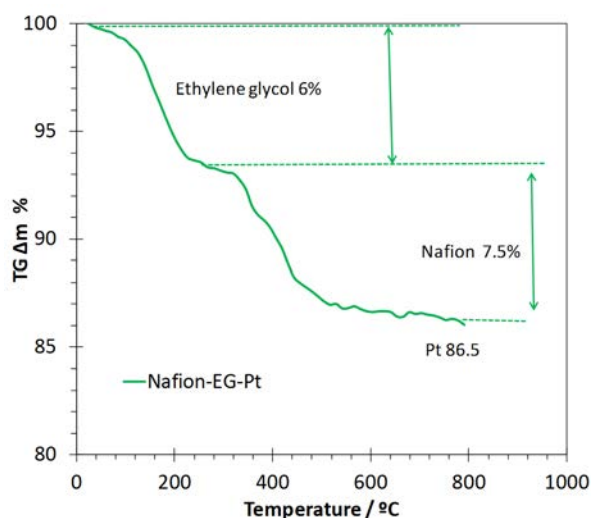


Figure 4.17: TGA analysis of purified colloidal Pt prepared using ethylene glycol (Nafion®-EG-Pt)

In the TGA analysis presented in Figure 4.17, the mass loss between 100-200 °C was attributed to residual ethylene-glycol remaining strongly adsorbed within Pt agglomerates following purification. This could not be removed by further purification cycles, and could present a problem for the preparation of catalysed electrodes – particularly GDEs – as it may reduce the porosity of the catalyst layer. The Vulcan XC-72R carbon black was added to the purified colloidal Pt following the same procedure used for Nafion®-Pt/C A described above, to produce a 50 wt % Pt on C supported catalyst.

The morphology of the final product was similar to that of Nafion®-Pt/C A, with agglomerated networks of Pt particles present on the carbon support (Figure 4.18 a). From the size distribution in Figure 4.18 it is clear that the *Nafion®-EG-Pt/C* catalyst has a significantly higher proportion of particles with sizes in the range 2 - 5 nm. The prevalence of small particles in catalysts produced by the EG-assisted synthesis can be attributed to i) the slower growth of colloidal Pt nanoparticles in the EG-containing continuous phase by virtue of its increased viscosity and therefore lower diffusion coefficient for Pt<sup>0</sup> and ii) a smaller nucleation radius for the formation of Pt nanoparticles as a result of lower solid-liquid interfacial energy in the presence of EG.

## 4 Preparation of Nafion®-Pt/C electrocatalysts

---

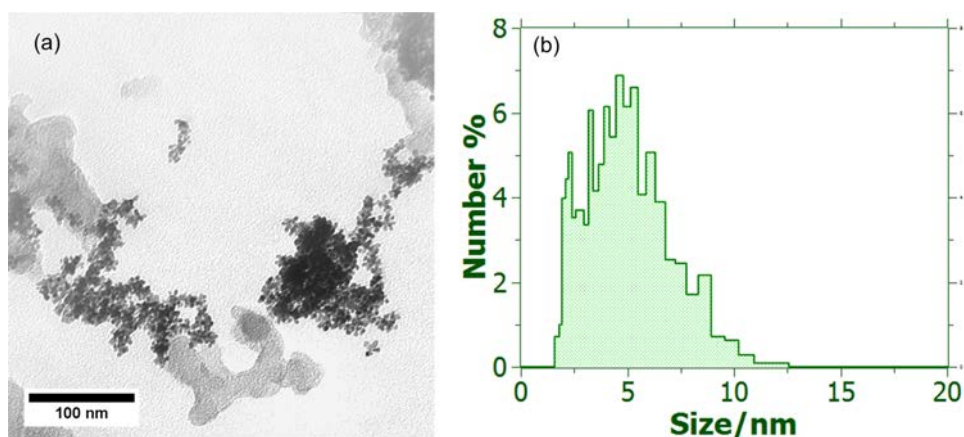


Figure 4.18: a) TEM micrograph and b) Pt particle size distributions for purified Nafion®-EG-Pt/C catalyst

### 4.4 Conclusions

A method has been developed for the synthesis of Nafion®-stabilised colloidal Pt nanoparticles in aqueous solution at room temperature and low pH, using sodium borohydride as the reducing agent. The colloidal product is stable and particles are well-dispersed, with sizes in the range 3-10 nm. The Nafion®:Pt ratio was found to have little effect on Pt particle size, but did effect the morphology of the product, with agglomerated Pt particles produced at Nafion®:Pt < 30:1 by mass. Addition of polyols to the reaction mixture was found to reduce average Pt particle size from 7.8 nm (without polyol additives) to 5.7 nm (using 50 vol % ethylene glycol) for synthesis performed on the 50mg scale, and this was attributed to lowering of the particle nucleation radius and growth rates by the polyol additives.

In preparing supported catalysts from Nafion®-stabilised colloidal Pt, the distribution of Pt particles on the carbon support can be varied between well-dispersed (Nafion®-Pt/C B) or agglomerated (Nafion®-Pt/C A) by adding the support either before or after purification, respectively. Purification by repeated centrifugation and re-dispersion was successful in removing soluble impurities and excess Nafion® from the reaction product. Some residual Nafion® remains following purification, indicating that it is strongly bound to Pt and/or carbon. This residual Nafion® is expected to provide excellent connectivity and proton conduction throughout the catalyst layer, and this hypothesis will be tested in the following chapter.

A summary of the three Nafion®-Pt/C catalysts that will be taken forward for electrochemical characterisation and *in-situ* testing is presented in Table 4.6.

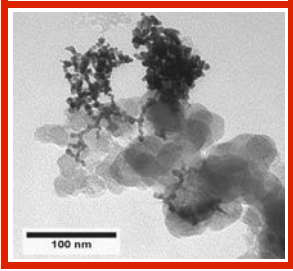
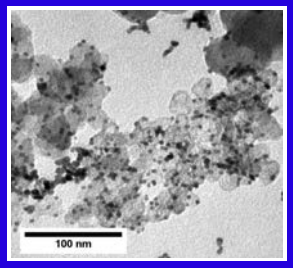
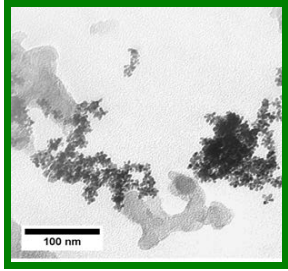
|  | Nafion®-Pt/C A  | Nafion®-Pt/C B   | Nafion®-EG-Pt/C   |
|--|---|--|---|
| TEM image  |  |  |  |
| Preparation route  | A   | B  | A   |
| Synthesis scale  | 50 mg   | 5 mg   | 50 mg   |
| Particle size / nm   | 7.8   | 5.6  | 5.7   |
| $A_{\text{phys}} / \text{m}^2 \cdot \text{g}^{-1} \text{Pt}$ | $37 \pm 3$  | $51 \pm 3$   | $50 \pm 3$  |
| Pt wt % on C   | 50  | 44   | 50  |
| Nafion®% (NFP)   | $4.8 \pm 0.9$   | $25 \pm 2$   | $1.7 \pm 0.8$   |

Table 4.6: Nafion®-Pt/C catalysts prepared for electrochemical characterisation



# 5 Electrochemical characterisation of Nafion®-Pt/C catalysts

The Nafion®-Pt/C electrocatalysts prepared as described in the previous chapter were characterised electrochemically in a half-cell rotating (ring-) disc electrode (RDE/RRDE) configuration using liquid electrolytes to determine their electrochemical surface area (ECSA), investigate their durability and measure their catalytic activity and selectivity towards the ORR.

## 5.1 Aims and objectives

The aims and objectives for the electrochemical characterisation of the Nafion®-Pt/C catalysts produced in this work are as follows:

- To develop a reproducible method for the **preparation of thin-film catalysed working electrodes** for RDE studies, from a range of catalyst materials both commercial and in-house prepared.
  - Catalyst films should be **homogeneous** and cover the **entire area** of the disc.
  - For a given catalyst, variations in ECSA,  $J_{lim}$  and specific activity should be **<10%** between identically-prepared electrodes.
- To develop reliable, reproducible methods for the electrochemical characterisation of electrocatalyst materials:
- The ECSA and ORR activities measured for **bulk polycrystalline Pt** and **commercially-available Pt/C** catalyst should agree quantitatively with those reported in references [109] and [108].
- To apply these methods for the characterisation of Nafion®-Pt/C catalysts, including:
  - Measurement of **ECSA**, **O<sub>2</sub> mass transport** parameters (diffusion coefficient), ORR **specific** and **mass activities** and reaction mechanisms
- To assess the viability of determining **optimal Nafion® content** for maximum catalyst utilisation using the RDE technique with high catalyst loadings on the working electrode.
- To conduct measurements at **elevated temperature** (60-70 °C), to simulate PEMFC operating conditions and allow comparison of ORR activities between RDE and *in-situ* tests.

---

## 5.2 Methods and Materials

### 5.2.1 Hardware

The experimental setup employed for the electrochemical characterisation of electrocatalysts in this work is shown in Figure 5.1. Electrochemical measurements were carried out using an Autolab PG302N potentiostat with an FRA2 impedance module, a SCAN250 analogue scan generator and a BA bipotentiostat/array. The electrochemical cell was enclosed in a grounded Faraday cage.

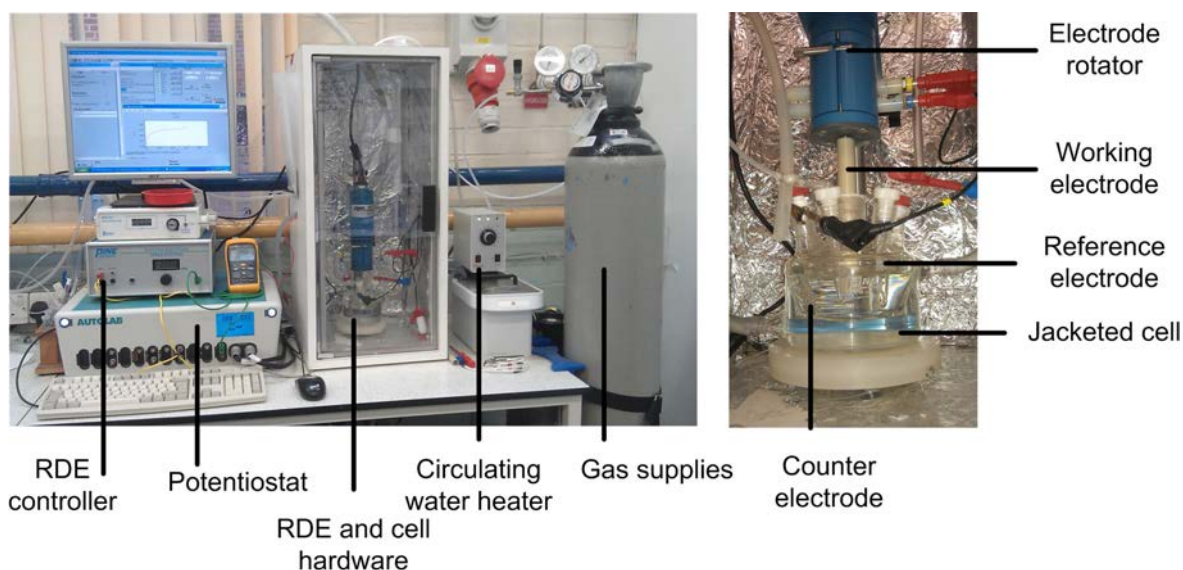


Figure 5.1: Experimental setup employed for the ex-situ electrochemical characterisation of electrocatalysts in this work.

### 5.2.2 Selection and preparation of materials

A jacketed glass electrochemical cell was cleaned by soaking in concentrated nitric acid for several hours. The cell was then rinsed thoroughly and boiled for 1 hour in UHQ water.

A 0.1 M  $\text{HClO}_4$  electrolyte solution (prepared from 70% TraceSelect, Sigma and UHQ water, 18.2  $\text{M}\Omega\cdot\text{cm}$  Millipore) was de-oxygenated by purging with ultra-pure nitrogen (BOC) for 20 minutes.

For this work, a reversible hydrogen electrode (RHE) was prepared in-house. The detailed procedures for the preparation and maintenance of these electrodes are described in the appendix, but briefly the electrode consisted of a platinised Pt gauze (300 mesh) sealed in a glass pipette, which was then filled with 0.1M  $\text{HClO}_4$ . A suitable volume of hydrogen was generated on the Pt gauze by electrolysis. Unless otherwise indicated, all potentials in this work are referred against the RHE. Counter electrodes for this study were made from platinised Pt gauze (300 mesh, Alfa Aesar) with surface areas of  $>10 \text{ cm}^2$ , which were flame-annealed prior to experiments to remove impurities.

### 5.2.3 Preparation of working electrodes

Glassy carbon RDE tips (5mm diameter, geometric surface area  $A=0.196\text{ cm}^2$ ) enclosed in PTFE or PEEK (for high-temperature experiments  $70^\circ\text{C}$ ) were purchased from Pine Instruments (USA). The electrodes were polished for 5 mins on Microcloth™ (Buehler) using  $1\text{ }\mu\text{m}$ ,  $0.3\text{ }\mu\text{m}$  and  $0.05\text{ }\mu\text{m}$  alumina slurries in sequence. The polished electrodes were rinsed with UHQ water, then sonicated (40 kHz bath) for 3 minutes in UHQ water to remove any residual alumina.

A known volume of catalyst ink was deposited on the glassy carbon (GC) disc to produce a Pt loading between  $20 - 100\text{ }\mu\text{g}_{\text{Pt}}\cdot\text{cm}^{-2}$  as required, and dried at room temperature either in a vacuum oven, or under ambient conditions whilst rotating at 200 - 500 RPM on an inverted RDE rotator, depending on which method produced the most homogeneous catalyst film for a particular ink.

### 5.2.4 Electrochemical methods

The catalysed working electrode was mounted in an RDE assembly (ASR, Pine Instruments, USA) and immersed in the electrolyte, taking care to remove any air bubbles from the electrode surface by rotating the electrode briefly at 1000 RPM. The cell was thermostated at  $25^\circ\text{C}$  or  $70^\circ\text{C}$  using a circulation heater.

The electrolyte was purged with nitrogen (Grade 5, ultra-high purity, BOC) for at least 30 minutes prior to electrochemical conditioning of the electrode by cycling between  $+0.05 - +1.0\text{ V}$  at  $250\text{ mV}\cdot\text{s}^{-1}$  for up to 200 cycles, until stable cyclic voltammograms were observed.

For the measurement of ECSA, cyclic voltammograms were recorded using analogue scan cyclic voltammetry (using the SCANGEN module) at  $25\text{ mV}\cdot\text{s}^{-1}$  between  $+0.05$  and  $+1.1\text{ V}$ .

Background linear sweep voltammograms (LSVs) were recorded whilst still under  $\text{N}_2$  purge, from  $+0.3 - +1.1\text{ V}$  at  $25\text{ mV}\cdot\text{s}^{-1}$  at various rotation rates 400, 505, 660, 896, 1286 and 2000 RPM.

The electrolyte was then purged with oxygen (ultra-high purity, BOC) for at least 30 mins, or until the open circuit potential stabilised.

LSV scans were then repeated in the  $\text{O}_2$  – purged electrolyte at the same rotation rates.

The Ohmic resistance of the electrolyte was measured using electrochemical impedance spectroscopy at 10 kHz, using an AC perturbation of 5 mV (see section 7.2.3 for a full description of this technique).

Finally, to ensure that the catalyst had not detached from the electrode, the electrolyte was purged once more with  $\text{N}_2$  before repeating ECSA measurements using cyclic voltammetry as above.

## 5.3 Results and Discussion

### 5.3.1 Method validation: Pt disc

Prior to conducting experiments with supported catalysts, the RDE methods were validated using a polycrystalline Pt disc. A 2mm diameter Pt disc electrode (geometric surface area  $0.0314 \text{ cm}^2$ ) was polished to a  $0.5 \mu\text{m}$  mirror finish and mounted immediately in the RDE assembly.

ECSA was measured from the charge due to  $\text{H}_{\text{upd}}$  desorption, found by integrating the shaded area of the cyclic voltammogram shown in Figure 5.2 (a) and using equation (3.8) (page 35). For the 2mm Pt disc, the ECSA was measured as  $0.035 \pm 0.004 \text{ cm}^2$ , giving an electrode roughness factor ( $r_f = 1.1 \pm 0.1$ ) close to unity as expected for a highly-polished surface.

**$\text{O}_2$  diffusion coefficient** The Levich plot in Figure 5.2 (c) shows a linear relationship ( $R^2$  value 0.9996) between limiting current density  $J_{\text{lim}}$  measured at 0.4 V and the square root of rotation rate  $\omega^{1/2}$  as predicted by the Levich equation. The experimental data are all within 10% of the

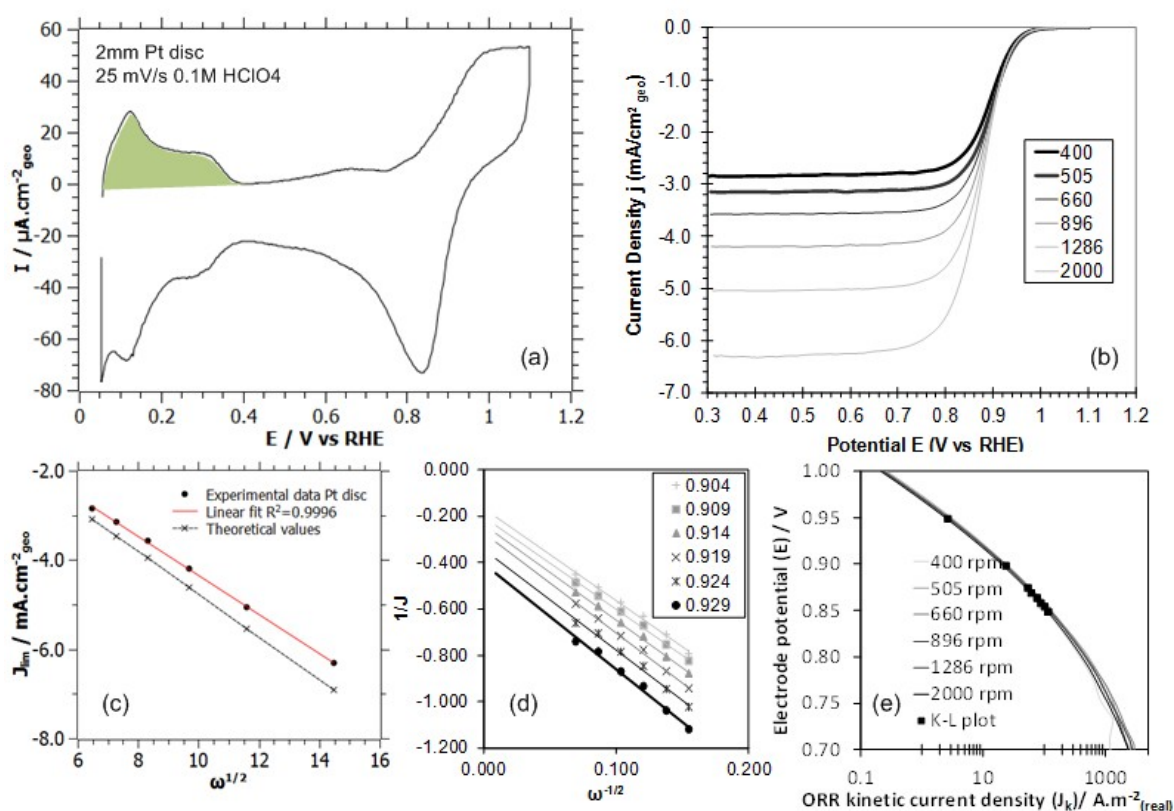


Figure 5.2: For 2mm Pt disc electrode in  $0.1 \text{ M HClO}_4$  at  $25^\circ\text{C}$ : (a) CV recorded at  $25 \text{ mV/s}$  in  $\text{N}_2$ -saturated electrolyte showing shaded region due to  $\text{H}_{\text{upd}}$  desorption; (b) background and  $iR$ -drop corrected anodic polarisation curves recorded in  $\text{O}_2$ -saturated electrolyte at  $25 \text{ mV/s}$ ; (c) Levich plot demonstrating linear dependence of limiting current on  $\omega^{1/2}$  and theoretical values for  $J_{\text{lim}}$  calculated from the Levich equation; (d) Koutecky-Levich plots used to calculate  $J_k$  values at the 6 potentials shown; (e) Tafel plot combining kinetic current data calculated using  $J_k = J_{\text{lim}} / (J_{\text{lim}} - J)$  (—) and via the K-L plots in (d) (■).

## 5 Electrochemical characterisation of Nafion®-Pt/C catalysts

theoretical values. The O<sub>2</sub> diffusion coefficient was calculated from the slope of Figure 5.2 (c) according to equation (3.10) assuming the values for  $n$ ,  $C$  and  $\nu$  given in Table 5.1.

| Levich equation                                    | $J_{lim}=0.62nFCD^{2/3}\nu^{-1/6}\omega^{1/2}$            | Ref   |
|--|---|-------|
| Number of electrons $n$                            | 4   |       |
| Faraday constant, $F$                              | 96485 C.mol <sup>-1</sup>                                 |       |
| Concentration O <sub>2</sub> , $C$ (25 °C)         | 1.1 x 10 <sup>-6</sup> mol.cm <sup>-3</sup>               | [110] |
| Kinematic viscosity H <sub>2</sub> O $\nu$ (25 °C) | 0.891 x 10 <sup>-3</sup> cm <sup>2</sup> .s <sup>-1</sup> | [144] |
| O <sub>2</sub> diffusion coefficient $D$ (25 °C)   | 1.93 x 10 <sup>-5</sup> cm <sup>2</sup> .s <sup>-1</sup>  | [145] |

Table 5.1: Accepted values for parameters in the Levich equation

The value obtained for  $D(O_2) = 1.69 \pm 0.07 \times 10^{-5} \text{ cm}^2.\text{s}^{-1}$ , which is in reasonable agreement with the accepted value of  $1.93 \times 10^{-5} \text{ cm}^2.\text{s}^{-1}$ . The small discrepancy is probably due to a sub-saturation O<sub>2</sub> concentration, which could be remedied by sealing the cell against the ambient atmosphere to prevent ingress of air and maximise the O<sub>2</sub> partial pressure above the electrolyte.

**ORR activity** The Tafel plots in Figure 5.2 (e) feature  $J_k$  data derived using both the K-L equation (line plots) and K-L plots (discrete points ■). Specific activity at +0.9 V was calculated as  $19.0 \pm 1.9 \text{ A.m}^{-2}_{\text{real}}$  using the K-L plot method and  $19.0 \pm 2.3 \text{ A.m}^{-2}_{\text{real}}$  directly using the K-L equation, demonstrating good agreement between the two methods. These values are somewhat higher than those typically reported for similar conditions (25°C, 1 atm O<sub>2</sub>, 0.1 M HClO<sub>4</sub>) in the literature (Table 5.2) but the discrepancy is well within the range which can reasonably be attributed to differences in Pt surface preparation and experimental conditions.

| T / °C | Conditions  | $J_k @0.9 \text{ V}$<br>/ $\text{A.m}^{-2}_{\text{real}}$ | Tafel slope,<br>b / mV.dec <sup>-1</sup> | # electrons<br>n                   | Ref       |
|--------|---|---|--|------------------------------------|-----------|
| 25     | Polished Pt poly disc, 0.1 M HClO <sub>4</sub>        | $19.0 \pm 1.9$  | -60/-120                                 | $3.36 \pm 0.13$<br>$3.68 \pm 0.14$ | This work |
| 25     | Pt poly, 0.1M HClO <sub>4</sub>                       | 21  | -  | -                                  | [146]     |
| 60     | Pt poly, 0.1 M HClO <sub>4</sub>                      | 27.7  | -65                                      | -                                  | [12]      |
| 60     | Pt poly, 0.1M HClO <sub>4</sub>                       | 24.6  | -65                                      | -                                  | [12]      |
| 25     | Flame-annealed Pt poly disc, 0.1 M HClO <sub>4</sub>  | $12 \pm 2.5$  | ~ -60 *                                  | -                                  | 18        |
| 25     | Sputter-cleaned Pt poly disc, 0.1 M HClO <sub>4</sub> | 8.5*  |  | -                                  | [147]     |
| 25     | Pt poly wire, 0.005 M HClO <sub>4</sub>               | 0.5   |  | -                                  | [148]     |
| 20     | Sputtered Pt film, 0.1 M HClO <sub>4</sub>            | -   | -74/-121                                 | -                                  | [110]     |
| 60     | Pt poly, 0.5 M H <sub>2</sub> SO <sub>4</sub>         | 1.1   | -58/-115                                 |                                    | [100]     |

Table 5.2: Experimental conditions and ORR kinetic parameters found for bulk Pt electrodes in this and previous work.

\* indicates values calculated from data given in the publication. Pt poly = bulk polycrystalline Pt.

---

**Reaction mechanism** The Koutecky-Levich plots in Figure 5.2 (d) are linear over the range of rotation rates employed here, indicating mixed kinetic-diffusion control with relatively slow electron transfer[92]. The number of electrons transferred per mole of reactants  $n$  can be estimated from the slopes of the K-L plots according to equation (3.11). The values obtained for  $n$  were constant over the potential range 0.85 – 0.9 V, with  $n = 3.36 \pm 0.13$  and  $n = 3.68 \pm 0.14$  found depending on whether the literature or experimentally-determined value for  $D$  was used in equation (3.11). The errors represent standard deviations for  $n$  over the potential range 0.85 – 0.9 V, and values are in good agreement with the results of previous studies.

From the curvature of the Tafel plot in Figure 5.2 (e) it is clear that there is no single Tafel slope for the reaction in the potential range 0.95 - 0.7 V. The slope is around -60 mV.dec<sup>-1</sup> at  $E > 0.85$  V, but doubles to -120 mV.dec<sup>-1</sup> for  $E < 0.8$  V. This finding is in good agreement with previous work, although there exists some debate in the literature as to the origins of this effect. Some insist it is a genuine kinetic phenomenon caused by a change in surface oxide coverage at *ca.* 0.8 V [110, 149], whilst others suggest that is merely due to the onset of mass transport effects at higher current densities [12].

The good agreement between data obtained for the Pt disc in this study, theoretical predictions and previous work assures the validity of the RDE method and experimental protocol, which will be carried forward to thin-film catalysed RDE studies.

## 5.3.2 Thin-film RDE studies

### Working electrode preparation

All Nafion®-Pt/C catalysts, and the E-Tek and TKK commercial Pt/C were found to disperse easily in 80/20 v/v water/isopropanol. Catalyst inks were stable against precipitation for days, and small quantities of precipitate could be redispersed by sonication (40kHz, bath).

Initially, catalyst films were formed on GC electrodes by simple drop-casting, followed by drying either in air or in a vacuum oven at 40 °C. However, the films produced by this method were found to vary significantly in their quality, determined by visual inspection of the electrode to assess film coverage and homogeneity. A new method was developed to improve the quality and reproducibility of catalyst thin film preparation.

*Spin-coating* is widely employed in the deposition of thin films on flat surfaces, most notably in the casting of polymer photoresists on silicon wafers for semiconductors. The thickness of the film is determined and controlled by the rate of rotation of the substrate during deposition and drying of the solution containing the film material. It was found that spin-coating the ink by rotating the electrode on an inverted RDE rotator at 100-300 RPM during drying improved the

## 5 Electrochemical characterisation of Nafion®-Pt/C catalysts

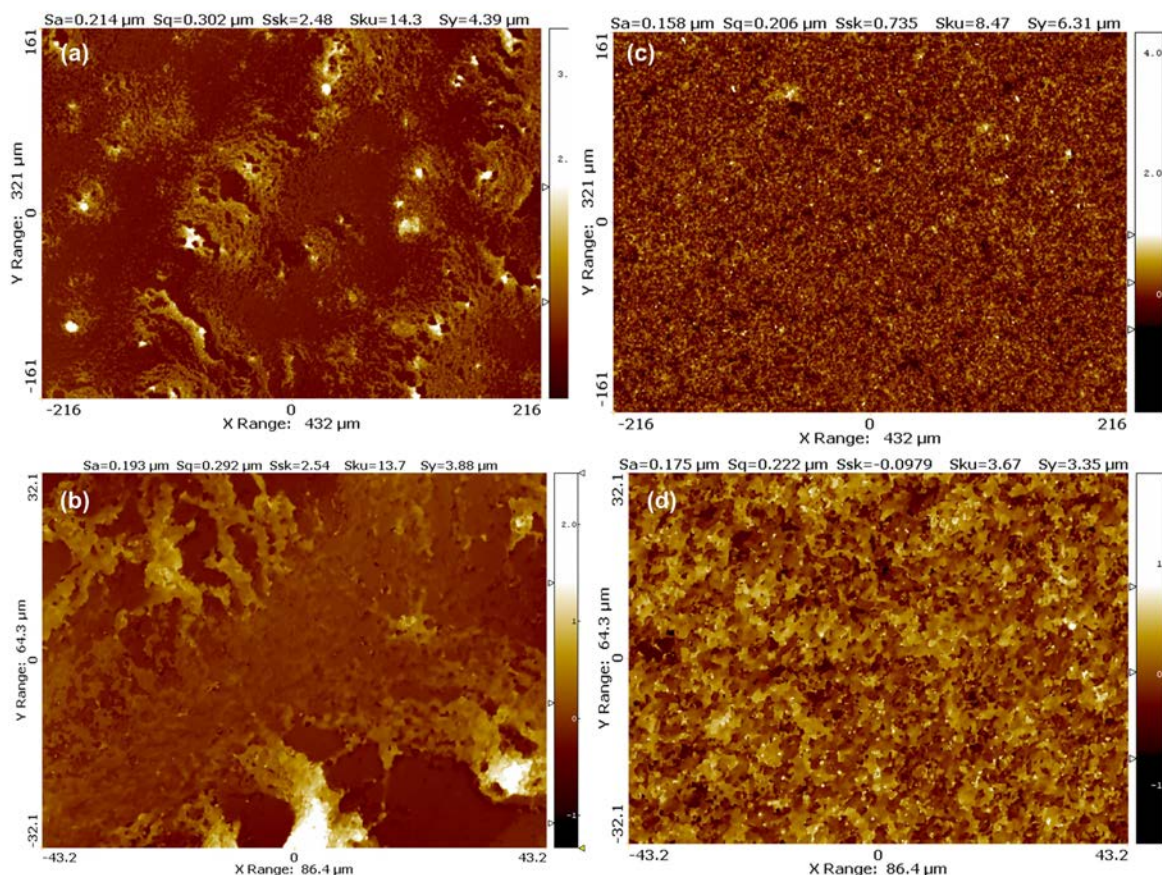


Figure 5.3: Laser interferometry profiles of thin catalyst films on GC electrodes prepared using (a, b) stationary drop-casting and (c, d) ethylene glycol modified spin-coating method. The spin-coating method produces a very even, homogeneous film, whereas the standard drop-casting method produces 'islands' of high catalyst loading and regions of bare glassy carbon.

homogeneity of the film to an extent, but that this method would frequently leave a bare patch of GC in the middle of the electrode, which was thought to be due to excessively rapid evaporation of the ink.

To slow the drying, 1  $\mu\text{l}$  of ethylene glycol was deposited on the polished GC electrode prior to casting of the catalyst ink. The ink was then pipetted carefully onto the EG-covered GC disc. The electrode was rotated at 100 RPM for 15 minutes, then at 300 RPM for 30 minutes before drying overnight in a vacuum oven at 40  $^{\circ}\text{C}$  and -900 mbar. This method, referred to as the *ethylene glycol-modified spin coating method* (EG-SC), was found to consistently produce very uniform films, covering the entire GC surface. The method employed here differs from traditional spin-coating in that the ink was not allowed to flow beyond the boundary of the GC disc and onto the encapsulating PTFE.

The surfaces of catalyst electrodes prepared using the drop-casting and EG-SC methods were compared using laser interferometry. The improved homogeneity offered by the EG-SC method is

clear by comparison of Figure 5.3 (c & d) with Figure 5.3 (a & b). In Figure 5.3 (a & b), 'islands' of high catalyst loading can be seen on the drop-cast film along with regions of bare glassy carbon, whereas the electrode prepared using the EG-SC method is highly uniform, even when viewed at high magnification (50 x) in Figure 5.3 (d). The enhanced reproducibility offered by the EG-SC method is evident from Figure 5.4, which compares 4 repeat measurements on electrodes prepared by EG-SC and stationary drop casting. Variations in specific activity of nearly an order of magnitude were observed between electrodes prepared using stationary drop casting, whereas values measured for EG-SC varied by < 10%.

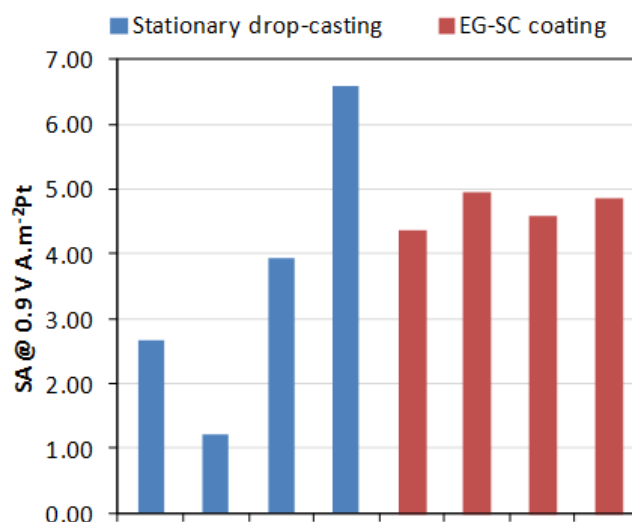


Figure 5.4: Comparison of specific activities measured on 4 electrodes prepared using the stationary drop casting and EG-SC methods, demonstrating the enhanced reproducibility offered by the latter. All electrodes prepared from the same ink TKK 50 wt%, at a Pt loading of  $20 \mu\text{g}_{\text{Pt}}\text{cm}^{-2}$

It is thought that the addition of EG improves the rheological properties of the ink droplet by increasing its viscosity and modifying its shear-thinning behaviour, as well as lowering the evaporation rate. The EG-SC method was employed for the preparation of all working electrodes in this study.

## **Catalyst utilisation**

The electrochemical surface areas (ECSAs) of the various catalysts were measured from the  $H_{\text{upd}}$  charge calculated from cyclic voltammograms recorded at 25mV/s between +0.05 V and +1.1 V, as described in section 5.2.4 (p 34). Physical surface areas were measured from TEM micrographs, assuming spherical, crystalline Pt particles as described in the previous chapter.



## 5 Electrochemical characterisation of Nafion®-Pt/C catalysts

### Effect of catalyst loading on utilisation

To examine the effect of working electrode catalyst loading  $L_{Pt}$  on the measured ECSA, a series of electrodes were prepared at catalyst loadings of 20, 40 and 80  $\mu\text{g}_{Pt}\cdot\text{cm}^{-2}$  for the Nafion®-Pt/C A and E-Tek catalysts. The Nafion® content was 20 % NFP for both catalysts, representing an optimal ionomer content for the Nafion®-Pt/C catalyst and a *sub-optimal* ionomer content for the E-Tek catalyst according to the results presented later in Figure 5.7, and from previous work which found the optimal ionomer content for the E-Tek catalyst to be *ca.* 33 % NFP.

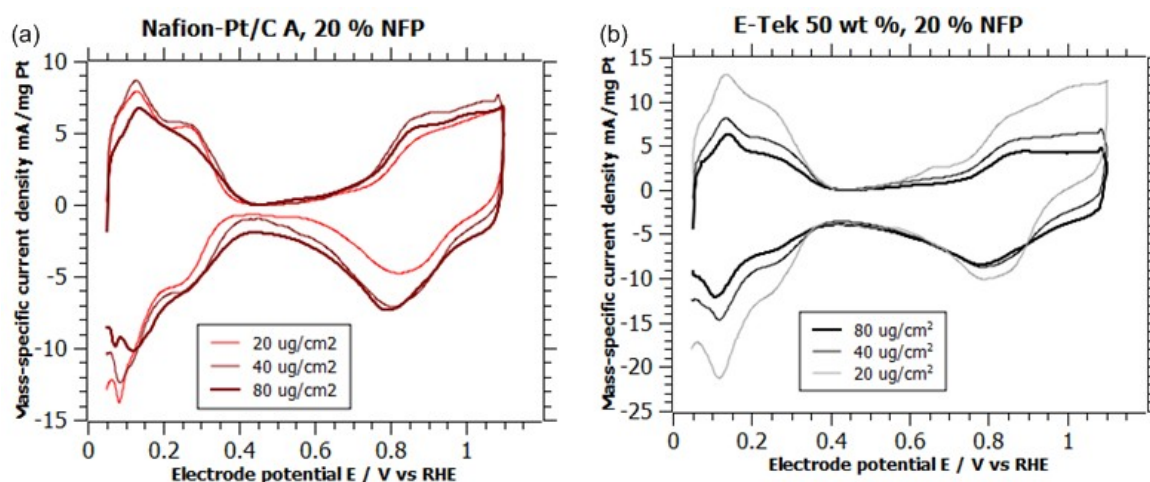


Figure 5.5: CVs recorded at 25 mV/s in  $N_2$ -saturated 0.1 M  $\text{HClO}_4$  for (a) the Nafion®-Pt/C catalyst with an optimised ionomer content and (b) for the E-Tek 50wt% Pt/C catalyst with a sub-optimal ionomer content.

The CVs in Figure 5.5 are normalised by Pt loading and show clear differences in the relationship between  $L_{Pt}$  and mass-specific current in the  $H_{upd}$  region between the catalyst with optimal ionomer content (Nafion®-Pt/C A) and that with sub-optimal ionomer content (E-Tek). ECSAs calculated from the  $H_{upd}$  charges are given in Table 5.3 and represented as a function of  $L_{Pt}$  in Figure 5.6. The Nafion®-Pt/C electrodes prepared at 20 % NFP gave around 100 % utilisation at all loadings, whilst the utilisation for the E-Tek electrodes fell from a maximum 76 % at low loading (20  $\mu\text{g}_{Pt}\cdot\text{cm}^{-2}$ ) to just 50 % at high loading (80  $\mu\text{g}_{Pt}\cdot\text{cm}^{-2}$ ).

These results indicate that at high Pt loadings ( $L_{Pt} > 40 \mu\text{g}_{Pt}\cdot\text{cm}^{-2}$  at least), thin-film catalyst layers with sub-optimal ionomer loadings will exhibit poor utilisation, whilst those prepared at optimal ionomer loading will show 100 % utilisation. This demonstrates the viability of using the RDE thin-film method for screening catalyst ink compositions to investigate optimal ionomer content, without the need for fabricating MEAs. These findings also highlight the danger of attempting kinetics measurements on thin-film electrodes with high Pt loadings, where the catalyst utilisation may be rather poor, leading to erroneously low values for mass activity. Accordingly, all electrodes for ORR kinetics measurements will be prepared at  $L_{Pt} = 20 \mu\text{g}_{Pt}\cdot\text{cm}^{-2}$ , so that catalyst utilisation is maximised.

The fact that the E-Tek catalyst affords only 76% utilisation under optimal conditions implies that up to 25% of the physical Pt surface area is either inaccessible to the liquid electrolyte or not in electrical contact with the carbon support. There may be several explanations for this, including isolation of Pt particles in hydrophobic micropores within the carbon support; excessive 'wetting' of the support by Pt such that the Pt particles are hemispherical instead of spherical; and detachment of Pt particles from the carbon support during sonication of the ink.

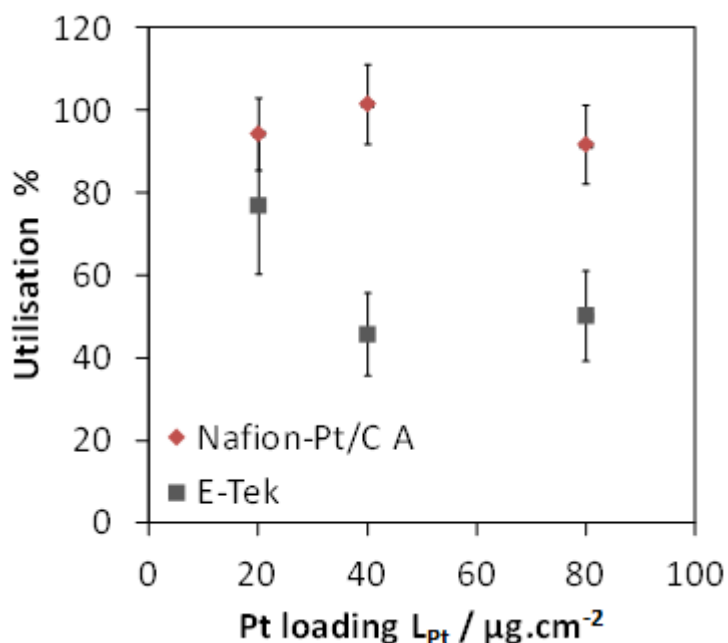


Figure 5.6: Demonstrating the variation in catalyst utilisation with  $L_{Pt}$  for an electrode with sub-optimal ionomer content (E-Tek), and the invariance of utilisation with  $L_{Pt}$  for an electrode with optimal ionomer content (Nafion®-Pt/C A). Both electrodes prepared at 20 % NFP.

|                       | $A_{\text{phys}} / \text{m}^2.\text{g}^{-1}_{\text{Pt}}$ | ECSA / $\text{m}^2.\text{g}^{-1}_{\text{Pt}}$ (Utilisation / %) |  |  |
|-----------------------|--|---|--|--|
|                       |  | $L_{Pt} = 20 \mu\text{g}_{\text{Pt}}.\text{cm}^{-2}$            | $L_{Pt} = 40 \mu\text{g}_{\text{Pt}}.\text{cm}^{-2}$ | $L_{Pt} = 80 \mu\text{g}_{\text{Pt}}.\text{cm}^{-2}$ |
| <b>Nafion®-Pt/C A</b> | 35   | 33 (93 %)   | 35 (100 %)   | 32 (91 %)  |
| <b>E-Tek 50 wt %</b>  | 71   | 55 (76 %)   | 32 (45 %)  | 35 (50 %)  |

Table 5.3: Comparison of ECSA and catalyst utilisation measured for Nafion®-Pt/C A and E-Tek catalysts with ionomer content = 20 % NFP at three catalyst loadings  $L_{Pt}=20, 40, 80 \mu\text{g}_{\text{Pt}}.\text{cm}^{-2}$ .

### Nafion® content optimisation

Having demonstrated the viability of ionomer content screening and optimisation using thin catalyst films in liquid electrolytes, the method was employed for the optimisation of the ionomer content in the Nafion®-Pt/C catalysts. In this investigation, Nafion® coverage and connectivity

## 5 Electrochemical characterisation of Nafion®-Pt/C catalysts

---

between Pt-Nafion® agglomerates on the carbon support was tuned by addition of Nafion® dispersion to the as-prepared Nafion®-Pt/C catalysts. In the case of Nafion®-Pt/C A, the as-prepared catalyst contained 5% NFP, and Nafion® dispersion was added to produce a series of catalyst inks containing Nafion® loadings between 10% and 35% NFP. For Nafion®-Pt/C B the Nafion® contents employed were 25% NFP (as-prepared) to 40% NFP. For comparison, a third series of catalyst inks were prepared according to a standard method using a commercial 50 wt % Pt/C catalyst (E-Tek) at various Nafion® loadings between 20-40% NFP. In accordance with the results of the loading study discussed above, electrodes with high Pt loading  $L_{Pt}=80 \text{ ug}_{Pt}\cdot\text{cm}^{-2}$  were employed in this study.

**Nafion® Pt/C A** From Figure 5.7 (a), the optimal Nafion® content of the *Nafion®-Pt/C-A* catalyst was found to be around 20 wt. %, which is far lower than the 33 wt. % optimum loading for conventional Pt/C catalysts reported previously and verified here. Close coordination between Pt and residual Nafion® in the *as-prepared* catalyst is thought to provide close to 100% utilization of Pt particles *within* agglomerates on the carbon support. However, the absence of free Nafion® in the *as-prepared* ink results in poor ionic connectivity between these agglomerates, such that not all are utilised. This accounts for the lower utilisation observed for Nafion®-Pt/C A at low Nafion® loading in Figure 5.7 (a). Addition of a small amount of Nafion® to the *as-prepared* catalyst facilitates connection between agglomerates, resulting in a rapid increase in utilisation with increasing ionomer content, up to a maximum at about 20 wt %. This optimum utilisation is obtained at a lower overall Nafion® loading indicating an enhanced percolation efficiency of the ionomer network within the *Nafion®-Pt/C* catalyst layer. At this optimum ionomer loading, the *Nafion®-Pt/C* catalyst demonstrates a two-fold increase in catalyst utilisation ( $95 \pm 7 \sim 100 \%$ ) compared with the conventionally-prepared catalyst ( $50 \pm 3 \%$ ) at its corresponding optimum. Beyond this optimum ionomer content, the electrical isolation of Pt/C agglomerates by an encapsulating ionomer film has a negative impact on utilisation, as observed for the standard catalyst preparation above 33 wt %. The fact that 100% utilisation is measured in spite of the apparent agglomeration of Pt particles is encouraging, as it implies that the degree of Pt-Pt particle contact is sufficiently low as to have very little effect on the active surface area of the catalyst, and proves that Pt particles and agglomerates are in good electrical contact with the carbon support. It would be impossible to attain such high utilisations if significant numbers of Pt particles were electrically isolated from the support.

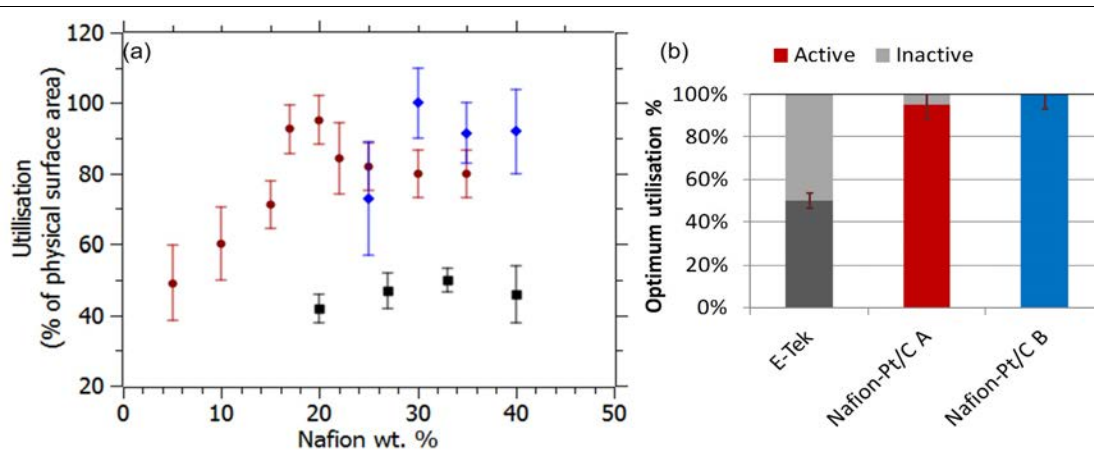


Figure 5.7: (a) Catalyst utilisation as a function of Nafion® content for Nafion®-Pt/C A (●), Nafion®-Pt/C B (◆) and E-Tek (■) catalysts and (b) optimum catalyst utilisations found in this study for each catalyst.

**Nafion®-Pt/C B** Interestingly, the Nafion®-Pt/C B catalyst had a higher optimum Nafion® content than Nafion®-Pt/C A. At around 30% NFP, this optimum Nafion® loading is similar to that found for the E-Tek catalyst, although the Nafion®-Pt/C B is fully utilised at this Nafion® loading, whilst the E-Tek catalyst only reaches 50% utilisation. The variation in optimum Nafion® content between the Nafion®-Pt/C A and B catalysts can only be attributed to their differing morphologies, as their physical surface areas, Pt particle size distributions and Pt/C ratios are very similar. The need for a higher Nafion® loading is indicative of a less efficient ionomer percolation in the Nafion®-Pt/C B catalyst, akin to that found in a standard catalyst preparation. This finding supports the assertion that the Pt agglomerates in the Nafion®-Pt/C A catalyst contain a highly-effective internal ionomer network: it is logical that to establish connectivity between relatively small numbers of agglomerates should require less ionomer than for numerous individual, well-dispersed Pt nanoparticles.

### 5.3.3 Oxygen reduction performance

Measurement of oxygen reduction kinetics was carried out using a rotating disc electrode in O<sub>2</sub>-saturated 0.1 M perchloric acid as described in section 5.2.4. The raw RDE data was corrected for background currents by subtracting an LSV scan performed at 25 mV/s under nitrogen purge, before correcting potentials for ohmic resistance using  $\Delta E = IR$  where  $I$  is the current at each data point and  $R$  is the ohmic resistance between the working and reference electrodes determined by impedance spectroscopy at 10 kHz. The effect of the background and Ohmic drop corrections on the measured data can be seen in Figure 5.8. A summary of the data collected during typical RDE experiments is presented in Figure 5.9. The raw O<sub>2</sub> RDE data has a small positive current response above +1 V due to Pt oxide formation and capacitive currents from the carbon support, which are removed by subtracting the background scan. Then, the Ohmic drop correction has the effect of

## 5 Electrochemical characterisation of Nafion®-Pt/C catalysts

shifting the curve in the mixed-control region towards more positive potentials by up to 50 mV. The effects appear subtle but are of great importance in making accurate and unambiguous measurements of kinetic current densities in subsequent analyses[108].

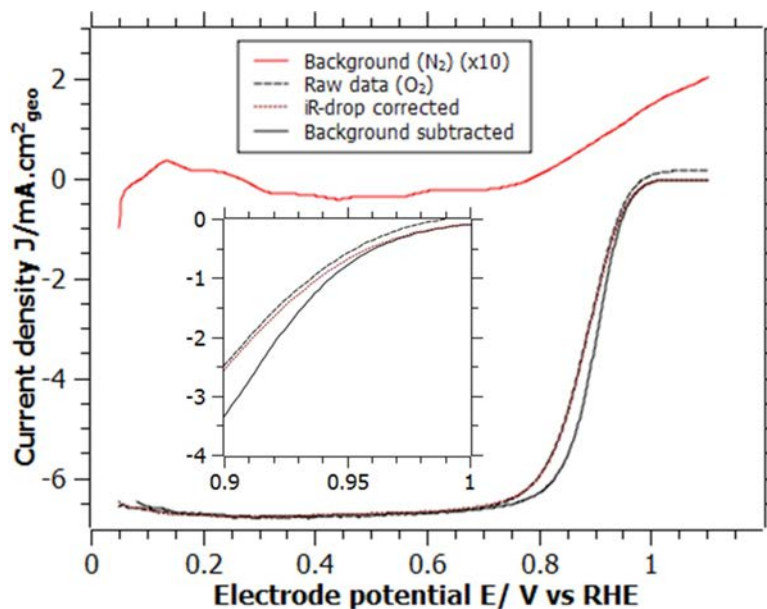


Figure 5.8: Anodic linear sweep voltammograms in  $N_2$  and  $O_2$ , showing the effect of background subtraction and Ohmic ( $iR$ -drop) corrections. Inset shows in more detail the effect of the Ohmic and background corrections over the potential range 0.9 – 1.0 V.

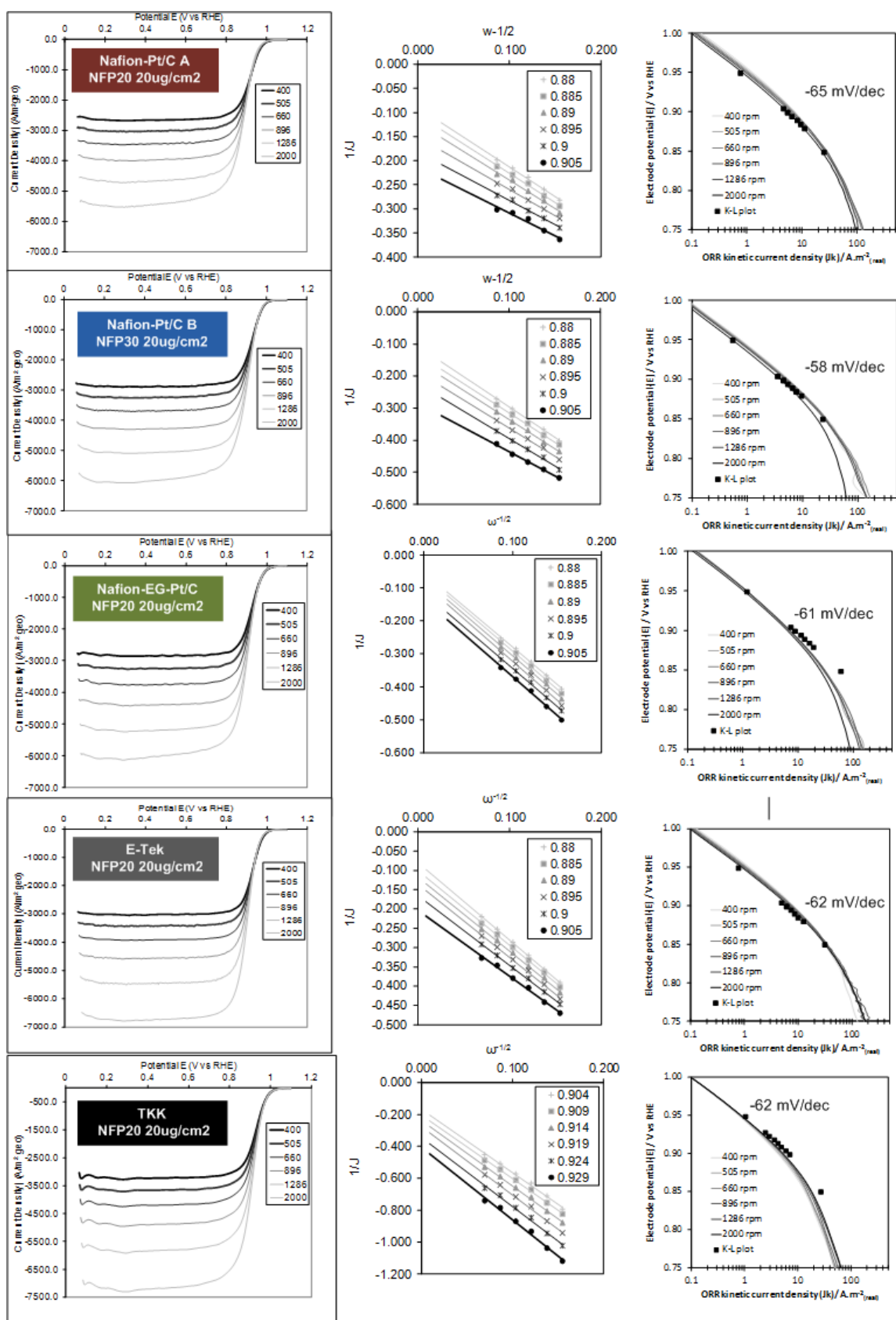


Figure 5.9: (left)  $iR$ -corrected, background-subtracted RDE data at various rotation rates; (centre) Koutecky-Levich plots; (right) mass-transport corrected Tafel plots for each electrocatalyst under test in  $\text{O}_2$ -saturated 0.1 M  $\text{HClO}_4$  at 25°C.

## 5 Electrochemical characterisation of Nafion®-Pt/C catalysts

### O<sub>2</sub> mass transport

Commenting generally on the results shown Figure 5.9, the limiting current densities observed for all thin-film catalysed RDEs were close to the theoretical values determined from the Levich equation for a 5mm diameter RDE in O<sub>2</sub>-saturated solution at 25°C, using the parameters shown previously in Table 5.1. For example, the Levich limiting current at 2000 RPM should be -6.7 mA.cm<sup>-2</sup>, and the experimental values shown in Table 5.4 are all within 10% of this figure, except that found for Nafion-Pt/C A, which was some 17% lower than expected. This discrepancy may be indicative of an additional barrier to the diffusion of O<sub>2</sub> presented by capping ionomer in the Nafion-Pt/C A catalyst.

|                     | $J_{lim} @ 2000 \text{ rpm} /$<br>$\text{mA.cm}^{-2}$ | $D_{eff} /$<br>$10^{-5} \text{ cm}^2.\text{s}^{-1}$ |
|---------------------|---|---|
| Nafion®-Pt/C A      | -5.53   | 1.61  |
| Nafion®-Pt/C B      | -6.29   | 2.06  |
| Nafion®-EG-<br>Pt/C | -6.54   | 2.00  |
| E-Tek               | -6.78   | 2.40  |
| TKK                 | -6.79   | 2.42  |

Table 5.4: Limiting current densities at 2000 RPM and effective O<sub>2</sub> diffusion coefficients at 25°C calculated from Figure 5.10 for each catalyst employed in this study.

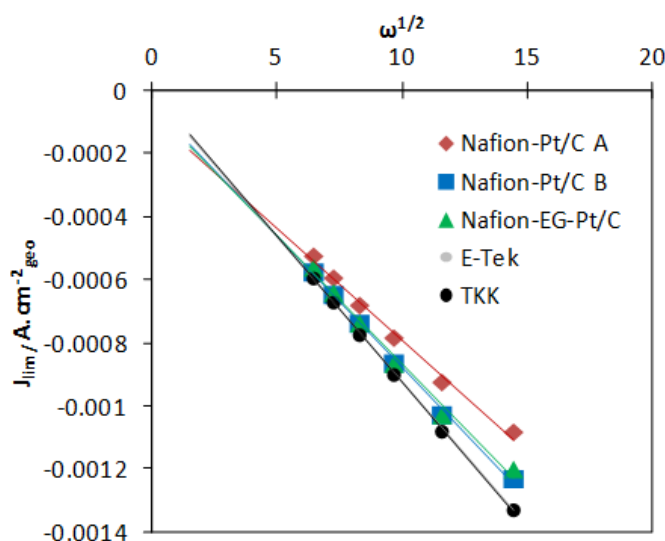


Figure 5.10: Levich plot for thin-film catalysed RDEs, showing linear relationships between limiting current densities  $J_{lim}$  and the square root of angular frequency  $\omega^{1/2}$  for each electrode prepared by the EG-SC method at Pt loadings of 20  $\mu\text{g}/\text{cm}^2$ .

The limiting currents were also found to be linearly dependent on  $\omega^{1/2}$  as predicted by the Levich equation. From the slopes of the Levich plots in Figure 5.10, effective diffusion coefficients ( $D_{eff}$ )

for each electrode were calculated and are summarised in Table 5.4. The diffusion of O<sub>2</sub> was found to be slower for Nafion®-stabilised electrocatalysts than for both the commercial catalysts. The Nafion®-Pt/C A catalyst had the lowest effective diffusion coefficient (1.61 x 10<sup>-5</sup> cm<sup>2</sup>.s<sup>-1</sup>), and it is thought that this is due to a relatively thick layer of Nafion® encapsulating Pt agglomerates on the carbon support. This impaired mass transport may be exacerbated in gas diffusion electrodes, reducing the performance of MEAs operating at high current densities, and this will be investigated further in *in-situ* testing in Chapter 5.

## **ORR Kinetics**

The background and iR-corrected RDE curves in Figure 5.11 (a) show variations in onset and half-wave potentials for ORR in the mixed kinetic/diffusion controlled region between 0.8 – 1.0 V, which are due to the differences in electrode kinetics, quantified by kinetic current densities shown in the Tafel plot in Figure 5.11 (b). Kinetic current densities in Figure 5.11 (b) are calculated using the Koutecky-Levich equation as described in section 3.3.4 (page 38), and at +0.9 V these are in good agreement with values obtained by extrapolating Koutecky-Levich plots as shown in the Tafel plots in Figure 5.9. The specific activities *SA* at +0.9 V calculated using the K-L plot method and mass activities *MA*, calculated according to

$$MA [A.g_{Pt}^{-1}] = SA [A.m_{real}^{-2}] \cdot ECSA [m^2.g_{Pt}^{-1}] \quad (5.1)$$

are shown in Figure 5.11 (c-d) and Table 5.5. Tafel slopes calculated in the range + 0.88 to + 0.9 V are given in Table 5.5.

| <b>Catalyst</b> | <b>Particle size / nm</b> | <b>A<sub>Phys</sub> / m<sup>2</sup>.g<sup>-1</sup><sub>Pt</sub></b> | <b>ECSA / m<sup>2</sup>.g<sup>-1</sup><sub>Pt</sub></b> | <b>u<sub>Pt</sub> %</b> | <b>SA @ 0.9V / A.m<sup>-2</sup><sub>real</sub></b> | <b>MA @ 0.9V / A.g<sup>-1</sup><sub>Pt</sub></b> | <b>Tafel slope b / mV.dec<sup>-1</sup></b> |
|-----------------|---------------------------|---|---|-------------------------|--|--|--|
| Nafion®-Pt/C A  | 7.8                       | 37  | 35  | 95                      | 6.19   | 169  | -65  |
| Nafion®-Pt/C B  | 5.6                       | 51  | 45  | 88                      | 6.00   | 328  | -58  |
| Nafion®-EG-Pt/C | 5.8                       | 49  | 46  | 94                      | 7.88   | 362  | -61  |
| E-Tek 50wt%     | 4                         | 71  | 55  | 76                      | 6.93   | 341  | -62  |
| TKK 46wt%       | 2.9                       | 98  | 91  | 93                      | 6.02   | 507  | -62  |

Table 5.5: Summary of physical and ORR electrocatalytic properties of the catalysts measured at 25°C in 1 atm O<sub>2</sub>-saturated 0.1M HClO<sub>4</sub>, including specific activities *SA* (A.m<sup>-2</sup><sub>real</sub>) and mass activities *MA* (A.g<sup>-1</sup><sub>Pt</sub>) at 0.9 V vs RHE.



## 5 Electrochemical characterisation of Nafion®-Pt/C catalysts

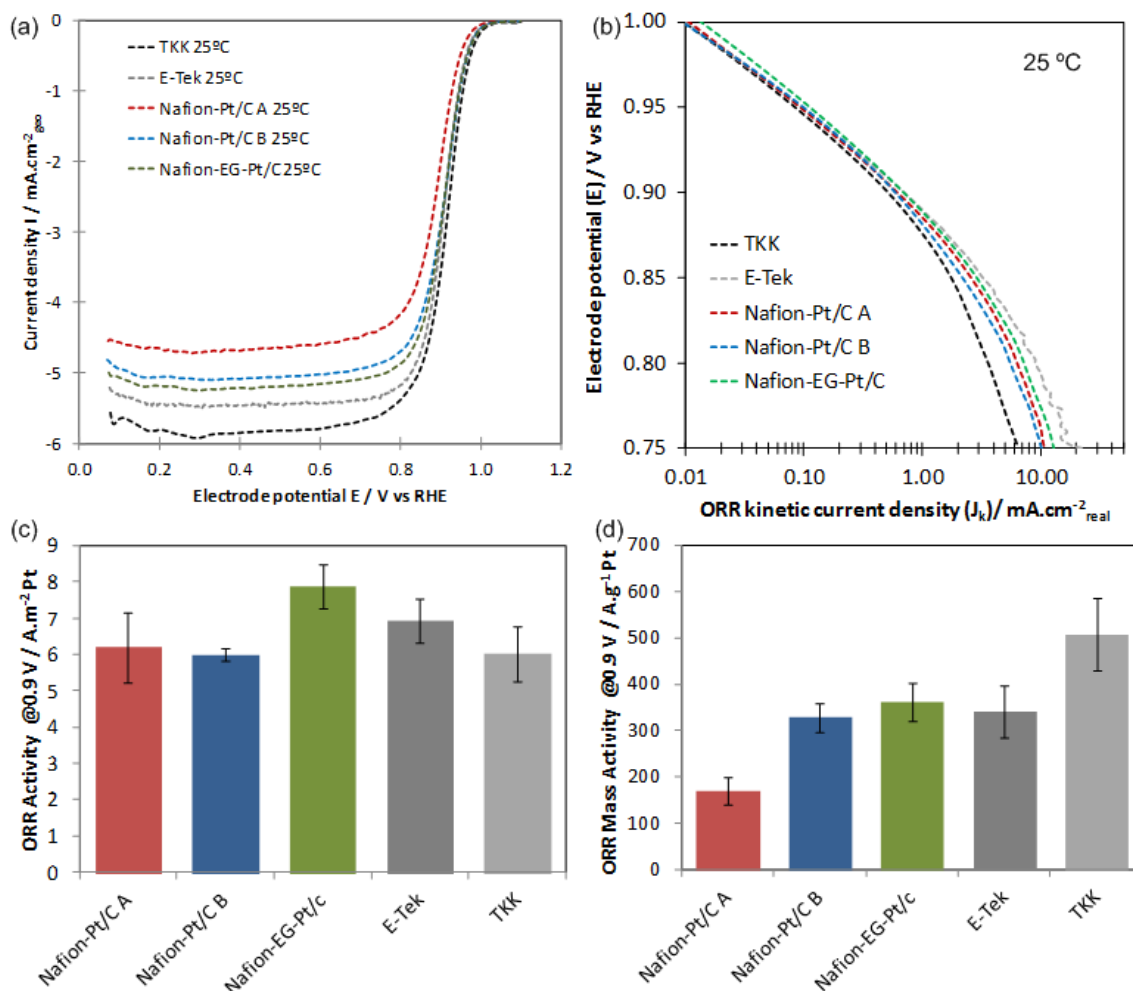


Figure 5.11: (a) *iR*-corrected RDE curves recorded at 1286 RPM, 25 mV/s in  $\text{O}_2$  saturated 0.1 M  $\text{HClO}_4$  at 25°C; (b) mass-transport corrected Tafel plots; (c) ORR specific activities and (d) ORR mass activities at 0.9 V. Catalysts in (c) and (d) are arranged in decreasing order of Pt particle size from left to right.

### Pt particle size effects

The results presented in Figure 5.11 (c) show no significant variations in specific activity between the catalysts on test. The SAs are all within experimental error of  $6 - 8 \text{ A} \cdot \text{m}^{-2}_{\text{real}}$ , with no obvious dependence on particle size. According to Mayrhofer *et al*, an increase in SA of approximately a factor of 2-3 should be expected for the 7.8 nm Nafion®-Pt/C A catalyst versus the 2.9 nm TKK catalyst [107]: an effect that has been attributed to geometric effects such as the increasing prevalence of less-active edge and corner sites[95, 108, 150-160], and as a result of stronger adsorption of reaction intermediates owing to a negative shift in the potential of zero charge for smaller particles[106]. However, more recently Nesselberger *et al* attributed such variations in SA to contributions to the ORR current from capacitive currents originating from the carbon support[108], which were not accounted for in the treatment of experimental data in ref [107]. By

removing the effect of capacitive currents (as has been performed in this work by subtraction of background scans), Nesselberger *et al* found very little variation in SA for Pt particles with sizes from 2- 8 nm, and the results obtained here are in good agreement with this finding.

The fact that Nafion®-Pt/C catalysts show similar SA to the commercial catalysts is encouraging, and shows that the reaction is not inhibited by capping Nafion® in contact with Pt surfaces.

The variations in mass activity between the catalysts shown in Figure 5.11 (d) are in keeping with the differences in particle size and specific surface area i.e. mass activity is found to increase with decreasing particle size.

## **Hydrogen peroxide production**

The amount of peroxide production on the Nafion®-Pt/C A catalyst was quantified and compared against that of the TKK catalyst using a rotating ring-disc electrode (RRDE).

### **RRDE collection efficiency calibration**

In an RRDE experiment, only a fraction of the electroactive species generated on the disc is detected by the ring. This fraction, known as the collection efficiency,  $N$ , must be measured in advance in order to quantify the rate of formation on the disc. Measurement of  $N$  is usually conducted using a reversible or quasi-reversible redox couple; in this case the ferri/ferrocyanide pair. A solution of 10 mM potassium ferrocyanide was prepared in a 0.1M NaOH background electrolyte. Using a TKK supported catalyst with a Pt loading of 20  $\mu\text{g}\cdot\text{cm}^{-2}$  on the GC disc as the working electrode and a silver/silver chloride reference electrode, the disc potential was swept cathodically from + 0.6 to + 0.0 V at 25  $\text{mV}\cdot\text{s}^{-1}$  whilst maintaining the ring potential constant at + 1.1 V vs. RHE. The ring potential was set such that the reaction occurring at the ring was entirely diffusion-limited.

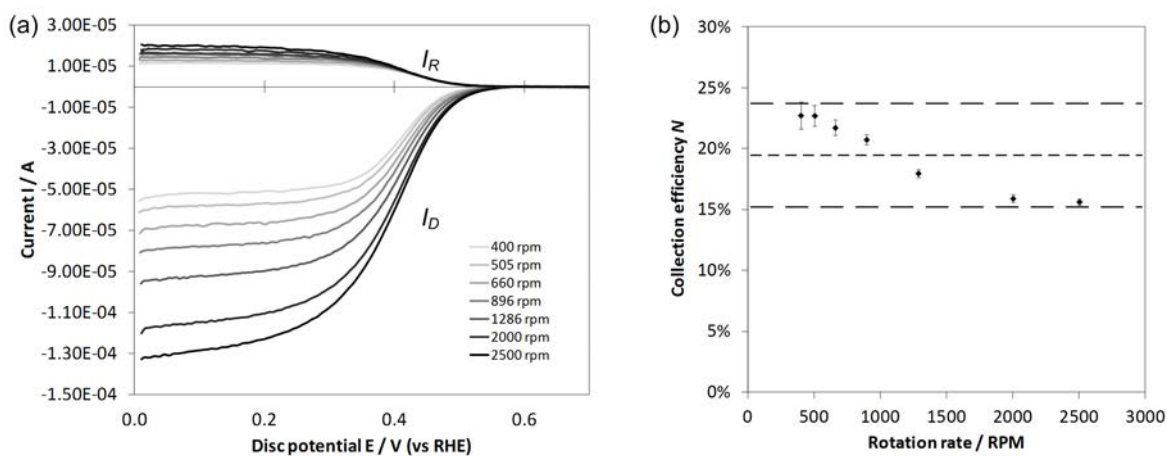
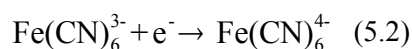


Figure 5.12: (a) Currents measured at the Pt/C catalysed disc and Pt ring electrodes for the  $\text{Fe}(\text{CN})_6^{3-} \rightarrow \text{Fe}(\text{CN})_6^{4-}$  reaction at several rotation rates; (b) illustrating the variation in collection efficiency as a function of rotation rate.

## 5 Electrochemical characterisation of Nafion®-Pt/C catalysts

---

Figure 5.12 (a) shows hydrodynamic linear sweep voltammograms for the RRDE experiment, in which the disc currents  $I_D$  correspond to the reduction reaction:



and the ring currents  $I_R$  are due to the reverse reaction; that is, the oxidation of the ferricyanide product formed on the disc.

Evidently the ring currents are far smaller in magnitude than the disc currents, and the collection efficiency  $N$  of the ring can be calculated according to  $N = I_R/I_D$ .

Figure 5.12 (b) shows the variation in collection efficiency with rotation rate. Ideally,  $N$  should be independent of rotation rate, but for the setup employed in this study a small variation in  $N$  was observed. This could be due to small asymmetries in the geometry of the RRDE; the plane of the disc may not be perfectly parallel to that of the ring, or there might be some eccentricity in the rotation of the electrode, for instance. For the range of rotation rates employed here (400 – 2500 RPM), the collection efficiency was measured at  $N = 19 \pm 4 \%$ .

### Measurement of H<sub>2</sub>O<sub>2</sub> production during ORR

The rate of peroxide production on the TKK catalyst was found to be ~10% at  $E = +0.1\text{V}$ , which is in good agreement with previous work on Pt/C catalysts with similar Pt particle sizes [100-101, 103]. Figure 5.13 shows that below +0.3 V, the rate of peroxide production is significantly higher on Nafion®-Pt/C A than on the TKK catalyst, with the former yielding 40 % H<sub>2</sub>O<sub>2</sub> at 0.1 V. The tendency toward the 2e<sup>-</sup> pathway may be attributed to a combination of particle size effects and modifications to the Pt surface by adsorbed Nafion®. Previous studies have found that the rate of H<sub>2</sub>O<sub>2</sub> production in the  $H_{upd}$  potential region is higher for larger Pt particles [101], and for Pt surfaces in contact with a layer of adsorbed Nafion® [101, 104]. Thus the enhanced Pt-Nafion® interface in the Nafion®-Pt/C A catalyst may be partly responsible for the higher rate of peroxide formation. Some of the unwanted enhancement in peroxide formation may also be ascribed to differences in the age of the catalyst inks as described by Biddinger *et al*, who found that selectivity towards the 4e<sup>-</sup> pathway improved upon resting inks for several days prior to testing [102].

Importantly, however, the rate of peroxide production is negligible over the range of potentials constituting the typical operating range of the PEMFC cathode (+0.6 to +1.0 V). Thus the Nafion®-Pt/C catalyst is unlikely to exacerbate durability problems under normal operating conditions.

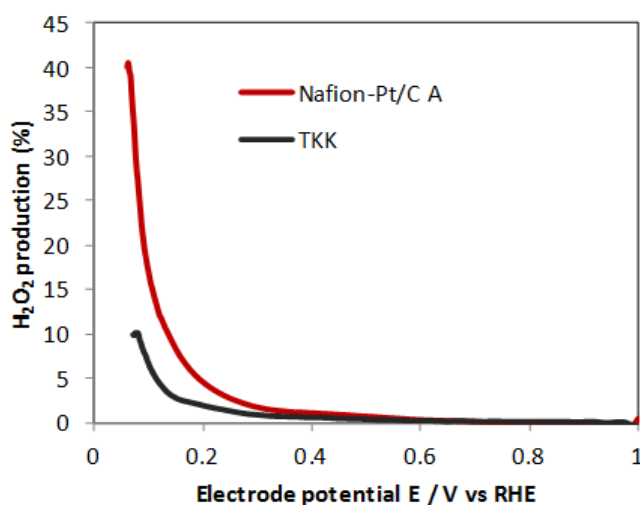


Figure 5.13: Peroxide production during ORR on both Nafion®-Pt/C A and TKK catalysts

### 5.3.4 RDE studies at elevated temperature

Whilst it has been shown that trends in SA and MA identified in low-temperature RDE tests are usually reflected qualitatively by trends in MEA performance, the absolute values obtained for kinetic parameters at 25°C cannot be compared directly with kinetic data obtained from *in-situ* testing, which requires cell temperatures of 60 - 80°C. For comparison with *in-situ* ORR activities, RDE experiments should be performed under conditions which are as close as possible to those used in single-cell testing on MEAs. Whilst the presence of the liquid electrolyte in RDE testing means that the two methods are inherently dissimilar, they can be made more comparable by ensuring that the temperature and O<sub>2</sub> partial pressure are similar in both methods. Thus additional RDE testing was carried out at 70 °C, with 1 atm O<sub>2</sub>-saturated 0.1 M HClO<sub>4</sub>.

According to the Nernst equation (2.4) (page 19), at 70°C the potential of the RHE shifts by -17mV relative to its potential at 25°C (0.00 V vs. SHE) [161]. The potential shift was verified experimentally by measuring the potential difference between a RHE immersed in 0.1M HClO<sub>4</sub> at 70°C and another RHE containing 0.1 M HClO<sub>4</sub> at 25°C placed momentarily into the same electrolyte solution. The working electrode potentials measured at elevated temperature were corrected accordingly, so that they refer to RHE(25°C) = 0.00 V vs. SHE.

#### Temperature dependence of O<sub>2</sub> concentration and diffusion coefficient

With increasing temperature, the solubility of oxygen in aqueous solution decreases rapidly, owing to the increasing vapour pressure of water. Meanwhile, diffusion becomes faster as the viscosity of the electrolyte decreases (Figure 5.14 (a)). These effects combine to produce a dramatic

## 5 Electrochemical characterisation of Nafion®-Pt/C catalysts

reduction in the Levich limiting current density at  $T > 60^\circ\text{C}$ . Figure 5.14 (b) shows the theoretical variation of  $J_{lim}$  according to the Levich equation (3.10) (page 37) with temperature based on the temperature dependence of the quantities  $D$ ,  $C[\text{O}_2]$  and  $\nu$ , with values normalised to  $J_{lim}$  at  $25^\circ\text{C}$ . Limiting current densities are fairly constant up to around  $50^\circ\text{C}$ , but for a given rotation rate,  $J_{lim}$  at  $70^\circ\text{C}$  should be around 20% lower than at  $25^\circ\text{C}$ .

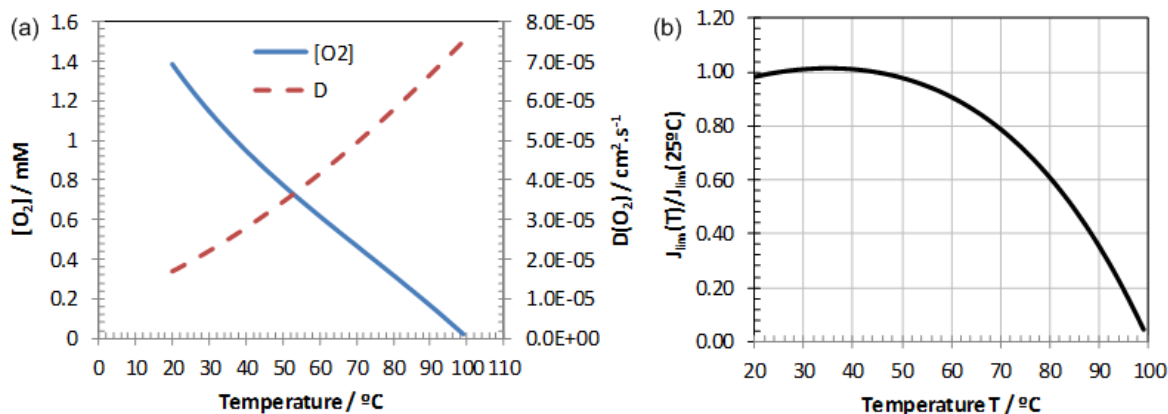


Figure 5.14: (a) Temperature dependence of oxygen concentration  $[\text{O}_2]$  and diffusion coefficient  $D(\text{O}_2)$  in aqueous solution; (b) plot showing the variation of Levich limiting current with temperature, normalised to the limiting current at  $25^\circ\text{C}$  (valid for all rotation rates).

The linearity of the Levich plots in Figure 5.15 (b) demonstrates that the mass transport characteristics of all the electrodes under test are well-described by Levich theory.

According to the Levich equation, at 1286 RPM and  $70^\circ\text{C}$ , the limiting current density for ORR should be  $J_{lim} = -4.4 \text{ mA}\cdot\text{cm}^{-2}$ . The limiting currents from the RDE voltammograms shown in Figure 5.15 are given in Table 5.6. Consistent with the results at  $25^\circ\text{C}$ , at  $70^\circ\text{C}$  the Nafion®-Pt/C A catalyst has a slightly lower  $J_{lim}$  than predicted by the Levich equation, which may be attributed to non-uniform distribution of Pt agglomerates on the carbon support or a rather thick layer of ionomer surrounding these Pt agglomerates, which may introduce additional mass transport resistances. The effective diffusion coefficient is correspondingly lower for the Nafion®-Pt/C A catalyst ( $D_{eff} = 3.7 \text{ cm}^2\cdot\text{s}^{-1}$ ) than for the other catalysts on test. By contrast, the Nafion®-Pt/C B catalyst with well-dispersed Pt particles has a higher  $J_{lim}$  than predicted by theory, which may be due to macroscopic roughness of the catalyst film on the RDE. Limiting currents measured for the other catalysts are in good agreement with the theoretical value (within 10%).

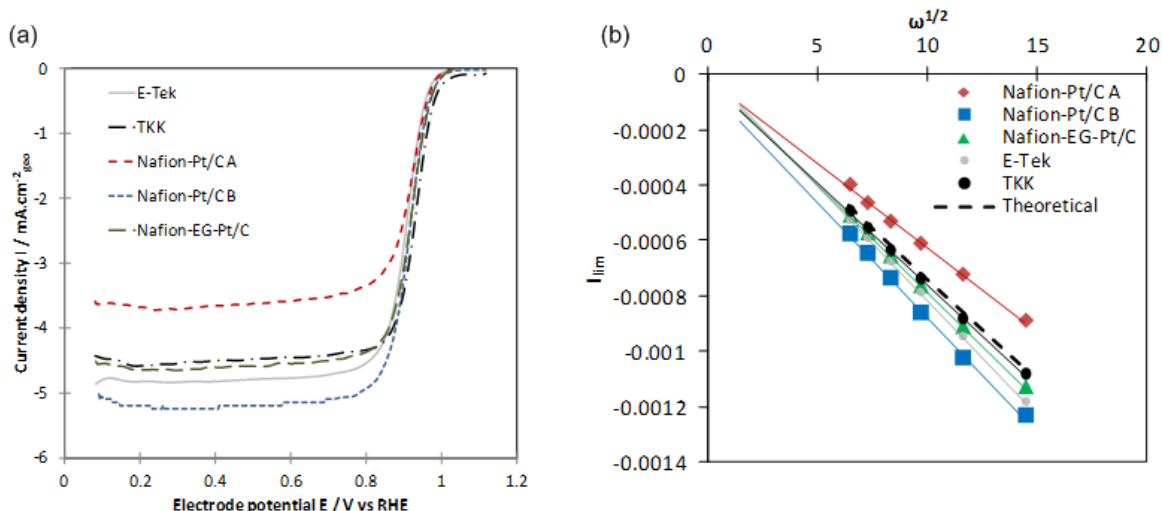


Figure 5.15: (a) RDE curves recorded at 25mV/s 1286 rpm 70°C in  $\text{O}_2$ -saturated 0.1M  $\text{HClO}_4$ ; (b) Levich plots for each catalyst under these conditions for rotation rates from 400-2000 rpm.

| 70°C            | $J_{\text{lim}}$ @ 1286 rpm / $\text{mA.cm}^{-2}$ | $D_{\text{eff}} / 10^{-5} \text{ cm}^2.\text{s}^{-1}$ |
|-----------------|---|---|
| Nafion®-Pt/C A  | -3.7  | 3.7   |
| Nafion®-Pt/C B  | -5.2  | 5.9   |
| Nafion®-EG-Pt/C | -4.6  | 5.3   |
| E-Tek           | -4.8  | 5.8   |
| TKK             | -4.5  | 4.9   |

Table 5.6: Limiting current densities and effective diffusion coefficients for catalysts measured at 70°C.

## ORR kinetics at 70°C

At 70°C the reaction kinetics for ORR are faster than at 25°C, but the lower  $\text{O}_2$  concentration negates this effect, such that measured specific activities are barely any higher than at 25°C. This effect can be compensated by correcting specific activities for  $\text{O}_2$  concentration according to

$$J_k = k [\text{O}_2]^\gamma \quad (5.3)$$

where  $J_k$  is the kinetic current density,  $k$  is the rate constant for the ORR,  $[\text{O}_2]$  is the  $\text{O}_2$  concentration in the electrolyte and  $\gamma$  is the reaction order. By assuming  $\gamma \approx 1$  for the ORR [22, 100, 162], from (5.3) one can obtain

$$\Delta J_k = k \Delta [\text{O}_2] \quad (5.4)$$

and by using values for  $[\text{O}_2]$  at 25°C ( $[\text{O}_2] = 1.260 \times 10^{-6} \text{ mol.cm}^{-3}$ ) and 70°C ( $[\text{O}_2] = 4.662 \times 10^{-7} \text{ mol.cm}^{-3}$ ) kinetic currents measured at 70°C can be adjusted to  $[\text{O}_2]$  at 25°C according to

## 5 Electrochemical characterisation of Nafion®-Pt/C catalysts

$$J_k|_{[O_2]=1.26 \times 10^{-6} \text{ mol.cm}^{-3}} = \frac{1.26 \times 10^{-6}}{4.66 \times 10^{-7}} \cdot J_k|_{[O_2]=4.66 \times 10^{-7} \text{ mol.cm}^{-3}} \quad (5.5)$$

The theoretical temperature dependence of specific activity at constant overpotential and O<sub>2</sub> concentration is given by the Arrhenius equation:

$$J_k = A \exp\left(\frac{-E_a}{RT}\right) \quad (5.6)$$

Where  $E_a$  is the activation energy in kJ.mol<sup>-1</sup> and the pre-exponential factor  $A$  is specific to the electrode and reaction in question. By assuming the activation energy for ORR on Pt/C to be  $E_a = 21$  kJ.mol<sup>-1</sup> [163], the specific activity at 70°C can be predicted from measurements obtained at 25°C according to

$$J_k|_{T=70^\circ\text{C}} = J_k|_{T=25^\circ\text{C}} \exp\left[\frac{E_a}{R} \left(\frac{1}{298} - \frac{1}{343}\right)\right] \quad (5.7)$$

Specific activities corrected for [O<sub>2</sub>] using (5.5) are given in Table 5.6, and are compared to the uncorrected values in Figure 5.16 (c). Values for SA predicted from measurements performed at 25°C using equation (5.2) are given in Table 5.7, and are clearly significantly lower than the [O<sub>2</sub>]-corrected values measured at 70°C. This discrepancy may be attributed to variations in the transfer coefficient  $\alpha$  with temperature [110], as well as uncertainties in the O<sub>2</sub> concentration at the Pt interface introduced by the presence of the ionomer within the thin film electrode.

| Catalyst        | Particle size / nm | 25°C  |   | 70°C ([O <sub>2</sub> ] corrected)                        |   |   |   |
|-----------------|--------------------|---|---|---|---|---|---|
|                 |                    | SA @ 0.9V / A.m <sup>-2</sup> <sub>real</sub> | MA @ 0.9V / A.g <sup>-1</sup> <sub>Pt</sub> | Theoretical SA @ 0.9V / A.m <sup>-2</sup> <sub>real</sub> | SA @ 0.9V / A.m <sup>-2</sup> <sub>real</sub> | MA @ 0.9V / A.g <sup>-1</sup> <sub>Pt</sub> | Tafel slope <i>b</i> / mV.dec <sup>-1</sup> |
| Nafion®-Pt/C A  | 7.8                | 6.19  | 169   | 19  | 26.70   | 860   | -65   |
| Nafion®-Pt/C B  | 5.6                | 6.00  | 328   | 18  | 23.80   | 1070  | -58   |
| Nafion®-EG-Pt/C | 5.8                | 7.88  | 362   | 24  | 23.80   | 1131  | -61   |
| E-Tek 50wt%     | 4                  | 6.93  | 341   | 21  | 23.40   | 798   | -62   |
| TKK 46wt%       | 2.9                | 6.02  | 507   | 14  | 22.10   | 1947  | -62   |

Table 5.7: Summary of physical and ORR electrocatalytic properties of the catalysts measured at 25°C and 70°C in 1 atm O<sub>2</sub>-saturated 0.1 M HClO<sub>4</sub>, including specific activities SA (A.m<sup>-2</sup><sub>real</sub>) and mass activities MA (A.g<sup>-1</sup><sub>Pt</sub>) at +0.9 V vs. RHE, normalised to an O<sub>2</sub> concentration of [O<sub>2</sub>]=1.260 x 10<sup>-6</sup> mol.cm<sup>-3</sup>. Theoretical SAs at 70°C are based on calculations from data obtained at 25°C using equation (5.7).

From the data in Table 5.7, Figure 5.16 (a) and (c) it is clear that the specific activities of all the catalysts are fairly similar, although there is evidence of a particle size effect in the gradually decreasing trend in SA with decreasing particle size. The effect is more pronounced than at 25°C,

---

suggesting that the origins of the effect (adsorption of OH) may be temperature-dependent. The existence of such a temperature dependence may explain some of the discrepancies in the literature between studies conducted at 25°C, which report negligible size effects in the range 2-8 nm [108], and those at higher temperatures which typically do identify such effects[12]. To the author's knowledge, there have been no previous studies concerning the temperature-dependence of the particle size effect for ORR on Pt, and this is worthy of further investigation.

The variations in mass activity in Figure 5.16 (b) and (d) follow the expected increasing trend with decreasing particle size, with the exception of the E-Tek catalyst whose mass activity is somewhat lower than those of Nafion®-Pt/C catalysts despite having a smaller Pt particle size. This finding is in keeping with the observations at 25°C, and is due to the relatively poor utilisation of the E-Tek catalyst (*ca.* 80%) compared with the other catalysts.

The Tafel slopes measured at 70°C are very similar to those measured at 25°C, whereas they should be around 10mV more negative according to  $b=2.303RT/\alpha nF$ . However, the curvature of the Tafel plot in the potential range 0.88-0.95 V creates difficulties in determining a single value for the slope, and differences in  $b$  of <10 mV.decade<sup>-1</sup> are hard to distinguish. Additionally, the increase in  $\alpha$  with increasing  $T$  has an opposing effect on  $b$  [110], and variations in  $\alpha$  could easily account for the observed deviations of Tafel slopes.



## 5 Electrochemical characterisation of Nafion®-Pt/C catalysts

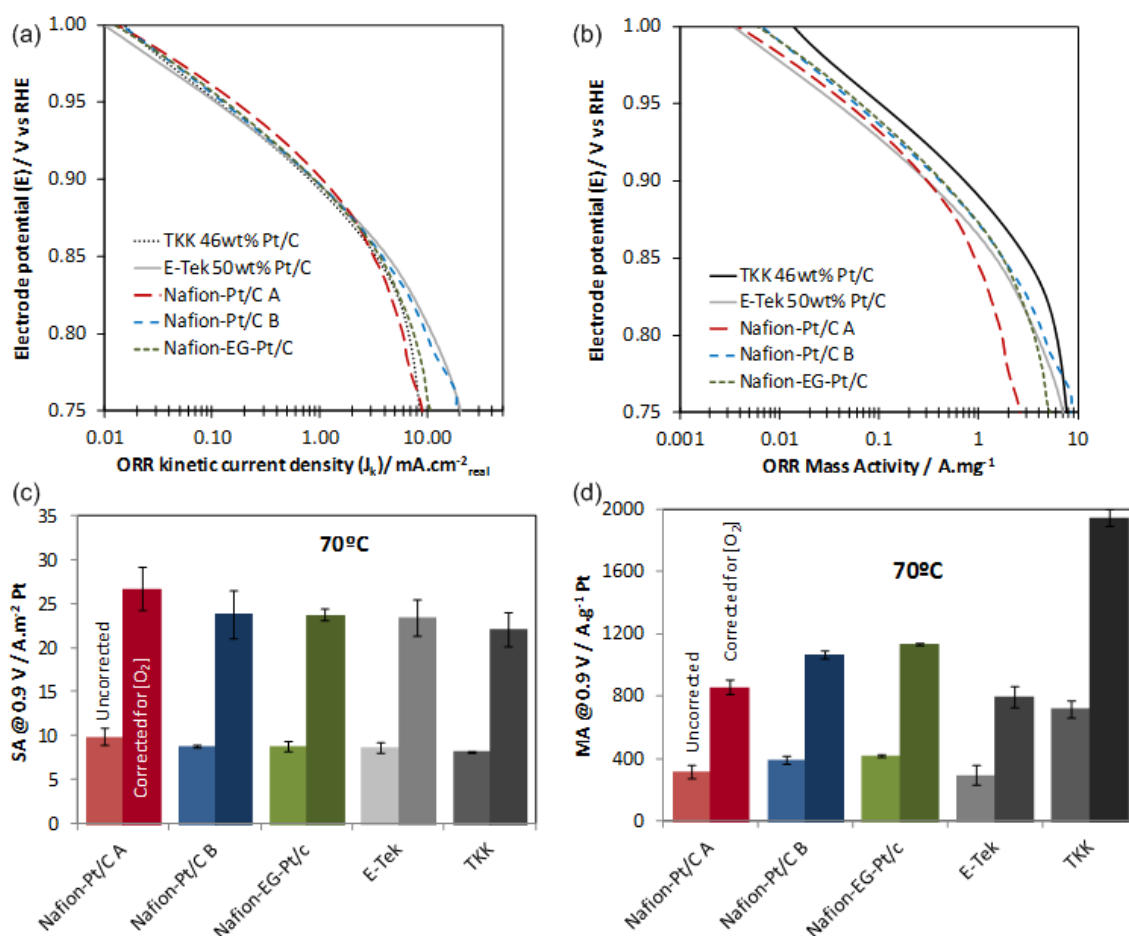


Figure 5.16: (a) Tafel plots with kinetic current densities normalised by ECSA; (b) ORR mass activity data for ORR at 70°C (not corrected for [O<sub>2</sub>]); (c) comparison of ORR specific activities and (d) mass activities at 0.9 V vs. SHE, showing uncorrected values and those that are corrected for [O<sub>2</sub>] according to equation (1.16).

The various discrepancies between data measured at 70°C and predicted quantities extrapolated from data measured at 25°C re-emphasise the need to carry out RDE experiments at temperatures as close as possible to the operating temperature of the PEMFC in order to make valid quantitative comparisons with results from *in-situ* testing.

## 5.4 Conclusions

The methods described in section 5.2 have afforded consistent, reliable and reproducible data describing the electrochemical characteristics of Nafion®-Pt/C and commercial catalysts. The results obtained for the Pt disc and TKK commercial catalyst are in good agreement with previous reports in the literature. The EG-SC method for preparing catalysed electrodes was particularly valuable in allowing reproducible preparation of high-quality, homogeneous catalyst films.

Reliable indications of optimum ionomer content in the catalyst ink can be derived from utilisation measurements made on electrodes prepared at high Pt loading > 80 μg<sub>Pt</sub>.cm<sup>-2</sup>. Using this method,

---

the optimum Nafion® content for the Nafion®-Pt/C A catalyst was found to be 20 % NFP, compared to *ca.* 33 % for the commercial (E-Tek) catalyst and Nafion®-Pt/C B type catalyst. It is thought that the lower optimum Nafion® loading is a direct result of a more efficient ionomer percolation afforded by the Nafion®-Pt/C preparation route. The Nafion®-Pt/C A catalyst achieved 100% utilisation even at high Pt loadings, although *in-situ* testing will be required to determine whether the new preparation route can improve utilisation in the much thicker catalyst layers within PEMFC electrodes.

The ORR kinetics experiments at both 25°C and 70°C indicate that the specific activities of all three Nafion®-Pt/C type catalysts on test are similar to those of the E-Tek and TKK catalysts. Combined with the near-100% utilisation measured for the Nafion®-Pt/C catalysts, this implies that the preparation route has no detrimental effect on ORR activity e.g. by blocking active sites via adsorption of capping Nafion® or other by-products of the colloidal synthesis. Furthermore, RRDE experiments show that the rate of peroxide production is essentially the same as for standard Pt/C, and the similarity of the Tafel slopes confirms that the reaction mechanism is unchanged.

At 25°C, there was little evidence of a particle size effect for ORR specific activity, but a subtle trend became apparent at 70°C, reconciling the work of Nesselberger *et al* [108] with that of Gasteiger *et al* [12], which at first sight provide differing opinions as to the existence of the size effect. The apparent temperature-dependence of the particle size effect was proposed as an important area for further investigation, but a systematic study is beyond the scope of this work.

## 6 Catalyst Durability

### 6.1 Background

Along with issues of cost, the long-term durability of PEM fuel cell systems remains a significant barrier to the widespread adoption of this technology; especially in applications with demanding start/stop duty cycles such as automotive and portable power systems.

#### 6.1.1 Degradation mechanisms

Nearly all PEMFC components are subject to degradation over the operating life of the system, including balance of plant components, flow-field plates, gaskets and seals. However, it is the membrane electrode assembly (MEA) and its components that present the most challenging degradation issues affecting the long-term durability of the PEMFC. Within the MEA the membrane, electrocatalyst and gas diffusion layer (GDL) materials are subject to chemical and mechanical wear.

The main degradation mechanisms applying to PEMFC electrocatalysts and catalyst layers can be broadly identified as (i) Pt dissolution; (ii) Pt nanoparticle migration and sintering and (iii) carbon corrosion [164] – illustrated schematically in Figure 6.1 and described in detail below.

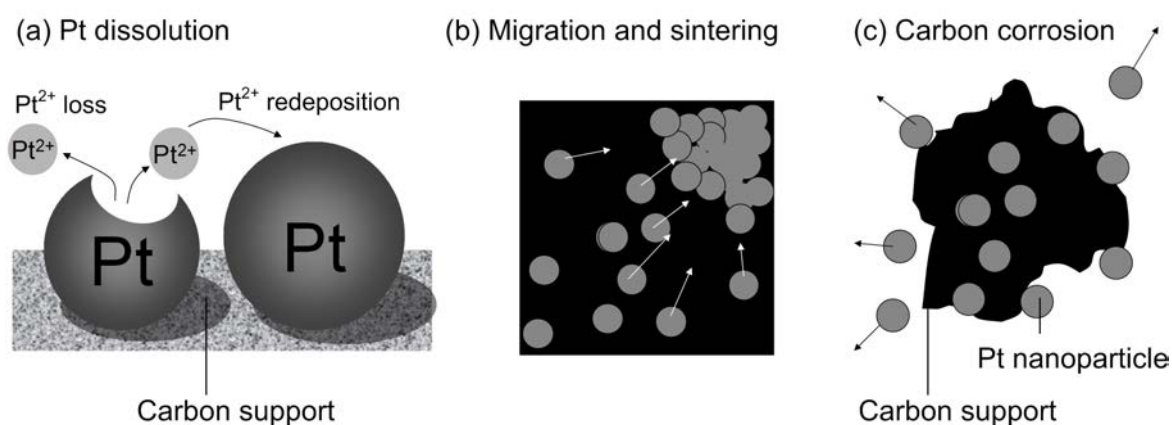
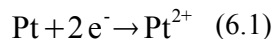


Figure 6.1: Schematic illustration of the three main degradation modes for Pt/C electrocatalysts; (a) Pt dissolution, which can be followed by loss of Pt or redeposition (Ostwald ripening); (b) Pt nanoparticle migration and sintering on the carbon support and (c) corrosion of the carbon support, with detachment of Pt nanoparticles.

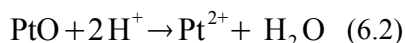
---

## **Pt dissolution & Ostwald ripening**

Pt has been observed to dissolve within a narrow potential window around +1.0 V vs. RHE [165], both directly according to:



and from its oxide:



The rate of reaction (6.1) is far faster than that of reaction (6.2), but the formation of passivating surface oxides at potentials positive of  $\sim +0.8$  V inhibits (6.1) under fixed potential conditions [165]. Only in the case of rapid anodic scans in the potential range +0.6 to +1.0 V can reaction (6.1) proceed at a significant rate, as there is insufficient time for surface oxides to form [166].

The PEMFC cathode presents an acidic and highly oxidative environment. The dissolution of metallic Pt under PEMFC operating conditions has been widely investigated and documented [159, 167-171]. For the reasons outlined above, it is particularly pronounced during rapid increases in cell voltage from around +0.6 V to OCV in response to sudden reduction in current demand on the fuel cell stack (e.g. during vehicle deceleration) [172]. Dissolved Pt then succumbs to one of three fates:

### **1. Removal from the cell/stack in the outlet water**

Soluble Pt species may be flushed from the electrode, particularly at high current densities where the flux of water from the cathode is large.

### **2. Migration into the ionomer membrane adjacent to the catalyst layer**

The ionomer membrane has a finite permeability to soluble Pt species and H<sub>2</sub> gas from the anode. Any Pt<sup>2+</sup> migrating within the membrane can be reduced by H<sub>2</sub> crossing from the anode side to form Pt nanoparticles inside the ionomer, which have been observed by several groups [171, 173-175]. Aside from the loss of ECSA, Pt particles embedded within the ionomer membrane also significantly compromise its durability by catalysing the production of hydrogen peroxide.

### **3. Pt particle growth via Ostwald ripening**

Smaller Pt nanoparticles are more prone to dissolution than larger ones [152, 167-168, 176-178], and soluble Pt species (Pt<sup>2+</sup>) can then be re-deposited at the surface of existing

## 6 Catalyst Durability

---

particles so that, effectively, smaller particles are consumed by larger ones. This growth continues until the size distribution of Pt particles is sufficiently narrow that all Pt particles in the population undergo dissolution at the same rate [179]. This process, known as Ostwald ripening, is one of the major degradation mechanisms for Pt/C catalysts at the PEMFC cathode [171].

Most strategies for the inhibition of Pt dissolution and its effects currently rely upon careful governance of cell or stack operating conditions, and therefore place restrictions on the duty cycle of the PEMFC system. For instance, PEMFC developers generally strive to minimise the time spent under open circuit conditions, and carefully control the anodic sweep rate during cell voltage transients from on-load to open circuit [166, 172] (0.6 – 1.0 V) such that passivating surface oxides have time to form before the Pt corrosion potential is reached. Smoothing of the current demand in this way requires a large sink load (e.g. battery or supercapacitor), which introduces additional cost and complexity into the PEMFC system.

### **Pt migration and sintering**

Nanoparticles supported on carbonaceous materials are not entirely static, but can migrate across the carbon substrate and sinter together to form agglomerates, resulting in loss of active surface area. Several strategies have been adopted to inhibit migration of Pt particles on the carbon support, and usually involve chemical modification of the carbon surface [152, 180-181] (e.g. by heat or acid treatment); modification of the Pt deposition method to enhance the metal-support interaction [182]; or recently the stabilisation of Pt particles using polymers [15-16].

### **Carbon corrosion**

Carbonaceous materials within the cathode can undergo corrosion via the oxidation reaction



Although the cathode potential is typically well above  $E^0$  for reaction (6.3), the kinetics are very slow, such that the rate of carbon corrosion remains negligible up to potentials of about 1.1 V. During startup and shutdown events, the presence of an air/fuel boundary in the anode flow field can drive the cathode potential upwards to about twice the normal OCV ( $\sim +2.0$  V), and significant corrosion of carbon components can then occur [21, 183-184].

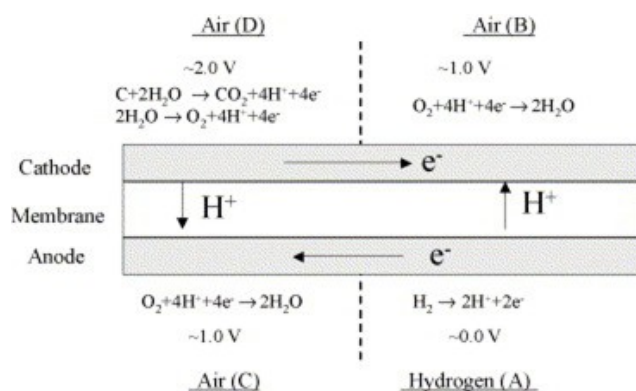


Figure 6.2: Schematic showing the reactions in four regions of a single cell during startup and shutdown, when an air/fuel boundary is established on the anode (areas C and A), which then drives the carbon oxidation reaction in area D. Reproduced from [21]

Carbon electrocatalyst supports are particularly prone to corrosion, resulting in loss of ECSA and dramatic thinning of the catalyst layer, which has been observed in post-mortem analysis of cells subjected to many startup/shutdown cycles [21].

Graphitic carbon materials, CNTs [75] and graphene supports [185] offer enhanced corrosion resistance. Alternative support materials such as TiO<sub>2</sub> [186], TiN [112, 186-187], TiB<sub>2</sub> [16-17], SnO<sub>2</sub> [188] and WC also enhance corrosion resistance but often sacrifice electrical conductivity [189].

Carbon corrosion phenomena are beyond the scope of this work, which focuses on the degradation behaviour of the precious metal component of the catalyst. For fair comparison with commercial catalysts, a standard Vulcan XC-72 R carbon black support has been used for all Nafion®-Pt/C catalysts in this study.

## 6.1.2 Durability testing

### *In-situ* testing

To test the long-term durability of PEMFC components and systems, ideally one would operate a full system under a realistic duty cycle for several thousand hours, with ex-situ post-mortem analysis of components to determine degradation pathways and failure modes. Indeed, this type of testing is necessary for definitive assessment of system durability prior to commercialisation. However, long-term testing of this nature is expensive and has very low throughput, making it impractical for screening of new materials. As an alternative, accelerated stress testing protocols can be applied *in-situ* to induce rapid degradation of cell components at far higher rates than would be typical under normal operating conditions, providing a reasonable indication of durability

## 6 Catalyst Durability

within a few days or even hours. Accelerated Stress Testing (AST) protocols are usually designed to activate a specific degradation pathway related to a single cell component, whilst minimising degradation of other components so that any enhancement in durability can be easily apportioned. AST testing typically involves repetitive cycling of one or more operating parameters, including potential/load [159, 190], temperature, relative humidity [191], gas composition, stoichiometry and flow rate [192-193]. The US DOE has defined a standard AST protocol for the *in-situ* assessment of electrocatalyst durability as shown in Table 6.1.

| <b>Electrocatalyst AST Cycle and Metrics</b>  |  |                                      |
|---|--|--------------------------------------|
| <b>Cycle</b>                                  | Triangle sweep cycle: 50 mV.s <sup>-1</sup> between +0.7 V and +0.9 V.<br>Single cell 25-50 cm <sup>2</sup>  |                                      |
| <b>Number</b>                                 | 30 000 cycles  |                                      |
| <b>Cycle time</b>                             | 16 s   |                                      |
| <b>Temperature</b>                            | 80°C   |                                      |
| <b>Relative Humidity</b>                      | Anode/Cathode 100 %/100 %  |                                      |
| <b>Fuel/Oxidant</b>                           | H <sub>2</sub> /N <sub>2</sub> (H <sub>2</sub> flow rate 200 scc.min <sup>-1</sup> , N <sub>2</sub> 75 scc.min <sup>-1</sup> for 50cm <sup>2</sup> cell) |                                      |
| <b>Pressure</b>                               | Atmospheric pressure   |                                      |
| <b>Metric</b>                                 | <b>Frequency</b>   | <b>Target</b>                        |
| Mass Activity @ 0.857 V                       | Beginning & end of test  | < 40 % loss of MA                    |
| Polarisation curve 0 – 1.5 A.cm <sup>-2</sup> | After 0, 1k, 5k, 10k, and 30k cycles   | <30 mV loss at 0.8 A/cm <sup>2</sup> |
| ECSA  | After 10, 100, 1k, 3k, 10k, 20k and 30k cycles   | <40% loss of initial ECSA            |

Table 6.1: Current US DOE *in-situ* AST cycle for electrocatalyst durability. Reproduced from [193]

In the DOE AST cycle, the lower potential limit of +0.7 V is set such that Pt surface oxides are reduced, leaving a bare Pt surface. The fast scan rate of 50 mV.s<sup>-1</sup> allows insufficient time for passivating surface oxides to form during the anodic scan, so that Pt can dissolve according to equation (6.1) when the potential is increased to +0.9 V. The upper potential limit is set so that the rate of carbon corrosion is negligible. ECSA and I-V curves are recorded at intervals during the AST, and provide metrics for quantitative measurement of degradation.

Similar AST protocols exist for activating degradation mechanisms of a variety of cell components, including carbon electrocatalyst support corrosion and MEA chemical and mechanical stability [193].

### 6.1.3 Ex-situ accelerated stress testing

The *in-situ* AST protocol described in Table 6.1 requires in excess of 200 hours on a single-cell test stand. The limited resources available for this study preclude long-term *in-situ* testing, so an accelerated stress-testing protocol based on the rotating-disc electrode (RDE) will be employed instead. There have been numerous reports of durability studies conducted in liquid electrolytes, using fixed potentials from +0.85 to +1.4 V [194-195] or potential cycling regimes similar to that shown in Table 6.1 [22]. Such studies are often coupled with spectroscopic or gravimetric techniques in order to monitor dissolution/corrosion processes [170, 173, 194-195]. Through judicious choice of the liquid electrolyte composition and AST parameters, the test duration can be reduced to less than 10 hours [22, 196]. Takahashi and Kocha [22] successfully demonstrated an AST regime for the evaluation of electrocatalyst durability in aqueous acidic electrolytes. They applied a square-wave potential cycle from +0.6 to +1.0 V, holding for 1 s at each potential as shown in Figure 6.3 (a). They measured ECSA and mass activity (MA) before and after 7200 cycles. Figure 6.3 (b) shows that, in aqueous 0.5 M H<sub>2</sub>SO<sub>4</sub>, ECSA decreased by 40 % and mass activity by 30% with respect to initial values. Degradation was significantly more pronounced in 0.5 M H<sub>2</sub>SO<sub>4</sub> than in either 0.1 M HClO<sub>4</sub> or 0.5 M H<sub>3</sub>PO<sub>4</sub>, and this was attributed to the ability of SO<sub>4</sub><sup>2-</sup> anions to form complexes with Pt species, which assists the dissolution process.

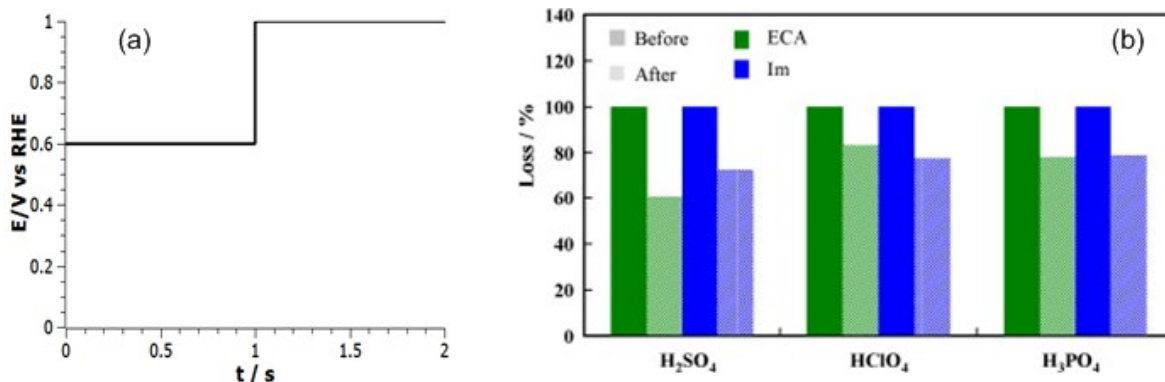


Figure 6.3: (a) AST potential cycle; (b) comparison of ECSA and mass activity ( $I_m$ ) for a TKK 46wt % Pt/C catalyst measured before and after 7200 AST cycles in three different electrolytes (0.5M H<sub>2</sub>SO<sub>4</sub>, 0.1M HClO<sub>4</sub> and 0.5M H<sub>3</sub>PO<sub>4</sub>) at 25°C. Reproduced from [22]

The authors did not conduct post-mortem physical characterisation to determine degradation modes for the electrocatalyst, but other studies have revealed that Pt particle growth, agglomeration and sintering are dominant under similar potential cycling regimes.



### 6.2 Aims and Objectives

The aims and objectives of the work presented in this chapter are as follows:

- To develop AST methods for the comparison of Pt/C electrocatalyst durability using *ex-situ* techniques.
- To compare the durability of Nafion®-Pt/C electrocatalysts against commercially-available catalysts prepared via standard methods.
- To conduct post-mortem analysis on electrocatalysts after AST testing, to elucidate degradation mechanisms.

### 6.3 Methods and Materials

Thin-film catalysed working electrodes were prepared using the EG-SC method described in section 5.3.2 (page 90).

This work employed the AST protocol described by Takahashi *et al* [22]. Experiments were conducted in N<sub>2</sub>-purged 0.5M H<sub>2</sub>SO<sub>4</sub> at 25°C, using a Hg/HgSO<sub>4</sub> reference electrode (- 654 mV vs SHE at 25°C) and a Pt gauze counter electrode. Although the temperature of 25°C is not representative of PEMFC operating conditions, extended experiments at more realistic temperatures (70-80°C) were not practical with the equipment available due to evaporation of the electrolyte. Sulphuric acid was chosen instead of perchloric acid for the following reasons:

- Complexation of Pt by SO<sub>4</sub><sup>2-</sup> accelerates dissolution processes, allowing shorter test durations.
- The presence of SO<sub>4</sub><sup>2-</sup> in the electrolyte provides an analogue for the free SO<sub>3</sub><sup>2-</sup> anions generated at the PEMFC cathode through degradation of the ionomer binder within the catalyst layer.
- Gradual decomposition of HClO<sub>4</sub> to form Cl<sup>-</sup> anions would be likely to result in gradually increasing dissolution rates in experiments with durations of several hours.

#### **AST protocol**

Initial ECSA was measured from cyclic voltammograms recorded at 25 mV.s<sup>-1</sup> using the  $H_{upd}$  method. The working electrode potential was then cycled between + 0.6 and + 1.0 V vs. RHE with a period of 2 s, as shown previously in Figure 6.3 (a). The upper and lower potential limits are chosen to reproduce open circuit and peak power output conditions in the operating PEMFC. The square-wave potential step cycle is chosen over a linear potential sweep, as this regime produces

---

---

the highest degradation loss due to Pt dissolution, which shortens the test duration [172]. The ECSA measurement was repeated after every 1200 cycles, up to a total of 9600 cycles. The total AST duration was around 8 hours.

### **Post-mortem analysis**

The observation of morphological changes in the catalyst after AST testing can assist in the elucidation of degradation mechanisms [159, 197]. TEM specimens were prepared from the post-AST catalyst by contact transfer of a small amount of catalyst material from the electrode surface to a formvar-coated TEM grid.

To verify that catalyst had not detached from the RDE during the test, Pt:C elemental ratios were measured by EDX in an SEM after testing, and compared with values measured for the same electrode prior to testing. The SEM was operated at low magnification (30x) so that the EDX analysis could be performed over the entire area of the catalysed disc. The subsurface depth of the excitation volume from which the EDX signal is generated in the SEM operating at 20 kV is sufficient that a strong carbon signal is generated from the bulk GC material beneath the catalyst film. Therefore catalyst detachment would be indicated by a significantly lower post-AST Pt:C ratio, even if the carbon support detaches along with Pt particles.

### **Catalysts under test**

AST testing was carried out using Nafion®-Pt/C A and B type catalysts with very similar Pt particle sizes (7.8, 7.9 nm average), and a Nafion®-EG-Pt/C catalyst with a slightly smaller particle size (5.8 nm), all prepared in 50 mg-scale syntheses, in order to study size-dependent variations in durability. The catalysts were benchmarked against Pt/C catalysts from E-Tek (HP 20 wt %) and TKK (TEC10E50E 46 wt %). The physical properties of the catalysts under test are summarised in Table 6.2.

## 6 Catalyst Durability

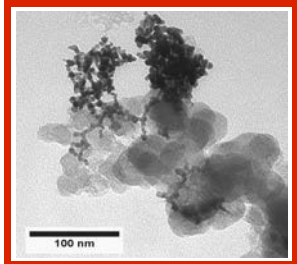
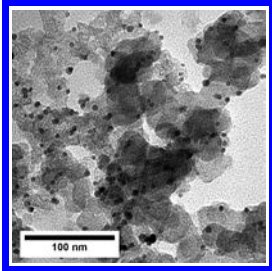
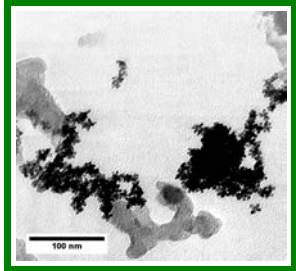
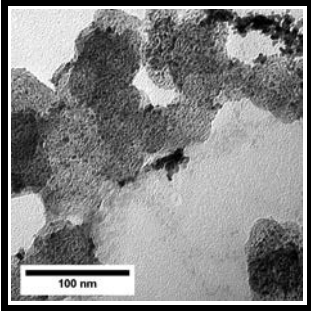
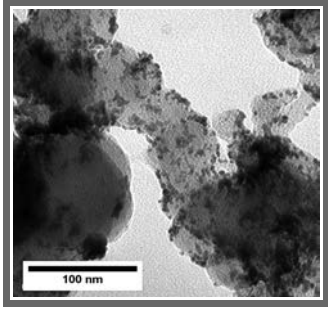
|  | Nafion®-Pt/C A   | Nafion®-Pt/C B   | Nafion®-EG-Pt/C A  |
|--|--|--|--|
| TEM image  |   |  |   |
| Preparation route  | A  | B  | A  |
| Synthesis scale  | 50 mg  | 50 mg  | 50 mg  |
| Pt particle size / nm  | 7.8  | 7.9  | 5.8  |
| $A_{\text{phys}} / \text{m}^2 \cdot \text{g}^{-1} \text{Pt}$ | $35 \pm 3$   | $34 \pm 3$   | $46 \pm 3$   |
|  | TKK 46 wt % Pt/C   |  | E-Tek 50 wt % Pt/C   |
| TEM image  |  |  |  |
| Preparation route  | Standard commercial  |  | Standard commercial  |
| Pt particle size / nm  | 2.9  |  | 4  |
| $A_{\text{phys}} / \text{m}^2 \cdot \text{g}^{-1} \text{Pt}$ | $98 \pm 10$  |  | $71 \pm 7$   |

Table 6.2: TEM micrographs and summary of physical characteristics of catalysts undergoing durability testing.

## 6.4 Results and discussion

The cyclic voltammograms in Figure 6.4 (b-f) show reductions in the  $H_{upd}$  current with successive AST cycles, indicating loss of Pt ECSA.

The loss of ECSA as a function of the number of AST cycles is shown for each catalyst in Figure 6.5, and ECSA values pre- and post-AST are given in Table 6.3.

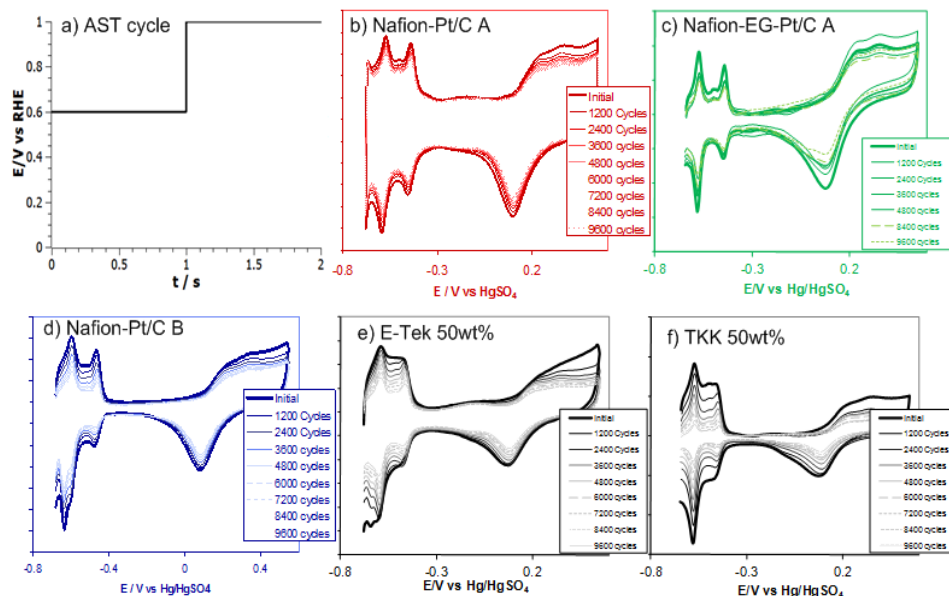


Figure 6.4: a) AST potential cycle, b-f) cyclic voltammograms after every 1200 cycles for the various catalysts on test, recorded at  $25\text{mV}\cdot\text{s}^{-1}$  at  $25^\circ\text{C}$  in  $0.5\text{M H}_2\text{SO}_4$

|                   | Avg Pt particle size / nm | Morphology   | ECSA pre-AST / $\text{m}^2\cdot\text{g}^{-1}$ Pt | ECSA post-AST / $\text{m}^2\cdot\text{g}^{-1}$ Pt | % ECSA loss |
|-------------------|---------------------------|--------------|--|---|-------------|
| Nafion®-Pt/C A    | 7.9                       | Agglomerated | 35   | 24  | 30          |
| Nafion®-EG-Pt/C A | 5.8                       | Agglomerated | 46   | 29  | 36          |
| Nafion®-Pt/C B    | 7.8                       | Dispersed    | 34   | 12  | 65          |
| E-Tek 20wt % Pt/C | 3.2                       | Dispersed    | 57   | 24  | 58          |
| TKK 46 wt% Pt/C   | 2.9                       | Dispersed    | 91   | 12  | 87          |

Table 6.3: Summary of catalyst properties and AST results

After 9600 cycles the Nafion®-Pt/C A and Nafion®-EG-Pt/C A catalysts both display significantly lower ECSA losses than the other catalysts on test, with total reductions in ECSA of 30% and 36% respectively compared to 65%, 58% and 87% for the Nafion®-Pt/C B, E-Tek and TKK catalysts.

## 6 Catalyst Durability

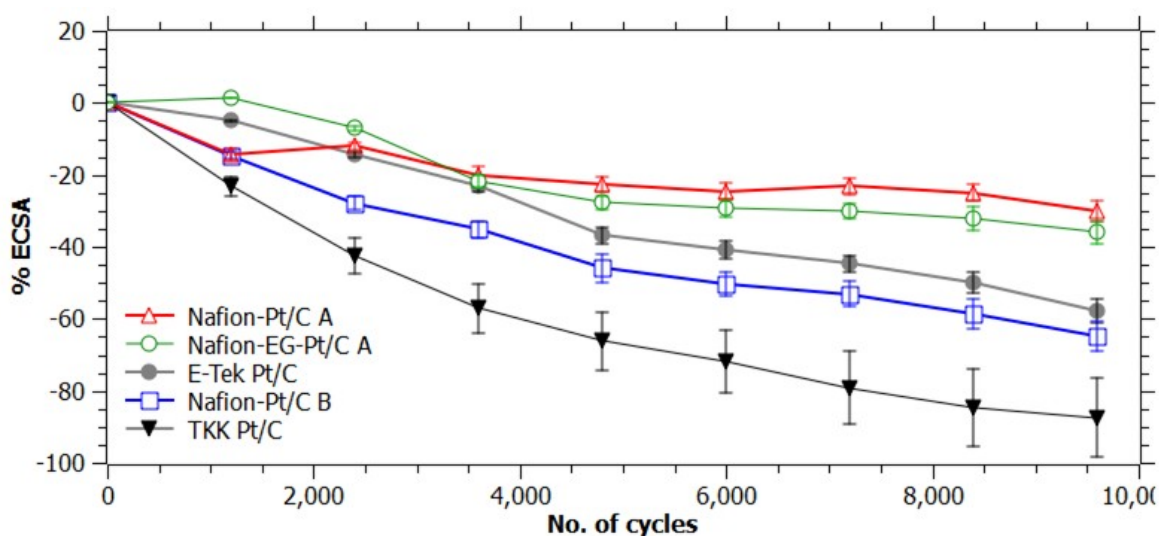


Figure 6.5: Comparison of catalyst durability during AST testing in 0.5M  $H_2SO_4$  at 25°C.

As shown in Table 6.3, following AST cycling the Nafion®-EG-Pt/C ( $29 \text{ m}^2 \cdot \text{g}^{-1}_{\text{Pt}}$ ) and Nafion®-Pt/C A ( $24 \text{ m}^2 \cdot \text{g}^{-1}_{\text{Pt}}$ ) catalysts retained higher ECSAs than the Nafion®-Pt/C B and TKK catalysts (both  $12 \text{ m}^2 \cdot \text{g}^{-1}_{\text{Pt}}$ ). The enhancements in durability appear to correlate with the agglomerated Pt morphology produced by the Nafion®-Pt/C 'A' preparation route, as demonstrated by the very similar degradation behaviour of the Nafion®-Pt/C A and Nafion®-EG-Pt/C A catalysts shown in Figure 6.5.

The fact that the Nafion®-Pt/C A catalyst displays significantly improved durability versus the Nafion®-Pt/C B catalyst, despite their near-identical Pt particle size distributions, implies that the enhancement in durability compared with the TKK and E-Tek catalysts cannot be attributed entirely to size-dependent dissolution and/or sintering rates.

The elemental composition data shown in Figure 6.6 are derived from EDX spectra collected from the entire surface of a catalysed E-Tek electrode, both before and after AST testing. The elemental compositions are very similar; in particular there is no increase in carbon content, and this confirms that there was no detachment of catalyst and/or ionomer from the electrode during the AST test.

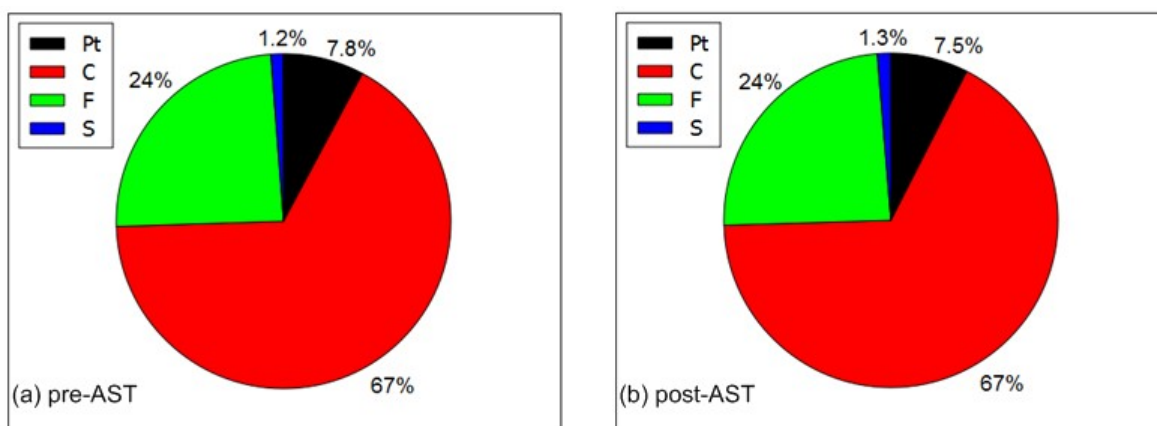


Figure 6.6: Elemental ratios for Pt, C, S and F measured by EDX across the entire area of the TF-catalysed electrode (E-Tek) (a) prior to AST testing and (b) following AST testing.

## 6.4.1 Degradation mechanisms

The post-mortem analysis of selected catalyst samples by TEM revealed that ECSA losses were accompanied by changes in morphology from which degradation mechanisms can be inferred. The TEM micrographs in Figure 6.7 (b) and (c) show significant agglomeration and particle growth for the Nafion®-Pt/C B and E-Tek catalysts, corresponding to losses in physical surface area of 49% and 68% respectively. The increases in Pt particle size, and widening of the size distributions in Figure 6.7 (b) and (c) are characteristic of Ostwald ripening. Conversely, there was no significant change in the particle size distribution for the Nafion®-Pt/C A catalyst (Figure 6.7 a), with the implication that its enhanced durability is likely due to inhibition of Ostwald ripening. The visible reduction in the crystallinity of the carbon support in the post-AST TEM images in Figure 6.7 suggests that carbon corrosion may also contribute to degradation under this AST protocol, and along with sintering of particles within Pt agglomerates this may account for the ECSA losses observed for Nafion®-Pt/C A, in the absence of any evidence of particle growth.

## 6 Catalyst Durability

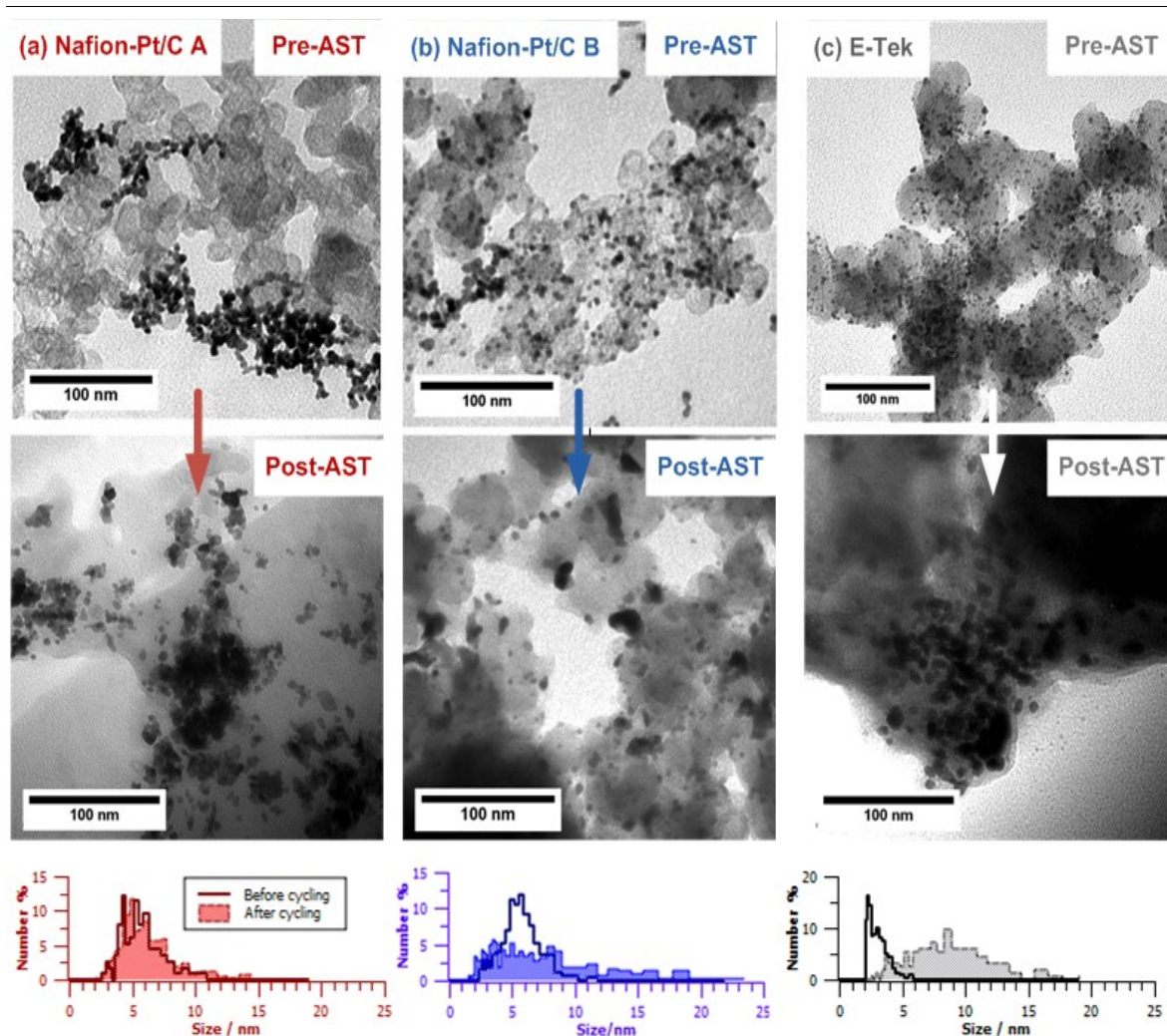


Figure 6.7: Post-AST TEM images and Pt particle size distributions (pre- and post-AST) for a) Nafion®-Pt/C A, b) Nafion®-Pt/C B and c) E-Tek catalysts

### 6.4.2 Stabilisation mechanism

Based on the evidence suggesting an inhibition of Ostwald ripening, a mechanism has been proposed for the enhanced durability of the Nafion®-Pt/C A-type catalysts. It was shown earlier that during the preparation of Nafion®-Pt/C A catalysts, residual Nafion® remains strongly bound within Pt agglomerates following purification. In the final, supported catalyst, these Pt agglomerates act as an anchor for a capping layer of Nafion®. The permeability of Nafion® films to metal cations is lower than in free solution[198]. Therefore it is proposed that this layer of Nafion® in close coordination with Pt acts as barrier to the diffusion of  $\text{Pt}^{2+}$  species away from the Pt surface. By maintaining a relatively high concentration of  $\text{Pt}^{2+}$  close to the Pt surface, the equilibrium in reaction (6.1) is shifted to the left, thereby reducing the rate of dissolution. Additionally, the restricted mobility of  $\text{Pt}^{2+}$  species may mean that Pt is less likely to be flushed from the electrode or deposited within the membrane.

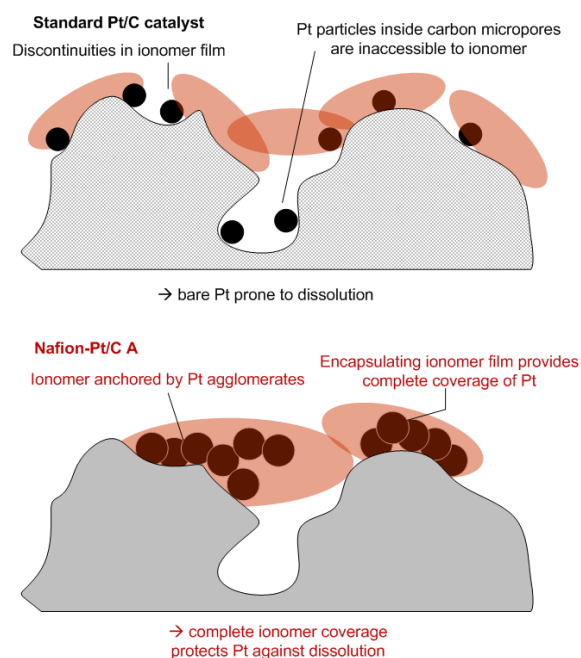


Figure 6.8: Schematic diagram illustrating the proposed morphological origins of the enhanced durability of Nafion®-Pt/C A type electrocatalysts compared with standard Pt/C.

By contrast, in standard Pt catalysts the randomly-percolating ionomer network does not provide full coverage of Pt surfaces. Discontinuities in the ionomer film, together with isolation of Pt particles within carbon micropores from the ionomer network[199], mean that a significant fraction of Pt surfaces are not covered with ionomer and are therefore prone to dissolution. The differing morphologies of the standard Pt/C and Nafion®-Pt/C A catalysts, which are thought to account for the enhanced durability of the latter, are represented schematically in Figure 6.8.

The proposed stabilisation mechanism is somewhat different to that suggested by Cheng *et al* [15], who attributed the enhanced durability of their Nafion®-Pt/C catalysts to inhibition of particle migration and sintering. Contrary to their findings, the Nafion®-Pt/C B catalyst (the most similar to theirs in terms of preparation route and Pt morphology) suffered much the same ECSA losses as the E-Tek catalyst during AST testing. Given that the AST testing protocol employed by Cheng *et al* differs significantly from that employed in this work, it is unsurprising that there are discrepancies in degradation behaviour. As it employs a less anodic upper potential and prevents the formation of passivating surface oxides, the square-wave potential cycle (+ 0.6 to +1.0 V) employed in AST testing in this study is likely to be more selective towards the activation of Pt dissolution than the potential sweep method (+ 0.6 to +1.2 V, 20 mV.s<sup>-1</sup>) employed by Cheng *et al*. Thus it appears that Nafion®-Pt/C B-type catalysts do not benefit from the same protection against Pt dissolution as Nafion®-Pt/C A-type catalysts, even though they are prepared from the same starting material (Nafion®-stabilised colloidal Pt). Only in the Nafion®-Pt agglomerates found in the Nafion®-Pt/C A type catalysts is sufficient ionomer retained to provide protection



## 6 Catalyst Durability

---

against dissolution. The highly-dispersed particles on the Pt/C and Nafion®-Pt/C B catalysts present a less-favourable topography for the retention of ionomer.

### 6.5 Conclusions

The Nafion®-Pt/C A and Nafion®-EG-Pt/C A catalysts offer roughly 2.9- and 2.4-fold enhancements in durability with respect to the TKK catalyst used in this study. This has been attributed to inhibition of particle growth mechanisms, which post-mortem characterisation of catalysts revealed to be the main degradation mode for E-Tek and Nafion®-Pt/C B catalysts during potential cycling from +0.6 to +1.0 V, consistent with previous studies. The inhibition of particle growth for catalysts prepared via the Nafion®-Pt/C A preparation route was in turn attributed to their unique morphology, characterised by loosely-agglomerated networks of Pt particles which, it is proposed, are coordinated with a capping layer of Nafion® ionomer that reduces the rate of Pt dissolution. The fact that the Nafion®-Pt/C A and Nafion®-EG-Pt/C A catalysts offer similar mass activity to the E-Tek and Nafion®-Pt/C B catalysts, whilst providing significantly enhanced durability, makes this route most attractive for the preparation of durable PEMFC electrocatalysts.

## 7 *In-situ* testing

### 7.1 Background

The environment in an operating PEMFC cathode catalyst layer differs substantially from that of an *ex-situ* test using a liquid electrolyte. A non-exhaustive list of the main differences is shown in Table 7.1 [200-201].

|                | <i>Ex-situ</i> (RDE) testing  | <i>In-situ</i> (MEA) testing   |
|----------------|---|--|
| Electrolyte    | Pervasive liquid electrolyte provides complete wetting of catalyst layer  | Catalyst layer relies on percolation of Nafion® ionomer, and liquid water present in pores for proton conductivity and triple-phase boundary creation.             |
| Mass transport | Mass transport is governed by diffusion of O <sub>2</sub> in solution, and the RDE rotation rate, which is limited to a maximum of around 2000 RPM, so that mass transport limited current densities are of the order 10 mA.cm <sup>-2</sup> at most. | O <sub>2</sub> is supplied in the gas phase, and rates of mass transport are considerably higher, with typical limiting current densities > 1 A.cm <sup>-2</sup> . |
| Hydration      | Ionomer within the catalyst layer is completely hydrated by the aqueous electrolyte.  | Hydration of ionomer relies on humidification of reactant gases, and therefore may not be optimal.   |
| Catalyst layer | Very thin (< 1 μm) catalyst layer   | Catalyst layer thickness typically ~ 10 μm, depending on composition and loading.  |

Table 7.1: Summary of the main differences between operating conditions in *ex-situ* and *in-situ* tests

Whilst *ex-situ* testing can provide valuable information regarding the intrinsic properties of a catalyst under controlled, reproducible conditions, it is only by fabricating MEAs and testing catalysts under real PEMFC operating conditions that a true indication of the practical utility of a novel catalyst can be gauged. In the following, MEAs are prepared from Nafion®-Pt/C A and Nafion®-Pt/C B type catalysts and compared against the commercial TKK and E-Tek catalysts.

---

## 7.2 Methods and materials

### 7.2.1 Catalyst ink preparation

For the preparation of MEAs, Nafion®-Pt/C catalysts were synthesised on a 50 mg scale as described in Chapter 3. Following purification, catalysts were dispersed in THF instead of water/isopropanol. The solvent THF was chosen because it has been shown previously to improve performance by enhancing the crystallinity of the ionomer within the catalyst layer upon drying [137]. Nafion® dispersion was added to the inks to achieve the optimum Nafion® concentration found in thick-film RDE tests as described in Chapter 4 (20 % NFP for Nafion®-Pt/C A; 33 % NFP for Nafion®-Pt/C B and standard Pt/C inks). Inks were ultrasonicated in an ice-cold water bath (Langford, 40kHz) for 45 minutes.

### 7.2.2 MEA fabrication

Cathode gas diffusion electrodes (GDEs) were prepared by hand spray-coating catalyst inks onto 4 x 4 cm sections of gas diffusion material (SGL 10BC) placed on a hotplate at 80 °C. SGL 10BC was chosen because it had been shown previously to offer superior performance to the alternatives available in this study [202]. The catalysed electrodes were dried in a vacuum oven overnight at 60°C, -900 mbar, and the catalyst loading was then determined gravimetrically.

Anodes were prepared from commercial gas diffusion electrodes (Johnson Matthey, 0.4 mg<sub>Pt</sub>.cm<sup>-2</sup> on SGL 34BC) by brushing Nafion® dispersion diluted to 1 wt % with THF onto the catalysed side to achieve a Nafion® loading of 33 % NFP, followed by drying in a vacuum oven. The Nafion® loading was verified gravimetrically.

Nafion® 212 membranes were used as-received without further treatment. Membrane Electrode Assemblies (MEAs) were prepared by hot-pressing anode and cathode GDEs either side of a Nafion® 212 membrane (120°C, 150 kPa, 60 s).

### 7.2.3 Single-cell PEMFC testing

Single-cell testing was carried out using a Scribner 850e-HT PEMFC test stand (Scribner Associates, USA) with Paxitech cell hardware. The MEA was placed between two PTFE gaskets and compressed between graphite flow-field plates with single-serpentine channel geometry by tightening tie-rods to 20 Nm bolt torque.

### **Activation**

Cell temperature was set to 70°C, with H<sub>2</sub> (120 cm<sup>3</sup>.min<sup>-1</sup>) and air (300 cm<sup>3</sup>.min<sup>-1</sup>) at 100 % RH and 2 bar.g backpressure flowing on the anode and cathode respectively. MEAs were activated by maintaining the cell voltage at 0.6 V for at least 12 hours, or until the current stabilised. Such treatment has been shown to accelerate the attainment of maximum performance in a new MEA, mainly by providing rapid hydration of the ionomer, which reduces the Ohmic resistance of the cell and increases the extent of the triple-phase boundary [203].

### **Polarisation curves**

Following activation, anodic polarisation curves were recorded from 0.25 V to open circuit in 0.01 V increments, 3s per point. Measurements were taken at reactant backpressures of 2 bar.g and 0 bar.g, 100 % RH. Nominal reactant stoichiometries on the anode and cathode were set at 4.0 (H<sub>2</sub>) and 2.0 (air) respectively, with minimum reactant gas flow rates of 120 cm<sup>3</sup>.min<sup>-1</sup> (H<sub>2</sub>) and 300 cm<sup>3</sup>.min<sup>-1</sup> (air).

### **In-situ ECSA measurements**

For *in-situ* measurement of ECSA, the cell was cooled to 25°C and the cathode gas was switched to N<sub>2</sub>. Once the open circuit voltage had dropped to < +0.1 V, the N<sub>2</sub> flow was stopped and cyclic voltammograms were recorded at 25mV/s between 0.0 to +1.0 V using an Autolab PGSTAT 302 potentiostat configured with the cathode as the working electrode, whilst the anode served simultaneously as the counter and pseudo-reference electrode. For true indication of ECSA, measurements must be performed at < 40°C. Above this temperature, adsorbed hydrogen is only very weakly bound to the Pt surface and can undergo spontaneous desorption, confounding accurate measurement of adsorption charge [204]. The N<sub>2</sub> flow on the cathode must be reduced to < 1 cm<sup>3</sup>.min<sup>-1</sup> per cm<sup>2</sup> active area or stopped altogether in order to minimise unwanted hydrogen evolution currents at potentials less than +0.05 V vs, RHE [204]. ECSA values were derived from cyclic voltammograms according to the method presented previously in section 3.3.3 (page 34).

### **Electrochemical Impedance Spectroscopy**

Electrochemical Impedance Spectroscopy (EIS) is a powerful technique for the quantitative measurement of various parameters affecting PEMFC performance. Importantly, it allows decoupling of the various losses (Ohmic, activation and mass-transport related) contributing to the overall performance of the cell or stack. In an EIS measurement, a sinusoidally-varying AC current is applied to the cell, and the voltage response (also sinusoidal) is recorded. If the applied

---

sinusoidal current has frequency  $\omega$  and amplitude  $I_0$ , the voltage response will have frequency  $\omega$  and amplitude  $E_0$ , but its phase may be shifted by an amount  $\phi$  with respect to the current signal (Figure 7.1 (a)). The applied current and resulting AC voltage can be described mathematically as a function of time  $t$  according to equations (7.1) and (7.2):

$$I(t) = I_0 \sin(\omega t) \quad (7.1)$$

$$E(t) = E_0 \sin(\omega t - \phi) \quad (7.2)$$

Expressed in terms of complex numbers, equations (7.1) and (7.2) become

$$\hat{I} = I_0 e^{i\omega t} \quad (7.3)$$

$$\hat{E} = E_0 e^{i(\omega t - \phi)} \quad (7.4)$$

The impedance  $\hat{Z}$  of the cell (and indeed any system with a linear I-E response) is a complex quantity defined according to equation (7.3) where  $\hat{i} = \sqrt{-1}$

$$\hat{Z} = \frac{\hat{E}}{\hat{I}} = \frac{E_0 e^{i(\omega t - \phi)}}{I_0 e^{i\omega t}} \quad (7.5)$$

The  $e^{i\omega t}$  terms in equation (7.3) cancel to give

$$\hat{Z} = \frac{E_0}{I_0} \cdot e^{-i\phi} \quad (7.6)$$

The complex quantity  $\hat{Z}$  has real and imaginary components  $Z'$  and  $Z''$ , which using Euler's equation  $e^{i\phi} = \cos(\phi) + i \sin(\phi)$  with (7.6) can be written [205]

$$\hat{Z} = Z' - Z'' = \frac{E_0}{I_0} \cos(\phi) - i \frac{E_0}{I_0} \sin(\phi) \quad (7.7)$$

The complex impedance of the cell can be represented graphically by plotting the real ( $Z'$ ) and imaginary ( $Z''$ ) components of  $\hat{Z}$  on a Nyquist plot (Figure 7.1 (b)).

In a typical EIS experiment on a PEMFC, measurements are performed at a number of different frequencies ( $\omega$ ) usually between 10 kHz and 0.1 Hz. Each frequency gives rise to a point on the Nyquist plot, producing an impedance spectrum similar to those shown in Figure 7.1 (c), (d) and (e).

The impedance response of a PEMFC system can be modelled by an *equivalent circuit* consisting of basic circuit elements. Each element within an equivalent circuit represents a physical attribute or process occurring within the cell, and has a characteristic impedance response as defined by its

## 7 In-situ testing

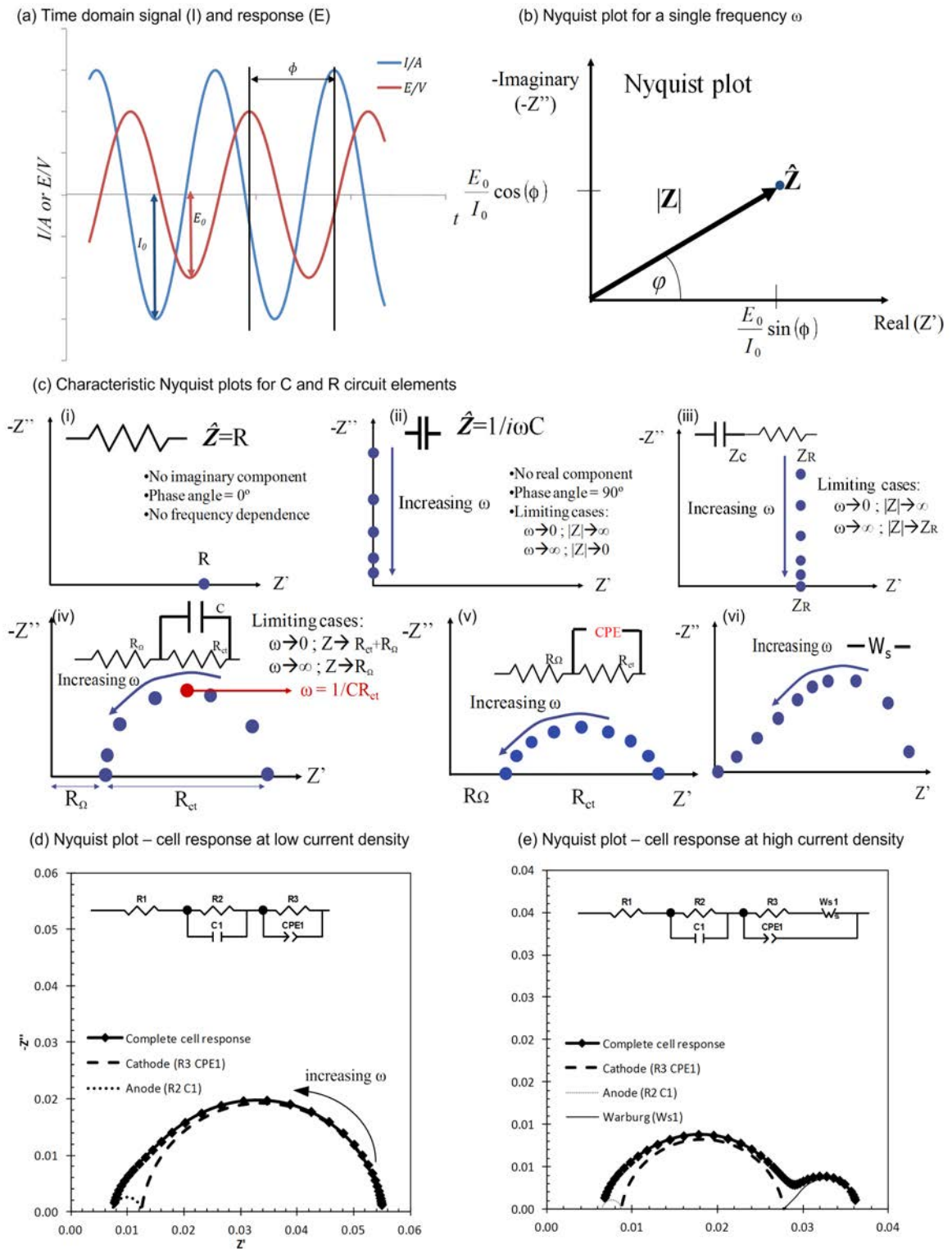


Figure 7.1: Summary of the data collection and processing steps in an EIS experiment. (a) Sinusoidal current (I) is applied and potential (E) recorded as a function of time  $t$ ; complex impedance  $\hat{Z}$  is calculated according to equation (7.3) and can be represented in terms of real ( $Z'$ ) and imaginary ( $Z''$ ) components on a Nyquist plot (b); an equivalent circuit is developed using R and C circuit elements, which represent physical processes within the cell and have characteristic impedance responses  $\hat{Z}(\omega)$  as shown in (c); equivalent circuit components are then assigned values by least-squares fitting to experimental data ( $\blacklozenge$ ) as shown in (d) for low current densities and (e) for high current densities.

transfer function. Transfer functions for the circuit elements employed in equivalent circuits for PEMFC studies are shown in Table 7.2.

| Element                      | Transfer Function   |
|------------------------------|---|
| Resistance (R)               | $\hat{Z} = R$ (7.8)   |
| Capacitance (C)              | $\hat{Z} = 1/\omega C$ (7.9)  |
| Constant Phase Element (CPE) | $\hat{Z} = 1/(\omega C)^n; 0 < n \leq 1$ (7.10)                               |
| Warburg ( $W_s$ )            | $\hat{Z} = \frac{R_w}{(\omega T)^n \tanh((\omega T)^n)}; 0 < n \leq 1$ (7.11) |

Table 7.2: Common circuit elements employed in PEMFC equivalent circuits and their corresponding transfer functions

Suitable equivalent circuits can be developed by considering the physical processes underlying the Ohmic, electrochemical and mass transport losses affecting the I-E response of the system as follows:

### Ohmic resistance

The series Ohmic resistance of the cell, which is the sum of the electrical resistance of cell components and cables, contact resistances at interfaces between components, and ionic resistance of ionomeric components of the cell, can be assigned to a single resistive circuit element (R1 in Figure 7.1 (d) and (e)). The complex impedance of a resistive circuit element has no imaginary component and is independent of frequency, appearing as a point on the Nyquist plot as shown in Figure 7.1 (c) i.

### Reaction kinetics and double layer capacitance

The electrochemical behaviour of the electrodes requires a slightly more complex model. As illustrated in Figure 7.2 (a), an electrochemical reaction taking place at a flat, planar electrode in a uniformly-accessible electrolyte can be modelled as a resistor ( $R_{ct}$ ) and capacitor ( $C_{dl}$ ) in parallel, with the resistor representing work performed in the conversion of reactants to products at the electrode surface (charge transfer), and the capacitor representing the double-layer capacitance of the electrode-electrolyte interface [205].

The impedance response of such a system then appears as a semicircle in the Nyquist plot, offset along the real ( $Z'$ ) axis by an amount determined by any series Ohmic resistance ( $R_{\Omega}$ ), as shown in Figure 7.1 (c) iv. For a PEMFC, the anode and cathode can be modelled by two such RC parallel elements as shown in Figure 7.2 (b). The resistive element  $R_{\Omega(PEM)}$  in Figure 7.2 (b) represents the Ohmic (ionic) resistance of the electrolyte membrane. In practice, there are also Ohmic (electrical)

## 7 In-situ testing

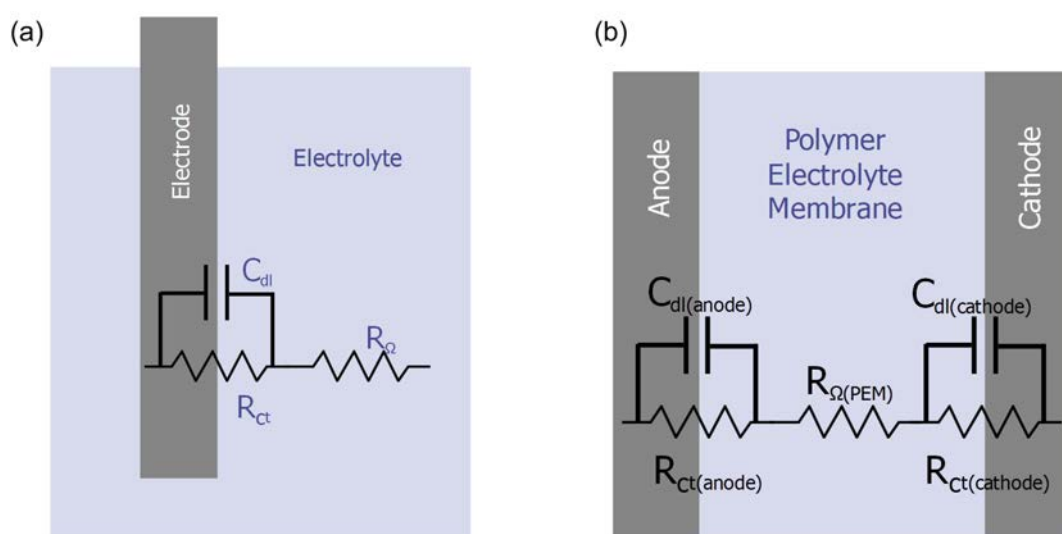


Figure 7.2: (a) general equivalent circuit model (Randles circuit) for an electrochemical interface; (b) typical equivalent circuit for a PEMFC

resistances due to the connecting cables and cell components, which are summed together with the membrane resistance into a single series resistance ( $R_1$  in the insets of Figure 7.1 (d) and (e)).

The impedance response of a real PEMFC electrode differs from the ideal semicircular profile produced by a standard parallel RC combination, in that it usually appears flattened or depressed towards the real ( $Z'$ ) axis of the Nyquist plot; an effect attributed to the highly-distributed nature of the electrode, whereby the double layer capacitance is distributed over the surface area of the pores within the electrode [206]. It is commonplace to fit the capacitive part of the PEMFC electrode impedance response using a constant phase element (CPE) [206-210], which differs from a conventional capacitor in that the phase difference between the input (current) and output (voltage) signals is allowed to assume an arbitrary (but constant) value, as opposed to the  $90^\circ$  phase shift of a true capacitor [211]. The value of the CPE element is related to the double-layer capacitance by the transfer function in equation (7.11), which includes an additional parameter  $n$  determining the CPE phase shift. The value of  $n$  is typically between 0.9 and 1.

### Mass transport effects

When operating at high current densities (typically  $> 0.5 \text{ A.cm}^{-2}$ ), the rate of diffusion of  $\text{O}_2$  within the cathode begins to have a significant effect on the I-V response of the system. These mass transport effects due to diffusion of reactants produce a characteristic impedance response at the low frequency ( $< 100 \text{ Hz}$ ) end of the Nyquist plot as shown in Figure 7.1 (e) and Figure 7.1 (c) vi.

Diffusion phenomena within PEMFC electrode are commonly represented by a Finite Length Warburg (or simply, Warburg) element in EIS equivalent circuits. The transfer function for the Warburg element is given in equation (7.7), and is a solution of the one-dimensional diffusion



equation for a particle [56]. The Warburg circuit element represents a repeating series of identical constant phase (T) and resistive elements ( $R_w$ ), or *transmission line*, as illustrated in Figure 7.3.

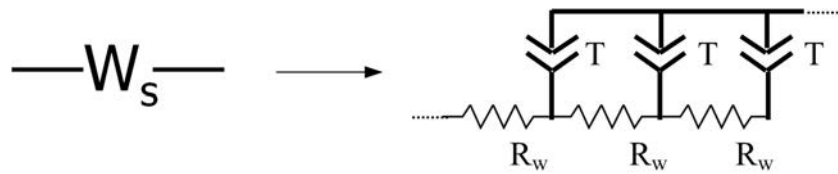


Figure 7.3: Transmission line model of the Warburg circuit element used in PEMFC equivalent circuits to represent diffusion (mass transport) processes.

The  $R_w$  parameter of the Warburg element can be interpreted in terms of a “resistance to mass transport”, and can therefore be used to quantify mass transport effects in PEMFCs operating at high current densities.

Typical equivalent circuits for a PEMFC system operating in low and high current density regimes are shown in the insets of Figure 7.1 (d) and (e). Once a suitable equivalent circuit model has been developed, values are calculated for the transfer function parameters of each circuit element using a complex non-linear least-squares method to fit the model to the experimental data. The Nyquist plots in Figure 7.1 (d) and (e) show experimental data to which the inset equivalent circuits have been fitted, together with the individual impedance responses of the anode, cathode and Warburg circuit elements.

In this study, AC impedance measurements were made at DC current densities of 62.5 and 500 mA.cm<sup>-2</sup> to investigate the activation- and mass transport-limited regimes of the cell's polarisation response respectively. The AC perturbation amplitude was set to 10% of the DC current, and measurements were performed at frequencies ranging from 10 kHz to 0.1 Hz. Equivalent circuit fitting was carried out using *ZView* [212].

## 7.3 Results and discussion

MEAs were prepared as described above for four catalysts as detailed in Table 7.3.

|   | MEA   |                   |             |             |
|---|---|-------------------|-------------|-------------|
|   | Nafion®-Pt/C<br>A   | Nafion®-Pt/C<br>B | E-Tek       | TKK         |
| <b>Anode</b>  | Johnson Matthey commercial GDE 0.4 mg <sub>Pt</sub> .cm <sup>-2</sup> 33% NFP |                   |             |             |
| <b>Cathode</b>  |   |                   |             |             |
| NFP %   | 20  | 30                | 33          | 33          |
| Pt loading / mg <sub>Pt</sub> .cm <sup>-2</sup>   | 0.13 ± 0.01   | 0.16 ± 0.01       | 0.15 ± 0.01 | 0.15 ± 0.01 |
| Pt wt % on C  | 50  | 50                | 50          | 46          |
| Sauter average Pt particle size / nm  | 7.8   | 5.6               | 4           | 2.9         |
| Physical surface area A <sub>phys</sub> / m <sup>2</sup> .g <sub>Pt</sub> <sup>-1</sup> | 35 ± 3  | 51 ± 3            | 72 ± 5      | 98 ± 10     |
| ECSA <sup>1</sup> (MEA) / m <sup>2</sup> .g <sub>Pt</sub> <sup>-1</sup>                 | 10.5 ± 0.9  | 9.4 ± 1.2         | 25.8 ± 4.0  | 43.1 ± 4.0  |
| U <sub>Pt</sub> / %   | 30.0 ± 3.6  | 18.4 ± 2.8        | 35.8 ± 6.1  | 43.9 ± 6.2  |
| Mass activity <sup>2</sup> @ 0.85 V / A.g <sup>-1</sup> <sub>Pt</sub>                   | 60.2 ± 4.6  | 61.6 ± 3.8        | 66.2 ± 4.4  | 186 ± 5     |
| E <sub>f</sub> / %  | 8.9 ± 0.8   | 8.3 ± 1.4         | 4.7 ± 1.1   | 6.9 ± 1.3   |

Table 7.3: Summary of MEAs prepared for in-situ testing. <sup>1</sup>ECsAs determined by in-situ cyclic voltammetry. <sup>2</sup>Mass activities at 0 bar.g cathode backpressure, 70°C, 100% RH anode and cathode, corrected for Ohmic and mass transport effects.

### 7.3.1 Polarisation curves

The polarisation curves in Figure 7.4 reveal distinct variations in the performance of the four MEAs. The TKK MEA gives the best performance, followed by the E-Tek, Nafion®-Pt/C B and finally the Nafion®-Pt/C A MEA, which performs worst. From Figure 7.4 (a), using reactant gases without backpressure the TKK MEA produces a maximum power density of around 0.26 W.cm<sup>-2</sup>, whilst the E-Tek, Nafion®-Pt/C B and Nafion®-Pt/C A MEAs produce 0.24 W.cm<sup>-2</sup>, 0.21 W.cm<sup>-2</sup> and 0.13 W.cm<sup>-2</sup> respectively. In Figure 7.4 (b) the polarisation data are normalised by Pt loading so, having a slightly lower Pt loading, the performance of the Nafion®-Pt/C A MEA increases slightly relative to the others, but the order of performance remains the same.

As shown in Figure 7.4 (c) and (d), the performance of all four MEAs increases dramatically when reactants are pressurised to 2 bar.g. An increase in reactant pressure has several effects:

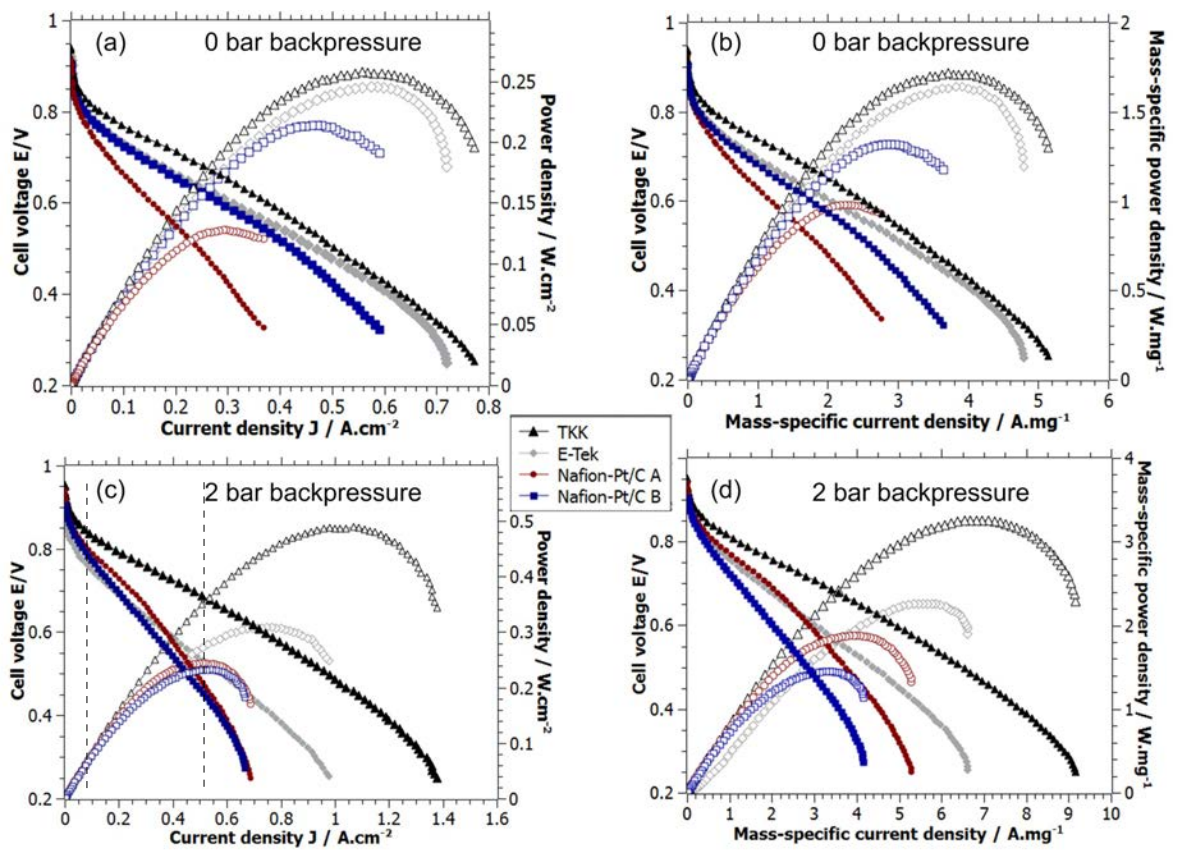


Figure 7.4: Polarisation curves recorded at (a,b) 0 bar and (c,d) 2 bar.g reactant backpressure for MEAs prepared from (●)Nafion®-Pt/C A, (■)Nafion®-Pt/C B, (◐)E-Tek and (▲)TKK catalysts. In (a,c) performance is normalised by active electrode area ( $\text{cm}^2$ ), whilst (b,d) show performance normalised by cathode Pt loading ( $\text{mg}^{-1}$ ). The dashed vertical lines in (c) indicate the current densities at which EIS measurements were performed.

1. The OCV increases in accordance with the Nernst equation:

$$\Delta E^{rev} = \Delta E^0 + \frac{RT}{nF} \ln \left( \frac{P_{H_2} \cdot P_{O_2}^{1/2}}{P_{H_2O}} \right) \quad (2.4)$$

where  $\Delta E^{rev}$  is the reversible cell voltage,  $\Delta E^0$  is the reversible cell voltage under standard conditions and  $P_{H_2}$ ,  $P_{O_2}$  and  $P_{H_2O}$  are the absolute partial pressures of hydrogen, oxygen and water vapour respectively.

2. ORR kinetics are improved in proportion with  $O_2$  partial pressure  $P_{O_2}$  according to

$$J_k = k P_{O_2}^\gamma \quad (7.12)$$

where  $J_k$  is the ORR kinetic current density,  $k$  is a reaction rate constant and  $\gamma \approx 1$  is the reaction order.

3. For a given reactant stoichiometry, the volumetric flow rate of reactant gases is inversely proportional to pressure according to:

## 7 In-situ testing

---

$$\dot{V} \propto \frac{RT}{P} \quad (7.13)$$

A reduction in flow rate results in less water being carried out from the cell, which can improve hydration of the membrane but may also cause flooding of the electrode, depending on the relative humidity conditions inside the cell and the cell operating temperature.

4. The homogeneity of the spatial current distribution over the electrode area is improved [213]. Generally, the local current density in an operating PEMFC electrode is higher close to the cathode inlet than at the cathode outlet, due to reactant concentration gradients and pressure drop between the inlet and outlet of the cathode flow field. These effects are reduced by increasing the operating pressure of the cell.

Despite the general uplift in performance, the Nafion®-Pt/C MEAs still perform poorly relative to those prepared from E-Tek and TKK catalysts, except in the activation region above 0.8 V where the Nafion®-Pt/C A and B MEAs show slightly better performance than the E-Tek MEA. This is interesting, as it suggests that the increased pressure conveys a greater benefit in terms of improving ORR kinetics for the Nafion®-Pt/C catalyst layers (particularly Nafion®-Pt/C A) than for the E-Tek catalyst layer.

The Nafion®-Pt/C A MEA shows a particularly significant increase in performance at 2 bar.g backpressure compared to 0 bar.g. In addition to there being significantly fewer losses in the activation region of the IV curve for Nafion®-Pt/C A at 2 bar.g, the slope of the linear (Ohmic) loss region between 0.1 and 0.4 A.cm<sup>-2</sup> also appears much shallower than it does at 0 bar.g. Poor hydration of the membrane and the ionomer component of the catalyst layer are thought to account for the relatively poor cathode kinetics and high apparent Ohmic resistance observed for the Nafion®-Pt/C MEAs at low pressure.

- Contrary to expectations, it is possible that the morphology of the Nafion®-Pt/C A catalyst layer, characterised by enhanced coverage of Pt with ionomer but with a lower catalyst layer ionomer loading, makes it more sensitive to dehydration than a standard catalyst layer.
- Although the optimum ionomer content for the Nafion®-Pt/C A catalyst was found to be 20 % NFP in thick-film RDE studies, it could be that there is insufficient connectivity between Nafion®-Pt agglomerates at this ionomer loading to provide adequate proton conductivity within the catalyst layer in an MEA environment (i.e. in the absence of the additional hydration and conductivity provided by close contact with a liquid electrolyte). Further experiments at different humidity levels and catalyst layer ionomer contents would be required to verify this.

- 
- It is also possible that this is a localised problem, resulting from non-uniform coverage of the catalyst ink on the GDL during preparation of the electrode. Techniques exist for the measurement of local current density [213-214], Ohmic and mass transport resistances [215], which would be helpful in diagnosing such issues but were not available for this study.

From Figure 7.5 (c), both the Nafion®-Pt/C A and B MEAs reached mass-transport limitation at around 0.7 A.cm<sup>-2</sup>, compared with 1.0 A.cm<sup>-2</sup> and 1.4 A.cm<sup>-2</sup> for the E-Tek and TKK MEAs. The inferior mass transport within the Nafion®-Pt/C electrodes is confirmed by higher mass transport resistances measured by EIS at 500 mA.cm<sup>-2</sup> (Figure 7.5 (c)).

It is worth noting that none of the MEAs tested here perform to the same level as other MEAs prepared from similar materials reported in the literature. For instance, Gastgeiger *et al* prepared MEAs from the E-Tek and TKK catalysts which showed power densities of 0.85W.cm<sup>-2</sup> at 0.6V [12]. Significant improvements to the materials and fabrication methods used in this study would be required to reach this level of performance. In particular, the deposition of the catalyst layer directly onto the membrane using a decal method has been shown to offer significantly better performance than coating catalyst onto the gas diffusion layer [216-217], and this method may improve ionic continuity between the membrane and the catalyst layer.

### 7.3.2 Electrochemical Impedance Spectroscopy

The results of the EIS studies shown in Figure 7.5 allow quantification and comparison of the various losses contributing to the performance of the four MEAs. EIS was carried out at 2 bar backpressure and at two DC current densities 62.5 and 500 mA.cm<sup>-2</sup> to investigate the activation and mass-transport dominated regions of the cells' polarisation responses. The charge transfer resistances shown in Figure 7.5 (c) are taken from the R3 circuit element values fitted to data shown in Figure 7.5 (a). The two Nafion®-Pt/C MEAs have significantly larger cathode charge transfer resistances than both the E-Tek and TKK MEAs, indicating inferior oxygen reduction kinetics. The lower surface area of the Nafion®-Pt/C catalysts may account at least in part for their higher charge transfer resistance, which is inversely proportional to the rate of the ORR according to equation (7.5) [218].

$$R_{ct} = \frac{RT}{nF} \frac{1}{J_0} \quad (7.14)$$

## 7 In-situ testing

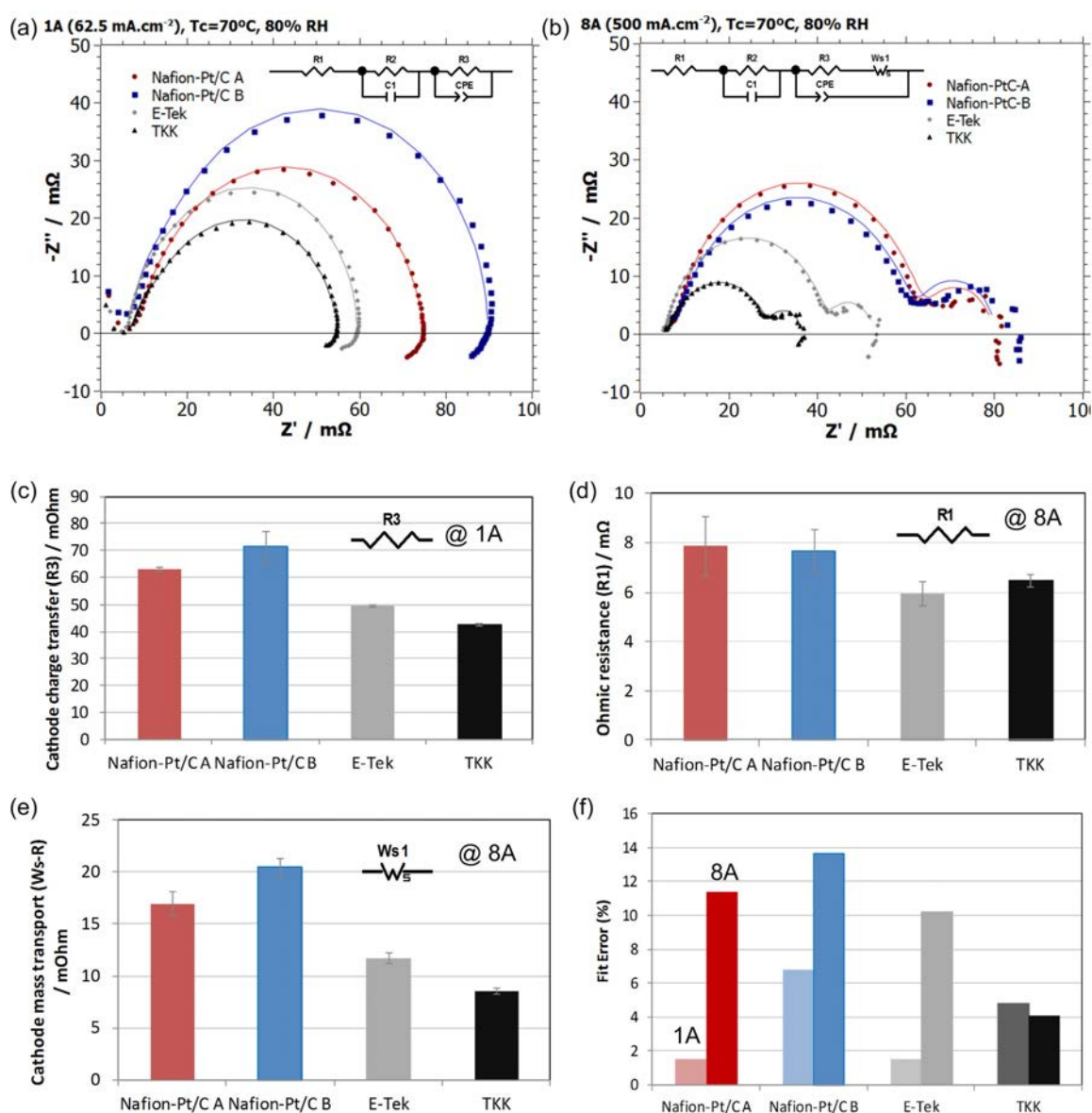


Figure 7.5: (a,b) Nyquist plots showing EIS data (points) and fitted spectra (solid lines) based on equivalent circuits (insets) (a) 1 A DC current, (b) 8 A DC current; equivalent circuit element fitted values for (c) R3 cathode charge transfer resistance, (d) R1 ohmic resistance, (e) Warburg Ws-R cathode mass transport resistance; (f) weighted sum-of-squares error in best fit for impedance data recorded at 1 A and 8 A.

The Ohmic resistances in Figure 7.5 (d) are measured from R1 circuit element values at 500 mA.cm<sup>-2</sup> DC offset, and are comparable, within the bounds of experimental error, for all four MEAs. The resistances include contributions from the ionic resistances of the membrane and catalyst layers, as well as the electrical bulk and contact resistances of the cell components and connecting leads. Given that all four MEAs employ the same Nafion® 212 membrane, cell hardware and compression force, it is unsurprising that the Ohmic resistances are so similar.

The most significant variations in results from EIS experiments were found in the mass transport resistance data shown in Figure 7.5 (e). Mass transport resistances are taken from values fitted for

the resistive component of the  $W_{s1}$  Warburg circuit element, representing diffusion of  $O_2$  at the cathode. Seeing as all four MEAs use the same gas diffusion material (SGL 10BC), were prepared by hot-pressing to the same pressure and tested under the same level of cell compression, the variations in mass transport resistance can be attributed to differences in catalyst layer mass transport. Therefore mass transport within the Nafion®-Pt/C catalyst layers appears to be significantly worse than in the standard E-Tek and TKK catalyst layers. For Nafion®-Pt/C A, this increase in mass transport resistance is in line with expectations based on lower limiting current densities observed in RDE experiments. However, the Nafion®-Pt/C B catalyst displayed better mass transport characteristics than Nafion®-Pt/C A in RDE experiments, yet in MEA tests it appears to have a higher mass transport resistance than Nafion®-Pt/C A catalyst layer. The reasons for this discrepancy between trends in mass transport characteristics observed in RDE and MEA studies are not entirely clear, and would be worthy of further investigation.

### 7.3.3 Catalyst utilisation

Cyclic voltammetry was carried out in driven cell mode using a potentiostat, with a scan rate of  $25 \text{ mV}\cdot\text{s}^{-1}$  and a cell temperature of  $25^\circ\text{C}$ , whilst the anode and cathode were supplied with  $H_2$  (12 ccpm) and  $N_2$  (zero flow during measurement) respectively. Catalyst utilisation was then calculated using ECSA values measured from  $H_{upd}$  regions of the cyclic voltammograms (Figure 7.6 a) as described in section 3.3.3 (page 34).

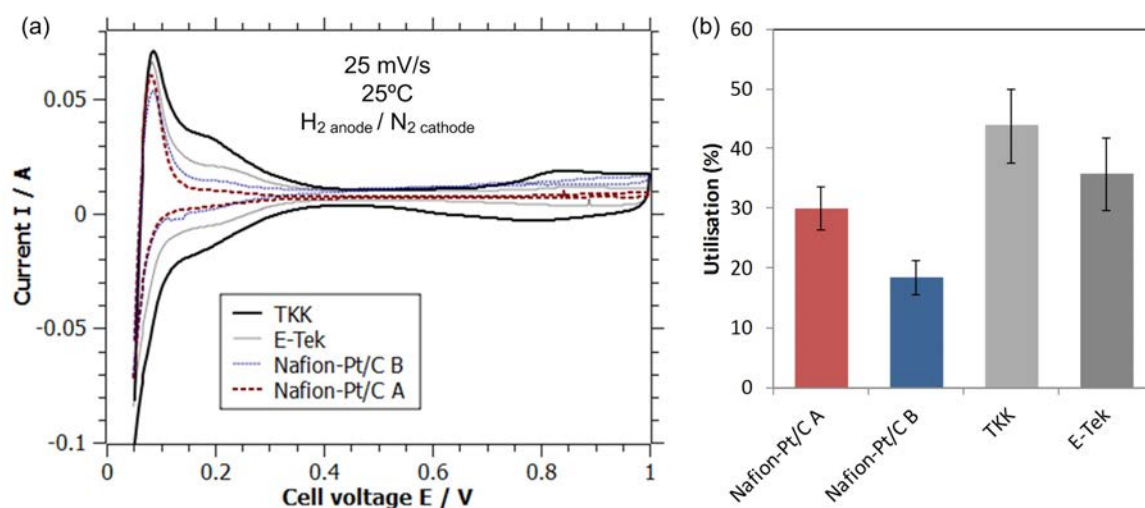


Figure 7.6: (a) Cyclic voltammograms recorded for MEAs operating in driven cell mode with humidified  $H_2$  supplied to the anode, whilst the cathode is purged with humidified  $N_2$ ,  $25 \text{ mV}\cdot\text{s}^{-1}$  cell temperature  $25^\circ\text{C}$ ; (b) comparison of catalyst utilisation values obtained from ECSAs measured from  $H_{upd}$  regions of the cyclic voltammograms and estimates of physical surface area shown in Table 7.3.

The results in Figure 7.6 (b) demonstrate significant variations in catalyst utilisation between the four MEAs. Clearly the Nafion®-Pt/C B MEA shows the lowest catalyst utilisation, at  $18.5 \pm 2.8$

## 7 In-situ testing

---

%, followed by the Nafion®-Pt/C A MEA with a utilisation of  $26 \pm 3$  %. Contrary to the original hypothesis, neither of the Nafion®-Pt/C catalysts offer any improvement in catalyst utilisation with respect to the standard catalysts: the TKK and E-Tek MEAs displaying  $44 \pm 6$  % and  $36 \pm 8$  % utilisation, respectively.

### 7.3.4 Effectiveness Factor, $E_f(\text{Pt})$

Catalyst utilisation data derived from  $H_{upd}$  charge measured by *in-situ* cyclic voltammetry does not provide a truly representative metric for catalyst layer performance for the following reasons:

- a) The  $H_{upd}$  processes occur in the potential range +0.05 to +0.4 V vs. RHE, whereas the cathode typically operates at +0.6 to +1.0 V. Therefore ECSA measurements made from  $H_{upd}$  data may not be truly representative of the active surface area under operating conditions, where surface coverage by adsorbates (including  $\text{SO}_3^-$  groups from coordinating Nafion®) may be considerably different.
- b) Cyclic voltammetry measurements are made at 25°C, so ionomer hydration and conductivity will differ considerably from operating conditions.

For these reasons, an alternative measure of catalyst layer performance was sought, which would compare the *in-situ* performance of a real catalyst layer under typical operating conditions with the ideal-case data obtained in RDE experiments.

Recently, Watanabe *et al* proposed an alternative metric for the evaluation of catalyst layer performance, which they call the effectiveness factor,  $E_{f(\text{Pt})}$ , and which is calculated according to equation (7.4).

$$E_{f(\text{Pt})} = \frac{\text{MA}_{0.85\text{V MEA}}}{\text{MA}_{0.85\text{V RDE}}} \quad (7.15)$$

where  $\text{MA}_{0.85\text{V MEA}}$  and  $\text{MA}_{0.85\text{V RDE}}$  are the ORR mass activities measured at +0.85V at a given temperature and  $\text{O}_2$  partial pressure respectively [219]. The potential +0.85 V vs RHE is chosen so as to minimise the effect of mass transport on the measured current density.

Put differently, the effectiveness factor provides a measure of the performance of the PEMFC catalyst layer in terms of ORR kinetics, with respect to the ideal case as measured in non-adsorbing liquid electrolyte experiments using the RDE technique. For proper comparison, the MEA and RDE experiments should be performed at the same temperature. An MEA displaying an ORR mass activity equivalent to that found for the same catalyst in an RDE experiment, at a given temperature, would have an effectiveness factor of 100%.



Values for  $MA_{0.9V\ MEA}$  were derived from MEA polarisation curves, after correcting for Ohmic resistance, mass transport and temperature effects as follows. Potentials were corrected for Ohmic resistance according to

$$E_{corrected} = E + IR \quad (7.16)$$

where  $I$  is the current measured at potential  $E$  and  $R$  is the Ohmic resistance of the MEA determined from EIS measurements at 10 kHz.

Kinetic current densities  $J_k$  were then calculated from measured currents by correcting for mass transport effects according to

$$J_k [A.cm^{-2}] = \frac{J.J_{lim}}{J_{lim} - J} \quad (7.17)$$

where  $J$  is the measured current density in  $A.cm^{-2}$  (normalised here by geometric surface area) and  $J_{lim}$  is the mass-transport limited current density measured for the MEA, which for practical purposes was taken to be equal to the current density measured at + 0.25 V. Mass activities in  $A.mg^{-1}_{Pt}$  were then calculated from mass transport-corrected current densities  $J_k$  according to

$$MA_{0.85V\ MEA} = \frac{J_k [A.cm^{-2}]}{L_{Pt} [mg.cm^{-2}]} \times 1000 \quad (7.18)$$

This analysis gave rise to the effectiveness factor results shown in Figure 7.7 (b).

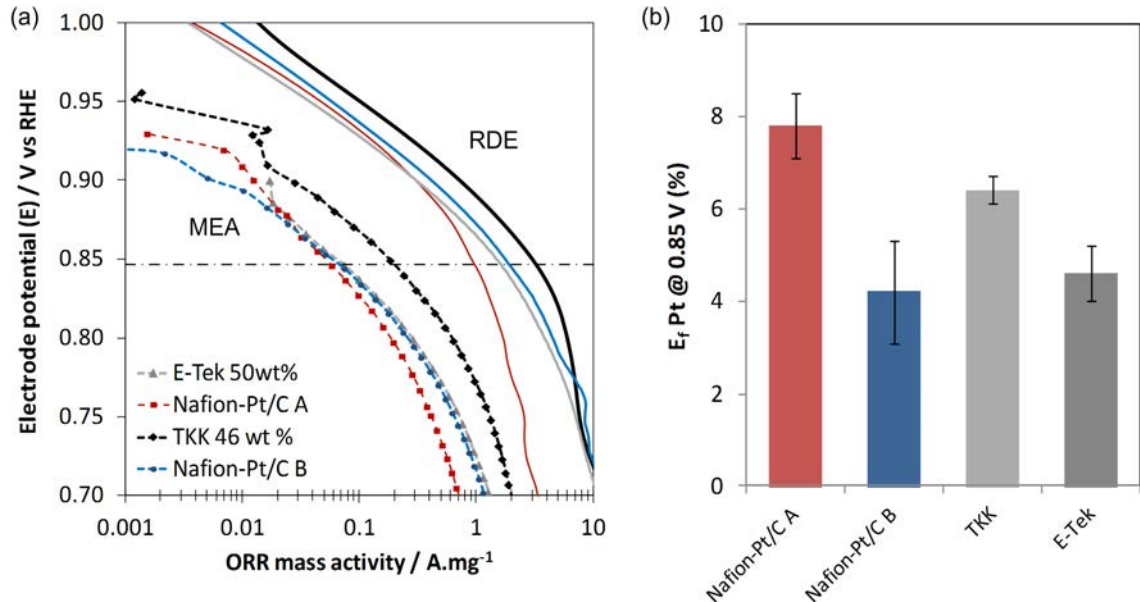


Figure 7.7: (a) Comparison of ORR mass activities measured in MEA and RDE (2000 rpm, 70°C) experiments in the potential range 1.0 - 0.7 V vs. RHE and (b) effectiveness factors of cathode catalyst layers for the four MEAs on test.

## 7 In-situ testing

---

In Figure 7.7 (a), the MEA data at potentials greater than +0.87 V are rather erratic, due to the poor sensitivity of the electronic load in the PEMFC test stand at low currents. The effectiveness factor results in Figure 7.7 (b) were taken by comparing MEA and RDE mass activities at +0.85 V (indicated by the dashed horizontal line in Figure 7.7 (a)) according to equation (7.4), where fortunately MEA data appear to be reliable.

The results in Figure 7.7 suggest that the Nafion®-Pt/C A MEA has a slightly higher effectiveness factor than the Nafion®-Pt/C B and standard commercial (TKK, E-Tek) MEAs. However, the improvement in effectiveness factor over the TKK MEA is barely significant ( $7.9 \pm 0.8$  % Nafion® Pt/C A vs.  $6.4 \pm 0.3$  % TKK). Given that there are bound to be significant irreproducibilities in the preparation of MEAs using the spray-coated GDE method employed in this study, it would be inappropriate to conclude from these results that the Nafion®-Pt/C A preparation route offers any advantage in terms of catalyst layer performance over standard commercial preparations. On the other hand, it is encouraging that the Nafion®-Pt/C A catalyst layer displays a significantly higher effectiveness factor than the Nafion®-Pt/C B catalyst layer: these two catalysts, being derived from the same starting material and processed using the same techniques, differ only in terms of their morphologies, with the enhanced Pt-ionomer interface proposed for the Nafion®-Pt/C A catalyst offering significantly better performance than the more commonplace, highly-dispersed morphology of the Nafion®-Pt/C B catalyst. Further studies involving multiple repeat experiments at various catalyst layer ionomer contents would be required in order to demonstrate conclusively whether the Nafion®-Pt/C A preparation route offers any benefit in terms of catalyst layer performance.

## 7.4 Conclusions

Significant variations in performance were observed between the four MEAs fabricated and characterised in this study. The MEAs prepared from Nafion®-Pt/C catalysts displayed generally poorer performance than those prepared using standard techniques from commercial catalysts. EIS measurements revealed that the charge transfer and mass transport losses were significantly higher for the Nafion®-Pt/C MEAs than for those fabricated using commercially-available materials. The Nafion®-Pt/C A catalyst offered no improvement in catalyst utilisation as calculated from ECSA values measured by cyclic voltammetry. Whilst the Nafion®-Pt/C A catalyst layer did have a slightly higher effectiveness factor than the other catalysts on test, the improvement was not sufficient to counteract its intrinsically lower mass activity (as measured in RDE experiments), with the result that the performance of the Nafion®-Pt/C A MEA was the lowest of those on test.

In light of the rather poor performance observed for the Nafion®-Pt/C catalysts, it is worth noting that the materials and preparation methods used to fabricate MEAs were taken from previous

---

---

studies involving standard commercially-available catalysts. Further optimisation of the MEA preparation route; investigating alternative catalyst compositions, ink solvents and deposition methods, for instance, would be likely to offer improvements in performance for the Nafion®-Pt/C catalysts.

Finally, the results presented herein represent beginning-of-life performance for the four MEAs. Given the significantly enhanced durability observed for the Nafion®-Pt/C A catalyst in *ex-situ* tests, it is likely that the Nafion®-Pt/C A MEA would show a lower rate of performance degradation than the other MEAs in the longer term. Constraints on time and equipment availability precluded long-term *in-situ* durability testing, but it would be of interest to conduct such experiments in future work.

## 8 Pt-Ti bimetallic catalysts

This chapter introduces the concept of bimetallic catalysts as a means to achieve enhanced Pt mass activity in ORR catalysis. In this study, and in parallel with the development of the Nafion®-Pt/C catalysts described thus far, bimetallic catalysts composed of Pt and Ti were prepared using wet-chemical colloidal methods which will be described in the following.

### 8.1 Background

In order to develop guiding principles for the improvement of Pt electrocatalysts through alloying, it is necessary to understand some of the detail regarding the rate-limiting aspects of the catalytic ORR, and why Pt has remained the catalyst of choice for this reaction to date.

Figure 8.1 (a) shows the ORR activities plotted versus the binding energies for oxygen on the surface of various elemental catalysts [23]. This representation of relative catalytic activity is known as a 'volcano' plot, and Pt evidently has the highest activity toward the ORR of all the elemental catalysts. The shape of the volcano plot can be rationalised by application of the Sabatier principle [220-221], which holds that a heterogeneous catalyst must bind reaction intermediates with sufficient strength to facilitate electron (and proton) transfer, but weakly enough so as to allow spectator species and reaction products to desorb from the surface and free-up active sites for further reaction. The elements on the lower left side of the volcano plot (W, Mo, Fe, Co, Ru) bind oxygen species rather strongly (large, negative binding energy  $\Delta E_{\text{O}}$ ), and therefore make poor catalysts for the ORR: stable surface-bound oxygen species are unlikely to undergo protonation and desorption. Conversely, the binding of oxygen species to Ag and Au on the lower right branch of the volcano is too weak to facilitate electron transfer. Of all the elemental catalysts, Pt offers the most favourable interaction with oxygen species, with an oxygen binding energy,  $\Delta E_{\text{O(Pt)}} = +1.57$  eV found from *in-silico* DFT calculations [23]. However, the optimum oxygen binding energy for maximal ORR activity has been shown to lie at around +1.8 - +2.0 eV [23], with the implication that, far from being an ideal ORR catalyst, Pt actually binds oxygen rather too strongly, which decreases the availability of the most active metallic Pt sites and lowers its intrinsic ORR activity. There is considerable scope for improving ORR kinetics through the development of catalysts with oxygen binding energies 0.3-0.4 eV more positive than that of Pt, and this has been the focus of much of the work carried out to date on bimetallic alloys of Pt.

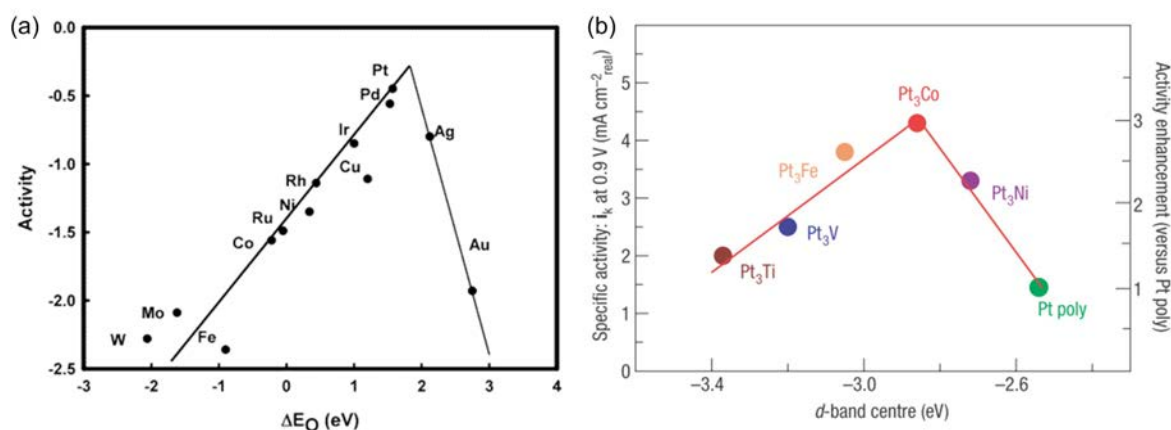


Figure 8.1: (a) Volcano plot for ORR catalysis on several transition metal surfaces. The activity scale is normalised by maximum theoretical activity (=0), and the binding energy for oxygen is shown in the horizontal axis. Reproduced from [23] (b) A volcano plot for bulk, ordered Pt<sub>3</sub>M bimetallic alloys (M=Ti, V, Fe, Co, Ni), with specific ORR activity @ 0.9 V plotted vs. the d-band centre as measured in UPS experiments. 'Pt poly' represents bulk, polycrystalline Pt. Reproduced from [24]

### 8.1.1 Ascending the volcano: Pt alloy catalysts

The enhanced activity of bimetallic electrocatalysts was first observed in studies on PAFCs in the early 1980s [222] before being applied to and studied further in PEMFCs from the early 1990s [162, 223-224]. From Figure 8.1 (b) it is clear that several Pt-M (M=Ti, V, Fe, Co, Ni) offer enhanced catalytic activity towards the ORR compared to Pt alone. The most common alloys, PtCo, PtNi and PtFe have been studied extensively from both theoretical and experimental perspectives: numerous reports in the literature confirm their enhanced ORR activity and identify the origins of the activity enhancement in terms of *geometric* and *electronic* effects.

#### Electronic effects

When certain base metals are introduced into a Pt lattice, sharing of Pt *d*-band electrons with unfilled *d*-type orbitals of the base metal leads to an increase in Pt *d*-band vacancy, characterised by an energetic downshift in the *d*-band density of states (DOS) away from the Fermi level,  $E_F$  [225]. This withdrawal of electron density from the surface corresponds to a decrease in binding energy for surface adsorbates, leading to an increase in surface site availability and more favourable interactions with reaction intermediates. This electronic effect (also sometimes called the ligand effect) is generally considered to be the most significant in determining binding energy of adsorbates on Pt-M alloy surfaces.

Mukerjee et al [224] found that the magnitude of the *d*-band vacancy is proportional to the electronegativity of the alloying species, as one would expect. Thus the binding energy of

## 8 Pt-Ti bimetallic catalysts

---

adsorbates, and therefore the catalytic activity, can be tuned by selection of appropriate alloying metals.

The data in Figure 8.1 (b) are from a study by Stamenkovic *et al* in which the ORR activities of well-defined bulk single-crystal surfaces prepared from various Pt-M alloys (M=Ti, V, Fe, Co, Ni) were measured using an RDE technique [24]. The authors measured the *d-band centre* of Pt surface atoms (the average energy of their *d* state electrons relative to the Fermi energy) using ultraviolet photoelectron spectroscopy and used this to quantify the strength of surface-adsorbate interactions. As shown in Figure 8.1 (b), the ordered intermetallic Pt<sub>3</sub>Co showed a threefold increase in ORR activity over that of pure Pt, and the downwards shift in its *d*-band centre by  $\sim 0.35$  eV relative to pure Pt is in good quantitative agreement with the optimum oxygen binding energy predicted in theoretical studies by Norskov *et al* [23].

### Geometric effects

As well as their effect on the electronic properties of surface Pt atoms, alloying metals can also influence the atomic-scale geometry and topography of the surface in several ways:

- The interatomic spacing of surface Pt atoms varies according to the lattice parameter of the underlying base metal or alloy phase. The resulting lattice strain can affect the binding energies and adsorption isotherm of surface adsorbates [95, 155, 222, 226], and may also influence aspects of the reaction mechanism e.g. energy of dissociation for dioxygen molecules adsorbed on adjacent Pt atoms [227].
- It has been proposed that the presence of 'islands' of a second, oxophilic metal on the surface may reduce the affinity of adjacent Pt atoms for oxygen adsorbates [95].
- Leaching of base metal atoms from a mixed Pt-M surface has been shown to produce a roughened Pt-'skeleton' surface with a large number of low-coordination Pt sites [24], which typically display a higher affinity for oxygen adsorbates, and therefore a lower ORR activity, than terrace (111), (100) sites [228].

In practice, enhancements in ORR activity for a given Pt-M alloy composition are due to a combination of electronic and geometric effects, and it is difficult to deconvolute the two.

### **8.1.2 Studies on bulk alloy surfaces vs. nanoparticle catalysts**

The majority of the studies referred to above, relating enhancements in ORR activity to changes in the electronic and geometric properties of the catalyst surface, were conducted on well-defined (typically single-crystal) extended surfaces. Practically-useful fuel cell catalysts composed of

---

carbon-supported, nanocrystalline analogues of these bulk materials are by no means guaranteed to exhibit the same enhancement in specific activity; even relative to pure-Pt catalysts of the same particle size (distribution) [229]. This is because the surface electronic and geometric properties determining ORR activity also vary with particle size and shape.

### **Particle size effects**

It has been found previously that nanosized Pt and Pt-Co particles exhibit stronger interactions with oxygen species than bulk surfaces, due to an increase in d-band electron density, shortening of the Pt nearest-neighbour distance, and increasing prevalence of under-coordinated surface atoms on decreasing particle size[150]. These effects can be expected to counteract the decrease in adsorbate binding energy provided by alloying, which may alter the shape of the volcano for small particles compared with extended surfaces, so that compositions appearing on the weak-binding branch of the bulk volcano plot (e.g. Pt<sub>3</sub>Ti, Pt<sub>3</sub>V) are shifted towards the peak activity when in nanocrystalline form.

### **Shape effects**

Various groups have observed significant variation in catalytic activity across different crystallographic surface planes. Stamenkovic *et al* [25] reported that the rate of ORR on the Pt<sub>3</sub>Ni(111) surface was around 10 times higher than on the PtNi(100) surface, and around 90 times higher than the pure Pt(111) surface (Figure 8.2).

This structure-sensitivity has implications for particle shape. As shown in the schematic in Figure 8.2, for a face-centred cubic (*fcc*) crystal structure, cubic particles have entirely (100)-type surfaces, whilst cubo-octahedral particles have a mixture of (100) and (111) surface planes and tetrahedral particles are terminated entirely by (111) faces. If the catalytic activity varies significantly between crystallographic planes then one would expect there to be a corresponding variation in specific catalytic activity. In the case of Pt<sub>3</sub>Ni, tetrahedral particles consisting entirely of the highly active (111)-type surface should exhibit superior specific activity to cubic particles with tenfold-inferior (100) surfaces. This prediction was recently verified in an experimental study on shape-controlled Pt<sub>3</sub>Ni nanoparticles [230].

## 8 Pt-Ti bimetallic catalysts

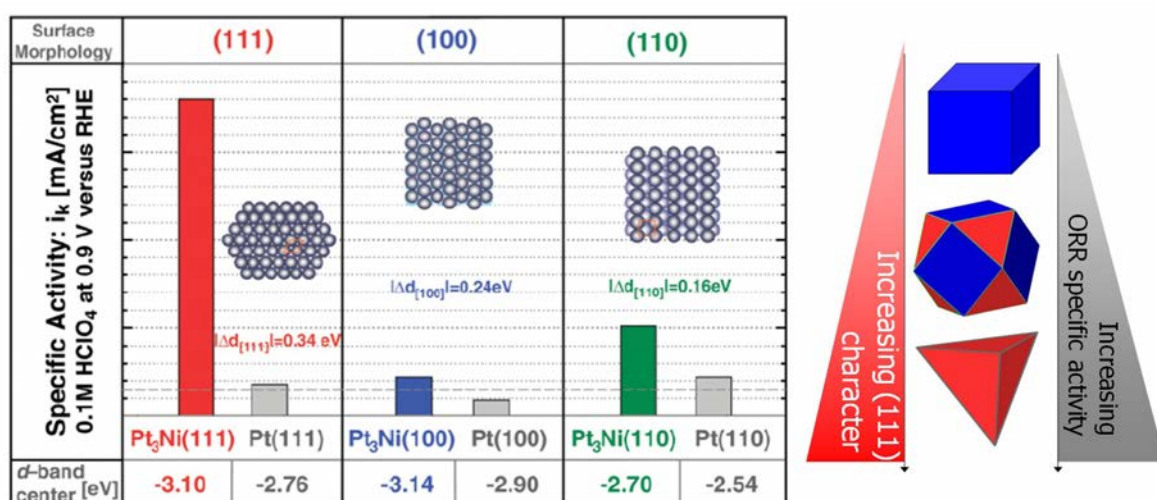


Figure 8.2: Relative rates of ORR on Pt<sub>3</sub>Ni and pure Pt surfaces, along with corresponding  $d$ -band centre shifts in eV. Reproduced from [25]. The accompanying schematic illustrates variation in crystallographic surface composition for particles of different geometries.

Despite the potential difficulties, studies on extended surfaces can still provide useful indications of ORR activity for nanocrystalline materials with similar compositions. Paulus *et al* conducted a study comparing the activity enhancement of carbon-supported bimetallic nanoparticles possessing ordered Pt<sub>3</sub>Co and Pt<sub>3</sub>Ni compositions with that of the analogous bulk materials [95, 231]. They found that the alloy materials offered consistent 1.5 to 2-fold enhancements in activity relative to pure Pt in both nanocrystalline and bulk forms.

### 8.1.3 Durability issues with Pt-M bimetallic catalysts

To be viable for practical PEMFC systems, catalysts must be durable as well as active. In addition to the various degradation modes identified in section 6.1.1, bimetallic catalysts are subject to additional degradation due to the segregation and/or dissolution of the base metal component of the catalyst.

In the presence of oxygen species, subsurface base metals within bimetallic nanoparticles have been observed to undergo segregation to the surface [232-235], thus lowering the proportion of active Pt surface sites.

Once at the surface, the base metal components of Pt-M bimetallic nanoparticles can be dissolved, so that the base metal content of the alloy catalyst is gradually reduced during operation [178, 233, 236-240].

Dissolved base metal species suffer a similar fate to dissolved Pt species formed at the PEMFC cathode; being either flushed from the cell in product water or deposited within the ionomer, decreasing its conductivity and lowering cell performance [237].



---

### 8.1.4 Pt-M alloys with enhanced durability

Recently, alloys of Pt with early transition metals (Sc, Y, Ti) have been identified as being potentially more durable than Pt-Co and Pt-Ni catalysts, whilst offering similar improvements in activity over pure Pt [241].

Figure 8.3 (a-d) shows the results of a combined computational and experimental study by Greeley *et al.*, which identified bimetallic species with Pt-skin structures expected to offer enhanced ORR activity on the basis of their binding energy for oxygen adsorbates, whilst also evaluating their thermodynamic stability in terms of the energy of formation of the alloy phase.

The plot in Figure 8.3 (b) shows the output of their computational screening procedure, with oxygen binding energy (relative to pure Pt) on the vertical axis ( $\Delta E_{O^*} - \Delta E_{O^*}^{Pt}$ ) and the energy of formation of the alloy ( $\Delta E_{alloy}$ ) on the horizontal axis. The white band in the centre of the plot represents the range of oxygen binding energies expected to result in an improvement of ORR activity. The thermodynamic stability of the alloy species increases from right (-1.2 eV per atom) to left (+0.2 eV per atom). The sub-surface composition of the alloys is also represented with red circles (50% alloying element) and blue squares (25% alloying element). From these results, it is clear that the alloys Pt<sub>3</sub>Sc, Pt<sub>3</sub>Y and Pt<sub>3</sub>Ti are expected to be the most thermodynamically stable – significantly more so than the 'traditional' Pt-M alloys (M=Ni, Co, Fe, Cr, Cu, Mo, Mn). It is worth noting that alloys with binding energies less negative than -1.23 eV (i.e. *all* of those in Figure 8.3) are still thermodynamically unstable against dissolution at the PEMFC cathode. However, the energy barrier associated with lattice migration and surface segregation of base metal atoms is likely to be determined in part by the energy of formation of the alloy [228], so the *kinetics* of these degradation processes should be far slower for the more thermodynamically stable alloys.

Having identified Pt<sub>3</sub>Y and Pt<sub>3</sub>Sc as potentially highly active and stable ORR catalysts, the authors performed electrochemical experiments on bulk polycrystalline specimens of these alloys, which confirmed that Pt<sub>3</sub>Y and Pt<sub>3</sub>Sc offer 6-fold and 1.5-fold enhancements in ORR activity (relative to pure Pt at 0.9 V *vs* RHE) respectively. The ORR activity of Pt<sub>3</sub>Y was the highest found to date for a polycrystalline Pt alloy, placing it close to the top of the volcano plot in Figure 8.3 (a). The RDE voltammograms in Figure 8.3 (c) show a clear positive shift in the ORR onset potential for Pt<sub>3</sub>Y and Pt<sub>3</sub>Sc relative to Pt. The authors also went some way toward demonstrating the stability of the alloys under potential cycling: the dashed lines in Figure 8.3 (d) show the performance of the alloy electrodes to be unchanged after 90 minutes of cycling from 1.0 to 0.05 V *vs* RHE at 20 mV.s<sup>-1</sup>. Whilst this is promising from a durability perspective, it is still possible that in

## 8 Pt-Ti bimetallic catalysts

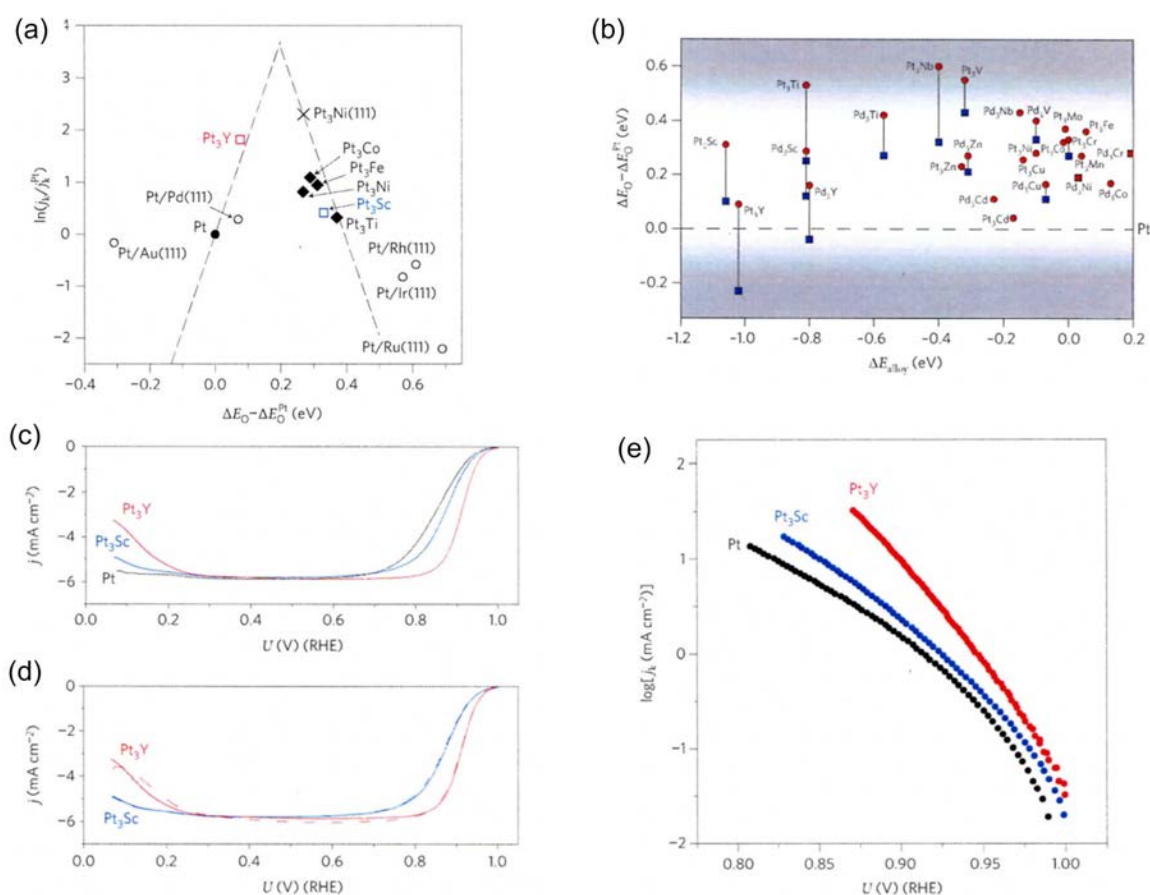


Figure 8.3: (a) ORR volcano plot featuring early transition metal alloys Pt<sub>3</sub>Y, Pt<sub>3</sub>Sc and Pt<sub>3</sub>Ti; (b) plot generated from computational data for oxygen binding energy (relative to Pt) and the energy of formation  $\Delta E_{ally}$  of Pt-M alloys; (c) linear sweep voltammograms for Pt and Pt<sub>3</sub>Y, Pt<sub>3</sub>Sc single-crystal surfaces obtained in RDE experiments at 23°C, 1600rpm in 0.1M HClO<sub>4</sub> at a scan rate of 20 mV.s<sup>-1</sup>; (d) anodic RDE sweeps comparing initial performance (solid lines) and that after 90 minutes of cycling (dashed lines); (e) Tafel plots of ORR specific activity for Pt and Pt<sub>3</sub>Sc, Pt<sub>3</sub>Y alloys.

nanocrystalline form the alloys may be prone to dissolution/leaching of base metals, and the authors acknowledge the need for *in-situ* PEMFC testing to confirm the expected stability. Whilst the authors did not make experimental investigations of the Pt<sub>3</sub>Ti system, it can be expected to have a similar activity to that of Pt<sub>3</sub>Sc, given the proximity of these two alloys on the volcano plot in Figure 8.3 (a).

The enhanced activity of nanocrystalline Pt<sub>3</sub>Y alloy electrocatalysts was recently demonstrated in half-cell (RDE) and PEMFC experiments by Yoo *et al* [242]. Catalyst films were prepared by high-pressure co-sputtering of Pt and Y onto glassy carbon (RDE) and carbon cloth (PEMFC) substrates, producing porous nanocrystalline Pt<sub>3</sub>Y films around 100 nm thick, with grain sizes of 8-10 nm. Alloy electrodes prepared in this way exhibited a 16-fold increase in ORR specific activity relative to similarly-prepared Pt electrodes. Accelerated stress testing conducted in 0.1M HClO<sub>4</sub> by cycling between 0.6-1.1 V produced no degradation in performance or reduction in yttrium content after 3,000 cycles.

---

Based on these recent studies, the preparation of well-defined, nanoparticle analogues of the bulk Pt<sub>3</sub>Y, Pt<sub>3</sub>Sc and Pt<sub>3</sub>Ti alloys is emerging as an area of great interest from the perspective of improving the activity and durability of ORR catalysts.

### 8.1.5 Bimetallic nanoparticles of Pt and early transition metals

Despite promising enhancements in ORR activity and superior durability compared to Pt-3d alloys, the work by Yoo *et al.* described above remains the only application to date of Pt-Y or Pt-Sc alloys as PEMFC cathode electrocatalysts. Moreover, there have been no documented attempts to develop methods for the wet-chemical preparation of well-defined Pt-Y or Pt-Sc alloy nanoparticles for use as ORR catalysts. This is unsurprising, as the highly negative reduction potentials of soluble Y<sup>3+</sup> and Sc<sup>3+</sup> precursors (Table 8.1), together with the highly oxophilic nature of metallic Y and Sc, necessitate the use of strong reducing agents and dry, aprotic solvents, making the synthesis of these materials rather challenging.



Table 8.1: Electrochemical series for reduction reactions of Na<sup>+</sup>, Y<sup>3+</sup>, Sc<sup>3+</sup>, Ti<sup>2+</sup> and Pt<sup>2+</sup> to metallic states.[138]

Despite similar challenges, the successful synthesis of Pt<sub>3</sub>Ti alloy nanoparticles has been reported previously by Abe *et al.* [243]. To overcome the highly negative reduction potential of Ti<sup>2+</sup>, they employed the powerful reducing agent sodium naphthalide for the concurrent reduction of a tetrahydrofuran (THF) adduct of TiCl<sub>4</sub> and an organometallic Pt salt (1,5-cyclooctadiene)PtCl<sub>2</sub>. The reaction was carried out under anhydrous conditions using dry THF as a solvent, at a variety of Pt:Ti precursor ratios. The authors found that the as-prepared product consisted of Pt-Ti alloy nanoparticles with a particle size of 3±0.4 nm. Upon vacuum annealing at 600°C, the atomically-disordered product was transformed to an ordered Pt<sub>3</sub>Ti phase similar to that commonly observed for the Cu<sub>3</sub>Au system, accompanied by an increase in particle size to 37 ± 23 nm. Although no electrochemical characterisation toward the ORR was carried out, the authors did find that the ordered Pt<sub>3</sub>Ti catalyst was more active than both Pt and Pt-Ru towards the electrocatalytic oxidation of methanol and formic acid.

The work of Abe *et al.* [243] serves as an important proof of principle for this study and others attempting the synthesis of Pt-early transition metal alloy nanoparticles. In particular, the method and reagents used for the wet-chemical synthesis of these Pt<sub>3</sub>Ti nanoparticles ought to be

## 8 Pt-Ti bimetallic catalysts

---

applicable broadly to any metal where a suitable precursor exists (that is, one that is soluble in THF and contains no oxygen functionalities). Importantly in this respect, metallic sodium (the active agent in sodium naphthalide) has a standard reduction potential of -2.71 V, which is more negative than that of Y, Sc and Ti, and should therefore facilitate the reduction of precursor species to zero-valent states for all three of these metals.

### 8.1.6 Core@shell nanoparticles

The introduction of a second metal into Pt nanoparticles gives rise to two additional degrees of freedom:

- Composition – the molar ratio of the alloying (or 'solute') metal to Pt.
- Combination fashion – the three-dimensional arrangement of the two metals within the particles.

Composition is relatively easy to control by changing the ratio of metallic precursors in chemical syntheses, or varying the deposition rate/time for layer-by-layer approaches to nanocatalyst fabrication (e.g. sputtering, electrodeposition).

To gain proper control over the arrangement of the two metals is more difficult. Two metals can take on any of several combination fashions as illustrated in Figure 8.4. The degree of segregation/mixing is determined both by intrinsic properties of the alloying species and by preparation conditions (temperature, pressure, concentration and chemical nature of precursors) [26, 244]. From the point of view of maximising Pt mass activity in ORR catalysis, the ideal structure is a 'core@shell' type arrangement (Figure 8.4 (a)) consisting of a single monolayer of Pt surrounding a base metal core.

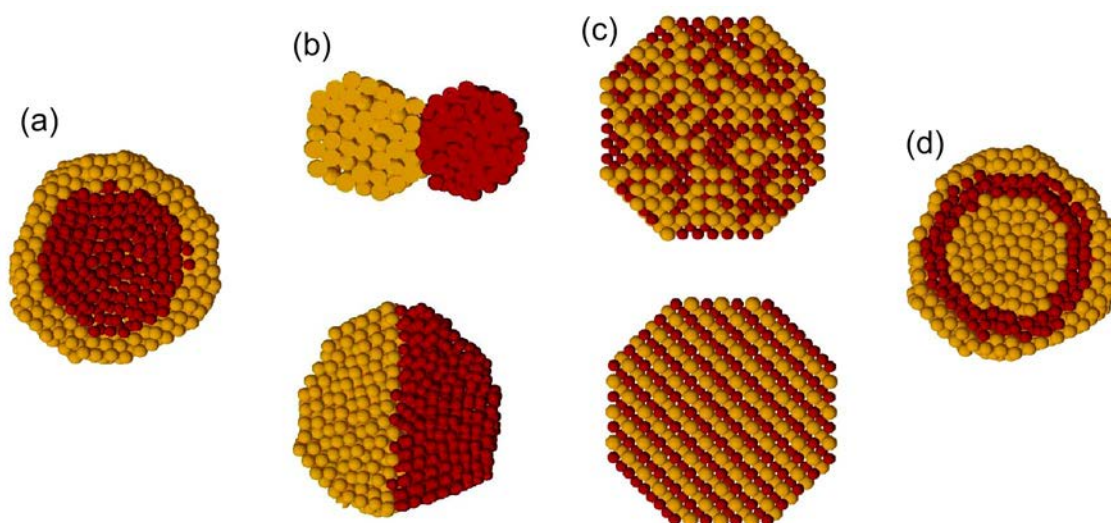


Figure 8.4: Possible combination fashions for two metals forming a bimetallic nanoparticle include (a) core-shell; (b) 'dipolar' or 'dumb-bell'; (c) intermixed random or ordered intermetallic alloys or (d) multi-layer 'onion-like' structures. Reproduced from [26].

## **Methods for the production of M@Pt nanoparticles**

Several methods exist for the production of metallic core@shell nanoparticles, and these can be broadly categorised into 'top-down' and 'bottom-up' approaches. The former approach involves firstly the production of nanoparticles consisting of an intermixed (either ordered or random) alloy of the two metals, followed by further treatment to induce segregation of the required species to the surface. The latter involves the deposition of the shell upon pre-formed cores.

### **Top-down methods**

For certain combinations of metals, it is thermodynamically favourable for one species to undergo surface segregation. It is then possible to produce a core@shell type structure simply by thermal annealing (usually under vacuum or an inert atmosphere) of mixed-alloy precursor particles. This method has been applied to produce core@shell nanoparticles with compositions including Pt@Pd [245-246], Cu@Pt [247] and Ru@Pt [248]. A computational study by Wang and Johnson suggested that Au@Pt and Ag@Pt structures should also be thermodynamically favoured [249]. At present, in the absence of any published data, it is uncertain whether nanocrystalline alloys of PtY, PtSc or PtTi will offer the luxury of automatic surface segregation of Pt upon thermal annealing. Encouragingly, though, a recent *in-silico* study has predicted stable Ti@Pt structures for Pt<sub>32</sub>Ti<sub>6</sub> clusters [250].

In a different approach, Mayrhofer *et al.* induced segregation of Pt to the surface of intermixed PtCo nanoparticles by treatment with CO [251]; an effect attributed to preferential binding of CO

## 8 Pt-Ti bimetallic catalysts

---

to Pt. Unfortunately, the opposite effect was observed upon exposure to an oxygen environment, with subsurface Co migrating to the surface [252].

Finally, electrochemical dealloying has shown to be effective in producing core@shell morphologies from mixed PtCu nanoparticles [253-254]. In this approach, Cu atoms are dissolved from the particle surfaces by electrochemical treatment, leaving a Pt-enriched shell surrounding a PtCu core [255]. This method has yet to be demonstrated for any system other than Cu@Pt.

### **Bottom-up methods**

An interesting approach for the formation of well-defined single-monolayer shells of Pt involves the galvanic displacement by Pt of an underpotentially-deposited monolayer of Cu on a noble metal shell. The method proceeds in two steps: (1) a monolayer of a sacrificial metal (Cu or Pb) is formed on a noble metal (Pd or Au) core by underpotential electrodeposition; (2) the sacrificial monolayer is exchanged for a Pt monolayer by Galvanic displacement. These steps can be repeated to form layers of Pt with well-defined thickness [158, 256]. In previous studies to date, the method has employed aqueous electrolytes and solutions for the electrodeposition and Galvanic displacement steps, which preclude the use of oxophilic base metal cores (Y, Sc, Ti). However, it is possible that the method could be adapted for such materials through the use of organometallic salts of Cu and Pt; and organic solvents or ionic liquids in place of the aqueous electrolyte.

The most common and versatile route for the synthesis of bimetallic nanoparticles with core@shell structures is wet-chemical colloidal synthesis. Usually in such methods, core particles are first formed by the reduction of a precursor of the core metal in a precipitation reaction as described earlier in section 4.2.1, followed by deposition of Pt shells by *in-situ* chemical reduction of a Pt<sup>2+</sup> or Pt<sup>4+</sup> precursor. Core@shell nanoparticles with a variety of compositions have been successfully prepared using this core-mediated sequential reduction approach, including Pt@Pd [246, 257-258], Ni@Pt [259], Au@Pt [260-261], Rh@Pt [262] and Ru@Pt [263].

### **Colloidal synthesis of M@Pt (M=Y, Sc, Ti): practical considerations**

In the core-mediated, sequential-reduction approach to the synthesis of M@Pt nanoparticles, the morphology of the heterogeneous product is determined by the intrinsic properties of the two metals, their interactions, and reaction conditions. In particular, the lattice mismatch between Pt and the core metal has a significant effect on the structure of the product. This mismatch induces a positive strain energy  $\gamma_{strain}$  which increases rapidly during Pt overgrowth on the core metal [264]. There is also an additional energy term  $\gamma_i$  associated with the Pt-M interface, and the interplay

---

between this interfacial energy and the surface energies of Pt ( $\gamma_{Pt}$ ) and the core metal ( $\gamma_M$ ) determines the structure of the Pt overgrowth on the core nuclei according to the overall excess energy  $\Delta\gamma$  given by equation (8.3) [265-266].

$$\Delta\gamma = \gamma_{Pt} + \gamma_i + \gamma_{strain} - \gamma_M \quad (8.6)$$

Depending on the value of  $\Delta\gamma$ , three overgrowth modes are possible, as illustrated in Figure 8.5.

- **Frank–van der Merwe (FM) mode**

For cases where the lattice mismatch between Pt and M is small, and the surface energy of M is large ( $|\gamma_{Pt} + \gamma_i + \gamma_{strain}| \ll |\gamma_M|$ ), then the excess free energy is negative during growth and epitaxial deposition of the Pt shell in a uniform layer around the core proceeds via the Frank–van der Merwe (FM) or layer-by-layer growth mode [266].

- **Volmer-Weber (VM) mode**

Conversely, if  $\Delta\gamma$  is positive (in the case of large interfacial energy, or low surface energy of M relative to Pt), then Pt is deposited preferentially at high-energy sites (steps, edges) on the substrate metal M, and forms islands in order to minimise the extent of the Pt-M interface. This island-type growth is known as the Volmer-Weber (VM) growth mode.

- **Stranski–Krastanov (SK) mode**

In some cases – in particular where the lattice mismatch between Pt and M is large – the excess energy at the onset of deposition is negative, resulting initially in epitaxial growth, but then becomes positive once the strain energy  $\gamma_{strain}$  reaches a critical value at a certain shell thickness, activating the growth of Pt islands. This island-on-shell growth is known as the Stranski–Krastanov growth mode.

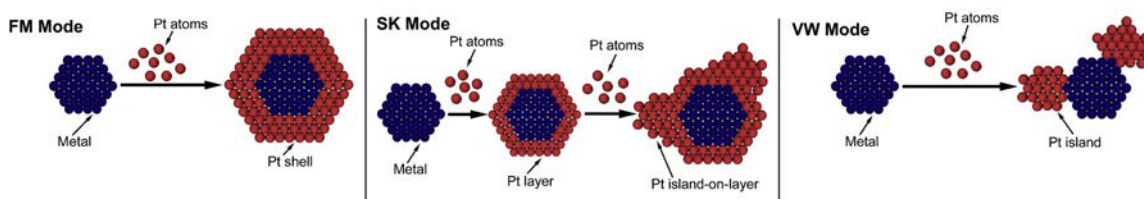


Figure 8.5: Three distinct modes for the overgrowth of Pt on a pre-formed metal core. Reproduced from [15].

The FM mode is the most desirable in order to maximise Pt utilisation and the ORR-enhancing effects of Pt-M electronic interactions. From the lattice constants given in Table 8.2, the mismatch for Pt-Sc and Pt-Y is quite small, whilst that of Pt-Ti is rather large. Therefore FM growth mode for Pt on Ti cores in particular is expected to be hindered by a large interfacial energy. Practically, this can be mitigated by minimising the surface energy of the Ti cores through the use of surfactants or capping ligands. Transition from the FM to the SK growth mode can be prevented by careful dosing of the Pt precursor to ensure that the shell thickness remains below the threshold

## 8 Pt-Ti bimetallic catalysts

for the onset of island growth. Further to this, it is important that the rate of addition of the Pt precursor is kept low enough to ensure that the bulk concentration of metallic Pt species does not exceed the supersaturation threshold for the formation of Pt crystal nuclei; otherwise a distinct population of pure-Pt nanoparticles will appear in the product in addition to (or instead of) the desired core@shell species [259].

|    | Crystal structure | Lattice constants / Å |       |       |
|----|-------------------|-----------------------|-------|-------|
|    |                   | $a_0$                 | $c_0$ |       |
| Sc | h.c.p.            | 3.31                  | 5.27  | [267] |
| Y  | h.c.p.            | 3.65                  | 5.73  | [267] |
| Ti | h.c.p.            | 2.95                  | 4.69  | [268] |
| Pt | c.c.p.            | 3.92                  | -     | [138] |

Table 8.2: Crystal structures and lattice parameters for Sc, Y, Ti and Pt at standard temperature and pressure 25°C, 1 atm.

### 8.1.7 Summary and implications for this work

Alloys of Pt with early transition metals (Y, Sc, Ti) have been identified as promising candidates for highly-active ORR electrocatalysts, with enhanced stability relative to alloys of Pt with 3d transition metals (Ni, Co, Fe).

Of the various possible combination fashions for Pt-M bimetallic nanoparticles, core@shell structures consisting of an early transition metal core surrounded by a Pt shell are expected to offer optimum Pt mass activity

Wet-chemical, colloidal methods exist for the preparation of core@shell nanoparticles with a variety of compositions, although to date none have been applied to the synthesis of Y@Pt, Sc@Pt or Ti@Pt. Abe *et al.* have shown that it is possible to prepare mixed alloy nanoparticles composed of Pt and early transition metals (specifically Pt<sub>3</sub>Ti) by using air-free synthetic methods with strong reducing agents in anhydrous, aprotic solvents [243].

## 8.2 Aims and objectives

In this work, the methods of Abe *et al.* [243] will be adapted to attempt the synthesis of Ti@Pt nanoparticles. Titanium was chosen over Y and Sc for this initial work because the synthesis of colloidal Ti is supported by previous studies in the literature, whereas there is currently a distinct absence of any prior work on the preparation of metallic Y and Sc colloids. Nevertheless, care will be taken to develop a general synthetic method, which should be applicable to Y and Sc with only minor modifications.



---

The aims and objectives for this study are thus:

- To develop a method for the production of **metallic Ti nanoparticles** that could be easily adapted for Y and Sc.
- To develop and test strategies for the production of **Ti@Pt** nanoparticles
- To perform **physical characterisation** of reaction products in order to determine their structure and composition.

## 8.3 Methods and materials

In the following, attempts to synthesise metallic Ti nanoparticles followed by deposition of Pt shells are described, along with the methods employed for the physical characterisation of the synthetic products.

### 8.3.1 General strategy for Ti@Pt nanoparticle synthesis

A core-mediated sequential-reduction method was developed for the synthesis of Ti@Pt nanoparticles in this work. The overall scheme is shown in Figure 8.6. Metallic Ti<sup>0</sup> cores were first formed by chemical reduction of a Ti<sup>4+</sup> precursor in anhydrous THF under inert atmosphere. A Pt<sup>2+</sup> precursor was then added slowly for the controlled formation of Pt shells. Given the difficulties anticipated in selecting the FM growth mode for the Pt shell, a strategy for the reduction of Ti core surface energy was developed, which involved the *in-situ* grafting of organic ligands to the surface of Ti cores during their nucleation using diazonium chemistry.

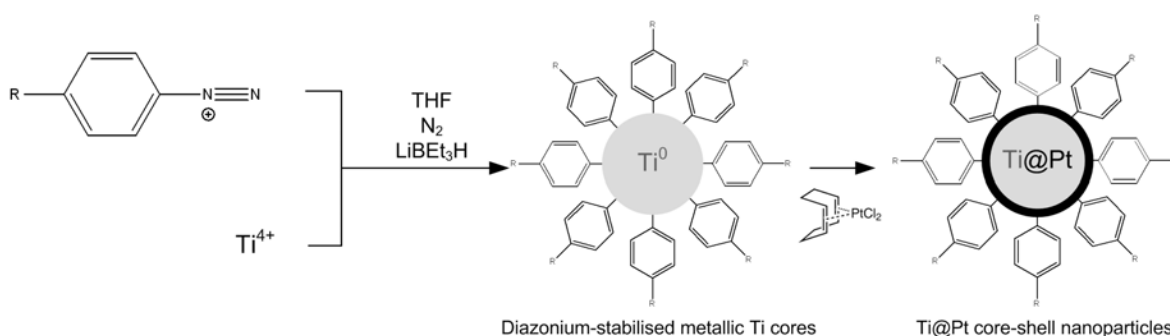


Figure 8.6: Overall synthetic protocol employed in this work for the synthesis of Ti@Pt nanoparticles. First a Ti<sup>4+</sup> precursor is reduced by LiBEt<sub>3</sub>H in the presence of a diazonium salt to produce ligand-stabilised metallic Ti cores, followed by addition of a Pt precursor which is reduced *in-situ* to form the Pt shells.

### 8.3.2 Synthesis of diazonium compounds

Diazonium compounds are commonly employed as reactive intermediates in organic synthesis, and are characterised by the diazonium ion  $\text{N}\equiv\text{N}^+$ , usually attached to an aromatic ring as in Figure 8.7 (a).

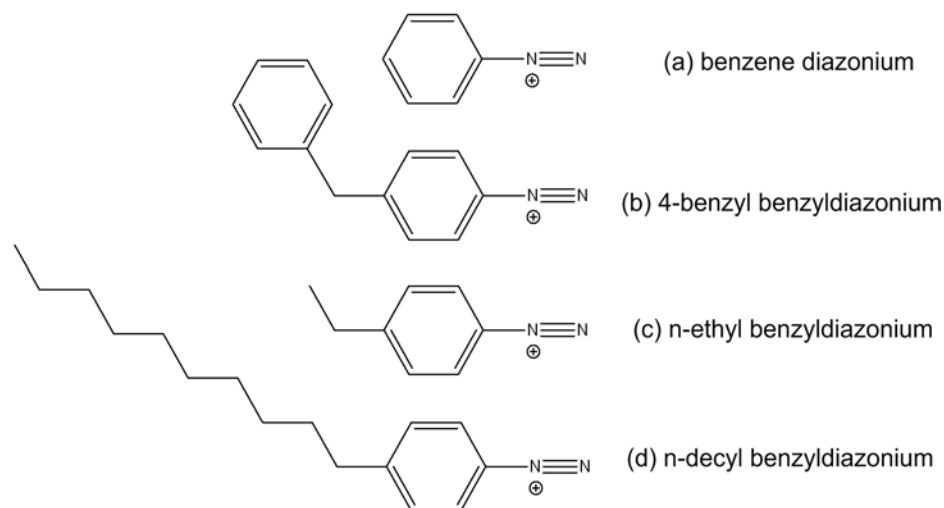


Figure 8.7: Diazonium ligands used in this study for the stabilisation of metallic Ti nanoparticles

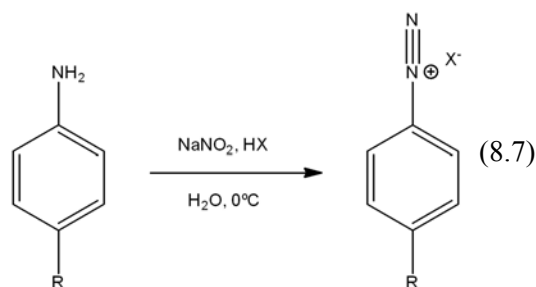
It is well known that organic ligands can be grafted to a wide range of surfaces (including polymers, metals, metal oxides and carbon materials) by reduction of their diazonium derivatives [269]. Treatment of a diazonium salt ( $\text{R-N}_2^+$ ) with a reducing agent results in the release of  $\text{N}_2$ , leaving an extremely reactive radical ( $\text{R}\bullet$ ), which forms a covalent bond with any available substrate – in this case colloidal Ti nanoparticles undergoing nucleation and growth.

The functionalisation of metal nanoparticles with organic ligands via their diazonium derivatives has been demonstrated previously for Pd [270], Au [271], Pt [271] and Ti [272] nanoparticles. In all of these studies, the diazonium salt was present along with the metal precursor prior to the reduction step, and the product(s) were found to consist of metallic nanoparticles capped by covalently-bound organic ligands. Of particular relevance to this work is that by Ghosh *et al.*, in which Ti nanoparticles capped by biphenyl ligands were prepared by reduction of  $\text{TiCl}_4$  with lithium triethylborohydride in the presence of biphenyldiazonium tetrafluoroborate [272]. Their product was shown to be metallic and was reported to be stable in air; unlike previous Ti nanopowders, which were found to be extremely pyrophoric [273]. The biphenylamine precursor employed by Ghosh *et al.* is a potent carcinogen and was unavailable for this study. The alternative compounds considered for this study are shown in Figure 8.7 (b-d).

Due to their inherent reactivity, diazonium salts were prepared immediately prior to use. The most common method for the preparation of diazonium salts is the oxidation of the analogous amine

---

precursor in acidic aqueous solution, using sodium nitrite as in scheme (8.7). The counter ion  $X^-$  for the diazonium salt is provided by the acid species in the reaction.



Because the diazotization is carried out in aqueous solution, it is important that the product can be isolated and dried thoroughly prior to use in the anhydrous synthesis of Ti nanoparticles. Diazonium halide salts are typically far too unstable to be isolated in dry form, and have been known to detonate upon solvent removal. Fortunately, the tetrafluoroborate salts are stable in crystalline form, and can be isolated and dried as required. Even so, they decompose readily on exposure to UV radiation and react with water, so care was taken to avoid prolonged exposure of the salt to light or moisture during work-up.

The three diazonium ligands were trialled in this work (Figure 8.7 (b-d)) were prepared according to the method described by Mirkhalaf and Schiffrin [271]. Amine precursors for each ligand (4-benzylaniline, 4-ethylaniline and 4-decylaniline) were purchased from Sigma Aldrich and used as-received. In a typical preparation, 2 mmol of the amine precursor was dissolved in 2 ml of a 50/50 v/v mixture of acetic and propionic acid (or hexanoic acid in the case of 4-benzylaniline), to which 2 ml 50 wt% aqueous solution of tetrafluoroboric acid ( $\text{HBF}_4$ , Sigma) was added before cooling to  $0^\circ\text{C}$  in an ice bath. One molar equivalent of an ice-cold 0.3 mM solution of  $\text{NaNO}_2$  was added dropwise under stirring. The mixture was stirred for 1hr and allowed to warm gently to  $\sim 10^\circ\text{C}$ . The coarse precipitate was filtered over a glass sinter and washed twice with cold fluoroboric acid, then twice with diethyl ether. The product, a colourless crystalline solid, was dried by vacuum desiccation over  $\text{CaCl}_2$ . The presence of the diazonium moiety in the product was confirmed by FTIR and NMR spectroscopy. Samples for NMR were prepared by dissolving  $\sim 1$  mg of the product in deuterated chloroform ( $\text{CDCl}_3$ ), and FTIR samples were prepared by evaporating a few drops of this solution from a KBr pellet.

### 8.3.3 Synthesis of unstabilised Ti-Pt nanoparticles

Early experiments on the synthesis of Ti@Pt nanoparticles were carried out using an adapted version of the method used by Abe *et al.* for the preparation of  $\text{Pt}_3\text{Ti}$  alloy nanoparticles. Whereas Abe *et al.* mixed the Ti and Pt precursor prior to co-reduction, it was hoped that reduction of the Ti

## 8 Pt-Ti bimetallic catalysts

---

precursor, followed sequentially by slow infusion and reduction of the Pt precursor might result in the desired core@shell product.

The experimental setup was as shown in Figure 8.8. Prior to each experiment, all glassware was cleaned by soaking in aqua regia, rinsed with HQ water followed by meticulous drying – first in an oven at 160°C for several hours, and then with a hot air gun once the apparatus was assembled and under vacuum/N<sub>2</sub> purge. The sodium naphthalide reducing agent was prepared by adding a freshly cut sliver of sodium metal (~15mg, washed with hexanes to remove residual mineral oil from storage) to a 1:1 stoichiometric quantity of naphthalene (reagent grade, Sigma) under N<sub>2</sub> purge in a 3-neck reaction vessel. Dry THF (50 ml) was added via cannula transfer to the addition flask, and from there in portions to the Na/naphthalene mixture under stirring using a PTFE-coated magnetic follower. The reaction was allowed to stir overnight, whereupon a clear, dark green solution of sodium naphthalide was formed.

A THF adduct of TiCl<sub>4</sub> (Ti(THF)<sub>2</sub>Cl<sub>4</sub>, Sigma) was used as received as the Ti precursor. In a typical synthesis, 20 mg Ti(THF)<sub>2</sub>Cl<sub>4</sub> was dissolved in 10 ml dry THF under N<sub>2</sub> purge in a dry flask. The solution was loaded into a dry, glass syringe without exposure to air and infused at 20 ml.min<sup>-1</sup> through a PTFE transfer line into the sodium naphthalide solution under continuous stirring. The reaction was allowed to stir for several hours. The Pt precursor solution was then prepared in the same manner as the Ti precursor by dissolving the required amount of (1,5-cyclooctadiene)PtCl<sub>2</sub> (99.9% metals basis, Sigma) in dry THF, and transferred into a syringe before infusing slowly at 3 ml.hour<sup>-1</sup> into the pre-formed Ti core mixture. Experiments were performed with Pt:Ti molar ratios of 1:1 and 2:1 by adjusting the quantity of the Pt precursor.

To isolate the product, the solvent and excess naphthalene were removed by vacuum distillation. The solid residue was washed with hexane and methanol to remove by-products, with the solid product separated from the washing solvent by centrifugation after each step.

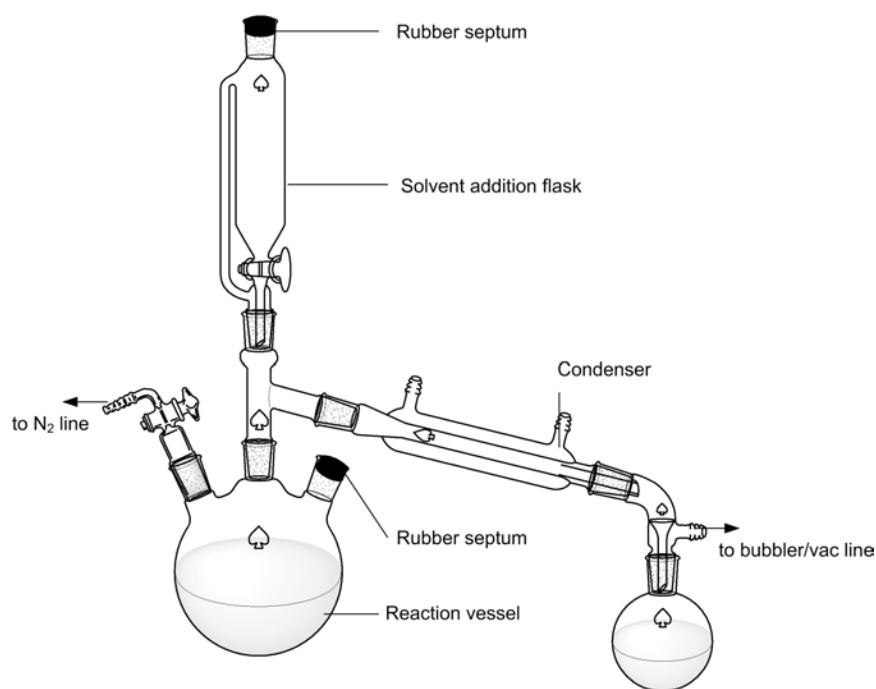


Figure 8.8: Diagram of apparatus used for synthetic work according to method of Abe *et al.*

### 8.3.4 Synthesis of ligand-stabilised Ti-Pt nanoparticles

Functionalisation of Ti core surfaces with organic ligands was expected to reduce the Ti surface energy and promote overgrowth of Pt shells, as proposed in section 8.1.6. Following the method of Ghosh *et al.* [272], Ti nanoparticles were synthesised by reduction of  $\text{TiCl}_4$  using lithium triethylborohydride ( $\text{LiEt}_3\text{BH}$ ) in anhydrous THF, in the presence of the diazonium salt prepared as described in section 8.1.6. The  $\text{LiEt}_3\text{BH}$  reducing agent (supplied by Sigma under the trade name Superhydride™) is slightly weaker than sodium naphthalide, with a standard reduction potential of approximately -2.2 V. However, it has been employed previously for the preparation of metallic Ti nanoparticles, and is a more convenient to use than sodium naphthalide.

The Ti precursor  $\text{Ti}(\text{THF})_2\text{Cl}_4$  was added to a dry,  $\text{N}_2$ -purged 3-neck reaction flask along with a calculated quantity of either the 4-benzyl, 4-decyl or 4-ethyl diazonium salt. Experiments were performed at a diazonium:Ti ratio of 4:1, with a quantity of the Ti precursor calculated to yield 10 mg of metallic Ti in the product. Dry THF was added directly to the diazonium/Ti precursor mixture by cannula transfer, followed by stirring for 2 hours to form a clear, yellow solution. The reducing agent, supplied as a 1M solution of  $\text{LiEt}_3\text{BH}$  in THF, was first diluted to 0.1M with dry THF, before loading a calculated volume of the solution into a dry glass syringe. To ensure complete reduction of the  $\text{Ti}^{4+}$  precursor and the diazonium salt, a 1.5-fold molar excess of  $\text{LiEt}_3\text{BH}$  was used, based on the molar equivalents of hydride required to reduce the  $\text{Ti}^{4+}$ , diazonium and (in the following step)  $\text{Pt}^{2+}$  species, calculated according to equation (8.1),

## 8 Pt-Ti bimetallic catalysts

---

$$n_{\text{LiBEt}_3\text{H}} = 1.5 \left( 4n_{\text{Ti}^{4+}} + n_{\text{R-N}_2^+} + 2n_{\text{Pt}^{2+}} \right) \quad (8.8)$$

where  $n_{\text{LiBEt}_3\text{H}}$  is the number of moles of hydride required for a reaction involving  $n_{\text{Ti}^{4+}}$ ,  $n_{\text{R-N}_2^+}$  and  $n_{\text{Pt}^{2+}}$  moles of  $\text{Ti}^{4+}$ , diazonium and  $\text{Pt}^{2+}$  species respectively.

The required volume of 0.1M  $\text{LiBEt}_3\text{H}$  solution was infused at  $5 \text{ ml}\cdot\text{hour}^{-1}$  through a PTFE transfer line into the stirring Ti/diazonium solution, and the mixture was left stirring for several hours.

### **Formation of Pt shells**

A calculated quantity of (1,5-cyclooctadiene) $\text{PtCl}_2$  was dissolved in 20 ml of dry THF under  $\text{N}_2$  purge in a dry flask. The solution was transferred to a dry, glass syringe before infusing slowly at  $5 \text{ ml}\cdot\text{hour}^{-1}$  into the pre-formed ligand-stabilised Ti core mixture. The mixture was allowed to stir for several hours before the product was concentrated by rotary evaporation to  $<20\text{ml}$ , then centrifuged and washed with toluene and isopropanol in sequence.

### **8.3.5 Physical characterisation of bimetallic Ti-Pt nanoparticles**

In addition to their size and dispersion, there are three physical aspects of the synthetic product that are of interest:

- Composition – what is the ratio of Ti to Pt, and are there any impurities present?
- Oxidation state of Ti – is Ti in its metallic state, or an oxidised form?
- Particle structure – has the desired Ti@Pt core@shell been produced and, if so, how thick is the Pt shell?

Two characterisation techniques were employed to answer these questions: namely x-ray photoelectron spectroscopy (XPS) and high-angle annular dark field scanning transmission electron microscopy (HAADF-STEM).

### **X-Ray Photoelectron Spectroscopy**

In this technique, a sample is irradiated by a monochromatic x-ray beam, resulting in the excitation and ejection of core-level electrons. The energies of ejected photoelectrons are related to their initial binding energies within their atomic orbitals. A detector measures the energy of these photoelectrons and produces a spectrum in which peaks appear at binding energies characteristic of individual electron orbitals for each element in the sample. Importantly, the binding energy of an electron is related to the oxidation state and local chemical environment of the atom. The higher

---

the oxidation state of the atom (i.e. the more electron-deficient), the higher the binding energy associated with its remaining electrons due to increased Coulombic interaction with the atomic nucleus. Therefore, the oxidation states of elements in the sample can be inferred from shifts in the energies of their characteristic photoelectrons in XPS spectra. Conveniently, photoelectron emissions from the  $2p$  band of  $\text{Ti}^{4+}$  display a large 'chemical shift' of around +4.6 eV relative to metallic Ti [274], and thus the oxidation state of Ti should be easily inferred from XPS studies in this work.

Although photoelectrons are generated throughout the sample, they are rapidly inelastically scattered or captured by surrounding atoms and ions. Therefore the only photoelectrons to reach the detector are those which are generated in the topmost atomic layers of the sample, with the exact depth determined by their energy. Typically for metals, 95% of the photoelectron signal detected in an XPS experiment is generated from the topmost 6-10 nm of the sample, with the implication that XPS measurements are very surface-sensitive.

XPS is a UHV technique, requiring samples to be in dry form on an electrically-conductive substrate to prevent artefacts in the data due to charging of the surface.

In this study, XPS samples were prepared by drop-casting aliquots of the purified colloidal products on onto silicon wafers, followed by vacuum drying. Measurements were carried out using the Thermo VG Escalab 250 spectrometer at the University of Leeds, with a monochromated Al  $K\alpha$  x-ray source. Spectra were fitted using CasaXPS software [275], employing Shirley-type non-linear baselines and charge correction with respect to the adventitious carbon C1s peak at 285.0 eV. Doublets assigned to metal oxide ( $\text{TiO}_2$ , PtO) species were fitted using Gaussian-Lorentzian lineshapes, whilst metallic species were fitted using asymmetric Doniach-Sunjic lineshapes.

### **High-angle annular dark field scanning transmission electron microscopy (HAADF-STEM)**

By contrast with conventional bright-field TEM imaging, HAADF-STEM is performed by rastering a tightly-focused electron beam (spot size  $\sim 1 \text{ \AA}$ ) across an electron-transparent sample. Secondary electrons emitted from each point are detected by an annular detector placed below the sample. Each point in the raster scan is assigned a brightness proportional to the intensity of the detected signal. Because atoms with higher atomic numbers ( $Z$ ) have more electrons, and therefore generate more secondary electrons, different elements in the sample can be distinguished by differences in brightness in the final image ( $Z$ -contrast). In addition, elemental analysis can be performed concurrently by energy-dispersive x-ray spectroscopy (EDX) or electron energy loss spectroscopy (EELS).

## 8 Pt-Ti bimetallic catalysts

---

The HAADF-STEM technique, together with EDX or EELS, has been used previously to discern core@shell structures in bimetallic nanoparticles.

Samples for STEM imaging were prepared by drop-casting the purified colloidal product onto carbon-coated Cu TEM grids. STEM imaging was performed using a Philips Tecnai F20 FEG-TEM operating at an accelerating voltage of 200 kV.

### 8.4 Results and discussion

The results presented in the following are in chronological order. Initial experiments on the formation of Ti@Pt nanoparticles were performed using the method described in section 8.3.3. As they did not yield the desired product, the method described in section 8.3.4 was applied for subsequent experiments.

#### 8.4.1 Synthesis and characterisation of unstabilised Ti-Pt nanoparticles

Sodium naphthalide and Ti precursor solutions were prepared as described in section 8.3.3. The colour of the naphthalide solution changed from dark green to dark brown upon addition of the clear, light brown Ti precursor solution, which was thought to indicate formation of metallic Ti nanoparticles. After stirring for 30 minutes, the mixture was found to contain a fine, dark brown precipitate. The precipitate was sampled for TEM imaging, but the sample turned white upon exposure to air, indicating oxidation of Ti to TiO<sub>2</sub>.

The apparent precipitation of Ti nanoparticles meant that the deposition of Pt shells was likely to be impossible in this case. Nonetheless, the Pt precursor was infused to the Ti/naphthalide mixture, whereupon the supernatant liquid turned dark brown. The coarse, dark brown Ti precipitate remained. The solvent was removed by vacuum distillation, yielding a clear, colourless distillate and a mixture of dark brown and white residues in the reaction flask. The white residue – presumably naphthalene – was soluble in hexane and was removed in the first washing step. The brown residue was easily redispersed in MeOH.

The bright-field TEM images of the purified product in Figure 8.9 (a-b) show that nanoparticles were produced, but that they were rather agglomerated and appear to be dispersed over a crystalline substrate, thought to be TiO<sub>2</sub>. The size distributions in Figure 8.9 (c) reveals a slight increase in average particle size upon increasing the ratio of Pt:Ti from 1:1 to 2:1. Whilst this size increase is in keeping with an increase in Pt shell thickness, it does not prove that the product has a core@shell structure. HAADF-STEM imaging was performed in an attempt to discern the structure of the particles synthesised at Pt:Ti=2:1.



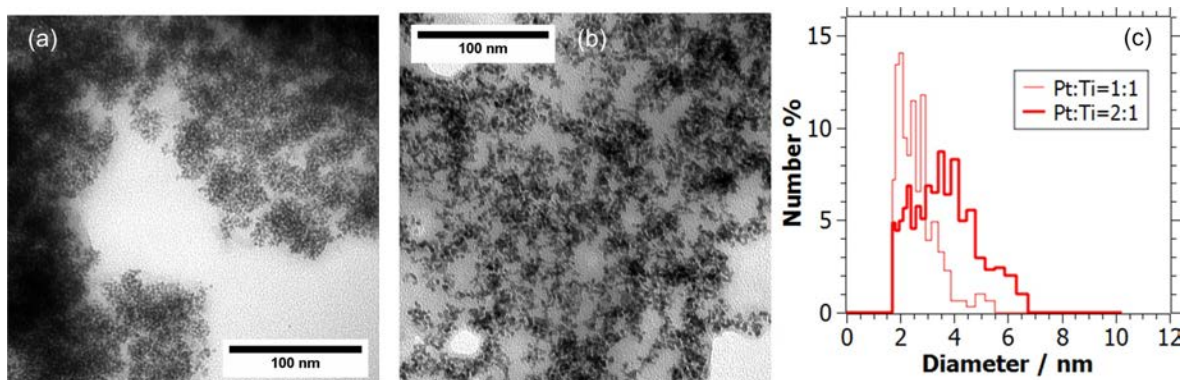


Figure 8.9: (a-b) Bright-field TEM images ( $\times 300\text{ K}$ ) of the purified product synthesised at (a) Pt:Ti=1:1 and (b) Pt:Ti=2:1, showing agglomerated metallic nanoparticles; (c) particle size distributions for the products synthesised at Pt:Ti= 1:1 and 2:1.

Figure 8.10 (a) shows a HAADF-STEM image in which the results of an EDX linescan across a single particle are superimposed. For a core@shell particle, the integrated intensities for the core and shell elements across the width of the particle should appear as illustrated in Figure 8.10 (b). The linescan in Figure 8.10 (a) may show the beginnings of such a pattern, but the analysis is hardly conclusive in identifying a core@shell structure. This analysis was performed close to the limits of the resolution and detection capabilities of the instrument, and longer integration times were precluded by image drift and beam-induced degradation of the sample.

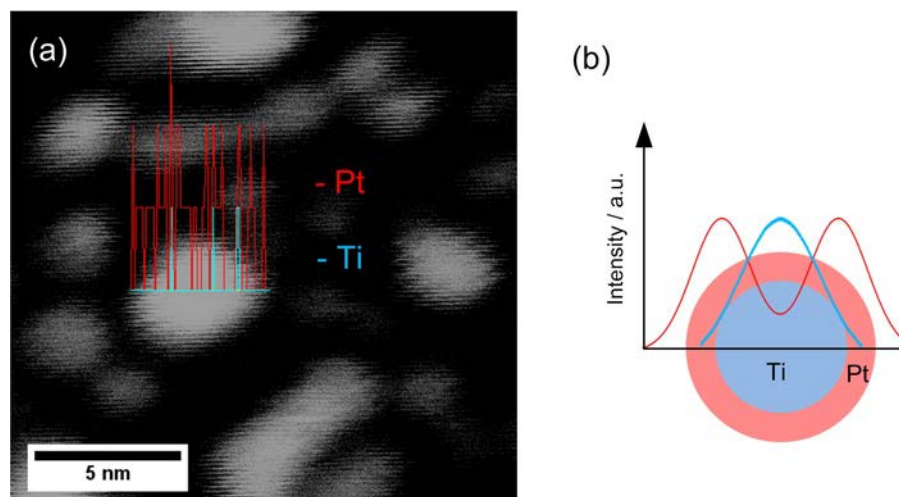


Figure 8.10: (a) HAADF-STEM image ( $\times 1.2\text{ M}$ ) of a group of particles in the Pt:Ti=2:1 product, together with an EDX linescan across a single particle; (b) schematic showing the EDX linescan profile expected for a Ti@Pt core@shell particle.

XPS analysis of the purified products synthesised at Pt:Ti=1:1 and 2:1 revealed that Ti was in its +4 oxidation state in both cases. The Ti 2p<sub>3/2</sub> and 2p<sub>1/2</sub> photoelectron peaks in the spectra shown in Figure 8.11 are found at 458.3 eV and 464.5 eV respectively, which correspond well with

## 8 Pt-Ti bimetallic catalysts

reference data for  $\text{TiO}_2$ [274]. The absence of peaks in the Ti 2p XPS spectra at 454.2 eV or 460.0 eV confirms that no metallic Ti was present in either sample[274].

On the basis of the sum of the evidence from TEM, HAADF-STEM and XPS analyses, it appears that the products produced via the method described in section 8.3.3 consist of metallic Pt nanoparticles dispersed on or within a  $\text{TiO}_2$  matrix. The agglomeration of the Ti cores prior to infusion of the Pt precursor precluded formation of Pt shells. Consequently, metallic Ti was either oxidised to  $\text{TiO}_2$  upon exposure to air, or leached from the product via the formation of titanium methoxide during methanol washing steps[243].

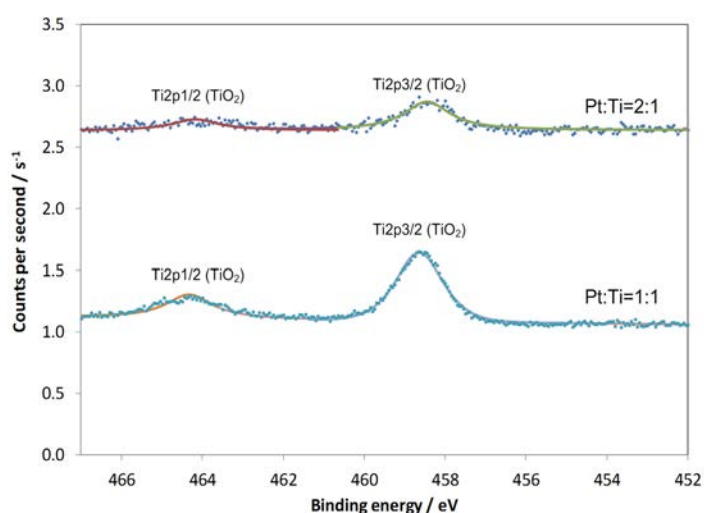


Figure 8.11: Ti 2p XPS spectra for products synthesised at Pt:Ti=1:1 and 2:1.

### 8.4.2 Synthesis of diazonium compounds

To prevent agglomeration of Ti cores and encourage the formation of Pt shells, subsequent experiments introduced capping ligands to the Ti cores during nucleation in an attempt to reduce their surface energy and provide steric stabilisation against agglomeration. Ligands were to be grafted to the Ti surface using diazonium chemistry, as described in section 8.3.4. Being inherently unstable, the diazonium compounds were synthesised just prior to use according to the method described in section 8.3.2.

The decyl- and benzyldiazonium products were isolated as white, crystalline solids, which were soluble in  $\text{CDCl}_3$  and MeOD respectively for NMR analysis. The synthesis of the ethyldiazonium salt was unsuccessful, as the reaction product was soluble in the washing solvent and could not be isolated by filtration.

The  $^1\text{H}$  NMR spectrum of the 4-decylaniline compound is shown in Figure 8.12 (a). The peaks at 7.3 ppm and 2.5 ppm are due to water and  $\text{CHCl}_3$  respectively, present in the NMR solvent. The

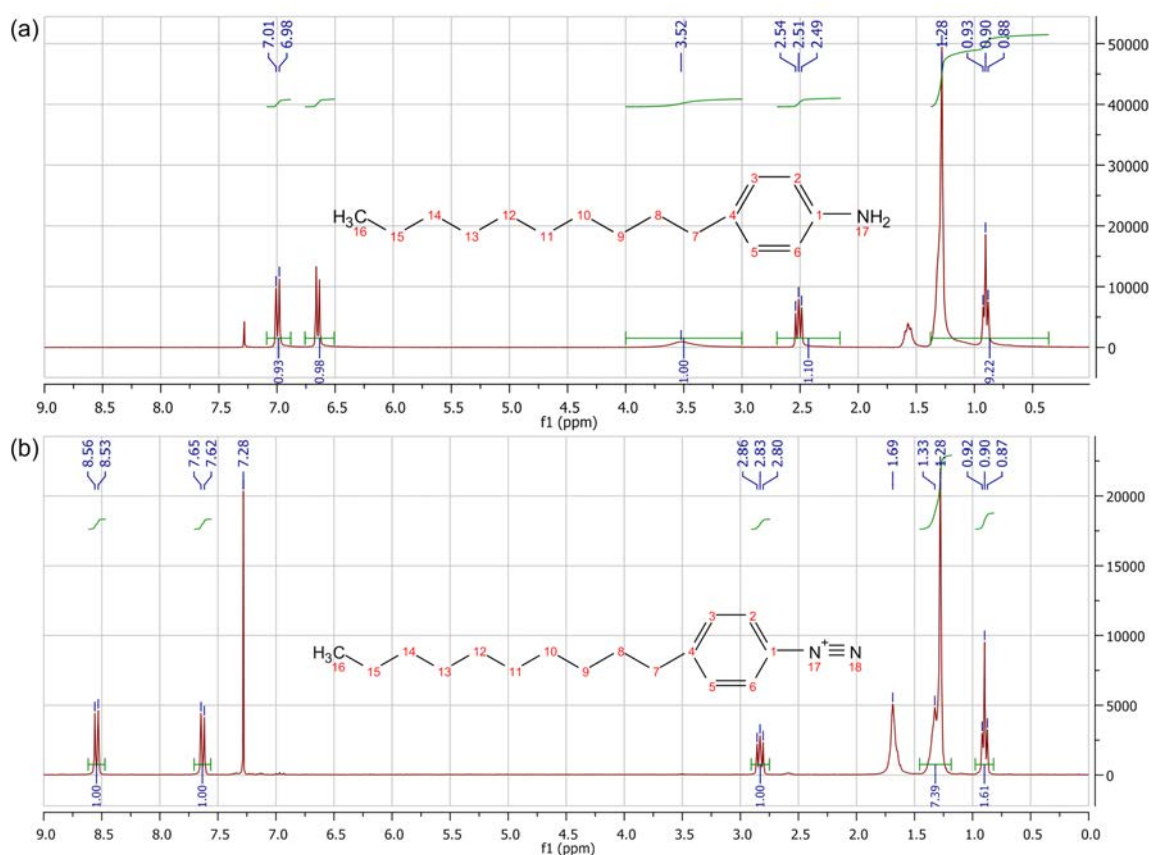


Figure 8.12:  $^1\text{H}$  NMR spectra for (a) 4-decylaniline and (b) 4-decyl diazonium tetrafluoroborate. The solvent was  $\text{CDCl}_3$ .

remaining peaks were all assigned to hydrogen atoms in the 4-decylaniline molecule: those at 0.75-1.75 ppm are from hydrogen atoms in  $\text{CH}_2$  and  $\text{CH}_3$  groups in the decyl chain, the broad peak at 3.5 ppm is due to  $\text{NH}_2$ , and the doublets at  $\sim 6.7$  and  $\sim 7.0$  ppm are assigned to hydrogen atoms on the phenyl ring. In the  $^1\text{H}$  NMR spectrum of the diazotized product shown in Figure 8.12 (b), the positive shift of these phenyl doublets to  $\sim 7.6$  ppm and  $\sim 8.6$  ppm, together with the disappearance of the broad  $\text{NH}_2$  peak at 3.5 ppm, is indicative of the formation of the diazonium compound [271]. Additionally, the presence of the diazonium moiety is confirmed by the peak at  $2250\text{ cm}^{-1}$  in the FTIR spectrum in Figure 8.13, which is characteristic of the  $\text{N}\equiv\text{N}$  vibrational stretch [271-272].

## 8 Pt-Ti bimetallic catalysts

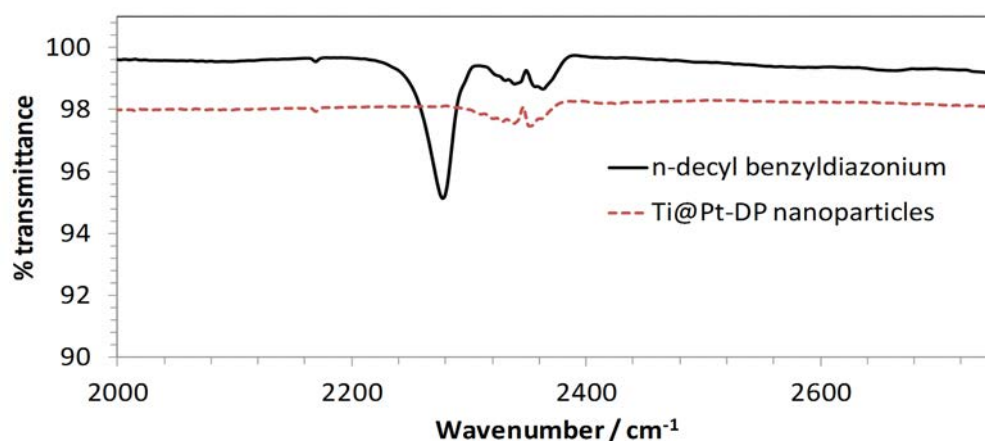


Figure 8.13: FTIR spectra for *n*-decyl diazonium tetrafluoroborate and Ti@Pt-DP nanoparticles. The absorbance peak at 2250  $\text{cm}^{-1}$  for the diazonium compound is characteristic of the  $\text{N}\equiv\text{N}$  vibrational stretch.

### 8.4.3 Synthesis of ligand-stabilised Ti@Pt nanoparticles

The synthesis of ligand-stabilised Ti-Pt nanoparticles was carried out using the decyldiazonium and benzyldiazonium compounds prepared above. The intended decylphenyl (DP) and benzylphenyl (BP)-stabilised core@shell products are represented schematically in Figure 8.14 and are referred to as Ti@Pt-DP and Ti@Pt-BP respectively in the following.

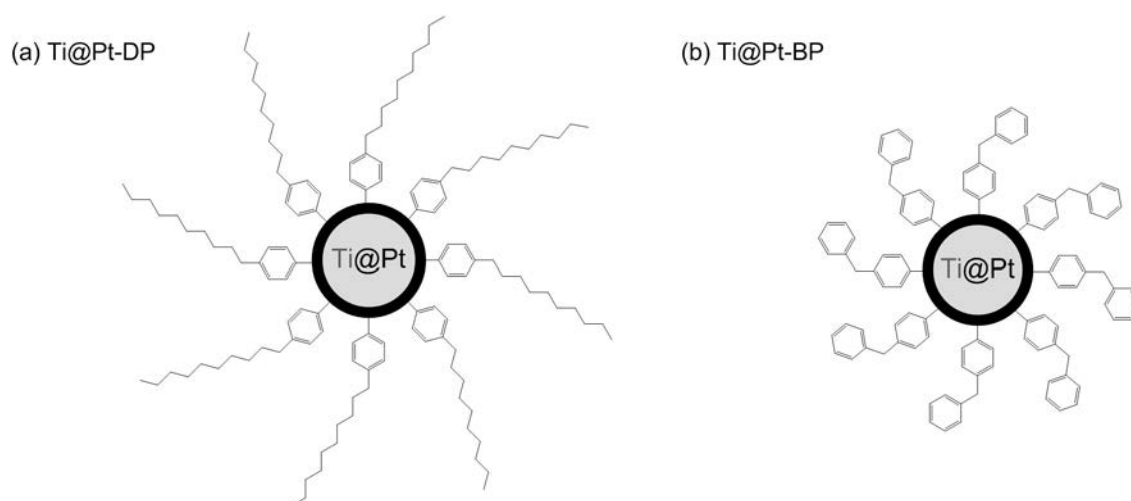


Figure 8.14: The intended products in this study were core@shell nanoparticles (Ti@Pt), stabilised by (a) decylphenyl (Ti@Pt-DP) and (b) benzylphenyl (Ti@Pt-BP) ligands.

---

## **Ti@Pt-BP nanoparticles**

The benzyldiazonium tetrafluoroborate compound was found to be insoluble in THF, so the reaction was carried out in freshly-distilled toluene instead, in which all precursor materials were readily soluble. Addition of the reducing agent produced a clear, dark red sol – as described by Ghosh *et al.* in their preparation of metallic biphenyl-stabilised Ti nanoparticles. Unfortunately, however, the mixture turned pale yellow during the course of stirring for 2 hrs, indicating the oxidation of the product. Upon removal of the solvent, the product was recovered as a fine, white powder assumed to be TiO<sub>2</sub>. It is thought that inadequate drying of the diazonium salt led to the oxidation of the Ti nanoparticles in this experiment. Since the aim was to produce metallic Ti particles, no further analysis or processing was performed on the product.

## **Ti@Pt-DP nanoparticles**

In the experiment using the decyldiazonium tetrafluoroborate salt, the dark red colouration of the colloidal Ti persisted after stirring overnight, whereupon the (1,5-cyclooctadiene)PtCl<sub>2</sub> precursor solution was infused slowly, followed by a stoichiometric aliquot of LiBEt<sub>3</sub>H solution. An opaque, black sol was produced, which contained a small quantity of a dark brown precipitate after stirring for several hours. The absence of the N≡N peak in the FTIR spectrum for the as-synthesised Ti@Pt-DP product in Figure 8.13 confirmed complete reaction of the diazonium compound. The product was purified by centrifugation and washed with toluene and isopropanol, in both of which it dispersed readily under sonication.

The TEM images and size distribution in Figure 8.15 reveal that the purified product consists of rather small (1.5-5.5 nm) particles, which cluster in agglomerates of around 50-150 nm diameter in (or on) an apparently amorphous substrate. Despite the introduction of capping ligands, the overall morphology is quite similar to that found for the product of the unstabilised Ti-Pt nanoparticles in Figure 8.9.

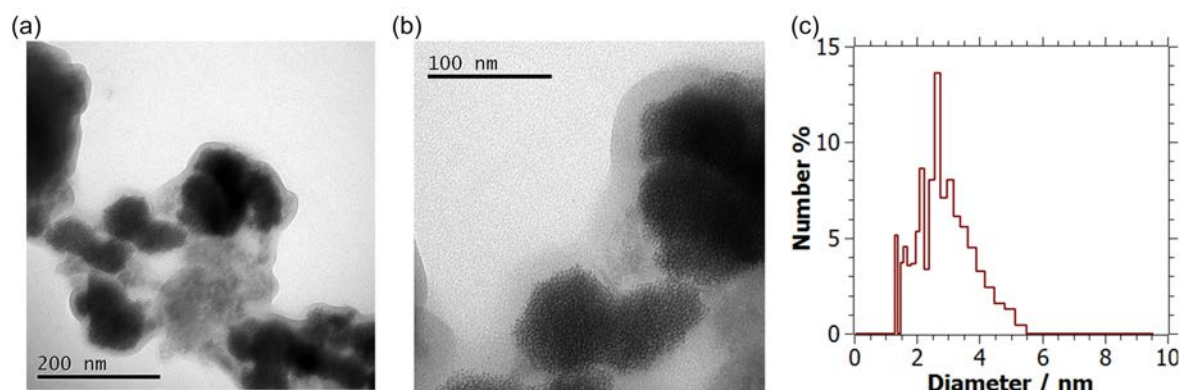


Figure 8.15: (a-b) Bright field TEM micrographs (JEOL 1200ex, 80kV accelerating voltage) of the purified Ti-Pt-DP product; (c) particle size distribution measured from (b).

## 8 Pt-Ti bimetallic catalysts

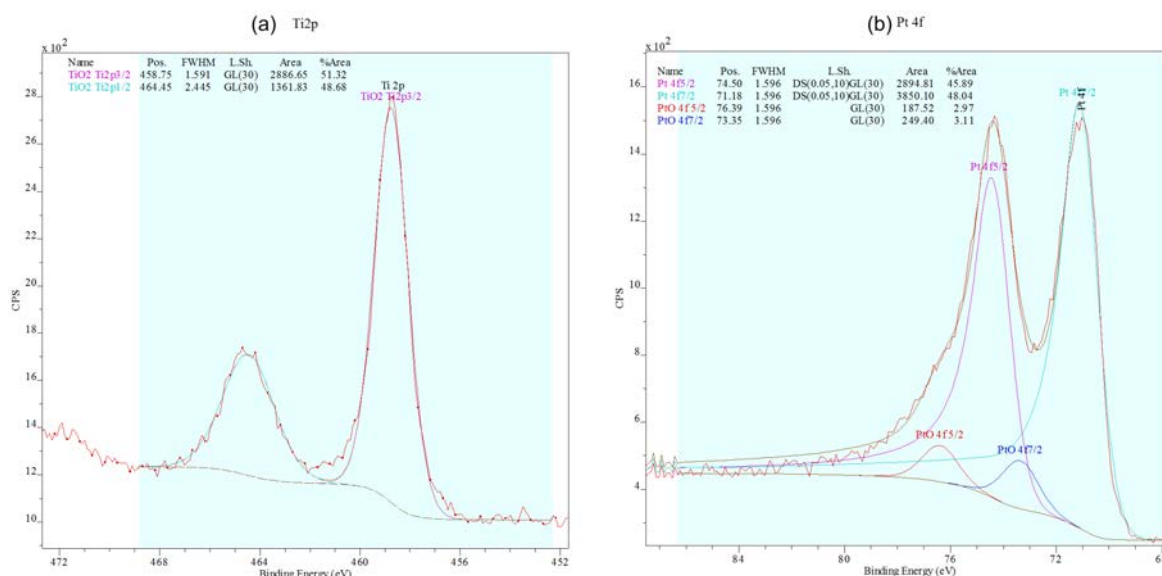


Figure 8.16: XPS spectra for (a) the Ti 2p and (b) the Pt 4f photoemission bands of the purified Ti@Pt-DP reaction product. Spectra were charge-corrected with respect to the C 1s peak at 285.0 eV and fitting was performed against a Shirley-type baseline with Gaussian-Lorentzian lineshapes for oxide species, and Doniach-Sunjc (asymmetric) lineshapes for metallic Pt.

The XPS spectrum for the Ti 2p photoemission band in Figure 8.16 (a) shows the Ti 2p<sub>3/2</sub> and Ti 2p<sub>1/2</sub> peaks at 458.75 eV and 464.45 eV respectively, corresponding to Ti in its +4 oxidation state i.e. TiO<sub>2</sub>. The absence of Ti 2p<sub>3/2</sub> peaks at 454-455 eV implies that no Ti is present in the metallic state, or as a Pt<sub>3</sub>Ti alloy[276-277]. The XPS spectrum of the Pt 4f core level in Figure 8.16 (b) shows Pt 4f<sub>7/2</sub> and Pt 4f<sub>5/2</sub> peaks at 71.18 eV and 74.50 eV respectively. Previous studies on Pt<sub>3</sub>Ti bulk alloy and oxidised Pt specimens have found that core level binding energies are increased relative to metallic Pt by between 0.4-0.9 eV and 1.6-3.8 eV for Pt<sub>3</sub>Ti or oxidised Pt surfaces respectively [276, 278]. As shown in Figure 8.16 (b), deconvolution of the Pt 4f spectrum reveals a second set of Gaussian-Lorentzian peaks corresponding to Pt<sup>2+</sup> species, with *ca.* 1.9 eV higher binding energy than metallic Pt [274, 278], implying the presence of Pt-O species as opposed to Pt<sub>3</sub>Ti.

Based on the TEM images and XPS data, it is thought that the product of the Ti@Pt-DP synthesis consists of Pt nanoparticles with oxidised surfaces supported on TiO<sub>2</sub>. The synthesis does not appear to have been successful in creating metallic Ti species, nor a Pt<sub>3</sub>Ti alloy, and there is no evidence of a core@shell structure. With regard to the oxidation of the Ti nanoparticles, it is thought that metallic Ti nanoparticles were produced initially, as indicated by the dark red coloration of the reaction mixture, but that they oxidised upon exposure to air and/or moisture either during deposition of Pt shells (due to inadequate drying of the Pt precursor) or during purification (as a result of failure to form complete Pt shells, and inadequate stabilisation against oxidation provided by the decylphenyl ligand). With regard to the latter, in-silico work has shown that aryl ligands adopt a flat conformation on Ti surfaces, whereas they stand upright on noble

---

metal surfaces [279]. This flat conformation may have frustrated packing of the decylphenyl ligand on the Ti surface, leading to poor stability against oxidation, as compared to the biphenyl ligand consisting of more compact, tessellating aryl groups, with which air-stable Ti particles were prepared by Ghosh *et al.* [272].

## 8.5 Conclusions and recommendations

Bimetallic nanoparticles consisting of a Ti core surrounded by a Pt shell hold promise as highly-durable cathode electrocatalysts with enhanced mass activity towards the ORR relative to pure Pt. Methods have been proposed and trialled for the production of Ti@Pt nanoparticles using wet chemical methods, employing strong reducing agents under anhydrous conditions and using diazonium chemistry to graft stabilising ligands to colloidal Ti cores prior to deposition of Pt shells. To date, the synthetic methods employed in this study have not been successful in producing Ti@Pt core@shell nanoparticles. Although it is thought that stable metallic Ti nanoparticles are formed during the initial reduction of TiCl<sub>4</sub> using LiBEt<sub>3</sub>H, the product underwent oxidation during purification upon exposure to air and/or moisture. Products were identified by TEM and XPS studies as consisting of agglomerated Pt nanoparticles supported on TiO<sub>2</sub>.

### 8.5.1 Further investigations

In light of the difficulties encountered during this study, a more effective strategy is sought for the formation of Pt shells on pre-formed Ti core nanoparticles. A continuous Pt or Pt-enriched shell should prevent oxidation of underlying Ti, affording a stable Ti@Pt product.

An interesting strategy for the directed formation of core@shell nanoparticles was recently reported by Serpell *et al.* [27]. In this work, core nanoparticles composed of a metal M<sup>1</sup> were prepared with stabilising ligands containing amide functionalities, which formed hydrogen bonds with the anionic precursor of a second metal M<sup>2</sup>. When subsequently reduced, concentric shells of M<sup>2</sup> were formed reliably around the M<sup>1</sup> cores. The process is summarised in Figure 8.17.

The act of binding the shell precursor to the pre-formed metallic cores prior to reduction appears to yield the desired core@shell morphology with good reliability. The authors used this method to prepare nanoparticles with compositions Au@Pd, Pd@Au, Pd@Pt and Pt@Pd, which is especially noteworthy considering that the Au@Pd and Pd@Pt structures are not thermodynamically favoured.

## 8 Pt-Ti bimetallic catalysts

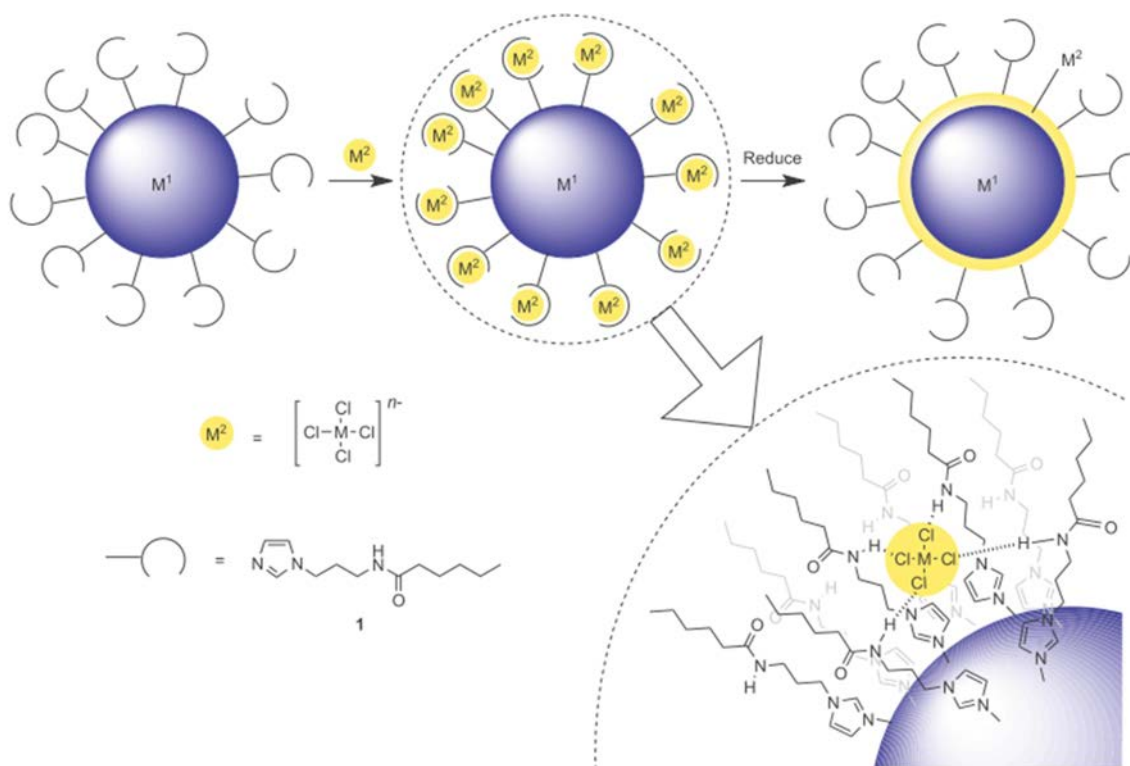


Figure 8.17: Schematic representation of the anion coordination strategy for the synthesis of core@shell ( $M1@M2$ ) nanoparticles reported by Serpell *et al.* Reproduced from [27]

Despite its apparent utility, the method described by Serpell *et al.* is not directly applicable for the synthesis of Ti@Pt nanoparticles, not least because the aqueous reaction mixture would be incompatible with the strong reducing agents required to produce metallic Ti. In addition, the non-covalently bound ligand is unlikely to offer sufficient stabilisation of the Ti core nanoparticles to prevent their agglomeration.

However, it may be possible to adapt the method of Serpell *et al.* for the synthesis of Ti@Pt nanoparticles, and indeed combinations of Pt with other early transition metals. A proposed reaction scheme is shown in Figure 8.18. A bipyridine ligand, grafted to the Ti surface using diazonium chemistry, is proposed as a replacement for the imidazole amide ligand employed by Serpell *et al.* It should be possible to graft bipyridine ligands to the surface of nucleating Ti nanoparticles via a 5-diazonium-2,2-bipyridine intermediate, which can be synthesised from its amine precursor as shown in Figure 8.18 (a). The reduction step in Figure 8.18 (b) should be carried out in an anhydrous, aprotic solvent such as THF, and must employ a strong reducing agent such as sodium naphthalide or lithium triethylborohydride.



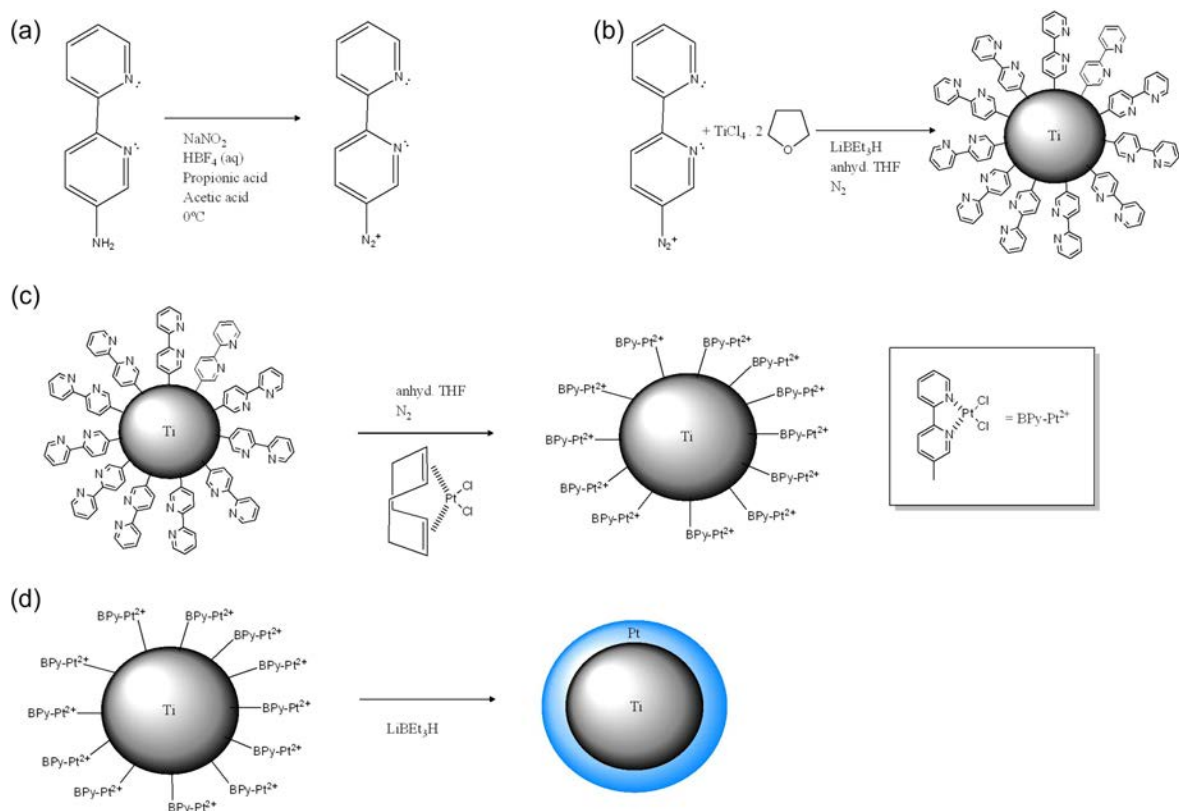


Figure 8.18: Proposed synthetic route for the production of Ti@Pt nanoparticles via ligand coordination of the Pt precursor with pre-formed Ti cores

The coordination of  $\text{Pt}^{2+}$  compounds with bipyridine ligands is documented extensively in the literature [280-283]. Upon introduction of a Pt precursor (1,5-cyclooctadiene) $\text{PtCl}_2$ , the labile cyclooctadiene ligand is expected to undergo exchange with the surface-bound bipyridine, binding the  $\text{Pt}^{2+}$  species in close proximity with the Ti surface (Figure 8.18 c). The Pt shell is then formed by chemical reduction of  $\text{Pt}^{2+}$  using  $\text{LiBEt}_3\text{H}$  as shown in Figure 8.18 (d).

It is unfortunate that there was insufficient time to attempt the synthetic method described above in this study, as it is considered to be a promising route for the preparation of core@shell nanoparticles with a variety of compositions involving early transition metal cores. Although merely speculative at this stage, by substitution of the  $\text{Ti}(\text{THF})_2\text{Cl}_4$  compound with ether-soluble Y(III) or Sc(III) compounds (e.g. tris(cyclopentadienyl)yttrium(III), tris(cyclopentadienyl)scandium(III)), it may also be possible to synthesise Y@Pt and Sc@Pt nanoparticles. In any case, the method outlined above is strongly recommended for further investigation.

## 9 Summary

Two routes have been investigated for achieving improvements in mass activity and durability for Pt-based oxygen reduction electrocatalysts:

1. Nafion-Pt/C electrocatalysts, derived from ionomer-stabilised colloidal Pt nanoparticles have been investigated for their potential to offer improved catalyst utilisation and catalyst layer effectiveness *via* enhancement of the triple phase reaction zone. The activity and durability of Nafion-Pt/C electrocatalysts has been compared against commercially-available electrocatalysts using *ex-situ* techniques as well as single-cell PEMFC methods.
2. Methods have been investigated for the wet-chemical synthesis of Pt-Ti bimetallic nanoparticles, which are expected on the basis of previous work to offer significant enhancements in surface-specific activity *vs.* pure Pt, as well as improved stability against degradation *via* leaching of the base metal component compared with alloys of Pt with *3d* transition metals.

The main conclusions of these two, parallel studies and the avenues identified for further investigation are summarised in the following.

### 9.1 Nafion-Pt/C

- Carbon-supported electrocatalysts (Nafion-Pt/C) have been derived from colloidal dispersions of Pt nanoparticles stabilised by Nafion ionomer, with the ability to control particle size, dispersion and catalyst ionomer content *via* modifications to reaction conditions and purification routes.
- In *ex-situ* tests, Nafion-Pt/C electrocatalysts were found to offer 100% catalyst utilisation, compared to only 50% for a standard, commercial catalyst (E-Tek) under the same conditions. The Nafion-Pt/C A catalyst with partially-agglomerated morphology achieved 100% utilisation at a lower overall ionomer content (20 wt%) than the Nafion-Pt/C B and E-Tek catalysts (33 wt%), which both featured well-dispersed Pt particles.
- The surface-specific ORR activities of the Nafion-Pt/C catalysts were similar to those of commercial (E-Tek, TKK) catalysts, indicating that closely-coordinated Nafion in the former had no adverse site-blocking effect.
- Nafion-Pt/C A type catalysts were found to offer between 2.4 – 2.9 - fold improvements in stability against voltage cycling, determined by measuring active surface area losses under an *ex-situ* AST protocol.

- 
- Contrary to the findings of the *ex-situ* utilisation study, *in-situ* single cell PEMFC testing using MEAs fabricated with Nafion-Pt/C catalysts on the cathode revealed that there was no enhancement in catalyst utilisation compared with standard, commercial catalyst preparations. However, the Nafion-Pt/C A catalyst layer offered a small but significant improvement in effectiveness factor compared with a commercial (TKK) catalyst layer ( $E_{f(Pt)} = 7.9 \pm 0.8$  % Nafion® Pt/C A vs.  $6.4 \pm 0.3$  % TKK).

Various avenues for further investigation *vis-à-vis* Nafion-Pt/C have been proposed in chapters 4 - 7 and are summarised as follows:

- Further improvements to the morphological properties of Nafion-stabilised colloidal Pt (reductions in mean particle size, narrowing of the size distribution, improvements in dispersion) may be possible *via* further optimisation of reaction conditions; specifically in relation to Nafion:Pt ratios, polyol additive concentrations and the design of the reaction vessel for scaled-up syntheses.
- Likewise, in the preparation of MEAs, there may be opportunities to realise improvements in catalyst utilisation, effectiveness factors and catalyst layer mass-transport characteristics *via* optimisation of Nafion-Pt/C catalyst composition (Pt:C ratios, alternative carbon support materials), ink formulation (alternative solvents, ionomer contents) and fabrication routes (CCM *via* spraying or decal methods).
- In-situ durability testing would be useful to determine whether the enhanced stability found for Nafion-Pt/C A in *ex-situ* AST testing is conveyed as expected under real PEMFC operating conditions.
- Comparison of specific activities measured in *ex-situ* experiments at 25°C and 70°C revealed the possible existence of a temperature-dependent particle size effect, which is worthy of further investigation.

## 9.2 Ti@Pt core@shell electrocatalysts

- Wet chemical methods were investigated for the synthesis of Ti@Pt core@shell nanoparticles, employing sodium naphthalide and lithium triethylborohydride reducing agents and anhydrous, aprotic solvents to produce metallic Ti cores prior to deposition of Pt shells.
- In initial experiments, agglomeration of Ti particles precluded deposition of Pt shells and prompted the adoption of a ligand-stabilised approach to the prevention of agglomeration.
- Attempts were made to graft covalently-bound ligands to metallic Ti nanoparticles using diazonium chemistry.

## 9 Summary

---

- Whilst the ligand-stabilised method was thought to be initially successful in yielding metallic Ti nanoparticles, subsequent XPS analysis of the product revealed that it contained TiO<sub>2</sub> and un-alloyed Pt. TEM imaging revealed that the product consisted of small Pt nanoparticles dispersed over a TiO<sub>2</sub> substrate.
- Oxidation of the Ti component is thought to occur during purification, due to incomplete encapsulation of Ti cores by Pt shells.

In terms of further work, it is proposed that modification of the Ti core-stabilising ligand to include functionalities which bind the Pt precursor material prior to shell deposition may offer a more successful route for the reliable formation of Pt shells.

## Index of Tables

|  |    |
|--|----|
| Table 1.1: Status and targets for PEMFC performance reported and specified by the US Department of Energy. Figures are for an 80kW (net) integrated PEMFC system suitable for automotive applications[34]. *durability based on time to 10% drop in rated power in an automotive drive cycle.....  | 11 |
| Table 3.1: Current commercially-available Pt/C electrocatalysts. HSA = high-surface area. ....   | 41 |
| Table 3.2: Summary of electrocatalyst properties reported in previous half-cell studies using hydrodynamic voltammetric techniques for the characterisation of Pt/C catalysts. Specific activities (SA) [A.m <sup>-2</sup> ] and mass activities (MA) [A.g <sup>-1</sup> ] are reported for the ORR at 0.9 V vs SHE. * denotes value calculated from data given in the publication, assuming a Tafel slope of -60 mV.dec <sup>-1</sup> . The columns on the right indicate whether certain requirements were met in terms of data quality and data analysis..... | 42 |
| Table 3.3: Particle sizes and surface areas obtained from XRD measurements on reaction products as reported by Liu et al in [14].....  | 48 |
| Table 3.4: Summary of ORR activities reported in previous works for Nafion®-stabilised Pt electrocatalysts. * indicates estimated values based on ECSA.....  | 55 |
| Table 3.5: Summary of reaction conditions and Nafion®-Pt product morphologies for the studies reviewed above. * 'molar' ratios as reported in [14].....  | 56 |
| Table 4.1 : Physical characterisation techniques for nanoparticles and supported catalysts. ....   | 67 |
| Table 4.2: Table 3: Summary of observations on varying Pt:Nafion® ratio and synthesis pH.....  | 72 |
| Table 4.3: Comparison of physical properties of polyol additives for size control of Nafion®-stabilised colloidal Pt.....  | 75 |
| Table 4.4: Comparison of physical surface areas (A <sub>phys</sub> ) and average particle diameters for colloidal Pt nanoparticles synthesised in the presence of various polyol additives (50 mg scale)...  | 76 |
| Table 4.5: Final compositions of the Nafion®-Pt/C A and B catalysts following purification.....  | 81 |
| Table 4.6: Nafion®-Pt/C catalysts prepared for electrochemical characterisation.....   | 84 |
| Table 5.1: Accepted values for parameters in the Levich equation.....  | 89 |
| Table 5.2: Experimental conditions and ORR kinetic parameters found for bulk Pt electrodes in this and previous work. * indicates values calculated from data given in the publication. Pt poly = bulk polycrystalline Pt.....   | 89 |

---

|   |     |
|---|-----|
| Table 5.3: Comparison of ECSA and catalyst utilisation measured for Nafion®-Pt/C A and E-Tek catalysts with ionomer content = 20 % NFP at three catalyst loadings $L_{Pt}=20, 40, 80 \mu\text{gPt.cm}^{-2}$ ..  | 94  |
| Table 5.4: Limiting current densities at 2000 RPM and effective O <sub>2</sub> diffusion coefficients at 25°C calculated from Figure 5.10 for each catalyst employed in this study.....   | 99  |
| Table 5.5: Summary of physical and ORR electrocatalytic properties of the catalysts measured at 25°C in 1 atm O <sub>2</sub> -saturated 0.1M HClO <sub>4</sub> , including specific activities SA (A.m <sup>-2</sup> real) and mass activities MA (A.g <sup>-1</sup> Pt) at 0.9 V vs RHE.....   | 100 |
| Table 5.6: Limiting current densities and effective diffusion coefficients for catalysts measured at 70°C.....  | 106 |
| Table 5.7: Summary of physical and ORR electrocatalytic properties of the catalysts measured at 25°C and 70°C in 1 atm O <sub>2</sub> -saturated 0.1 M HClO <sub>4</sub> , including specific activities SA (A.m <sup>-2</sup> real) and mass activities MA (A.g <sup>-1</sup> Pt) at +0.9 V vs. RHE, normalised to an O <sub>2</sub> concentration of [O <sub>2</sub> ]=1.260 x 10 <sup>-6</sup> mol.cm <sup>-3</sup> . Theoretical SAs at 70°C are based on calculations from data obtained at 25°C using equation (5.7)..... | 107 |
| Table 6.1: Current US DOE in-situ AST cycle for electrocatalyst durability. Reproduced from [193].....  | 115 |
| Table 6.2: TEM micrographs and summary of physical characteristics of catalysts undergoing durability testing.....  | 119 |
| Table 6.3: Summary of catalyst properties and AST results.....  | 120 |
| Table 7.1: Summary of the main differences between operating conditions in ex-situ and in-situ tests.....   | 127 |
| Table 7.2: Common circuit elements employed in PEMFC equivalent circuits and their corresponding transfer functions.....  | 132 |
| Table 7.3: Summary of MEAs prepared for in-situ testing. 1ECSAs determined by in-situ cyclic voltammetry. 2Mass activities at 0 bar.g cathode backpressure, 70°C, 100% RH anode and cathode, corrected for Ohmic and mass transport effects.....  | 135 |
| Table 8.1: Electrochemical series for reduction reactions of Na <sup>+</sup> , Y <sup>3+</sup> , Sc <sup>3+</sup> , Ti <sup>2+</sup> and Pt <sup>2+</sup> to metallic states.[138].....   | 152 |
| Table 8.2: Crystal structures and lattice parameters for Sc, Y, Ti and Pt at standard temperature and pressure 25°C, 1 atm.....   | 157 |

---

## Index of figures

|  |    |
|--|----|
| Figure 1.1: (a) Historical global average atmospheric CO <sub>2</sub> concentrations over the last 400,000 years (ice core data); (b) rising global atmospheric CO <sub>2</sub> levels since 2005; (c) UK energy demand by sector since 1980; (d) CO <sub>2</sub> emissions reductions by sector 2010-2060 thought to be necessary in order to limit global surface temperature rise to < 1.5°C [1].....   | 2  |
| Figure 1.2: Several possible routes for the production of hydrogen from solar energy. Reproduced from [2].....   | 3  |
| Figure 1.3: William Grove's gaseous voltaic battery, demonstrated in 1839, consisted of platinum electrodes contained within sealed glass test tubes, in contact with a sulphuric acid solution.....   | 4  |
| Figure 1.4: Schematic showing the operating temperatures, anode and cathode reactants and electrolyte charge carriers for several types of fuel cell: Alkaline fuel cell (AFC), microbial fuel cell (MFC), proton exchange membrane fuel cell (PEMFC), direct methanol fuel cell (DMFC), phosphoric acid fuel cell (PAFC), molten carbonate fuel cell (MCFC) and solid oxide fuel cell (SOFC). Reproduced from [3] .....   | 5  |
| Figure 1.5: Ragone plot comparing energy storage and generation technologies in terms of their peak power density and mass-specific energy density. Adapted from [4].....  | 10 |
| Figure 1.6: (a) Historical and projected costs for automotive fuel cell systems (state of the art technology projected to high volume production 500k units/year); (b) breakdown of stack costs based on current leading technologies scaled to high volume (500k units/year) production rates; (c) commodity price of refined platinum over the last 10 years (US\$/troy oz); (d) historical and projected global demand for platinum, with future demand based on two scenarios for adoption of FCVs (50% takeup, 80% takeup). Reproduced from [5](a) & (b), [6](c) and [7] (d)..... | 12 |
| Figure 2.1: A generalised chemical structure for perfluorinated sulfonated ionomers.....   | 15 |
| Figure 2.2: (a) Schematic diagram of a PEMFC stack consisting of 3 individual cells (reproduced from [8]), (b) PEMFC single cell showing reactions taking place at anode and cathode (reproduced from [8]), (c) SEM cross section of a PEMFC MEA with the proton exchange membrane (PEM), catalyst layers (CL) and gas diffusion layers (GDL) labelled, (d) TEM image of a typical Pt/C electrocatalyst.....   | 17 |
| Figure 2.3: (a) Variation in reversible (open circuit) cell potential as given by the Nernst equation for a fuel cell operating on H <sub>2</sub> and O <sub>2</sub> ; (b) comparison of maximum theoretical efficiencies of an H <sub>2</sub> /O <sub>2</sub> fuel cell and a Carnot heat engine operating at various temperatures, and 100 kPa pressure. Reproduced from [9].....  | 19 |

|  |    |
|--|----|
| Figure 2.4: A typical PEMFC polarisation curve, showing contributions of mixed potential, activation, Ohmic and mass transport losses to the overall polarisation response.....  | 20 |
| Figure 2.5: (a) Forward and reverse components of the measured current due to the reaction in equation (2.9) as a function of applied overpotential; (b) plots of current vs. overpotential showing the effect of exchange current density $J_0$ on the shape of the curve; (c) Tafel plots of $\log J_k $ vs. overpotential, illustrating the determination of $J_0$ and the Tafel slope, b.....  | 24 |
| Figure 3.1: Schematic representations of (a) a cross-section of the (cathode) catalyst layer, illustrating the porous structure formed by ionomer-coated Pt/C agglomerates and showing pathways for reactant and proton transport; (b) a single Pt/C agglomerate, showing partial ionomer coverage resulting in under-utilisation of Pt particles ( $\bullet$ ), and inactive Pt particles ( $\circ$ ) within microporous regions of the carbon support.....   | 28 |
| Figure 3.2: SEM images of 3M's NSTF catalyst for the PEMFC, which is fabricated by physical deposition of Pt onto a microstructured corrugated substrate coated with conductive organic whiskers. Reproduced from [10].....  | 30 |
| Figure 3.3: A typical 3-electrode half-cell.....   | 32 |
| Figure 3.4: Typical cyclic voltammogram for a Pt electrode, showing regions of Hupd adsorption (Had) and desorption (Hdes). The linear baselines indicated in red are set so as to eliminate contributions to current from charge/discharge of the electrochemical double layer (Coulombic current).....   | 35 |
| Figure 3.5: (a) Schematic of the RDE assembly and its mass transport characteristics (b) a practical RDE setup as part of an electrochemical half-cell.....  | 37 |
| Figure 3.6: (a) Rotating disc voltammograms recorded at $25 \text{ mV s}^{-1}$ in a $10 \text{ mM}$ solution of potassium ferricyanide and potassium ferrocyanide in a background electrolyte of $0.5 \text{ M KCl}$ , using a $5 \text{ mm}$ Pt disc working electrode. Rotation rates $\omega = 600, 933, 1600, 2000, 2500 \text{ rpm}$ . The vertical lines at $\eta_1$ - $\eta_{10}$ indicate the overpotentials within the mixed kinetic/diffusion-controlled regions chosen for the plots in (b) and (c); (b) Koutecky–Levich plots for the anodic branches and (c) cathodic branches of the voltammograms. Extrapolation of the linear plots to $\omega^{-1/2}=0$ yields the kinetic current $J_k$ for each overpotential $\eta$ . (d) Tafel plot using $i_k$ values determined from the intercepts of Koutecky–Levich plots. Reproduced from [11]..... | 38 |
| Figure 3.7: Schematic of the RRDE assembly and its mass transport characteristics.....   | 40 |
| Figure 3.8: (a) Cyclic voltammograms of carbon-supported Pt, Pt-black, and polycrystalline Pt in terms of Pt-surface area normalized current densities ( $\text{mA cm}^{-2}\text{Pt}$ ), recorded in $0.1 \text{ M HClO}_4$ at $25^\circ\text{C}$ and $20 \text{ mV/s}$ . (b) ORR current densities on 20% Pt/Vulcan ( $14.3 \text{ mg Pt cm}^{-2}$ ) at $1600 \text{ rpm}$ in $0.1 \text{ M HClO}_4$ at $60^\circ\text{C}$ : sweeps at $5 \text{ mV/s}$ (solid line) and $20 \text{ mV/s}$ (dashed line); positive-going  |    |



## Index of figures

|   |    |
|---|----|
| sweep only). (c) Specific activities, $i_s$ and (d) mass activities, $i_m$ , for the ORR at 60°C on Pt/C catalysts (two repeats each) (Pt-loadings ranging from 12.7 to 14.3 mg Pt cm <sup>-2</sup> ). Data are shown for the positive-going sweep at 5 mV/s going from 0 to 1.0 V (RHE) in O <sub>2</sub> -saturated 0.1 M HClO <sub>4</sub> at 1600 rpm. All potentials are referred to the reversible hydrogen electrode under the same conditions. Reproduced from [12] ..... | 43 |
| Figure 3.9: Pt-Ru/C electrocatalysts prepared by MeOH reduction a) in the presence of Nafion® dispersion and b) without Nafion®. Reproduced from [13].....  | 45 |
| Figure 3.10: UV-vis absorption spectra of Nafion® (10 <sup>-3</sup> M), H <sub>2</sub> PtCl <sub>6</sub> (10 <sup>-4</sup> M) and Nafion:H <sub>2</sub> PtCl <sub>6</sub> = 2:1 mixture (10 <sup>-4</sup> M) solutions. Reproduced from [14] .....  | 45 |
| Figure 3.11: TEM images of Nafion®-Pt nanoparticle colloids synthesized at different reflux temperatures with Nafion®/Pt = 2:1: (a) 65 °C, (b) 75 °C and (c) 82 °C. Reproduced from [14]..  | 46 |
| Figure 3.12: TEM micrographs of Nafion®-stabilised colloidal Pt synthesised at 82 °C in the presence of different Nafion®/Pt 'molar' ratios: (a) 1:2, (b) 2:1, (c) 4:1 and (d) 8:1. TEM images of Pt black (E-TEK) and 20 wt% Pt/C (E-TEK) electrocatalysts are shown in (e) and (f). Reproduced from [14].....   | 47 |
| Figure 3.13: (a) RDE data recorded at 5 mV.s <sup>-1</sup> 3000 RPM in O <sub>2</sub> -purged 1 M H <sub>2</sub> SO <sub>4</sub> for Nafion®-stabilised colloidal Pt synthesised at different Nafion®:Pt ratios, compared against E-Tek 40 wt% Pt/C and Pt black; (b) Inverse Levich plots for the various catalysts, from limiting currents ( $i_{lim}$ ) recorded at E=+0.4 V. Reproduced from [14].....  | 49 |
| Figure 3.14: (A) TEM image, (B) energy dispersive X-ray spectrum and (C) atomic force microscope image of the Nafion®-stabilised Pt colloids deposited on mica surfaces, (D) TEM image of 40 wt % Nafion®-Pt/C catalyst. Reproduced from [15] .....   | 50 |
| Figure 3.15: (A) Cyclic voltammograms for 40 wt % Nafion®-Pt/C and 40 wt % commercial Pt/C in 0.5 M H <sub>2</sub> SO <sub>4</sub> recorded at 50 mV.s <sup>-1</sup> ; (B) RDE voltammograms for Nafion®-Pt/C and commercial Pt/C in O <sub>2</sub> -purged 0.5 M H <sub>2</sub> SO <sub>4</sub> at 25°C, 1600 RPM, sweep rate of 5 mV.s <sup>-1</sup> . Reproduced from [15] .....   | 51 |
| Figure 3.16: (a) ECSA losses for Nafion®-Pt/C and standard Pt/C as a function of the number of AST cycles (0.5 M H <sub>2</sub> SO <sub>4</sub> 25°C, +0.6 to +1.2 V, 20 mV.s <sup>-1</sup> ); (b) pre- and post-AST cyclic voltammograms for Nafion®-Pt/C and standard Pt/C; and Pt particle size distributions for (c) Nafion®-Pt/C and (d) standard Pt/C catalysts, showing increases in particle size after 12300 cycles (Nafion®-Pt/C) and 4500 cycles (standard Pt/C).....  | 52 |
| Figure 3.17: (A) Schematic of the Pt colloid particles and the Pt/TiB <sub>2</sub> catalysts with Nafion® acting as a stabiliser ; (B) TEM image of the Pt colloid particles and (C) SEM micrograph of TiB <sub>2</sub> powders . Reproduced from [16] .....  | 53 |

|   |    |
|---|----|
| Figure 3.18: RDE voltammograms for Nafion®-Pt/TiB2 and commercial Pt/C catalysts recorded in O2-saturated 0.5M H2SO4 at 25°C, 1600 rpm. Reproduced from [17] .....  | 54 |
| Figure 3.19: (a) Comparison of catalyst durability Pt/TiB2 vs Pt/C during AST testing (cyclic voltammetry +0.6 to +1.2 V, 20mV.s-1, 0.5 M H2SO4 25°C); pre- and post-AST particle size distributions for (b) Pt/TiB2 catalyst and (c) Pt/C catalyst.....  | 55 |
| Figure 4.1: (a) Theoretical plot based on equation (4.4) illustrating the variation of overall Gibbs free energy with nucleus radius at a fixed interfacial tension $\sigma_{SL}=0.2 \text{ J.m}^{-2}$ and $T=500 \text{ K}$ , showing critical nucleation radii $r^*$ at $S=10,20,100$ and $1000$ ; (b) the rate of nucleation vs. supersaturation $S$ as given by equation (4.6), for various values of the interfacial tension $\sigma_{SL}$ . Reproduced from [18]..... | 61 |
| Figure 4.2: Schematic showing the proposed stabilisation mechanism for PVP. Reproduced from [19].....   | 63 |
| Figure 4.3: Reaction scheme for the synthesis of Nafion®-stabilised colloidal Pt using NaBH4. .   | 64 |
| Figure 4.4: TG data recorded in air for (a) Vulcan XC-72 carbon black, and supported catalysts containing 20, 40 and 46 wt% Pt on C; (b) a Nafion® 112 membrane, a 46wt% Pt/C catalyst and a catalyst layer containing both Pt/C and Nafion®. Reproduced from [20]. Copyright 2006 American Chemical Society.....   | 69 |
| Figure 4.5: (a) UV-visible spectra for H2PtCl6 solution and Nafion®-stabilised colloidal Pt nanoparticles; (b) Low-magnification TEM micrograph of as-synthesised Nafion®-stabilised colloidal Pt; (c) HR-TEM micrograph of colloidal Pt nanoparticles showing lattice fringes.....   | 70 |
| Figure 4.6: (a-c) TEM images and particle size distributions of Nafion®-stabilised colloidal Pt prepared at various Pt:Nafion® m/m ratios, and (d) at elevated pH.....  | 71 |
| Figure 4.7: DLS size distributions for as-synthesised colloidal Pt prepared at Pt:Nafion® ratios of 1:1, 1:5 and 1:30.....  | 71 |
| Figure 4.8: Pt particle size distributions and TEM micrographs for colloidal Pt synthesised at three batch scales 5mg, 50mg and 100mg.....  | 73 |
| Figure 4.9: Particle size distributions and (inset) TEM micrographs for as-prepared synthetic products using a) water alone (no additives), b) 50/50 water/ethylene glycol, c) 50/50 water/propane-1,2-diol and d) 50/50 water/glycerol. All products synthesised on the 50 mg scale. ....  | 76 |
| Figure 4.10: Comparison of preparation routes for Nafion®-Pt/C A and B. Pt particles can be made to agglomerate (A) or disperse evenly (B) on the carbon support depending on whether the support is added after (A) or before (B) removal of excess Nafion® by centrifugation .....  | 77 |

## Index of figures

---

|  |    |
|--|----|
| Figure 4.11: a) Thermogravimetric mass loss profiles obtained in air with a 50 K.min <sup>-1</sup> thermal ramp and b) Nafion® content of the colloidal Pt as a function of the number of centrifugation steps.....  | 78 |
| Figure 4.12: TEM images and (inset) schematic illustrations of the morphology of Nafion®-stabilised colloidal Pt before and after purification.....  | 78 |
| Figure 4.13: a) STEM micrograph of purified Nafion®-stabilised Pt nanoparticles (grey/white), b) EDX map of elemental sulphur distribution (red) indicating the presence of Nafion® within Pt agglomerates.....  | 79 |
| Figure 4.14: a) TEM micrograph and b) Pt particle size distribution for Nafion®-Pt/C A catalyst following purification of colloidal Pt and addition of the carbon support.....   | 79 |
| Figure 4.15: TGA curves for a) Vulcan XC-72R, Nafion® and a mixture of both and b) purified Nafion®-Pt/C B catalyst after 4 centrifugation cycles; obtained by heating from 25 - 800 °C at 10 °C.min <sup>-1</sup> in air.....   | 80 |
| Figure 4.16: a) TEM micrograph and b) Pt particle size distribution for purified Nafion®-Pt/C B catalyst.....  | 81 |
| Figure 4.17: TGA analysis of purified colloidal Pt prepared using ethylene glycol (Nafion®-EG-Pt).....   | 82 |
| Figure 4.18: a) TEM micrograph and b) Pt particle size distributions for purified Nafion®-EG-Pt/C catalyst.....  | 83 |
| Figure 5.1: Experimental setup employed for the ex-situ electrochemical characterisation of electrocatalysts in this work.....   | 86 |
| Figure 5.2: For 2mm Pt disc electrode in 0.1 M HClO <sub>4</sub> at 25°C: (a) CV recorded at 25 mV/s in N <sub>2</sub> -saturated electrolyte showing shaded region due to Hupd desorption; (b) background and iR-drop corrected anodic polarisation curves recorded in O <sub>2</sub> -saturated electrolyte at 25 mV/s; (c) Levich plot demonstrating linear dependence of limiting current on $\omega^{1/2}$ and theoretical values for $J_{lim}$ calculated from the Levich equation; (d) Koutecky-Levich plots used to calculate $J_k$ values at the 6 potentials shown; (e) Tafel plot combining kinetic current data calculated using $J_k = J \cdot J_{lim} / (J_{lim} - J)$ (–) and via the K-L plots in (d) (■)..... | 88 |
| Figure 5.3: Laser interferometry profiles of thin catalyst films on GC electrodes prepared using (a, b) stationary drop-casting and (c, d) ethylene glycol modified spin-coating method. The spin-coating method produces a very even, homogeneous film, whereas the standard drop-casting method produces 'islands' of high catalyst loading and regions of bare glassy carbon.....   | 91 |

---

---

|   |     |
|---|-----|
| Figure 5.4: Comparison of specific activities measured on 4 electrodes prepared using the stationary drop casting and EG-SC methods, demonstrating the enhanced reproducibility offered by the latter. All electrodes prepared from the same ink TKK 50 wt%, at a Pt loading of 20 $\mu\text{gPt.cm}^{-2}$ .....                                      | 92  |
| Figure 5.5: CVs recorded at 25 mV/s in N <sub>2</sub> -saturated 0.1 M HClO <sub>4</sub> for (a) the Nafion®-Pt/C catalyst with an optimised ionomer content and (b) for the E-Tek 50wt% Pt/C catalyst with a sub-optimal ionomer content.....  | 93  |
| Figure 5.6: Demonstrating the variation in catalyst utilisation with LPt for an electrode with sub-optimal ionomer content (E-Tek), and the invariance of utilisation with LPt for an electrode with optimal ionomer content (Nafion®-Pt/C A). Both electrodes prepared at 20 % NFP.....  | 94  |
| Figure 5.7: (a) Catalyst utilisation as a function of Nafion® content for Nafion®-Pt/C A (●), Nafion®-Pt/C B (◆) and E-Tek (■) catalysts and (b) optimum catalyst utilisations found in this study for each catalyst.....   | 96  |
| Figure 5.8: Anodic linear sweep voltammograms in N <sub>2</sub> and O <sub>2</sub> , showing the effect of background subtraction and Ohmic (iR-drop) corrections. Inset shows in more detail the effect of the Ohmic and background corrections over the potential range 0.9 – 1.0 V.....  | 97  |
| Figure 5.9: (left) iR-corrected, background-subtracted RDE data at various rotation rates; (centre) Koutecky-Levich plots; (right) mass-transport corrected Tafel plots for each electrocatalyst under test in O <sub>2</sub> -saturated 0.1 M HClO <sub>4</sub> at 25°C.....   | 98  |
| Figure 5.10: Levich plot for thin-film catalysed RDEs, showing linear relationships between limiting current densities $J_{\text{lim}}$ and the square root of angular frequency $\omega^{1/2}$ for each electrode prepared by the EG-SC method at Pt loadings of 20 $\mu\text{g/cm}^2$ .....   | 99  |
| Figure 5.11: (a) iR-corrected RDE curves recorded at 1286 RPM, 25 mV/s in O <sub>2</sub> saturated 0.1 M HClO <sub>4</sub> at 25°C; (b) mass-transport corrected Tafel plots; (c) ORR specific activities and (d) ORR mass activities at 0.9 V. Catalysts in (c) and (d) are arranged in decreasing order of Pt particle size from left to right..... | 101 |
| Figure 5.12: (a) Currents measured at the Pt/C catalysed disc and Pt ring electrodes for the Fe(CN) <sub>6</sub> <sup>3-</sup> → Fe(CN) <sub>6</sub> <sup>4-</sup> reaction a several rotation rates; (b) illustrating the variation in collection efficiency as a function of rotation rate.....   | 102 |
| Figure 5.13: Peroxide production during ORR on both Nafion®-Pt/C A and TKK catalysts.....   | 104 |
| Figure 5.14: (a) Temperature dependence of oxygen concentration [O <sub>2</sub> ] and diffusion coefficient D(O <sub>2</sub> ) in aqueous solution; (b) plot showing the variation of Levich limiting current with temperature, normalised to the limiting current at 25°C (valid for all rotation rates).....  | 105 |

---

## Index of figures

---

|  |     |
|--|-----|
| Figure 5.15: (a) RDE curves recorded at 25mV/s 1286 rpm 70°C in O <sub>2</sub> -saturated 0.1M HClO <sub>4</sub> ; (b) Levich plots for each catalyst under these conditions for rotation rates from 400-2000 rpm.....   | 106 |
| Figure 5.16: (a) Tafel plots with kinetic current densities normalised by ECSA; (b) ORR mass activity data for ORR at 70°C (not corrected for [O <sub>2</sub> ]); (c) comparison of ORR specific activities and (d) mass activities at 0.9 V vs. SHE, showing uncorrected values and those that are corrected for [O <sub>2</sub> ] according to equation (1.16).....  | 109 |
| Figure 6.1: Schematic illustration of the three main degradation modes for Pt/C electrocatalysts; (a) Pt dissolution, which can be followed by loss of Pt or redeposition (Ostwald ripening); (b) Pt nanoparticle migration and sintering on the carbon support and (c) corrosion of the carbon support, with detachment of Pt nanoparticles.....  | 111 |
| Figure 6.2: Schematic showing the reactions in four regions of a single cell during startup and shutdown, when an air/fuel boundary is established on the anode (areas C and A), which then drives the carbon oxidation reaction in area D. Reproduced from [21] .....   | 114 |
| Figure 6.3: (a) AST potential cycle; (b) comparison of ECSA and mass activity ( <i>I<sub>m</sub></i> ) for a TKK 46wt % Pt/C catalyst measured before and after 7200 AST cycles in three different electrolytes (0.5M H <sub>2</sub> SO <sub>4</sub> , 0.1M HClO <sub>4</sub> and 0.5M H <sub>3</sub> PO <sub>4</sub> ) at 25°C. Reproduced from [22].....   | 116 |
| Figure 6.4: a) AST potential cycle, b-f) cyclic voltammograms after every 1200 cycles for the various catalysts on test, recorded at 25mV.s <sup>-1</sup> at 25°C in 0.5M H <sub>2</sub> SO <sub>4</sub> .....   | 120 |
| Figure 6.5: Comparison of catalyst durability during AST testing in 0.5M H <sub>2</sub> SO <sub>4</sub> at 25°C.....   | 121 |
| Figure 6.6: Elemental ratios for Pt, C, S and F measured by EDX across the entire area of the TF-catalysed electrode (E-Tek) (a) prior to AST testing and (b) following AST testing.....   | 122 |
| Figure 6.7: Post-AST TEM images and Pt particle size distributions (pre- and post-AST) for a) Nafion®-Pt/C A, b) Nafion®-Pt/C B and c) E-Tek catalysts.....  | 123 |
| Figure 6.8: Schematic diagram illustrating the proposed morphological origins of the enhanced durability of Nafion®-Pt/C A type electrocatalysts compared with standard Pt/C.....  | 124 |
| Figure 7.1: Summary of the data collection and processing steps in an EIS experiment. (a) Sinusoidal current ( <i>I</i> ) is applied and potential ( <i>E</i> ) recorded as a function of time <i>t</i> ; complex impedance is calculated according to equation (7.3) and can be represented in terms of real ( <i>Z'</i> ) and imaginary ( <i>Z''</i> ) components on a Nyquist plot (b); an equivalent circuit is developed using R and C circuit elements, which represent physical processes within the cell and have characteristic impedance responses as shown in (c); equivalent circuit components are then assigned values by least-squares fitting to experimental data (♦) as shown in (d) for low current densities and (e) for high current densities..... | 131 |

---

|  |     |
|--|-----|
| Figure 7.2: (a) general equivalent circuit model (Randles circuit) for an electrochemical interface; (b) typical equivalent circuit for a PEMFC .....  | 133 |
| Figure 7.3: Transmission line model of the Warburg circuit element used in PEMFC equivalent circuits to represent diffusion (mass transport) processes.....  | 134 |
| Figure 7.4: Polarisation curves recorded at (a,b) 0 bar and (c,d) 2 bar.g reactant backpressure for MEAs prepared from (●)Nafion®-Pt/C A, (■)Nafion®-Pt/C B, (◆)E-Tek and (▲)TKK catalysts. In (a,c) performance is normalised by active electrode area (.cm <sup>2</sup> ), whilst (b,d) show performance normalised by cathode Pt loading (.mg <sup>-1</sup> ). The dashed vertical lines in (c) indicate the current densities at which EIS measurements were performed.....                                  | 136 |
| Figure 7.5: (a,b) Nyquist plots showing EIS data (points) and fitted spectra (solid lines) based on equivalent circuits (insets) (a) 1 A DC current, (b) 8 A DC current; equivalent circuit element fitted values for (c) R3 cathode charge transfer resistance, (d) R1 ohmic resistance, (e) Warburg Ws-R cathode mass transport resistance; (f) weighted sum-of-squares error in best fit for impedance data recorded at 1 A and 8 A.....  | 139 |
| Figure 7.6: (a) Cyclic voltammograms recorded for MEAs operating in driven cell mode with humidified H <sub>2</sub> supplied to the anode, whilst the cathode is purged with humidified N <sub>2</sub> , 25 mV.s <sup>-1</sup> cell temperature 25°C; (b) comparison of catalyst utilisation values obtained from ECSAs measured from Hupd regions of the cyclic voltammograms and estimates of physical surface area shown in Table 7.3.....  | 140 |
| Figure 7.7: (a) Comparison of ORR mass activities measured in MEA and RDE (2000 rpm, 70°C) experiments in the potential range 1.0 - 0.7 V vs. RHE and (b) effectiveness factors of cathode catalyst layers for the four MEAs on test.....  | 142 |
| Figure 8.1: (a) Volcano plot for ORR catalysis on several transition metal surfaces. The activity scale is normalised by maximum theoretical activity (=0), and the binding energy for oxygen is shown in the horizontal axis. Reproduced from [23] (b) A volcano plot for bulk, ordered Pt3M bimetallic alloys (M=Ti, V, Fe, Co, Ni), with specific ORR activity @ 0.9 V plotted vs. the d-band centre as measured in UPS experiments. 'Pt poly' represents bulk, polycrystalline Pt. Reproduced from [24]..... | 146 |
| Figure 8.2: Relative rates of ORR on Pt3Ni and pure Pt surfaces, along with corresponding d-band centre shifts in eV. Reproduced from [25]. The accompanying schematic illustrates variation in crystallographic surface composition for particles of different geometries.....  | 149 |
| Figure 8.3: (a) ORR volcano plot featuring early transition metal alloys Pt3Y, Pt3Sc and Pt3Ti; (b) plot generated from computational data for oxygen binding energy (relative to Pt) and the energy of formation ΔE <sub>alloy</sub> of Pt-M alloys; (c) linear sweep voltammograms for Pt and Pt3Y, Pt3Sc  |     |

## Index of figures

---

|   |     |
|---|-----|
| single-crystal surfaces obtained in RDE experiments at 23°C, 1600rpm in 0.1M HClO <sub>4</sub> at a scan rate of 20 mV.s <sup>-1</sup> ; (d) anodic RDE sweeps comparing initial performance (solid lines) and that after 90 minutes of cycling (dashed lines); (e) Tafel plots of ORR specific activity for Pt and Pt <sub>3</sub> Sc, Pt <sub>3</sub> Y alloys..... | 151 |
| Figure 8.4: Possible combination fashions for two metals forming a bimetallic nanoparticle include (a) core-shell; (b) 'dipolar' or 'dumb-bell'; (c) intermixed random or ordered intermetallic alloys or (d) multi-layer 'onion-like' structures. Reproduced from [26].....  | 154 |
| Figure 8.5: Three distinct modes for the overgrowth of Pt on a pre-formed metal core. Reproduced from [15].....   | 156 |
| Figure 8.6: Overall synthetic protocol employed in this work for the synthesis of Ti@Pt nanoparticles. First a Ti <sup>4+</sup> precursor is reduced by LiBEt <sub>3</sub> H in the presence of a diazonium salt to produce ligand-stabilised metallic Ti cores, followed by addition of a Pt precursor which is reduced in-situ to form the Pt shells.....           | 158 |
| Figure 8.7: Diazonium ligands used in this study for the stabilisation of metallic Ti nanoparticles .....   | 159 |
| Figure 8.8: Diagram of apparatus used for synthetic work according to method of Abe et al.....  | 162 |
| Figure 8.9: (a-b) Bright-field TEM images (x 300 K) of the purified product synthesised at (a) Pt:Ti=1:1 and (b) Pt:Ti=2:1, showing agglomerated metallic nanoparticles; (c) particle size distributions for the products synthesised at Pt:Ti= 1:1 and 2:1. ....   | 166 |
| Figure 8.10: (a) HAADF-STEM image (x1.2 M) of a group of particles in the Pt:Ti=2:1 product, together with an EDX linescan across a single particle; (b) schematic showing the EDX linescan profile expected for a Ti@Pt core@shell particle.....   | 166 |
| Figure 8.11: Ti 2p XPS spectra for products synthesised at Pt:Ti=1:1 and 2:1.....   | 167 |
| Figure 8.12: H <sup>1</sup> NMR spectra for (a) 4-decylaniline and (b) 4-decyl diazonium tetrafluoroborate. The solvent was CDCl <sub>3</sub> .....   | 168 |
| Figure 8.13: FTIR spectra for n-decyl diazonium tetrafluoroborate and Ti@Pt-DP nanoparticles. The absorbance peak at 2250 cm <sup>-1</sup> for the diazonium compound is characteristic of the N≡N vibrational stretch.....   | 169 |
| Figure 8.14: The intended products in this study were core@shell nanoparticles (Ti@Pt), stabilised by (a) decylphenyl (Ti@Pt-DP) and (b) benzylphenyl (Ti@Pt-BP) ligands.....   | 169 |
| Figure 8.15: (a-b) Bright field TEM micrographs (JEOL 1200ex, 80kV accelerating voltage) of the purified Ti-Pt-DP product; (c) particle size distribution measured from (b).....  | 170 |

---

---

|   |     |
|---|-----|
| Figure 8.16: XPS spectra for (a) the Ti 2p and (b) the Pt 4f photoemission bands of the purified Ti@Pt-DP reaction product. Spectra were charge-corrected with respect to the C 1s peak at 285.0 eV and fitting was performed against a Shirley-type baseline with Gaussian-Lorentzian lineshapes for oxide species, and Doniach -Sunjic (asymmetric) lineshapes for metallic Pt..... | 171 |
| Figure 8.17: Schematic representation of the anion coordination strategy for the synthesis of core@shell (M1@M2) nanoparticles reported by Serpell et al. Reproduced from [27].....   | 173 |
| Figure 8.18: Proposed synthetic route for the production of Ti@Pt nanoparticles via ligand coordination of the Pt precursor with pre-formed Ti cores.....   | 174 |



## Bibliography

1. Davis, S.J., K. Caldeira, and H.D. Matthews, *Future CO<sub>2</sub> Emissions and Climate Change from Existing Energy Infrastructure*. Science, 2010. **329**(5997): p. 1330-1333.
2. Turner, J.A., *A Realizable Renewable Energy Future*. Science, 1999. **285**(5428): p. 687-689.
3. Pollet, B.G., I. Staffell, and J.L. Shang, *Current Status of Hybrid, Battery and Fuel Cell Electric Vehicles: from Electrochemistry to Market Prospects*. Electrochimica Acta, 2012.
4. Tester, J.W. *Energy Transfer, Conversion and Storage Toolbox 5*. 2005 [8th April 2012]; Available from: <https://eresourcecenter.org/kc/CourseWare/MitSustainable/Conversion>.
5. Papageorgopoulos, D., *PEMFC R&D at the DOE Fuel Cell Technologies Program*, D.o. Energy, Editor. 2011, United States Government: Arlington, VA.
6. *Platinum Today*. [14th April 2012]; Available from: <http://platinum.matthey.com/pgm-prices/price-charts/>.
7. Carlson, E.J., J.S. P. Kopf, and S. Sriramulu, *Cost Analysis of PEM Fuel Cell Systems for Transportation*. 2005, National Renewable Energy Laboratory: Cambridge, Massachusetts.
8. *PEMFC stack diagram*, h-tec Systems.
9. Larminie, J. and A. Dicks, *Fuel Cell Systems Explained*. 2003: Wiley.
10. Debe, M.K., *Nanostructured Thin Film Electrocatalysts for PEM Fuel Cells - A Tutorial on the Fundamental Characteristics and Practical Properties of NSTF Catalysts*. ECS Transactions, 2012. **45**(2): p. 47-68.
11. Pollet, B.G. and O.J. Curnick, *Introduction to Electrochemistry*, in *Power Ultrasound in Electrochemistry: From Versatile Laboratory Tool to Engineering Solution*, B.G. Pollet, Editor. 2012, Wiley-Blackwell.

- 
12. Gasteiger, H.A., et al., *Activity benchmarks and requirements for Pt, Pt-alloy, and non-Pt oxygen reduction catalysts for PEMFCs*. Applied Catalysis B: Environmental, 2005. **56**(1-2): p. 9-35.
  13. Sarma, L.S., et al., *Carbon-supported Pt–Ru catalysts prepared by the Nafion® stabilized alcohol-reduction method for application in direct methanol fuel cells*. Journal of Power Sources, 2005. **139**(1-2): p. 44-54.
  14. Liu, Z., Z.Q. Tian, and S.P. Jiang, *Synthesis and characterization of Nafion®-stabilized Pt nanoparticles for polymer electrolyte fuel cells*. Electrochimica Acta, 2006. **52**(3): p. 1213-1220.
  15. Cheng, N., et al., *Improved lifetime of PEM fuel cell catalysts through polymer stabilization*. Electrochemistry Communications, 2009. **11**(8): p. 1610-1614.
  16. Yin, S., et al., *A highly stable catalyst for PEM fuel cell based on durable titanium diboride support and polymer stabilization*. Applied Catalysis B: Environmental, 2010. **93**(3-4): p. 233-240.
  17. Yin, S., et al., *A highly stable TiB<sub>2</sub>-supported Pt catalyst for polymer electrolyte membrane fuel cells*. Journal of Power Sources, 2011. **196**(19): p. 7931-7936.
  18. Martucci, A. *Homogeneous Nucleation*. 2009 [cited 2012 21/03/2012]; Available from: <http://www.dim.unipd.it/martucci/Lezione2.pdf>.
  19. Borodko, Y., et al., *Charge-Transfer Interaction of Poly(vinylpyrrolidone) with Platinum and Rhodium Nanoparticles*. The Journal of Physical Chemistry C, 2007. **111**(17): p. 6288-6295.
  20. Baturina, O.A., S.R. Aubuchon, and K.J. Wynne, *Thermal Stability in Air of Pt/C Catalysts and PEM Fuel Cell Catalyst Layers*. Chemistry of Materials, 2006. **18**(6): p. 1498-1504.
  21. Tang, H., et al., *PEM fuel cell cathode carbon corrosion due to the formation of air/fuel boundary at the anode*. Journal of Power Sources, 2006. **158**(2): p. 1306-1312.
  22. Takahashi, I. and S.S. Kocha, *Examination of the activity and durability of PEMFC catalysts in liquid electrolytes*. Journal of Power Sources, 2010. **195**(19): p. 6312-6322.
-

## Bibliography

---

23. Norskov, J.K., et al., *Origin of the Overpotential for Oxygen Reduction at a Fuel-Cell Cathode*. The Journal of Physical Chemistry B, 2004. **108**(46): p. 17886-17892.
24. Stamenkovic, V.R., et al., *Trends in electrocatalysis on extended and nanoscale Pt-bimetallic alloy surfaces*. Nat Mater, 2007. **6**(3): p. 241-247.
25. Stamenkovic, V.R., et al., *Improved Oxygen Reduction Activity on Pt<sub>3</sub>Ni(111) via Increased Surface Site Availability*. Science, 2007. **00315**(05811): p. 493-498.
26. Ferrando, R., J. Jellinek, and R.L. Johnston, *Nanoalloys: From Theory to Applications of Alloy Clusters and Nanoparticles*. Chemical reviews, 2008. **108**(3): p. 845-910.
27. Serpell, C.J., et al., *Core@shell bimetallic nanoparticle synthesis via anion coordination*. Nat Chem, 2011. **3**(6): p. 478-483.
28. Hoffert, M.I., et al., *Advanced Technology Paths to Global Climate Stability: Energy for a Greenhouse Planet*. Science, 2002. **298**(5595): p. 981-987.
29. Hart, A.B. and G.J. Womack, *Fuel Cells - Theory and Application*. 1967, London: Chapman and Hall.
30. Solvay. *Solvay has successfully commissioned the largest PEM fuel cell in the world at Solvin's Antwerp plant*. 2012 7th April 2012]; Available from: <http://www.reuters.com/article/2012/02/06/idUS88888+06-Feb-2012+HUG20120206>.
31. Steele, B.C.H. and A. Heinzl, *Materials for fuel-cell technologies*. Nature, 2001. **414**(6861): p. 345-352.
32. Adcock, P.L., et al., *Prospects for the application of fuel cells in electric vehicles*. Journal of Power Sources, 1992. **37**(1-2): p. 201-207.
33. *2011 UK Greenhouse Gas Emissions, Provisional Figures and 2010 Greenhouse Gas Emissions, Final Figures by Fuel Type and End User*. 2012, Department of Energy and Climate Change.
34. *Fuel Cell Technologies Program Multi-Year Research, Development and Demonstration Plan*. 2011, US Department of Energy. p. 3.4 - 1.

- 
35. Amolins, M.W. and X. Wang. *Investigation of Non-Platinum Based Electrocatalysts for Proton Exchange Membrane Fuel Cell Cathodes*.
  36. Artyushkova, K., et al., *Non-platinum electrocatalysts for PEMFCs: structure and mechanism of oxygen reduction reaction*. Section Title: Electrochemical, Radiational, and Thermal Energy Technology, 2006. **51**(1): p. 320-321.
  37. Bashyam, R. and P. Zelenay, *A class of non-precious metal composite catalysts for fuel cells*. Nature, 2006. **443**(7107): p. 63-66.
  38. Cracknell, J.A., K.A. Vincent, and F.A. Armstrong, *Enzymes as Working or Inspirational Electrocatalysts for Fuel Cells and Electrolysis*. Section Title: Electrochemical, Radiational, and Thermal Energy Technology, 2008. **108**(7): p. 2439-2461.
  39. Ishihara, A., et al., *Progress in non-precious metal oxide-based cathode for polymer electrolyte fuel cells*. Electrochimica Acta. **In Press, Accepted Manuscript** (Journal Article).
  40. Jaouen, F., et al., *Recent advances in non-precious metal catalysis for oxygen-reduction reaction in polymer electrolyte fuel cells*. Energy & Environmental Science, 2011. **4**(1): p. 114-130.
  41. Lee, K., L. Zhang, and J. Zhang, *Non-noble Electrocatalysts for the PEM Fuel Cell Oxygen Reduction Reaction*, in *PEM Fuel Cell Catalysts and Catalyst Layers*, J. Zhang, Editor. 2008, Springer. p. 715.
  42. Liu, L., *Development of platinum-free electrocatalysts for oxygen reduction reaction in the PEM fuel cell*. Section Title: Unit Operations and Processes, 2006(Journal Article): p. 121.
  43. Matter, P.H., E.J. Biddinger, and U.S. Ozkan, *Non-precious metal oxygen reduction catalysts for PEM fuel cel*. Section Title: Electrochemical, Radiational, and Thermal Energy Technology, 2007. **20** (Journal Article): p. 338-366.
  44. Othman, R., A.L. Dicks, and Z. Zhu, *Non precious metal catalysts for the PEM fuel cell cathode*. International Journal of Hydrogen Energy, (0).
  45. Susac, D., et al., *A Methodology for Investigating New Nonprecious Metal Catalysts for PEM Fuel Cells*. The Journal of Physical Chemistry B, 2006. **110**(22): p. 10762-10770.
-

## Bibliography

---

46. Tarasevich, M., et al., *Development of platinum-free catalyst and catalyst with low platinum content for cathodic oxygen reduction in acidic electrolytes*. Journal of Applied Electrochemistry, 2007. **37**(12): p. 1503-1513.
47. Tasic, G.S., et al., *Non-noble metal catalyst for a future Pt free PEMFC*. Electrochemistry Communications. **In Press, Accepted Manuscript**(Journal Article).
48. Zhang, L., et al., *Progress in preparation of non-noble electrocatalysts for PEM fuel cell reactions*. Section Title: Electrochemical, Radiational, and Thermal Energy Technology, 2006. **156**(2): p. 171-182.
49. Lefevre, M., et al., *Iron-Based Catalysts with Improved Oxygen Reduction Activity in Polymer Electrolyte Fuel Cells*. Science, 2009. **324**(5923): p. 71-74.
50. Scott, K. and A.K. Shukla, *Polymer electrolyte membrane fuel cells: Principles and advances*. Reviews in Environmental Science and Biotechnology, 2004. **3**(3): p. 273-280.
51. Li, M. and K. Scott, *A polytetrafluoroethylene/quaternized polysulfone membrane for high temperature polymer electrolyte membrane fuel cells*. Journal of Power Sources, 2011. **196**(4): p. 1894-1898.
52. Wu, X., M. Mamlouk, and K. Scott, *A PBI-Sb<sub>0.2</sub>Sn<sub>0.8</sub>P<sub>2</sub>O<sub>7</sub>-H<sub>3</sub>PO<sub>4</sub> Composite Membrane for Intermediate Temperature Fuel Cells*. Fuel Cells, 2011. **11**(5): p. 620-625.
53. Wang, X., et al., *A novel phosphoric acid loaded quaternary 1,4-diazabicyclo-[2.2.2]-octane polysulfone membrane for intermediate temperature fuel cells*. International Journal of Hydrogen Energy, 2011. **36**(14): p. 8550-8556.
54. Ravikumar and K. Scott, *Freestanding sulfonated graphene oxide paper: a new polymer electrolyte for polymer electrolyte fuel cells*. Chemical Communications, 2012. **48**(45): p. 5584-5586.
55. Zhang, J., et al., *PEM fuel cell open circuit voltage (OCV) in the temperature range of 23°C to 120°C*. Journal of Power Sources, 2006. **163**(1): p. 532-537.
56. Bard, A.J. and L.R. Faulkner, *Electrochemical Methods: Fundamentals and Applications*. Second Edition ed. 2001: Wiley.

- 
57. Petrow, H.G. and R.J. Allen, *Finely particulated colloidal platinum compound and sol for producing the same, and method of preparation of fuel cell electrodes and the like employing the same*. 1977: United States.
  58. Srinivasan, S., et al., *Advances in solid polymer electrolyte fuel cell technology with low platinum loading electrodes*. Journal of Power Sources, 1988. **22**(3–4): p. 359-375.
  59. Malek, K., et al., *Self-Organization in Catalyst Layers of Polymer Electrolyte Fuel Cells*. The Journal of Physical Chemistry C, 2007. **111**(36): p. 13627-13634.
  60. Ignaszak, A., S. Ye, and E. Gyenge, *A Study of the Catalytic Interface for O<sub>2</sub> Electroreduction on Pt: The Interaction between Carbon Support Meso/Microstructure and Ionomer (Nafion®) Distribution*. The Journal of Physical Chemistry C, 2009. **113**(1): p. 298-307.
  61. Esparbé, I., et al., *Structure and electrocatalytic performance of carbon-supported platinum nanoparticles*. Journal of Power Sources, 2009. **190**(2): p. 201-209.
  62. Friedmann, R. and T. Van Nguyen, *Optimization of the Microstructure of the Cathode Catalyst Layer of a PEMFC for Two-Phase Flow*. Journal of the Electrochemical Society, 2010. **157**(2): p. B260-B265.
  63. Tabe, Y., et al., *Effects of Cathode Catalyst Layer Structure and Properties Dominating Polymer Electrolyte Fuel Cell Performance*. Journal of the Electrochemical Society, 2011. **158**(10): p. B1246-B1254.
  64. Zhang, J.Z., K. Hongsirikarn, and J.G. Goodwin Jr, *Effect and siting of Nafion® in a Pt/C proton exchange membrane fuel cell catalyst*. Journal of Power Sources, 2011. **196**(19): p. 7957-7966.
  65. Song, J.M., et al., *Preparation of High Catalyst Utilization Electrodes for Polymer Electrolyte Fuel Cells*. Langmuir, 2006. **22**(14): p. 6422-6428.
  66. Hsieh, Y.-F., et al., *Pulse Electrodepositions of PtRu on Large-Area Carbon Nanotubes for Enhancement of Methanol Electro-Oxidation*. Journal of the Electrochemical Society, 2010. **157**(1): p. B39-B44.
  67. Pollet, B.G., E.F. Valzer, and O.J. Curnick, *Platinum sonoelectrodeposition on glassy carbon and gas diffusion layer electrodes*. International Journal of Hydrogen Energy, 2011. **36**(10): p. 6248-6258.
-

## Bibliography

---

68. Wei, Z.D., et al., *Electrodepositing Pt on a Nafion®-bonded carbon electrode as a catalyzed electrode for oxygen reduction reaction*. *Electrochimica Acta*, 2005. **50**(11): p. 2279-2287.
69. Chou, J., et al., *Efficient Electrocatalyst Utilization: Electrochemical Deposition of Pt Nanoparticles Using Nafion® Membrane as a Template*. *The Journal of Physical Chemistry B*, 2006. **110**(14): p. 7119-7121.
70. Kongkanand, A., et al., *Single-Wall Carbon Nanotubes Supported Platinum Nanoparticles with Improved Electrocatalytic Activity for Oxygen Reduction Reaction*. *Langmuir*, 2006. **22**(5): p. 2392-2396.
71. Lee, K., et al., *Progress in the synthesis of carbon nanotube- and nanofiber-supported Pt electrocatalysts for PEM fuel cell catalysis*. Section Title: *Electrochemical, Radiational, and Thermal Energy Technology*, 2006. **36**(5): p. 507-522.
72. Nagle, L.C. and J.F. Rohan, *Aligned carbon nanotube–Pt composite fuel cell catalyst by template electrodeposition*. *Journal of Power Sources*, 2008. **185**(1): p. 411-418.
73. Niu, J.J. and J.N. Wang, *Activated carbon nanotubes-supported catalyst in fuel cells*. *Electrochimica Acta*, 2008. **53**(27): p. 8058-8063.
74. Shao, Y., et al., *Novel catalyst support materials for PEM fuel cells: current status and future prospects*. *Journal of Materials Chemistry*, 2009. **19**(1): p. 46-59.
75. Wu, Y.N., et al., *Shortened Carbon Nanotubes as Enhanced Support for High-performance Platinum Catalysts*. *Fuel Cells*, 2010: p. n/a-n/a.
76. Gross, A.F. and A.P. Nowak, *Hierarchical Carbon Foams with Independently Tunable Mesopore and Macropore Size Distributions*. *Langmuir*, 2010(Journal Article).
77. Ambrosio, E., et al., *Mesoporous carbons as low temperature fuel cell platinum catalyst supports*. *Journal of Applied Electrochemistry*, 2008. **38**(7): p. 1019-1027.
78. Yang, S.-Y., et al., *Constructing a hierarchical graphene–carbon nanotube architecture for enhancing exposure of graphene and electrochemical activity of Pt nanoclusters*. *Electrochemistry Communications*, 2010. **12**(9): p. 1206-1209.

- 
79. Hinds, G., *Preparation and characterisation of PEM fuel cell electrocatalysts: a review*. 2005, National Physical Laboratory: Teddington, Middlesex.
80. Foster, S.E., et al. *Development and Characterisation of a Novel Electrode Fabrication Technique for use in Solid Polymer Fuel Cells*. in *19th International Power Sources Symposium*. 1995. Brighton, UK.
81. Lee, P.-C., et al., *In situ formation of platinum nanoparticles in Nafion® recast film for catalyst-incorporated ion-exchange membrane in fuel cell applications*. *Journal of Membrane Science*, 2008. **322**(2): p. 441-445.
82. Kucernak, A.R. and E. Toyoda, *Studying the oxygen reduction and hydrogen oxidation reactions under realistic fuel cell conditions*. *Electrochemistry Communications*, 2008. **10**(11): p. 1728-1731.
83. Basura, V., P. Beattie, and S. Holdcroft, *Solid-state electrochemical oxygen reduction at Pt-Nafion® 117 and Pt-BAM3G™ 407 interfaces*. *Journal of Electroanalytical Chemistry*, 1998. **458**(1-2): p. 1-5.
84. Wang, J.X., N.M. Markovic, and R.R. Adzic, *Kinetic Analysis of Oxygen Reduction on Pt(111) in Acid Solutions: Intrinsic Kinetic Parameters and Anion Adsorption Effects*. *The Journal of Physical Chemistry B*, 2004. **108**(13): p. 4127-4133.
85. Subbaraman, R., et al., *Three Phase Interfaces at Electrified Metal–Solid Electrolyte Systems I. Study of the Pt(hkl)–Nafion® Interface*. *The Journal of Physical Chemistry C*, 2010. **114**(18): p. 8414-8422.
86. Santos, M.C., D.W. Miwa, and S.A.S. Machado, *Study of anion adsorption on polycrystalline Pt by electrochemical quartz crystal microbalance*. *Electrochemistry Communications*, 2000. **2**(10): p. 692-696.
87. Markovic, N.M., et al., *Oxygen reduction reaction on Pt(111): effects of bromide*. *Journal of Electroanalytical Chemistry*, 1999. **467**(1-2): p. 157-163.
88. Stamenkovic, V., N. M. Markovic, and P.N. Ross, *Structure-relationships in electrocatalysis: oxygen reduction and hydrogen oxidation reactions on Pt(111) and Pt(100) in solutions containing chloride ions*. *Journal of Electroanalytical Chemistry*, 2001. **500**(1-2): p. 44-51.
-



## Bibliography

---

89. Greef, R., et al., *Instrumental Methods in Electrochemistry*. Ellis Horwood Series in Physical Chemistry, ed. T.J. Kemp. 1990.
90. Shijun, L., L. Baitao, and L. Yingwei, *Physical Characterization of Electrocatalysts*, in *PEM Fuel Cell Catalysts and Catalyst Layers*, Z. Jiujuun, Editor. 2008, Springer. p. 488.
91. Mayrhofer, J.J., et al., *Measurement of oxygen reduction activities via the rotating disc electrode method: From Pt model surfaces to carbon-supported high surface area catalysts*. *Electrochimica Acta*, 2008. **53**(7): p. 3181-3188.
92. Treimer, S., A. Tang, and D.C. Johnson, *A Consideration of the Application of Koutecký-Levich Plots in the Diagnoses of Charge-Transfer Mechanisms at Rotated Disk Electrodes*. *Electroanalysis*, 2002. **14**(3): p. 165-171.
93. Gloaguen, F., et al., *An evaluation of the macro-homogeneous and agglomerate model for oxygen reduction in PEMFCs*. *Electrochimica Acta*, 1998. **43**(24): p. 3767-3772.
94. Perez, J., E.R. Gonzalez, and E.A. Ticianelli, *Oxygen electrocatalysis on thin porous coating rotating platinum electrodes*. *Electrochimica Acta*, 1998. **44**(8-9): p. 1329-1339.
95. Paulus, U.A., et al., *Oxygen reduction on high surface area Pt-based alloy catalysts in comparison to well defined smooth bulk alloy electrodes*. *Electrochimica Acta*, 2002. **47**(22-23): p. 3787-3798.
96. Lin, R.-B. and S.-M. Shih, *Kinetic analysis of the hydrogen oxidation reaction on Pt-black/Nafion® electrode*. *Journal of Solid State Electrochemistry*, 2006. **10**(4): p. 243-249.
97. Schmidt, T.J., et al., *Characterization of High-Surface-Area Electrocatalysts Using a Rotating Disk Electrode Configuration*. *Journal of the Electrochemical Society*, 1998. **145**(7): p. 2354-2358.
98. Markovic, N.M. and P.N. Ross, *Surface science studies of model fuel cell electrocatalysts*. *Surface Science Reports*, 2002. **45**(4-6): p. 117-229.
99. Vielstich, W., A. Lamm, and H.A. Gasteiger, *Handbook of Fuel Cells - Fundamentals Technology and Applications*. 2003: Wiley.

- 
100. Paulus, U.A., et al., *Oxygen reduction on a high-surface area Pt/Vulcan carbon catalyst: a thin-film rotating ring-disk electrode study*. Journal of Electroanalytical Chemistry, 2001. **495**(2): p. 134-145.
  101. Antoine, O. and R. Durand, *RRDE study of oxygen reduction on Pt nanoparticles inside Nafion®: H<sub>2</sub>O<sub>2</sub> production in PEMFC cathode conditions*. Journal of Applied Electrochemistry, 2000. **30**(7): p. 839-844.
  102. Biddinger, E.J., et al., *RRDE Catalyst Ink Aging Effects on Selectivity to Water Formation in ORR*. Electrochemical and Solid-State Letters, 2010. **13**(8): p. B98-B100.
  103. Inaba, M., et al., *Effect of Agglomeration of Pt/C Catalyst on Hydrogen Peroxide Formation*. Electrochemical and Solid-State Letters, 2004. **7**(12): p. A474-A476.
  104. Ohma, A., K. Fushinobu, and K. Okazaki, *Influence of Nafion® Film on Oxygen Reduction Reaction and Hydrogen Peroxide Formation on Pt Electrode for Proton Exchange Membrane Fuel Cell*. Electrochimica Acta, 2010. **55**(28): p. 8829-8838.
  105. Garsany, Y., et al., *Experimental Methods for Quantifying the Activity of Platinum Electrocatalysts for the Oxygen Reduction Reaction*. Analytical Chemistry, 2010.
  106. Mayrhofer, K.J.J., et al., *The Impact of Geometric and Surface Electronic Properties of Pt-Catalysts on the Particle Size Effect in Electrocatalysis*. The Journal of Physical Chemistry B, 2005. **109**(30): p. 14433-14440.
  107. Mayrhofer, K.J.J., et al., *Measurement of oxygen reduction activities via the rotating disc electrode method: From Pt model surfaces to carbon-supported high surface area catalysts*. Electrochimica Acta, 2008. **53**(7): p. 3181-3188.
  108. Nesselberger, M., et al., *The Particle Size Effect on the Oxygen Reduction Reaction Activity of Pt Catalysts: Influence of Electrolyte and Relation to Single Crystal Models*. Journal of the American Chemical Society, 2011. **133**(43): p. 17428-17433.
  109. Garsany, Y., I.L. Singer, and K.E. Swider-Lyons, *Impact of film drying procedures on RDE characterization of Pt/VC electrocatalysts*. Journal of Electroanalytical Chemistry, 2011. **662**(2): p. 396-406.
  110. Wakabayashi, N., et al., *Temperature-dependence of oxygen reduction activity at a platinum electrode in an acidic electrolyte solution investigated with a channel*
-

## Bibliography

---

- flow double electrode*. Journal of Electroanalytical Chemistry, 2005. **574**(2): p. 339-346.
111. Lee, M., et al., *The effectiveness of platinum/carbon electrocatalysts: Dependence on catalyst layer thickness and Pt alloy catalytic effects*. Electrochimica Acta, 2011. **56**(13): p. 4783-4790.
112. Avasarala, B., et al., *Titanium nitride nanoparticles based electrocatalysts for proton exchange membrane fuel cells*. Journal of Materials Chemistry, 2009. **19**(13): p. 1803-1805.
113. Ho, V.T.T., et al., *Nanostructured  $Ti_{0.7}Mo_{0.3}O_2$  Support Enhances Electron Transfer to Pt: High-Performance Catalyst for Oxygen Reduction Reaction*. Journal of the American Chemical Society, 2011. **133**(30): p. 11716-11724.
114. Zook, L.A. and J. Leddy, *Density and Solubility of Nafion®: Recast, Annealed, and Commercial Films*. Analytical Chemistry, 1996. **68**(21): p. 3793-3796.
115. Lehmani, A., et al., *Ion transport in Nafion® 117 membrane*. Journal of Electroanalytical Chemistry, 1997. **428**(1-2): p. 81-89.
116. Hongsirikarn, K., et al., *Effect of cations ( $Na^+$ ,  $Ca^{2+}$ ,  $Fe^{3+}$ ) on the conductivity of a Nafion® membrane*. Journal of Power Sources, 2010. **195**(21): p. 7213-7220.
117. van der Vliet, D., et al., *On the importance of correcting for the uncompensated Ohmic resistance in model experiments of the Oxygen Reduction Reaction*. Journal of Electroanalytical Chemistry, 2010. **647**(1): p. 29-34.
118. Cushing, B.L., V.L. Kolesnichenko, and C.J. O'Connor, *Recent Advances in the Liquid-Phase Syntheses of Inorganic Nanoparticles*. Chemical Reviews, 2004. **104**(9): p. 3893-3946.
119. Furedi-Milhofer, H., *Spontaneous precipitation from electrolytic solutions*. Pure and Applied Chemistry, 1981. **53**(11): p. 2041-2055.
120. Sugimoto, T., *Preparation of monodispersed colloidal particles*. Advances in Colloid and Interface Science, 1987. **28**(Journal Article): p. 65-108.
121. Lifshitz, I.M. and V.V. Slyozov, *The kinetics of precipitation from supersaturated solid solutions*. Journal of Physics and Chemistry of Solids, 1961. **19**(1-2): p. 35-50.
-

- 
122. Tokuyama, M., K. Kawasaki, and Y. Enomoto, *Kinetic equations for Ostwald ripening*. Physica A: Statistical and Theoretical Physics, 1986. **134**(2): p. 323-338.
123. Miyazaki, A., I. Balint, and Y. Nakano, *Morphology Control of Platinum Nanoparticles and their Catalytic Properties*. Journal of Nanoparticle Research, 2003. **5**(1): p. 69-80.
124. Bock, C., H. Halvorsen, and B. MacDougall, *Catalyst Synthesis Techniques*, in *PEM Fuel Cell Catalysts and Catalyst Layers*, J. Zhang, Editor. 2008, Springer. p. 447.
125. Turkevich, J., P. Cooper-Stevenson, and J. Hillier, *A study of the nucleation and growth processes in the synthesis of colloidal gold*. Discussions of the Faraday Society, 1951. **11**(Journal Article): p. 55-75.
126. Jiang, Q.-l., et al., *Preparation of high active Pt/C cathode electrocatalyst for direct methanol fuel cell by citrate-stabilized method*. Transactions of Nonferrous Metals Society of China, 2011. **21**(1): p. 127-132.
127. Khan, M.R. and S.D. Lin, *Using Pt sols to prepare low Pt-loading electrodes for polymer electrolyte fuel cells*. Journal of Power Sources, 2006. **162**(1): p. 186-191.
128. Lin, C.-S., M.R. Khan, and S.D. Lin, *The preparation of Pt nanoparticles by methanol and citrate*. Journal of Colloid and Interface Science, 2006. **299**(2): p. 678-685.
129. Zhang, Z. and Y. Wu, *Investigation of the NaBH<sub>4</sub>-Induced Aggregation of Au Nanoparticles*. Langmuir, 2010(Journal Article).
130. Glavee, G.N., et al., *Borohydride reduction of cobalt ions in water. Chemistry leading to nanoscale metal, boride, or borate particles*. Langmuir, 1993. **9**(1): p. 162-169.
131. Glavee, G.N., et al., *Borohydride Reduction of Nickel and Copper Ions in Aqueous and Nonaqueous Media. Controllable Chemistry Leading to Nanoscale Metal and Metal Boride Particles*. Langmuir, 1994. **10**(12): p. 4726-4730.
132. Mayer, A.B.R., J.E. Mark, and S.H. Hausner, *Colloidal platinum-polyacid nanocatalyst systems*. Die Angewandte Makromolekulare Chemie, 1998. **259**(1): p. 45-53.
-

## Bibliography

---

133. Rasband, W., *ImageJ*.
134. Koestner, R., et al., *AFM Imaging of Adsorbed Nafion® Polymer on Mica and Graphite at Molecular Level*. *Langmuir*, 2011. **27**(16): p. 10157-10166.
135. Wang, Y., et al., *Preparation of Tractable Platinum, Rhodium, and Ruthenium Nanoclusters with Small Particle Size in Organic Media*. *Chemistry of Materials*, 2000. **12**(6): p. 1622-1627.
136. Wang, Y., et al., *Metal Nanoclusters Stabilized with Simple Ions and Solvents—Promising Building Blocks for Future Catalysts*. *Topics in Catalysis*, 2005. **35**(1): p. 35-41.
137. Uchida, M., et al., *New Preparation Method for Polymer-Electrolyte Fuel Cells*. *Journal of the Electrochemical Society*, 1995. **142**(2): p. 463-468.
138. Haynes, W.M., ed. *CRC Handbook of Chemistry & Physics*. 92nd edition ed. 2012.
139. Corradini, F., et al., *Ethane-1,2-diol-water solvent system: relative permittivity as a function of temperature and binary composition*. *Journal of the Chemical Society, Faraday Transactions*, 1993. **89**(1): p. 123-127.
140. Kapadi, U.R., et al., *Studies of viscosity and excess molar volume of binary mixtures of propane-1,2 diol with water at various temperatures*. *Fluid Phase Equilibria*, 2001. **192**(1–2): p. 63-70.
141. Cheng, N.-S., *Formula for the Viscosity of a Glycerol–Water Mixture*. *Industrial & Engineering Chemistry Research*, 2008. **47**(9): p. 3285-3288.
142. Cristancho, D.M., et al., *Volumetric properties of glycerol + water mixtures at several temperatures and correlation with the Jouyban-Acree model*. *Revista Colombiana de Ciencias Químico-Farmacéuticas*, 2011. **40**(1): p. 92-115.
143. Antolini, E., et al., *Influence of Nafion® loading in the catalyst layer of gas-diffusion electrodes for PEFC*. *Journal of Power Sources*, 1999. **77**(2): p. 136-142.
144. Atkins, P.W., *Physical Chemistry Fifth Edition*. 5 ed. 1994, Oxford: Oxford University Press.
145. van Stroe-Biezen, S.A.M., et al., *Diffusion coefficients of oxygen, hydrogen peroxide and glucose in a hydrogel*. *Analytica Chimica Acta*, 1993. **273**(1-2): p. 553-560.

- 
146. Strmčnik, D., et al., *Active sites for PEM fuel cell reactions in model and real systems*. 2007, Univerza v Ljubljani: Ljubljana.
147. Stamenkovic, V., et al., *Surface Composition Effects in Electrocatalysis: Kinetics of Oxygen Reduction on Well-Defined Pt<sub>3</sub>Ni and Pt<sub>3</sub>Co Alloy Surfaces*. *The Journal of Physical Chemistry B*, 2002. **106**(46): p. 11970-11979.
148. Takasu, Y., et al., *Size effects of platinum particles on the electroreduction of oxygen*. *Electrochimica Acta*, 1996. **41**(16): p. 2595-2600.
149. Damjanovic, A. and D.B. Sepa, *An analysis of the pH dependence of enthalpies and Gibbs energies of activation for O<sub>2</sub> reduction at Pt electrodes in acid solutions*. *Electrochimica Acta*, 1990. **35**(7): p. 1157-1162.
150. Antolini, E., et al., *Effects of geometric and electronic factors on ORR activity of carbon supported Pt-Co electrocatalysts in PEM fuel cells*. Section Title: *Electrochemical, Radiational, and Thermal Energy Technology*, 2005. **30**(11): p. 1213-1220.
151. Cheng, C.H., et al., *Effect of Pt Nano-Particle Size on the Microstructure of PEM Fuel Cell Catalyst Layers: Insights from Molecular Dynamics Simulations*. *Electrochimica Acta*, 2009. **In Press, Accepted Manuscript**(Journal Article).
152. Han, K.S., et al., *Heat treatment and potential cycling effects on surface morphology, particle size, and catalytic activity of Pt/C catalysts studied by <sup>13</sup>C NMR, TEM, XRD and CV*. *Electrochemistry Communications*, 2007. **9**(2): p. 317-324.
153. Kim, J.W., et al., *Size-controlled synthesis of Pt nanoparticles and their electrochemical activities toward oxygen reduction*. *International Journal of Hydrogen Energy*. **In Press, Corrected Proof**.
154. Kinoshita, K., *Particle Size Effects for Oxygen Reduction on Highly Dispersed Platinum in Acid Electrolytes*. *Journal of the Electrochemical Society*, 1990. **137**(3): p. 845-848.
155. Min, M.-k., et al., *Particle size and alloying effects of Pt-based alloy catalysts for fuel cell applications*. *Electrochimica Acta*, 2000. **45**(25-26): p. 4211-4217.
156. Peuckert, M., et al., *Oxygen Reduction on Small Supported Platinum Particles*. *Journal of the Electrochemical Society*, 1986. **133**(5): p. 944-947.
-

## Bibliography

---

157. Sun, Y., et al., *Collapse in Crystalline Structure and Decline in Catalytic Activity of Pt Nanoparticles on Reducing Particle Size to 1 nm*. Journal of the American Chemical Society, 2007. **129**(50): p. 15465-15467.
  158. Wang, J.X., et al., *Oxygen Reduction on Well-Defined Core-Shell Nanocatalysts: Particle Size, Facet, and Pt Shell Thickness Effects*. Journal of the American Chemical Society, 2009. **131**(47): p. 17298-17302.
  159. Yang, Z., et al., *Systematic Study on the Impact of Pt Particle Size and Operating Conditions on PEMFC Cathode Catalyst Durability*. Journal of the Electrochemical Society, 2011. **158**(11): p. B1439-B1445.
  160. Yano, H., et al., *Particle-size effect of nanoscale platinum catalysts in oxygen reduction reaction: an electrochemical and <sup>195</sup>Pt EC-NMR study*. Physical Chemistry Chemical Physics, 2006. **8**(42): p. 4932-4939.
  161. Bratsch, S.G., *Standard Electrode Potentials and Temperature Coefficients in Water at 298.15 K*. Journal of Physical and Chemical Reference Data, 1989. **18**(1): p. 1-21.
  162. Mukerjee, S. and S. Srinivasan, *Enhanced electrocatalysis of oxygen reduction on platinum alloys in proton exchange membrane fuel cells*. Journal of Electroanalytical Chemistry, 1993. **357**(1-2): p. 201-224.
  163. Anderson, A.B., et al., *Activation Energies for Oxygen Reduction on Platinum Alloys: Theory and Experiment*. The Journal of Physical Chemistry B, 2005. **109**(3): p. 1198-1203.
  164. Wu, J., Yuan, X. Z.; Martin, J. J.; Wang, H.; Zhang, J.; Shen, J.; Wu, S.; Merida, W., *A review of PEM fuel cell durability: Degradation mechanisms and mitigation strategies*. Journal of Power Sources, 2008. **184**(1): p. 104-119.
  165. Tang, L.; Han, B.; Persson, K.; Friesen, C.; He, T.; Sieradzki, K.; Ceder, G. Journal of the American Chemical Society 2009, **132**(2): p. 596-600
  166. Uchimura, M. and S.S. Kocha, *The Impact of Cycle Profile on PEMFC Durability*. ECS Transactions, 2007. **11**(1): p. 1215-1226.
  167. Gu, Z. and P.B. Balbuena, *Dissolution of Oxygen Reduction Electrocatalysts in an Acidic Environment: Density Functional Theory Study*. The Journal of Physical Chemistry A, 2006. **110**(32): p. 9783-9787.
-

- 
168. Han, B., K. Persson, and G. Ceder, *Ab-initio prediction of platinum nanoparticle dissolution in an acid aqueous environment*. Section Title: Electrochemical, Radiational, and Thermal Energy Technology, 2008. **53**(2): p. 707-708.
169. Hu, C.-C. and K.-Y. Liu, *Voltammetric investigation of platinum oxides. I. Effects of ageing on their formation/reduction behavior as well as catalytic activities for methanol oxidation*. *Electrochimica Acta*, 1999. **44**(16): p. 2727-2738.
170. Ofstad, A.B., et al., *Assessment of Platinum Dissolution from a Pt/C Fuel Cell Catalyst: An Electrochemical Quartz Crystal Microbalance Study*. *Journal of the Electrochemical Society*, 2010. **157**(5): p. B621-B627.
171. Yasuda, K., et al., *Platinum dissolution and deposition in the polymer electrolyte membrane of a PEM fuel cell as studied by potential cycling*. *Physical Chemistry Chemical Physics*, 2006. **8**(6): p. 746-752.
172. Kocha, S. *Durable Electrocatalysts and Supports for Automotive PEMFCs in Hydrogen and Fuel Cells*. 2011. Xcaret, Mexico.
173. Andersen, S.M., L. Grahl-Madsen, and E.M. Skou, *Studies on PEM fuel cell noble metal catalyst dissolution*. *Solid State Ionics*. **In Press, Corrected Proof**.
174. Gasteiger, H.A., et al., *Electrocatalysis and Catalyst Degradation Challenges in Proton Exchange Membrane Fuel Cells*, in *Hydrogen and Fuel Cells: Fundamentals, Technologies and Applications*, D. Stolten, Editor. 2010, Wiley-VCH.
175. Darling, R.M. and J.P. Meyers, *Mathematical Model of Platinum Movement in PEM Fuel Cells*. *Journal of the Electrochemical Society*, 2005. **152**(1): p. A242-A247.
176. Garbarino, S., et al., *Effect of Size on the Electrochemical Stability of Pt Nanoparticles Deposited on Gold Substrate*. *The Journal of Physical Chemistry C*, 2010(Journal Article).
177. Komanicky, V., et al., *Stability and Dissolution of Platinum Surfaces in Perchloric Acid*. *Journal of the Electrochemical Society*, 2006. **153**(10): p. B446-B451.
178. Watanabe, M., et al., *Activity and Stability of Ordered and Disordered Co-Pt Alloys for Phosphoric Acid Fuel Cells*. *Journal of the Electrochemical Society*, 1994. **141**(10): p. 2659-2668.
-



## Bibliography

---

179. Houk, L.R., et al., *The Definition of Critical Radius for a Collection of Nanoparticles Undergoing Ostwald Ripening*. Langmuir, 2009(Journal Article).
  180. Prado-Burguete, C., et al., *The effect of oxygen surface groups of the support on platinum dispersion in Pt/carbon catalysts*. Journal of Catalysis, 1989. **115**(1): p. 98-106.
  181. Bezerra, C.W.B., et al., *A review of heat-treatment effects on activity and stability of PEM fuel cell catalysts for oxygen reduction reaction*. Section Title: Electrochemical, Radiational, and Thermal Energy Technology, 2007. **173**(2): p. 891-908.
  182. Ang, S.-Y. and D.A. Walsh, *Highly stable platinum electrocatalysts for oxygen reduction formed using supercritical fluid impregnation*. Journal of Power Sources, 2010. **195**(9): p. 2557-2563.
  183. Meyers, J.P. and R.M. Darling, *Model of Carbon Corrosion in PEM Fuel Cells*. Journal of the Electrochemical Society, 2006. **153**(8): p. A1432-A1442.
  184. Xu, F., et al., *Investigation of the Carbon Corrosion Process for Polymer Electrolyte Fuel Cells Using a Rotating Disk Electrode Technique*. Journal of the Electrochemical Society, 2010. **157**(8): p. B1138-B1145.
  185. Kou, R., et al., *Stabilization of Electrocatalytic Metal Nanoparticles at Metal–Metal Oxide–Graphene Triple Junction Points*. Journal of the American Chemical Society, 2011 **133** (8) p. 2541-2547.
  186. Huang, S.-Y., et al., *Development of a Titanium Dioxide-Supported Platinum Catalyst with Ultrahigh Stability for Polymer Electrolyte Membrane Fuel Cell Applications*. Journal of the American Chemical Society, 2009(Journal Article).
  187. Avasarala, B. and P. Haldar, *Electrochemical Oxidation Behavior of Titanium Nitride based Catalyst Supports under PEM Fuel Cell Conditions*. Electrochimica Acta. **In Press, Accepted Manuscript**.
  188. Takasaki, F., et al., *Carbon-Free Pt Electrocatalysts Supported on SnO<sub>2</sub> for Polymer Electrolyte Fuel Cells: Electrocatalytic Activity and Durability*. Journal of the Electrochemical Society, 2011. **158**(10): p. B1270-B1275.
  189. Sharma, S. and B.G. Pollet, *Support materials for PEMFC and DMFC electrocatalysts—A review*. Journal of Power Sources, 2012. **208**(0): p. 96-119.
-

- 
190. Ferreira, P.J., et al., *Instability of Pt/C Electrocatalysts in Proton Exchange Membrane Fuel Cells*. Journal of the Electrochemical Society, 2005. **152**(11): p. A2256-A2271.
191. Panha, K., et al., *Accelerated durability testing via reactants relative humidity cycling on PEM fuel cells*. Applied Energy. **In Press, Corrected Proof**.
192. Borup, R.L., et al., *PEM fuel cell durability with transportation transient operation*. Section Title: Electrochemical, Radiational, and Thermal Energy Technology, 2006. **3**(1, Proton Exchange Membrane Fuel Cells 6): p. 879-886.
193. Garland, N., T. Benjamin, and J. Kopasz, *DOE Fuel Cell Program: Durability Technical Targets and Testing Protocols*. ECS Transactions, 2007. **11**(1): p. 923-931.
194. Shao, Y., et al., *Durability Study of Pt/C and Pt/CNTs Catalysts under Simulated PEM Fuel Cell Conditions*. Journal of the Electrochemical Society, 2006. **153**(6): p. A1093-A1097.
195. Dam, V.A.T. and F.A. de Bruijn, *The Stability of PEMFC Electrodes*. Journal of the Electrochemical Society, 2007. **154**(5): p. B494-B499.
196. Mitsushima, S., et al., *Dissolution of platinum in acidic media*. Electrochimica Acta, 2008. **54**(2): p. 455-460.
197. Schlögl, K., et al., *Identical-location TEM investigations of Pt/C electrocatalyst degradation at elevated temperatures*. Journal of Electroanalytical Chemistry, 2011. **662**(2): p. 355-360.
198. Okada, T., et al., *Ion and water transport characteristics of Nafion® membranes as electrolytes*. Electrochimica Acta, 1998. **43**(24): p. 3741-3747.
199. Ikeda, K., N. Nonoyama, and Y. Ikogi, *Analysis of ionomer coverage of Pt surface in PEMFC*. ECS Transactions, 2010. **33**(1): p. 1189-1197.
200. Qi, Z., *Electrochemical Methods for Catalyst Activity Evaluation*, in *PEM Fuel Cell Catalysts and Catalyst Layers*, J. Zhang, Editor. 2008, Springer. p. 547.
201. Zhang, J. and J. Zhang, *Catalyst Layer/MEA Performance Evaluation*, in *PEM Fuel Cell Catalysts and Catalyst Layers*, J. Zhang, Editor. 2008, Springer. p. 965.
-

## Bibliography

---

202. Millington, B., S. Du, and B.G. Pollet, *The effect of materials on proton exchange membrane fuel cell electrode performance*. Journal of Power Sources, 2011. **196**(21): p. 9013-9017.
203. Silva, V.B. and A. Rouboa, *Hydrogen-fed PEMFC: Overvoltage analysis during an activation procedure*. Journal of Electroanalytical Chemistry, 2012. **671**(0): p. 58-66.
204. Carter, R.N., et al., *Artifacts in Measuring Electrode Catalyst Area of Fuel Cells through Cyclic Voltammetry*. ECS Transactions, 2007. **11**(1): p. 403-410.
205. Raistrick, I.D., D.R. Franceschetti, and J.R. Macdonald, *Theory*, in *Impedance Spectroscopy*. 2005, John Wiley & Sons, Inc. p. 27-128.
206. Martin, M.H. and A. Lasia, *Influence of experimental factors on the constant phase element behavior of Pt electrodes*. Electrochimica Acta, 2011. **56**(23): p. 8058-8068.
207. Ciureanu, M., H. Wang, and Z. Qi, *Electrochemical Impedance Study of Membrane-Electrode Assemblies in PEM Fuel Cells. II. Electrooxidation of H<sub>2</sub> And H<sub>2</sub>/Co Mixtures on Pt/Ru-Based Gas-Diffusion Electrodes*. The Journal of Physical Chemistry B, 1999. **103**(44): p. 9645-9657.
208. Eikerling, M. and A.A. Kornyshev, *Electrochemical impedance of the cathode catalyst layer in polymer electrolyte fuel cells*. Journal of Electroanalytical Chemistry, 1999. **475**(2): p. 107-123.
209. Nara, H., et al., *Impedance Analysis Counting Reaction Distribution on Degradation of Cathode Catalyst Layer in PEFCs*. Journal of the Electrochemical Society, 2011. **158**(9): p. B1184-B1191.
210. Yuan, X.-Z., et al., *EIS Applications*, in *Electrochemical Impedance Spectroscopy in PEM Fuel Cells*. 2010, Springer: London. p. 263-345.
211. Bonanos, N., B.C.H. Steele, and E.P. Butler, *Applications of Impedance Spectroscopy*, in *Impedance Spectroscopy*. 2005, John Wiley & Sons, Inc. p. 205-537.
212. Johnson, D., *ZView*. 2012, Scribner Associates.

- 
213. Reshетенko, T.V., et al., *Systematic study of back pressure and anode stoichiometry effects on spatial PEMFC performance distribution*. *Electrochimica Acta*, 2011. **56**(24): p. 8700-8710.
214. Zhang, G., et al., *Simultaneous measurement of current and temperature distributions in a proton exchange membrane fuel cell*. *Journal of Power Sources*, 2010. **195**(11): p. 3597-3604.
215. Brett, D., et al., *What Happens Inside a Fuel Cell? Developing an Experimental Functional Map of Fuel Cell Performance*. *ChemPhysChem*, 2010
216. Bender, G., T.A. Zawodzinski, and A.P. Saab, *Fabrication of high precision PEFC membrane electrode assemblies*. *Journal of Power Sources*, 2003. **124**(1): p. 114-117.
217. Xie, J., et al., *Porosimetry of MEAs Made by "Thin Film Decal" Method and Its Effect on Performance of PEFCs*. *Journal of the Electrochemical Society*, 2004. **151**(11): p. A1841-A1846.
218. Calvo, E.J., *Chapter 1 Fundamentals. The Basics of Electrode Reactions*, in *Comprehensive Chemical Kinetics*, C.H. Bamford and R.G. Compton, Editors. 1986, Elsevier. p. 1-78.
219. Lee, M., et al., *New evaluation method for the effectiveness of platinum/carbon electrocatalysts under operating conditions*. *Electrochimica Acta*, 2010. **55**(28): p. 8504-8512.
220. Nørskov, J.K., et al., *Universality in Heterogeneous Catalysis*. *Journal of Catalysis*, 2002. **209**(2): p. 275-278.
221. Bligaard, T. and J.K. Nørskov, *Heterogeneous catalysis*, in *Chemical Bonding at Surfaces and Interfaces*. 2008, Elsevier: Amsterdam. p. 255-321.
222. Jalan, V. and E.J. Taylor, *Importance of Interatomic Spacing in Catalytic Reduction of Oxygen in Phosphoric Acid*. *Journal of the Electrochemical Society*, 1983. **130**(11): p. 2299-2302.
223. Mukerjee, S. and S. Srinivasan, *Enhanced electrocatalysis of oxygen reduction on platinum alloys in proton exchange membrane fuel cells*. *Journal of Electroanalytical Chemistry*, 1993. **357**(1-2): p. 201-224.
-

## Bibliography

---

224. Mukerjee, S., et al., *Role of Structural and Electronic Properties of Pt and Pt Alloys on Electrocatalysis of Oxygen Reduction*. Journal of the Electrochemical Society, 1995. **142**(5): p. 1409-1422.
225. Liu, H., D. Xia, and J. Zhang, *Platinum-based Alloy Catalysts for PEM Fuel Cells*, in *PEM Fuel Cell Catalysts and Catalyst Layers*, J. Zhang, Editor. 2008, Springer. p. 631.
226. Mavrikakis, M., B. Hammer, and J.K. Nørskov, *Effect of Strain on the Reactivity of Metal Surfaces*. Physical Review Letters, 1998. **81**(13): p. 2819.
227. Tarasevich, M., A. Sadkowsky, and E.B. Yeager, *Oxygen Electrochemistry*, in *Comprehensive Treatise in Electrochemistry*, B.E. Conway, et al., Editors. 1983, Plenum Press: New York. p. 301.
228. Stephens, I.E.L., et al., *Understanding the electrocatalysis of oxygen reduction on platinum and its alloys*. Energy & Environmental Science, 2012.
229. Stonehart, P., "Development of Advanced Noble Metal-Alloy Electrocatalysts for Phosphoric Acid Fuel Cells (PAFC)". Berichte der Bunsengesellschaft für physikalische Chemie, 1990. **94**(9): p. 913-921.
230. Zhang, J., et al., *Synthesis and Oxygen Reduction Activity of Shape-Controlled Pt<sub>3</sub>Ni Nanopolyhedra*. Nano Letters, 2010(Journal Article).
231. Paulus, U.A., et al., *Oxygen Reduction on Carbon-Supported Pt–Ni and Pt–Co Alloy Catalysts*. The Journal of Physical Chemistry B, 2002. **106**(16): p. 4181-4191.
232. Bardi, U., et al., *Structure of the cobalt oxide layer formed by low pressure oxidation of the Pt<sub>80</sub>Co<sub>20</sub>(100) surface: a study by LEED, LEIS and XPS*. Surface Science, 1991. **251–252**(0): p. 727-730.
233. Maillard, F., et al., *Durability of Pt<sub>3</sub>Co/C nanoparticles in a proton-exchange membrane fuel cell: direct evidence of bulk Co segregation to the surface*. Electrochemistry Communications. **In Press, Accepted Manuscript** (Journal Article).
234. Menning, C. and J. Chen, *Theoretical Prediction and Experimental Verification of Stability of Pt–3d–Pt Subsurface Bimetallic Structures: From Single Crystal Surfaces to Polycrystalline Films*. Topics in Catalysis, 2010. **53**(5): p. 338-347.
-

- 
235. Bardi, U., B.C. Beard, and P.N. Ross, *Surface oxidation of a Pt-20% CO alloy: An x-ray photoelectron spectroscopy and low-energy electron diffraction study on the [100] and [111] oriented single-crystal surfaces*. Journal of Vacuum Science & Technology A: Vacuum, Surfaces, and Films, 1988. **6**(3): p. 665-670.
236. Antolini, E., J.R.C. Salgado, and E.R. Gonzalez, *The stability of Pt-M (M = first row transition metal) alloy catalysts and its effect on the activity in low temperature fuel cells: A literature review and tests on a Pt-Co catalyst*. Special issue including selected papers presented at the International Workshop on Molten Carbonate Fuel Cells and Related Science and Technology 2005 together with regular papers, 2006. **160**(2): p. 957-968.
237. Li, H., et al., *Effect of Co<sup>2+</sup> on oxygen reduction reaction catalyzed by Pt catalyst, and its implications for fuel cell contamination*. Electrochimica Acta. **In Press, Accepted Manuscript** (Journal Article).
238. Ma, Y. and P.B. Balbuena, *Surface Properties and Dissolution Trends of Pt3M Alloys in the Presence of Adsorbates*. The Journal of Physical Chemistry C, 2008. **112**(37): p. 14520-14528.
239. Menning, C.A. and J.G. Chen, *Stability and dissolution of monolayer Pt-3d bimetallic electrocatalysts*. Section Title: Electrochemical, Radiational, and Thermal Energy Technology, 2008. **53**(2): p. 719-720.
240. Menning, C.A., H.H. Hwu, and J.G. Chen, *Experimental and Theoretical Investigation of the Stability of Pt-3d-Pt(111) Bimetallic Surfaces under Oxygen Environment*. Section Title: Surface Chemistry and Colloids, 2006. **110**(31): p. 15471-15477.
241. GreeleyJ, et al., *Alloys of platinum and early transition metals as oxygen reduction electrocatalysts*. Nat Chem, 2009. **1**(7): p. 552-556.
242. Yoo, S. J.; Lee, K.-S.; Hwang, S. J.; Cho, Y.-H.; Kim, S.-K.; Yun, J. W.; Sung, Y.-E.; Lim, T.-H., *Pt<sub>3</sub>Y electrocatalyst for oxygen reduction reaction in proton exchange membrane fuel cells*. International Journal of Hydrogen Energy, 2012, **37**, (12), 9758-9765..
-

## Bibliography

---

243. Abe, H., et al., *Electrocatalytic Performance of Fuel Oxidation by Pt<sub>3</sub>Ti Nanoparticles*. Journal of the American Chemical Society, 2008. **130**(16): p. 5452-5458.
244. Carbone, L. and P.D. Cozzoli, *Colloidal heterostructured nanocrystals: Synthesis and growth mechanisms*. Nano Today, 2010. **5**(5): p. 449-493.
245. Fiermans, L., et al., *Pd Segregation to the Surface of Bimetallic Pt–Pd Particles Supported on H-β Zeolite Evidenced with X-Ray Photoelectron Spectroscopy and Argon Cation Bombardment*. Journal of Catalysis, 2000. **193**(1): p. 108-114.
246. Lee, H., et al., *Localized Pd Overgrowth on Cubic Pt Nanocrystals for Enhanced Electrocatalytic Oxidation of Formic Acid*. Journal of the American Chemical Society, 2008. **130**(16): p. 5406-5407.
247. Zhou, S., et al., *Pt–Cu Core–Shell and Alloy Nanoparticles for Heterogeneous NO<sub>x</sub> Reduction: Anomalous Stability and Reactivity of a Core–Shell Nanostructure*. Angewandte Chemie International Edition, 2005. **44**(29): p. 4539-4543.
248. Babu, P.K., et al., *Electronic Alterations Caused by Ruthenium in Pt–Ru Alloy Nanoparticles as Revealed by Electrochemical NMR*. The Journal of Physical Chemistry B, 2003. **107**(31): p. 7595-7600.
249. Wang, L.-L. and D.D. Johnson, *Predicted Trends of Core@Shell Preferences for 132 Late Transition-Metal Binary-Alloy Nanoparticles*. Journal of the American Chemical Society, 2009(Journal Article).
250. Jennings, P.C., B.G. Pollet, and R.L. Johnston, *Theoretical studies of Pt-Ti nanoparticles for potential use as PEMFC electrocatalysts*. Physical Chemistry Chemical Physics, 2012. **14**(9): p. 3134-3139.
251. Mayrhofer, K.J.J., et al., *Adsorbate-Induced Surface Segregation for Core–Shell Nanocatalysts*. Angewandte Chemie International Edition, 2009. **48**(19): p. 3529-3531.
252. Mayrhofer, K.J.J., et al., *Degradation of Carbon-Supported Pt Bimetallic Nanoparticles by Surface Segregation*. Journal of the American Chemical Society, 2009. **131**(45): p. 16348-16349.
-

- 
253. Koh, S. and P. Strasser, *Electrocatalysis on Bimetallic Surfaces: Modifying Catalytic Reactivity for Oxygen Reduction by Voltammetric Surface Dealloying*. Journal of the American Chemical Society, 2007. **129**(42): p. 12624-12625.
254. Mani, P., R. Srivastava, and P. Strasser, *Dealloyed Pt-Cu Core-Shell Nanoparticle Electrocatalysts for Use in PEM Fuel Cell Cathodes*. Section Title: Electrochemical, Radiational, and Thermal Energy Technology, 2008. **112**(7): p. 2770-2778.
255. Koh, S. and P. Strasser, *Lattice-strained Pt nanoparticle catalysts for the electroreduction of oxygen at PEMFC cathodes*. Prepr.Symp.- Am.Chem.Soc., Div.Fuel Chem., 2006. **51**(2): p. 761.
256. Zhang, J., et al., *Platinum Monolayer Electrocatalysts for O<sub>2</sub> Reduction: Pt Monolayer on Pd(111) and on Carbon-Supported Pd Nanoparticles*. The Journal of Physical Chemistry B, 2004. **108**(30): p. 10955-10964.
257. Habas, S.E., et al., *Shaping binary metal nanocrystals through epitaxial seeded growth*. Nat Mater, 2007. **6**(9): p. 692-697.
258. Li, Y., et al., *Synthesis of bimetallic Pt-Pd core-shell nanocrystals and their high electrocatalytic activity modulated by Pd shell thickness*. Nanoscale, 2012. **4**(3): p. 845-851.
259. Chen, Y., et al., *Ni@Pt Core-Shell Nanoparticles: Synthesis, Structural and Electrochemical Properties*. The Journal of Physical Chemistry C, 2008. **112**(5): p. 1645-1649.
260. Park, I.-S., et al., *Electrocatalytic activity of carbon-supported Pt-Au nanoparticles for methanol electro-oxidation*. Surface Imaging/Spectroscopy at Solid/Liquid Interface (ISSIS) - Selection of papers from the International Symposium on Surface Imaging/Spectroscopy at Solid/Liquid Interface (ISSIS) , May 28 to June 1, 2006, Krakow, Poland, 2007. **52**(18): p. 5599-5605.
261. Zhao, D. and B.-Q. Xu, *Platinum covering of gold nanoparticles for utilization enhancement of Pt in electrocatalysts*. Physical Chemistry Chemical Physics, 2006. **8**(43): p. 5106-5114.
262. Alayoglu, S. and B. Eichhorn, *Rh-Pt Bimetallic Catalysts: Synthesis, Characterization, and Catalysis of Core-Shell, Alloy, and Monometallic*
-



## Bibliography

---

- Nanoparticles*. Journal of the American Chemical Society, 2008, 130, (51), 17479-17486.
263. Alayoglu, S., et al., *Ru-Pt core-shell nanoparticles for preferential oxidation of carbon monoxide in hydrogen*. Nat Mater, 2008. 7(4): p. 333-338.
264. Peng, Z. and H. Yang, *Designer platinum nanoparticles: Control of shape, composition in alloy, nanostructure and electrocatalytic property*. Nano Today, 2009. 4(2): p. 143-164.
265. Chambers, S.A., *Epitaxial growth and properties of thin film oxides*. Surface Science Reports, 2000. 39(5-6): p. 105-180.
266. Venables, J., *Atomic Interactions and Surface Processes in Heteroepitaxy*, in *Thin Films: Heteroepitaxial Systems*. 1999, World Scientific Publishing Co.
267. Spedding, F.H., A.H. Daane, and K.W. Herrmann, *The crystal structures and lattice parameters of high-purity scandium, yttrium and the rare earth metals*. Acta Crystallographica, 1956. 9(7): p. 559-563.
268. Pawar, R.R. and V.T. Deshpande, *The anisotropy of the thermal expansion of [alpha]-titanium*. Acta Crystallographica Section A, 1968. 24(2): p. 316-317.
269. Mahouche-Chergui, S., et al., *Aryl diazonium salts: a new class of coupling agents for bonding polymers, biomacromolecules and nanoparticles to surfaces*. Chemical Society Reviews, 2011. 40(7): p. 4143-4166.
270. Ghosh, D. and S. Chen, *Palladium nanoparticles passivated by metal-carbon covalent linkages*. Journal of Materials Chemistry, 2008. 18(7): p. 755-762.
271. Mirkhalaf, F., J. Paprotny, and D.J. Schiffrin, *Synthesis of Metal Nanoparticles Stabilized by Metal-Carbon Bonds*. Journal of the American Chemical Society, 2006. 128(23): p. 7400-7401.
272. Ghosh, D., et al., *Titanium Nanoparticles Stabilized by Ti-C Covalent Bonds*. Chemistry of Materials, 2008. 20(4): p. 1248-1250.
273. Bönemann, H., et al., *Preparation, characterization, and application of fine metal particles and metal colloids using hydrotriorganoborates*. Journal of Molecular Catalysis, 1994. 86(1-3): p. 129-177.
274. Wagner, C.D., et al., *NIST X-Ray Photoelectron Spectroscopy Database 2007*.
-

- 
275. Fairley, N., *CasaXPS Manual*. 2009.
276. Derry, G.N. and P.N. Ross, *Valence and core state modifications in Pt<sub>3</sub>Ti*. Solid State Communications, 1984. **52**(2): p. 151-154.
277. Schierbaum, K.D., et al., *The interaction of Pt with TiO<sub>2</sub>(110) surfaces: a comparative XPS, UPS, ISS, and ESD study*. Surface Science, 1996. **345**(3): p. 261-273.
278. Peuckert, M. and H.P. Bonzel, *Characterization of oxidized platinum surfaces by X-ray photoelectron spectroscopy*. Surface Science, 1984. **145**(1): p. 239-259.
279. Jiang, D.-e., B.G. Sumpter, and S. Dai, *Structure and Bonding between an Aryl Group and Metal Surfaces*. Journal of the American Chemical Society, 2006. **128**(18): p. 6030-6031.
280. Achar, S. and V.J. Catalano, *A search for the elusive red form in substituted Pt(II) bipyridine complexes*. Polyhedron, 1997. **16**(9): p. 1555-1561.
281. Paul, A.K., et al., *Some potential antitumor 2,2'-dipyridylamine Pt(II)/Pd(II) complexes with amino acids: Their synthesis, spectroscopy, DNA binding, and cytotoxic studies*. Journal of Inorganic Biochemistry, 1993. **50**(1): p. 9-20.
282. Falvello, L.R., et al., *Evidence of C<sub>1</sub> activation of acetone by a platinum(II) complex. Synthesis and structural characterization of [Pt(CH<sub>2</sub>COCH<sub>3</sub>)Cl(bipy)] (bipy = 2,2'-bipyridyl)*. Inorganica Chimica Acta, 1997. **264**(1-2): p. 297-303.
283. Kolp, B., et al., *Platinum(II) Compounds with Enantiomerically Pure Bis(pinene)-Fused Bipyridine Ligands – Diimine-Dichloro Complexes and Their Substitution Reactions*. European Journal of Inorganic Chemistry, 2001. **2001**(5): p. 1207-1220.
284. Goski, C.G., *Handbook of Electrochemistry*. 2007: Elsevier. 892.

## Appendices

### Calculation of particle size distributions from TEM images using ImageJ

The following method was developed to derive particle size distributions from TEM micrographs of nanoparticles dispersed on support materials using the ImageJ image analysis software:

Open file for analysis in ImageJ

1. Zoom in on the Scale bar
2. Select 'Line Selection' tool and draw a straight line (hold "Shift" whilst dragging) across the scale bar
3. Analyse → Set Scale...
  - a. "Distance in pixels" should be completed for you with the length of the line you just drew. If not, close the "Set Scale" dialog box and repeat steps 2 & 3.
  - b. "Known Distance" is the length of the scale bar on the image (in nanometers, or micrometres)
  - c. "Unit of Length" – type in "nm" or "µm" as appropriate
  - d. Click OK

This sets up ImageJ to measure lengths in nm (or µm) instead of the default pixels. You should see the image dimensions reported in the proper units in the status bar above the image. If not, repeat steps 3 & 4.

4. Press Ctrl+Shift+A to clear line selection
5. Right click on image → Original Scale
6. Apply an Unsharp Mask
  - a. Process → Filters → Unsharp Mask...
  - b. "Radius" = 2.0 px
  - c. "Mask Weight" = 0.8
  - d. Click OK

---

Image should appear sharper, or less blurred. We do this to increase contrast at the edges of the particles, so that they are better defined for the next process...

7. Apply a Fast Fourier Transform band pass filter
  - a. Process → FFT → Band Pass...
  - b. Upper limit = 18 px (remove all 'features' with dimension > 18 px – need to change depending on resolution of image)
  - c. Lower limit = 3px (excludes random noisy pixels)
  - d. Click OK

The FFT Bandpass filter removes features whose size falls outside a certain length scale from the image. Do this to remove all large agglomerates and 'opaque' regions of the image. Requires that 'features' (particles) are well-defined in the image – hence the Unsharp mask in the previous step.

The resulting image should appear 'greyed-out', except for small particles which should stand out as being darker than the background.

8. Apply a contrast Threshold...
  - a. Image → Adjust → Threshold (Ctrl+Shift+T)
  - b. Change the sliders so that only the particles are selected in red.
  - c. Click "Apply" and close the Threshold dialog box.

9. Run particle size analysis
  - a. Analyse → Analyse Particles...
  - b. Size(nm<sup>2</sup>) = 3-2000 (if in pixels instead of nm, repeat steps 2-4)
  - c. Circularity = 0.85-1.00
  - d. Show: Outlines
  - e. Display Results : Yes
  - f. Clear Results: Yes
  - g. Click OK

This process identifies all 'particles' of a given circularity and reports the area of each particle's projected image in nm<sup>2</sup> (provided scale is properly set in steps 2-4). Using circularity range 0.85-1.00 helps to exclude agglomerates by ignoring irregularly-shaped particles. The results are

## Bibliography

---

displayed in a new image, with the each particle numbered and outlined. (This image can then be superimposed onto the original to check that particles have been correctly identified, if desired)

### 10. Collect results

- a. Select the “Results” window
- b. Select All (Ctrl+A)
- c. Copy (Ctrl+C)
- d. Paste into Excel for analysis

---

## Preparation of Reversible Hydrogen Electrodes

A 100 mesh Pt gauze (Alfa Aesar) was welded to a 1mm diameter Pt wire. The gauze was platinised by chronoamperometric electrodeposition for 60s at 0.2V vs Ag/AgCl in a 20mM solution of  $\text{H}_2\text{PtCl}_6$  or  $\text{K}_2\text{PtCl}_6$  (Sigma) in 0.5 M KCl. The platinised gauze was then sealed into a glass pipette tip as shown in the figure below by heating with a blowtorch. The electrode was filled with 0.1M  $\text{HClO}_4$  using a syringe with a stainless steel needle, taking care to remove all air bubbles. The electrode was placed into a 0.1M  $\text{HClO}_4$  solution and connected to the -ve terminal of a 30V power supply. A separate Pt wire counter electrode was connected to the +ve terminal. A bubble of hydrogen was generated inside the electrode compartment by electrolysis at 20-30 V. The electrode was transferred carefully to the experimental cell to avoid leakage of the filling solution and ingress of air.

